

High-performance computing and laboratory experiments on strato-rotational instabilities

**Von der Fakultät für Maschinenbau, Elektro- und Energiesysteme
der Brandenburgischen Technischen Universität Cottbus-Senftenberg
zur Erlangung des akademischen Grades eines
Doktors der Ingenieurwissenschaften**

genehmigte Dissertation

vorgelegt von

Master of Science (M. Sc.)

Gabriel MALTESE MELETTI DE OLIVEIRA

geboren am 8.Oktober.1988, Rio de Janeiro (Brasilien)

Vorsitzender: Uwe Harlander (BTU CS)

Gutachter : Innocent Mutabazi (Université du Havre)

Gutachter: Christoph Egbers (BTU CS)

Tag der mündlichen Prüfung: 18.Dezember.2020

High-performance computing and laboratory experiments on strato-rotational instabilities

Brandenburg University of Technology Cottbus–Senftenberg
Faculty of Mechanical Engineering, Electrical and Energy Systems
Chair of Aerodynamics and Fluid mechanics

Aix-Marseille University

École doctorale Sciences pour l'Ingénieur: Mécanique, Physique, Micro et Nanoélectronique

Laboratoire de Mécanique, Modélisation & Procédés Propres (M2P2)

Thesis presented to obtain the academic degree of Doctor of Engineering at the Brandenburg University of Technology Cottbus–Senftenberg/Ph.D. in Mechanics and Physics of Fluids at the Aix-Marseille University

presented by

Master of Science (M. Sc.)

Gabriel MALTESE MELETTI DE OLIVEIRA

Born on the 06th of October 1988 in Petropolis, Rio de Janeiro (Brazil)

The defense occurred on the 18/Dec./2020. The committee is composed by:

Reviewer:	Innocent Mutabazi (Université du Havre)
Reviewer:	Christoph Egbers (BTU CS)
Referee:	Caroline Nore (Université Paris Saclay)
Referee:	Nikki Verkauteren (FU-Berlin)
Invited/Guest:	Fred Feudel (Universität Potsdam)
Invited/Guest:	Stéphane Abide (Université de Perpignan)
Supervisor:	Uwe Harlander (BTU CS)
Supervisor:	Stéphane Viazzo (Aix-Marseille Université)

Instabilités strato-rotationnelles : calculs intensifs et expériences

Aix-Marseille Université

École doctorale Sciences pour l'Ingénieur: Mécanique, Physique, Micro et Nanoélectronique

Laboratoire de Mécanique, Modélisation & Procédés Propres (M2P2)

Université Technique de Brandebourg Cottbus-Senftenberg

École doctorale pour l'Ingénierie mécanique, systèmes électriques et énergétiques

Laboratoire d'Aérodynamique et mécanique des fluides (LAS)

Thèse présentée pour obtenir le grade universitaire
de docteur en Mécanique et Physique des Fluides

Présentée par

Gabriel MALTESE MELETTI DE OLIVEIRA

né le 06 octobre 1988 à Petropolis, Rio de Janeiro (Brésil)

Thèse soutenue publiquement le 18 décembre 2020 devant le jury composé de:

Rapporteur:	Innocent Mutabazi (Université du Havre)
Rapporteur:	Christoph Egbers (BTU CS)
Examinatrice:	Caroline Nore (Université Paris Saclay)
Examinatrice:	Nikki Verkauteren (FU-Berlin)
Invité:	Fred Feudel (Universität Potsdam)
Invité:	Stéphane Abide (Université de Perpignan)
Directeur de thèse:	Uwe Harlander (BTU CS)
Directeur de thèse:	Stéphane Viazzo (Aix-Marseille Université)

“C’est véritablement utile puisque c’est joli”
– A. de Saint-Exupéry –

Contents

Abstract	xiii
1 Introduction	1
1.1 Introduction to Strato-Rotational Instabilities in Accretion Discs	1
1.2 Outline	5
2 Fundamentals	7
2.1 Equations of motion	7
2.1.1 Stable density stratification	9
2.2 Wave propagation in a fluid	10
2.2.1 Gravity waves	13
2.2.2 Inertial waves	13
2.2.3 Inertial-gravity waves	14
2.3 Taylor-Couette Instability	15
2.4 The Strato-Rotational Instability (SRI)	19
2.5 Ekman boundary layers	21
2.6 Turbulence Energy equations	22
2.6.1 Turbulent energy spectra	25
2.7 Non-dimensional variables	27
3 Experimental methods	31
3.1 Experimental Setup	32
3.2 Particle image velocimetry (PIV) method	34
3.2.1 PIV Cross-correlation	36
3.2.2 Polynomial undistortion Method	37
3.3 PIV error measurements	39
3.3.1 Convergence and number of experimental images acquired	40
3.4 Temperature stratification	41
4 Numerical Methods	43
4.1 Problem formulation	43
4.2 Time discretization and projection method	45
4.2.1 Time discretization	45
4.2.2 Projection method	46
4.3 Spatial discretization	48
4.3.1 Variable layout	48
4.3.2 Compact schemes	49
4.3.3 Solution of Poisson/Helmoltz equations	51
4.4 High-performance computing	52

4.4.1	The pencil decomposition	52
4.4.2	Parallel Diagonal Dominant	54
4.5	Numerical code utilization	55
4.5.1	Code description	55
4.5.2	Example of a numerical simulation	57
4.5.3	Flow control parameters	57
5	Numerical and experimental observations	63
5.1	Comparison of experimental and numerical SRI data	63
5.1.1	Numerical and experimental observations of the SRI linear stability marginal curves	67
6	Pattern formation	71
6.1	Pattern changes associated with the amplitude modulations	74
6.1.1	Circulation cells and spiral inclination	77
6.2	Influence of rotation, stratification, and geometry in the SRI spiral patterns . . .	78
6.2.1	The role of stratification	79
6.2.2	Influence of the Reynolds numbers in the amplitude modulations	81
6.2.3	Cavity geometry changes	84
6.2.3.1	Smaller height	84
6.2.3.2	Larger cavity heights	85
6.2.3.3	Wide gap and critical layer position	89
6.3	Energy spectra	94
6.4	Wavenumbers of upward and downward traveling spirals	99
6.5	Modes and spiral components separation	101
6.6	Toy model	106
6.7	Impacts of the SRI modulation on momentum transport	108
7	Conclusions	113
A	Appendices	119
A.1	Radon transforms	119
	References	121

List of Figures

1.1	(a) Image of a circumstellar disk surrounding a young star called HL Tauri, located at the Tauri constellation, observed by the Atacama Large Millimeter/submillimeter Array (ALMA) collaboration. Image obtained from (Brogan et al. 2015). (b) Image of an accretion disc around the young <i>AB Aurigae</i> star, obtained by the ESO's Very Large Telescope (VLT) spotting signs of planet birth (Boccaletti et al. 2020), highlighting the spiral structure observed in accretion disks.	2
-----	---	---

1.2	Velocity isosurfaces snapshots of the SRI showing its non-axisymmetric spirals obtained by numerical simulation with $\mu = 0.35$, $\eta = 0.517$, a linear stable axial temperature gradient with $\partial T/\partial z \approx 5.7K/m$, $Fr \approx 1.5$ and $Re = 400$. The aspect ratio between cavity height and gap is $\Gamma = H/(r_{out} - r_{in}) = 10$. No-slip and impermeable Dirichlet boundary conditions are imposed ($u_\phi(r_{in}) = \Omega_{in}r_{in}$, $u_\phi(r_{out}) = \Omega_{out}r_{out}$, $u_z(z = 0) = 0$, $u_z(z = H) = 0$, $u_r(r_{in}) = 0$, $u_r(r_{out}) = 0$), and the bottom and top lids of the cavity rotate with the outer cylinder rotation Ω_{out}	3
1.3	SRI marginal linear stability curves redrawn from Rüdiger et al. (2017) for 3 different values of Rn . Bigger values of Rn (and N) lead to larger instability regions. The black dashed vertical line in the left represents the Rayleigh limit $\mu = \eta^2$, which separates stable and unstable non-stratified TC cases (any to the left of this line in the diagram would be TC unstable). The green dashed vertical line in the right represents the Keplerian line $\mu = \eta^{3/2}$. SRI unstable (red circles) and stable (blue crosses) cases with $\eta = 0.517$, $Rn \approx 250$, $\mu = 0.35$ with different Reynolds numbers were investigated numerically and experimentally in this article.	4
2.1	Cartesian and cylindrical coordinates.	8
2.2	Schematic representation of wave crests and of the wave package propagating in the $x - y$ plane, adapted from Kundu and Cohen (2001), Pedlosky (2013). The crest spacing along the coordinate axes is larger than the wavelength $\lambda = \frac{2\pi}{K}$ inside the package. The vector diagram on the top left side of the image shows how the trace velocities c_x and c_y are combined to give the phase velocity vector c . In the wave package, it is represented how every individual crests moves with phase speed c , and how the whole package moves with a different group velocity c_g , of amplitude $A(\xi, t)$ in the direction of the wavenumber \mathbf{K}	11
2.3	Schematic representation of (a) Wavenumber vector (\mathbf{K}) direction; (b) Phase velocity travelling in the direction of the wave number vector and orthogonal to the group velocity, as observed in internal waves generated by buoyancy and rotation. Reproduced from Pedlosky (2013).	12
2.4	Schematic representation of Taylor vortices with counter-rotating pair of rolls reproduced from Cross and Hohenberg (1993).	15
2.5	Different Taylor vortex spiral regimes visualized using machine oil with aluminum powder, reproduced by Van Dyke (1982). The different regimes are obtained by increasing the inner cylinder angular velocity (from left to right) while keeping the outer cylinder at rest. Considering the critical Reynolds numbers Re_{cr} where the spirals appear, and the Reynolds numbers based on the inner cylinder Re (a) $Re = 1.16Re_{cr}$ (b) $Re = 8.5Re_{cr}$ (c) $Re = 1625Re_{cr}$	18
2.6	Different Taylor-Couette Regimes in cavities with long cylinders co-axially rotating with a different inner and outer Reynolds numbers (respectively represented by R_i , in the y -axis and R_o , in the x -axis). The diagram shows regimes for counter-rotating ($R_o < 0$) and co-rotating cylinders ($R_o > 0$), and is reproduced from Andereck et al. (1986).	19

2.7	Marginal instability curves obtained by Rüdiger et al. (2017) with linear stability analysis for different values of Rn . The horizontal axis shows the ratio between outer and inner cylinder angular velocity (μ), and the vertical axis shows the Reynolds numbers. The vertical black dashed line on the left shows the Rayleigh limit, which separates non-stratified TC unstable and stable regimes, as indicated in the diagram (rotation ratios to the left of the Rayleigh line are TC unstable). The green vertical dashed line on the right represents the Keplerian line. The regions inside the marginal instability curves (for different Rn) represent SRI unstable solutions according to the linear theory.	21
2.8	Experimental end gap effects visualized with Kalliroscope particles, reproduced from Shionoya (1987). (a) Inner cylinder at rest ($Re = 0$) and outer cylinder rotating with $Re_{out} = 1000$; Kalliroscope flakes fill only the lower half of the cylinder as the system is spun up from rest. (b) Laminar TC profile obtained for cylinders rotating in the same direction with $Re = 1124$, and $\mu = 0.89$; (c) Laminar TC profile obtained for cylinders rotating in the same with $Re = 4005$, $\mu = 0.89$; (d) Laminar Taylor vortices with $Re = 240$ and counter-rotating cylinders with $\mu = -1.25$	23
2.9	Energy spectra schematically representing (a) High Reynolds number Kolmogorov turbulence reproduced from Pope (2001); (b) Two-dimensional turbulent flow with an energy and enstrophy cascade reproduced from Kyushu University (2017).	25
2.10	Schematic representation of energy input in the large scales, where turbulence production occurs, and its transference along the inertial region to the smallest scales, where energy it is dissipated. The larger scales correspond to the small wavenumbers k . The sub-index EI stands for the interface between Energy (E) and Inertial (I) ranges, and DI for the separation of the dissipation D and I inertial scales of the flow, while ℓ_0 represent the larger scales, and η the Kolmogorov scales. Reproduced from Pope (2001)	26
3.1	Schematic representation of the SRI experimental setup.	32
3.2	Experimental Setup.	32
3.3	PIV images	35
3.4	PIV cross correlation to obtain velocity profiles (Image obtained from Pawar et al. (2014)).	36
3.5	Comparison of analytical TC profile with $Re = 1000$ and $\mu = 0.35$ (black dashed curve) with two different experiments acquired with 24 frames per second (fps), 24fps - 1 st Exp and 2 nd Exp, that show good agreement between each other and with the TC profile, and the same experiment computed with 12 fps (12fps - 1 st Exp), skipping one frame in the PIV computations, that shows no agreement with the TC profile, highlighting a poor time resolution.	37
3.6	(a) Superposed calibration grid and PIV images, both undistorted using the 5 th -order polynomial method; (b) PIV instantaneous velocity field. Reproduced from Seelig et al. (2018) with the friendly permission from <i>Torsen Seeling</i> , who developed the undistortion method here applied together with <i>Andreas Krebs</i> at the <i>BTU Cottbus-Senftenberg</i>	38

3.7	Stable u_ϕ Taylor-Couette profile with $Re = 1000$ and $\mu = 0.35$ (a) Comparison of TC analytical solution (black dashed line) and time mean PIV measurements (continuous red line) (b) Error ε between PIV measurements and analytical solutions in %. The left hand side of the images represent the region near the inner cylinder wall, and the right hand side is the region near the outer cylinder. The smaller figure inserted on the top left side of figure b shows the absolute error $ \varepsilon $	39
3.8	PIV data convergence of time series obtained at mid-height position ($z \approx H/2$) and at 3 different radial positions (a) u_ϕ convergence, $Re = 400$ (b) $u'_\phi u'_r$ convergence, $Re = 800$. The dashed lines indicate the final averaged velocities obtained.	40
3.9	Experimental temperature profiles at the beginning (blue curve on the right), and at the end (red curve on the left) of a measurement. The dashed lines are the linear fits in the center height region where the PIV measurements are performed.	41
4.1	Schematic representation of the numerical configuration.	44
4.2	Schematic representation of the 2-D space full staggered grid arrangement with velocity and pressure shifted in space by half a grid ($h/2$).	49
4.3	(a) Function applied to obtain a non-uniform grid, with $\beta = 5$, and different values of the control parameter γ . Examples of curves obtained with different values of γ ; (b) $\phi-r$ grid with a zoom near the cylinder wall to highlight grid refinement.	51
4.4	Three states of the 2d-pencil decomposition divided in 3×4 processor grids (respectively in r and z directions). Reproduced from Abide et al. (2018) with the friendly permission of <i>Stéphane Abide</i>	53
4.5	Matrix partition of the over 4 processors. (a) Tridiagonal matrix $Mx = (\tilde{M} + \Delta M)x$; (b) Inverse of the tridiagonal matrix $\tilde{M}^{-1}\tilde{M}x = (\mathbf{I} + \tilde{M}^{-1}\Delta M)x = \tilde{M}^{-1}b$. Reproduced from Abide et al. (2017) with the friendly permission of <i>Stéphane Abide</i>	54
4.6	Scaling tests on <i>HLRN</i> computers for $\phi \times r \times z$ meshes of sizes $32 \times 512 \times 512$ and $128 \times 256 \times 512$. The x-axis is the number of nodes (n) used on the computations and the y-axis presents (a) the speedup (b) the time (in seconds) necessary to complete 100 iterations.	56
4.7	SRI snapshots showing the azimuthal-radial ($\phi - r$) cross section obtained with the CS2D-Annular code, with $\mu = 0.35$, $\eta = 0.517$, a linear stable axial temperature gradient with $\partial T/\partial z \approx 5.7K/m$, $Fr \approx 1.5$ and $Re = 400$. The aspect ratio between cavity height and gap is $\Gamma = H/(r_{out} - r_{in}) = 10$. No-slip and impermeable Dirichlet boundary conditions are imposed ($u_\phi(r_{in}) = \Omega_{in}r_{in}$, $u_\phi(r_{out}) = \Omega_{out}r_{out}$, $u_z(z = 0) = 0$, $u_z(z = H) = 0$, $u_r(r_{in}) = 0$, $u_r(r_{out}) = 0$). The bottom and top lids of the cavity rotate with the outer cylinder Ω_{out} . The images are shown in the laboratory frame of reference	58

- 4.8 Velocity isocontour snapshots of the SRI showing non-axisymmetric spirals obtained by numerical simulation with $\mu = 0.35$, $\eta = 0.517$, a linear stable axial temperature gradient with $\partial T/\partial z \approx 5.7K/m$, $Fr \approx 1.5$ and $Re = 400$. The aspect ratio between cavity height and gap is $\Gamma = H/(r_{out} - r_{in}) = 10$. No-slip and impermeable Dirichlet boundary conditions are imposed ($u_\phi(r_{in}) = \Omega_{in}r_{in}$, $u_\phi(r_{out}) = \Omega_{out}r_{out}$, $u_z(z = 0) = 0$, $u_z(z = H) = 0$, $u_r(r_{in}) = 0$, $u_r(r_{out}) = 0$). The bottom and top lids of the cavity rotate with the outer cylinder Ω_{out} . The images are shown in a laboratory frame of reference 59
- 4.9 Comparison of mean time velocity profiles when the number of grid points in the radial direction increases from 64 to 128, keeping constant the number of grid points in $\phi = 32$ and $z = 200$ 60
- 4.10 (a) Convergence obtained from numerical simulations at mid-height position ($Z = H/2$) for 3 different radial locations (a) u_ϕ time series convergence, $Re = 400$ (b) $u'_\phi u'_r$ convergence, $Re = 800$. The dashed lines indicate the final averaged velocities. 60
- 5.1 u_ϕ space-time diagram for $Re = 400$ in a reference frame co-rotating with the outer cylinder at mid-height axial position ($H/2$). The horizontal axis shows time in minutes and the vertical axis, the radius in mm (the bottom of the image is near the inner cylinder region, and the top, close to the outer cylinder). Both figures(a),(b) show 12 minutes of measurements. 64
- 5.2 Time average azimuthal velocity profiles ($\overline{u_\phi}$). The lines with star and circle markers represent two different experimental data performed with $Re = 400$, $\mu = 0.35$ and temperature between top and bottom lids $\Delta T \approx 4K$, leading to $Rn \approx 250$ and $Fr \approx 1.5$. The solid red curve was obtained from numerical simulation, and the black dashed line is the non-stratified analytical TC profile. The bottom left figure is showing the deviations from the TC profile. 65
- 5.3 Comparison of two different experiments and the numerical simulation spectra with the ordinate axis shown in logarithmic scale. The spectra are obtained from u_ϕ time series at axial position $z \approx H/2$ and radial position $r \approx r_{in} + d/2$, $\mu \approx 0.35$ and initial temperature between top and bottom lids of $\Delta T \approx 4K$, leading to $\partial T/\partial z \approx 5.7K/m$, $Rn \approx 250$ and $Fr = 1.5$ 66
- 5.4 Comparison of u'_ϕ and u'_r at $r \approx (r_{in} + r_{out})/2$ and $z \approx H/2$, with $\Delta T \approx 4K$. Figures (a),(b) show experimental data and figures (c),(d) show numerical simulation results with Reynolds numbers $Re = 400$ (left-hand side images) and $Re = 600$ (right-hand side images). 66
- 5.5 u_ϕ space-time diagrams (Hovmöller) showing the SRI stability with $Re = 1000$, $\mu = 0.35$ and a temperature difference from top to bottom of $\Delta T \approx 4K$ in the frame of reference co-rotating with the outer cylinder. On top of the space-time diagrams, the velocity profile at mid-gap position ($r \approx r_{in} + d/2$) in the space-time diagrams together the analytical TC-profile presented in black dashed line. 68

- 5.6 u_ϕ power spectra obtained from numerical simulations at mid-height ($z \approx H/2$) and mid-gap ($r \approx r_{in} + d/2$) position. The simulations were performed with $\mu = 0.35$ and initial temperature difference of $\Delta T = 4K$ ($Re \approx 250$, $Fr \approx 1.5$). The horizontal axis shows frequencies in Hz , and the vertical axis shows spectra amplitudes $P = |FFT(u_\phi)|^2$ (a) shows the SRI amplitudes for increasing Re . Note that the SRI peak is no longer present in the spectrum for $Re \geq 1000$ (green dashed line at $P \approx 0$). The black dashed vertical line on the left corresponds to the buoyancy frequency for the $Re = 400$ case, while the dashed vertical line on the right corresponds to $f = 2\Omega_{in}$ for the same case, both corrected by the Doppler shift due to the azimuthal mean flow. The spectra have been taken from a reference frame co-rotating with the outer cylinder (b) Spectra for different Reynolds numbers with the amplitude (P) in logarithmic scale and obtained from u_ϕ time series in a laboratory frame of reference. For a better display, the spectra are staggered by multiplying constant exponential functions $c_{te} = e^n$ to displace them vertically in the log scale axis, where n is chosen arbitrarily. Dashed vertical lines are used for highlighting coincident peaks of different spectra. A small picture showing the spectra normalized by the inner cylinder rotation ($\Omega_{in}/2\pi$) is displayed on the bottom right corner. 68
- 6.1 Numerical simulation time series for $Re = 400$, $\mu = 0.35$ and $dT \approx 4K$ at mid-gap position ($r \approx r_{in} + d/2$) and mid height position ($z \approx H/2$), and their respective amplitude envelopes highlighting low frequency amplitude variations in time (a) SRI time series in the time interval $0 < t < 3$ hours and their respective amplitude envelopes, highlighting low frequency amplitude modulations (b) Velocity amplitude envelopes, highlighting regular low frequency amplitude modulations within the time interval $0 < t < 8$ hours. Note that the time intervals are different in figures(a),(b) (respectively, $0 < t < 3$ hours and $0 < t < 8$ hours), so that the SRI oscillations have been included into figure (a) only. (c) Power spectrum of u_ϕ amplitude envelope (both u_ϕ and u_r envelopes present similar spectra). 72
- 6.2 u_ϕ space-time diagrams at mid-height axial position ($z \approx H/2$) during amplitude modulation transition for $Re = 600$, $\mu = 0.35$ and $\Delta T/\Delta z = 5.71 \text{ K m}^{-1}$. The reference frame co-rotates with the outer cylinder, and the velocities represented by the colour scales are given in mm/s . The horizontal axis shows time in minutes, and the vertical axis, the radius in mm , where the bottom region is closer to the inner cylinder wall, and the top is closer to the outer one. On top of the space-time diagrams, the velocity time-series at mid-gap position ($r \approx r_{in} + d/2$) in the space-time diagrams is displayed that highlights its amplitude modulation. 73
- 6.3 Comparison between experimental (blue curve) and numerical simulation (red curve) u_ϕ time series at mid-gap ($r_{in} + d/2$) and mid-height position ($H/2$). The results are for $\mu = 0.35$ and $\Delta T/\Delta z = 5.71 \text{ K m}^{-1}$. Please, note that the time intervals are different in figures (a) and (b). 73

- 6.4 u_ϕ comparison obtained from numerical simulations with $\mu = 0.35$ (left hand side) and $\mu = 0.3572$ (Keplerian line, at the right hand side) in the laboratory frame of reference, highlighting similar mean flows on the top figures(a),(b), and similar the amplitude modulations in time in the bottom figures(c),(d). The results are for for mid-height position ($z \approx H/2$) with $\Delta T = 4K$, and the time series are for a mid-gap radial position ($r \approx r_{in} + d/2$). 74
- 6.5 u_ϕ structures during amplitude modulation at radial position $r = r_{in} + d/2$; (a) Time series with horizontal coloured lines indicating intervals selected before (black), during (green), and after (red) a local minimum amplitude value; (b) Interval 01, from $t = 312$ to 322 minutes – SRI spiral with downward inclination; (c) Interval 02, from $t = 318$ to 338 minutes – transition from a SRI spiral with downward to upward inclination; (d) Interval 03, from $t = 336$ to 346 minutes – SRI spiral with upward inclination. 75
- 6.6 Comparison of the simulation time average axial velocity profiles with time averages taken during an upward traveling spiral period, during a downward traveling spiral period, and during the transition from an upward to a downward spiral period. The results are from numerical simulation performed with $Re = 400$, $\mu = 0.35$ and $\Delta T/\Delta z = 5.71 \text{ K m}^{-1}$ at a fixed radial position $r = r_{in} + d/2$. 76
- 6.7 Time mean stream lines $\langle \psi \rangle$ showing the base flow circulation for $Re = 400$, $\mu = 0.35$ and $\Delta T/\Delta z = 5.71 \text{ K m}^{-1}$. The time mean $\langle \psi \rangle$ is obtained from u_r and u_z averaged over ϕ 79
- 6.8 Circulation patterns obtained with stream lines $\langle \psi \rangle$ averaged over ϕ (left-hand side) and background circulation patterns $\langle \psi' \rangle = \langle \psi \rangle - \langle \psi \rangle$ (right-hand side) in $[\text{mm s}^{-2}]$. Note that the base flow $\langle \psi \rangle$ was removed from the right-hand side images for taking into account the only background circulation, excluding Ekman effects. The results are from numerical simulation performed with $Re = 400$, $\mu = 0.35$ and $\Delta T/\Delta z = 5.71 \text{ K m}^{-1}$ in the $r - Z$ 80
- 6.9 $\mathbf{v} = (u_r, u_z)$ snapshots during an upward and downward traveling spiral moment. The results are from numerical simulation performed with $Re = 400$, $\mu = 0.35$ and $\Delta T/\Delta z = 5.71 \text{ K m}^{-1}$ 81
- 6.10 Numerical simulation snapshot showing changes in the axial wavenumber in simulations with temperatures $\Delta T/\Delta z = 2.85 \text{ K m}^{-1}$ (left-hand side), $\Delta T/\Delta z = 5.71 \text{ K m}^{-1}$ (middle images) and $\Delta T/\Delta z = 11.43 \text{ K m}^{-1}$ (right-hand side images), respectively corresponding to Froude numbers $Fr \approx 2.2$, $Fr \approx 1.5$, and $Fr \approx 1.0$. Figure (a), on top, show temperature averaged on the azimuth direction $\langle \Delta T \rangle$ for one snapshot (in full red line), and the temperature at the mid gap position $r = 110\text{mm}$ (in blue dashed line), highlighting the equivalence of these profiles. Figure (b), in the middle, show snapshots of u_ϕ in the radial-axial cross section. The bottom figure (c) show the snapshot of u_r in the radial-axial cross section. The parameters of the simulation are: $Re = 400$, and $\mu = 0.35$ 82
- 6.11 Changes in u_ϕ when different temperature gradients in the axial direction are imposed. (a) Mean velocity profiles ($\overline{u_\phi}$). (b)-(d) show the time series near the mid-gap and mid-height position ($r \approx r_{in} + d/2$ and $z \approx H/2$), highlighting changes in the low-frequency modulations with the temperature gradient. The smaller images inserted inside (b)-(d) show smaller time intervals of each respective time series (intervals where chosen arbitrarily, in regions where amplitudes do not vary much), highlighting the SRI oscillations. The velocities are presented in the laboratory frame of reference. 83

- 6.12 Simulation with $Re = 400$, $\mu = 0.35$, $\Delta T/\Delta z \approx 5.71 \text{ K m}^{-1}$ and cylinder's height half of the experimental height $H = 0.35m$ (case 10 in table 6.3). (a) Temperature time series obtained at mid-gap region $r \approx r_{in} + d/3$ and in 3 different axial positions; (b) u_ϕ space-time diagram at $r \approx r_{in} + d/3$ showing the standing chessboard pattern achieved when the secondary instability is not reached. 85
- 6.13 Stream lines comparing the base flow circulation to the circulation at a given time, averaged on the azimuthal direction. The simulations are performed with half experimental height ($H/2$) and $Re = 400$, $\mu = 0.35$ and $\Delta T/\Delta z = 5.71 \text{ K m}^{-1}$ (case 10 in table 6.3). Note that base flow circulation and instantaneous circulation are almost the same. 86
- 6.14 Space-time diagram with $Re = 400$, $\mu = 0.35$, $\Delta T/\Delta z \approx 5.71 \text{ K m}^{-1}$ and height $H = 0.35m$ (half of the experimental cavity). The x-axis show time in minutes, and the y-axis shows the axial direction (z). (a) u_ϕ time series obtained closer to the inner cylinder (at $r \approx r_{in} + d/3$) and at an axial position $z \approx H/3$. (b)-(d) u_r space-time diagrams on different time intervals. 87
- 6.15 u_ϕ numerical simulations for cavities with large heights (H) compared to the experimental setup at $r \approx r_{in} + d/3$, with $\mu = 0.35$ and $\Delta T/\Delta z \approx 5.71 \text{ K m}^{-1}$ (a) time series at $z \approx H/2$ for $H = 1400mm$ (b) time series at $z \approx H/2$ for $H = 2800mm$ (c)-(f) Space-time diagrams at different time intervals showing the occurrence of different spiral patters in time. 88
- 6.16 u_ϕ numerical simulations with $Re = 400$, $\mu = 0.35$ and periodic solutions in the axial direction z ($\Delta z \rightarrow \infty$) (a) Time series obtained at $r \approx r_{in} + d/2$ and $z \approx H/2$ with temperature gradient $\Delta T/\Delta z \approx 5.71 \text{ K m}^{-1}$ (case 14 in table 6.3); (b) Time series obtained at $r \approx r_{in} + d/2$ and $z \approx H/2$ with temperature gradient $\Delta T/\Delta z \approx 11.43 \text{ K m}^{-1}$ (case 15 in table 6.3); (c) Mean flow ($\overline{u_\phi}$) comparison of the axial periodic simulations with $\Delta T/\Delta z \approx 5.71 \text{ K m}^{-1}$ and $\Delta T/\Delta z \approx 11.43 \text{ K m}^{-1}$ with the non-stratified TC profile (black dashed line). 89
- 6.17 u_ϕ space-time diagram with $Re = 400$, $\mu = 0.35$, $\Delta T/\Delta z \approx 5.71 \text{ K m}^{-1}$ and periodic boundary conditions in the axial direction. The x-axis show time in minutes, and the y-axis shows the axial direction. (a) Simulation starting from the initial condition described on chapter 4. (b) Simulation using as initial conditions a downward travelling spiral obtained from a bounded top and bottom lids simulation. 90
- 6.18 u_ϕ space-time diagram with $Re = 400$, $\mu = 0.35$, $\Delta T/\Delta z \approx 11.43 \text{ K m}^{-1}$ and periodic boundary conditions in the axial direction at different time intervals, revealing changes in the spiral pattern in time. (a) Upward spiral propagation; (b) Downward spiral propagation; (c) Transition from an upward to a downward spiral propagation. 91

- 6.19 Critical layers position for the mode $m = 1$, when the mean flow velocity equals the drift speed ($\langle u_\phi \rangle = \omega/m$) and $\langle u_\phi \rangle = \omega/m \pm N/m$. The simulation was performed with $Re = 400$, $\mu = 0.35$, and the experimental geometry (case 16 in table 6.4). (a) Presents $\langle u_\phi \rangle$ space averaged in ϕ (blue curve). The dashed black line shows the drift speed $c = \omega/m$, and the red lines show $c \pm N/m$. The intersection of the curves with the mean flow are the critical layer positions. (b),(c) Present the circulation of the flow at a given time, and the radial position of the critical layers as vertical dashed lines. The dashed vertical line in the middle represents the classical critical layer, where $\langle u_\phi \rangle = \omega/m$, and the other two dashed vertical lines represents the radial position where $\langle u_\phi \rangle = c \pm N/m$. (b) shows the instantaneous circulation at a given time; and (c) Shows the fluctuation circulation ψ' 92
- 6.20 u_r time series at $r \approx 90\text{mm}$ and $z \approx H/2$, with $Re = 400$, $\mu = 0.35$, and height $H = 700\text{mm}$, for different values of $d = r_{out} - r_{in}$, obtained by changing the outer radii and maintaining $r_{in} = 75\text{mm}$. (a) $r_{out} = 170\text{mm}$, $\Delta T/\Delta z = 5.71 \text{ K m}^{-1}$; (b) $r_{out} = 180\text{mm}$, $\Delta T/\Delta z = 5.71 \text{ K m}^{-1}$; (c) $r_{out} = 180\text{mm}$, $\Delta T/\Delta z = 11.43 \text{ K m}^{-1}$ 93
- 6.21 Energy spectra in the azimuthal (E_ϕ), radial (E_r) and axial (E_z) directions with different power laws fitting the energy transfer region of the spectra presented in dashed lines. The spectra were obtained from simulations with $\mu = 0.35$ and $\Delta T = 4\text{K}$, and bounded cavity height $H = 700\text{mm}$ (same geometry as the experimental setup). Figure (a) presents a $Re = 400$ simulation where amplitude modulations and pattern changes are observed (case 02 in table 6.1); (b) shows a simulation with $Re = 800$, where no pattern changes or amplitude modulations occur (case 08 in table 6.2). 95
- 6.22 Comparison of E_ϕ (left hand side images) and E_r (right hand side images) with (a,b) different Reynolds number (top images); (c,d) different stratification values (middle images); (e,f) different cavity heights H (bottom images). The x-axis in figures 6.22 shows the azimuthal (m) and radial (l) wavenumbers. All parameters are changed with respect to a standard simulation with $Re = 400$, $\mu = 0.35$, $H = 700\text{mm}$ and $\Delta T/\Delta z = 5.71 \text{ K m}^{-1}$. The non-stratified TC flow is presented as black dashed lines. 97
- 6.23 Energy spectra in the axial direction (E_z). (a) Different Re , for fixed $H = 700\text{mm}$, $\Delta T = 4\text{K}$. (b) Different stratification (ΔT), with fixed $Re = 400$, and $H = 700\text{mm}$. (c) Different cylinder's heights, with fixed $Re = 400$ and $\Delta T/\Delta z \approx 5.71 \text{ K m}^{-1}$; (d) Comparison of axial periodic and non-periodic top and bottom boundary conditions; The x-axis in all figures present the axial wavenumber k . The smaller figures inserted on the top right corner of each image show the spectra arbitrarily dislocated in the y-axis for better visualization of the results, and have the inverse wavelength (λ^{-1}) in the x-axis, instead of the wavenumber k . The non-stratified TC flow is presented in black dashed line in all figures (with $Re = 400$, $\mu = 0.35$, $H = 700\text{mm}$ and $\Delta T = 0\text{K}$). All simulations were performed with $\mu = 0.35$ 98

- 6.24 2-dimensional power spectra obtained from numerical simulations space-time diagrams of u_ϕ in the axial direction during (a) upward spiral propagation; (b) downward spiral propagation (c) transition from a downward an upward propagating spiral. The y-axis represents axial wavenumber k (axial modes), while the x-axis is the frequency in Hz . The amplitudes of the spectra are normalized by the maximum amplitude value of the upward (and downward) propagating spirals $P_{0,max}$. The spectra are obtained in a frame of reference fixed in the laboratory. During the transition, the maximum amplitude of the spectra were half of the maximum amplitude found while the spiral is travelling upward or downward ($P/P_{0,max} = 0.5$). 100
- 6.25 u'_ϕ 2D-fft (top images (a),(b)) and space-time diagrams (bottom images (c),(d)) of two simulations that do not change their spiral patterns in time. The left hand side images (a),(c) show simulations with $Re = 400$ and half of the experimental cavity height ($H = 350mm$). The right hand side images correspond to simulations with the same experimental height ($H = 700mm$) and $Re = 800$. Note that the time interval in the x-axis of figures c ($\Delta t = 400$ min) and (d) ($\Delta t = 200$ min) are different. In both simulations, $\mu = 0.35$ and $\Delta T/\Delta z \approx 5.71 \text{ K m}^{-1}$ 101
- 6.26 Separation of upward and downward axial traveling components in u_ϕ space-time diagram using the Radon Transform. Figures (a),(c),(e), on the left hand side, show time intervals when the spiral is traveling downwards. Figures (b),(d),(f), on the right hand side, show a time interval when the spiral is traveling upwards. Figures (a),(b) on top show the 2D-FFT of the upward and downward space-time diagrams. Simulation performed with $Re = 400$, $\mu = 0.35$, $\Delta T/\Delta z \approx 5.71 \text{ K m}^{-1}$, and $H = 700$ mm. 103
- 6.27 Separation of upward and downward axial traveling components space-time diagram using the Radon Transform. Results are of u_ϕ numerical simulations with $Re = 400$, $\mu = 0.35$, $\Delta T/\Delta z \approx 5.71 \text{ K m}^{-1}$ and cavity height four times larger than the experimental setup ($H = 2800mm$). (a) Space-time diagram showing the full spiral propagation; (b) 2D-FFT of the full spiral. (c) Space-time diagram of the spiral component traveling upward; (d) Space-time diagram of the spiral component traveling downward. 104
- 6.28 (a) Experimental and (b) numerical power spectra with $Re = 400$, $\mu = 0.35$ and $\Delta T/\Delta z \approx 5.71 \text{ K m}^{-1}$; (c) Experimental and (d) numerical harmonic signals corresponding to one peak in the different frequency bands selected. The harmonics were normalized by their maximum amplitude value, and arbitrarily dislocated in the y-axis, for better visualization and comparison. Note that the time interval in figures (a) and (b) are different. 105
- 6.29 u_ϕ space-time diagram of the toy model composed of 2 plane waves with sinusoidal amplitude modulations with $\omega_A = 7 \times 10^{-4}$, out of phase an angle $\theta = \pi/3$, and traveling in opposite axial directions with wavenumbers of wave₁ and wave₂ respectively $(m_1, l_1, k_1) = (1, 1, 4)$ and $(m_2, l_2, k_2) = (1, 1, -4)$. The frequency $\omega = 0.03$, and the maximum amplitude of each wave is $A = 10$ 106

6.30	Snapshots with different spiral patterns in the ϕ - z cross-section comparing $u'_\phi = u_\phi - \bar{u}_\phi$ obtained from numerical simulations (a,b,c) and the toy model (d,e,f). The radial position is fixed at $r \approx r_{in} + d/3$. Figures (a),(d) on top, show moments when the spirals are traveling downwards; Figures (b),(e), in the middle, show the transition from upward to downward spiral propagation; Figures (c),(f) in the bottom, show spirals traveling upwards. The simulations were performed with $Re = 400$, $\mu = 0.35$ and $\Delta T = 4K$. The toy model is composed by two plane waves with frequencies $\omega = 0.01$, and wavenumbers $(m_1, l_1, k_1) = (1, 1, 4)$ and $(m_2, l_2, k_2) = (1, 1, -4)$, maximum amplitude of the waves is of $A = 3mm/s$, and the frequency of the sinusoidal amplitude modulations of $\omega_A = 0.001$, 90° out of phase ($\theta = \pi/2$).	107
6.31	$u'_\phi u'_r$ snapshots of numerical simulations with $Re = 400$ and $\mu = 0,35$ and different stratification values ($\Delta T/\Delta z$). The left hand side show the azimuth-radial cross section ($\phi - r$) at mid-height position ($z \approx H/2$), and the right hand side shows the radial-axial cross section at $\phi = 0$	109
6.32	$u'_\phi u'_r$ time series for increasing Reynolds number with a fixed temperature gradient $\Delta T/\Delta z = 5.71 K m^{-1}$. The velocities are obtained at position $r = 90 mm$ (near the inner cylinder) and $z \approx H/2$ (mid-height). Note time of the upper figures (a),(b) is of $0 \leq t \leq 420$ minutes, and of the bottom images (c),(d),(e) are of $0 \leq t \leq 220$ minutes. The small figures inserted show the SRI oscillations in a 5 minutes time window. Figure (e) has two inserted figures, when the SRI occur at the transient phase ($t < 90$ minutes) and another inserted image after the flow becomes stable (for $t > 90$ minutes).	111
6.33	$u'_\phi u'_r$ numerical simulations time series at $r = 90 mm$ and $z \approx H/2$ for different stratification values, and with $Re = 400$, $\mu = 0.35$, and $H = 700 mm$. The images inserted inside each figure show a smaller time interval of 5 minutes, highlighting the higher frequency SRI oscillations.	112
6.34	Mean azimuthal space mean $\langle u'_\phi u'_r \rangle$ at a fixed radial position very close to the inner cylinder wall ($r \approx 76.14 mm$) and mid-height axial position $z \approx H/2$. The results are from numerical simulation with different stratification values ($\Delta T/\Delta z$) and with the same $Re = 400$, $\mu = 0.35$ and the same geometry of our experimental setup (cases 01 and 02 in table 6.1, of section 6.2.1).	112

List of Tables

3.1	Experimental setup parameters	33
3.2	M5 silicone oil properties at $25^\circ C$	33
4.1	Fourth-order compact scheme coefficients for the inner nodes.	50
4.2	Fourth-order compact scheme coefficients of the boundary relations	50
4.3	Boundary conditions	61

6.1	Parameters of simulations changing stratification	79
6.2	Parameters of simulations changing Re	84
6.3	Parameters of simulations changing the cylinder height	84
6.4	Parameters of simulations changing the gap width	90

Abstract

Stratified vortices can be found from small to large scales in geophysical and astrophysical flows. On the one hand, tornadoes and hurricanes can lead to devastation and even a large number of casualties. On the other hand, vortices can distribute heat and momentum in the atmosphere which is important for a habitable environment on Earth. In the astrophysical context, accretion disks (from which solar systems are formed) can be seen as stratified vortices. In such systems, understanding the mechanisms that can result in an outward transport of angular momentum is a central problem. For a planet or star to be formed in a disk, angular momentum has to be carried away from its center to allow matter aggregation by gravity; otherwise, its rotation speed would be far too large, avoiding this matter aggregation (and the consequent star formation) to happen. In such gas systems, turbulence is the most likely mechanism to achieve such a large angular momentum transport. However, it was shown that the flow profile of accretion disks is stable with respect to purely shear instabilities, and the question arises about how the turbulence can be generated. Among other candidates, the strato-rotational instability (SRI) has attracted attention in recent years. The SRI is a purely hydrodynamic instability that can be modeled by a classical Taylor-Couette (TC) system with stable density stratification due to axial salinity or temperature gradients.

In this thesis, a combined experimental and high-performance computing study of new specific behaviors of the strato-Rotational Instability (SRI) is performed. The density stratification causes a change in the marginal instability transition when compared to classical non-stratified TC systems, making the flow unstable in regions where – without stratification – it would be stable. This characteristic makes the SRI a relevant phenomenon in planetary and astrophysical applications, particularly in accretion disk theory.

Despite many advances in the understanding of strato-rotational flows, the confrontation of experimental data with non-linear numerical simulations remains relevant, since it involves linear aspects and non-linear interactions of SRI modes which still need to be better understood. These comparisons also reveal new non-linear phenomena and patterns not yet observed in the SRI, that can contribute to our understanding of geophysical flows.

The experiment designed to investigate these SRI related phenomena consists of two concentric cylinders that can rotate independently, with a silicon oil confined between both vertical cylinders. For obtaining a stable density stratification along the cylinder axis, the bottom lid of the setup is cooled, and its top part is heated, with temperature differences varying between $3K < \Delta T < 4.5K$, establishing an axial linear gradient, leading to Froude numbers $Fr = \Omega_{in}/N$ between $1.5 < Fr < 4.5$, where Ω_{in} is the inner cylinder rotation, and N is the buoyancy frequency. The flow field resulting from the cylinder's rotation interacting with the stable density stratification is measured using Particle Image Velocimetry (PIV). This thesis focuses on cases of moderate Reynolds numbers (Re , based on the inner cylinder radius and angular velocities), varying between $Re = 300$ and $Re = 1300$, with a fixed rotation ratio between outer and inner cylinders of $\mu = \Omega_{out}/\Omega_{in} = 0.35$, a value slightly smaller than the Keplerian velocity profile, but beyond the Rayleigh limit. Direct numerical simulations are performed using the same configuration as the experimental setup. The numerical method consists of a parallel high-

order compact scheme incompressible code, that solves the Boussinesq equations combining a 2D-pencil decomposition and the reduced Parallel Diagonal Dominant spectral-like method for efficient parallelization. Both simulations and experiments show, in agreement with recent linear stability analyses, the occurrence of a return to stable flows with respect to the SRI when the Reynolds numbers increase. Low-frequency velocity amplitude modulations related to two competing spiral wave modes are found which have not been reported yet. These modes are observed in the experiment and numerical simulations. These modulations are associated with spirals in the axial direction formed due to the instability. Such modulations are associated with changes in the spiral axial direction of propagation in time, and the activation of different wavenumbers in time. Recent astronomical observations also captured spirals in an accretion disk at an early stage of a star formation in the center of the disk, making the study of these spiral signatures and dynamics a recent and relevant topic to astrophysical applications, since they might play an important role on our further understanding of planets and stars formations in accretion disks.

Résumé

Les vortex en écoulements stratifiés peuvent se manifester à petite et grande échelles dans les applications géophysique et astrophysique. Les tornades et les ouragans peuvent entraîner de nombreux dommages à la fois matériels et humains. En effet, les tourbillons distribuent la chaleur et la quantité de mouvement dans l'atmosphère et sont donc très importants afin de garantir un environnement habitable sur Terre. Dans le contexte astrophysique, les disques d'accrétion (à partir desquels les systèmes solaires sont formés) peuvent être considérés comme des tourbillons en milieux stratifiés. En ce qui concerne la formation des planètes, la compréhension des mécanismes qui peuvent entraîner un transport vers l'extérieur du moment cinétique constitue par conséquent un problème central. Pour qu'une planète ou une étoile se forme dans un disque, le moment angulaire doit être transporté loin de son centre afin de permettre l'agrégation de matière par gravité; sinon, sa vitesse de rotation serait beaucoup trop grande pour permettre cette agrégation de matière (et la formation d'étoiles qui en résulte). Dans de tels systèmes constitués de gaz, la turbulence est le mécanisme le plus probable permettant de réaliser un transport de moment angulaire aussi important. Cependant, il a été montré que le profil des écoulements des disques d'accrétion est stable et la question se pose de savoir comment la turbulence peut être générée. Parmi les autres candidats, l'instabilité strato-rotationnelle (SRI) a attiré l'attention ces dernières années. SRI est une instabilité purement hydrodynamique qui peut être modélisée par un système classique de Taylor-Couette (TC) avec une stratification stable due à un gradient axial de salinité ou de température.

Dans cette thèse, nous proposons une étude à la fois expérimentale et numérique en se focalisant sur la mise en évidence de nouveaux comportements spécifiques à l'instabilité strato-rotationnelle (SRI). La stratification axiale provoque un changement de la transition de l'instabilité marginale par rapport au système classique non stratifié TC, rendant l'écoulement instable dans les régions où sans stratification il resterait stable. Cette caractéristique fait de l'instabilité SRI un phénomène pertinent dans les domaines planétaire et astrophysique, en particulier dans la théorie de la formation des disques d'accrétion.

Malgré de nombreuses avancées dans la compréhension des écoulements strato-rotationnels, la confrontation de données expérimentales avec des simulations numériques non linéaires est pertinente, car elle implique à la fois les aspects linéaires ainsi que les interactions non linéaires des modes SRI qui doivent encore être mieux compris. Ces comparaisons révèlent également de nouveaux phénomènes et motifs non linéaires encore jamais observés pour les SRI, contribuant ainsi à une meilleure compréhension des écoulements géophysiques.

Le dispositif expérimental conçu pour étudier ces phénomènes liés à l'instabilité SRI consiste en deux cylindres qui peuvent tourner indépendamment, la cavité étant remplie avec de l'huile de silicone. Afin d'obtenir une stratification stable le long de l'axe du cylindre, le couvercle inférieur de l'installation est refroidi tandis que sa partie supérieure est chauffée. Les différences de température varient dans l'intervalle $3\text{ K} < \Delta T < 4.5\text{ K}$, générant un gradient

linéaire axial, conduisant à des nombres de Froude $Fr = \Omega_{in}/N$ compris entre $1,5 < Fr < 4,5$, où Ω_{in} est la vitesse de rotation interne du cylindre et N est la fréquence de flottabilité (Brunt-Väisälä). Le champ résultant de la rotation des cylindres interagissant avec la stratification de densité stable est mesuré en utilisant la technique de vélocimétrie par image de particules (PIV). Dans cette thèse, nous nous sommes concentrés sur des cas à nombres de Reynolds modérés (Re , basé sur le rayon du cylindre intérieur et les vitesses angulaires), variant entre $Re = 300$ et $Re = 1300$. Le rapport de rotation entre cylindres extérieur et intérieur est fixé à $\mu = \Omega_{out}/\Omega_{in} = 0.35$, une valeur légèrement inférieure au profil de vitesse képlérien, mais au-delà de la limite de Rayleigh. Cette configuration expérimentale est également étudiée par simulations numériques directes à l'aide d'un code parallèle incompressible avec une approximation de Boussinesq, basé sur des schémas compacts d'ordre élevé et des séries de Fourier. D'un point de vue algorithmique, une décomposition bi-dimensionnelle est mise en oeuvre afin d'obtenir une parallélisation efficace.

Zusammenfassung

Geschichtete Wirbel können mit unterschiedlichen Skalen in geophysikalischen und astrophysikalischen Strömungen gefunden werden. Einerseits können Tornados und Hurrikane zu Verwüstungen und sogar zu einer großen Anzahl von Opfern führen und andererseits transportieren Wirbel Wärme und Impuls in der Atmosphäre und sind daher für eine bewohnbare Umwelt auf der Erde wichtig. Im astrophysikalischen Kontext können Akkretionsscheiben (aus denen Sonnensysteme gebildet werden) als geschichtete Wirbel angesehen werden. Der Impulstransport in einer solchen Scheibe ist bei der Bildung von Planeten noch nicht vollständig verstanden. Planeten oder Sterne können in einer Scheibe gebildet werden, wenn der Drehimpuls vom Scheibenzentrum weggetragen wird, um eine Materieansammlung durch Schwerkraft zu ermöglichen, da sonst die Rotationsgeschwindigkeit der Scheibe viel zu groß für eine Aggregation von Materie wäre. In solchen Gassystemen ist Turbulenz der wahrscheinlichste Mechanismus für den notwendigen Drehimpulstransport. Es wird jedoch gezeigt, dass das Strömungsprofil von Akkretionsscheiben stabil ist und es stellt sich somit die Frage, wie die Turbulenz erzeugt werden kann. In den letzten Jahren hat die Strato-Rotationsinstabilität (SRI) viel Aufmerksamkeit erregt, da diese ein rein hydrodynamische Instabilität ist. Sie kann mit einem klassischen Taylor-Couette (TC) -System, welches jedoch eine axiale Dichteschichtung aufweist, relativ einfach experimentell und numerisch modelliert werden.

In dieser Arbeit wird eine kombinierte experimentelle und numerische Studie zum Verständnis von strömungsmechanischen Phänomenen im Bereich der Strato-Rotations-Instabilität durchgeführt. Im Allgemeinen bewirkt eine Dichteschichtung eine Änderung des Übergangs zur Instabilität im Vergleich zum klassischen, nicht geschichteten TC-System. Ohne Schichtung wäre die Strömung in nun instabilen Bereichen stabil. Diese Eigenschaft kann mit der SRI untersucht werden, um Phänomene in planetarischen und astrophysikalischen Anwendungen zu erforschen, insbesondere mit dem Fokus auf die Akkretionsscheibentheorie. Trotz vieler Fortschritte beim Verständnis der Impulsflüsse in Strato-Rotations-Systemen bleibt die Gegenüberstellung experimenteller Daten mit nichtlinearen numerischen Simulationen relevant, da sie beides, lineare Aspekte und nichtlineare Wechselwirkungen von SRI-Moden beinhaltet, die noch besser verstanden werden müssen. Diese Vergleiche zeigen neue nichtlineare Phänomene und Muster, die bei der SRI bislang noch nicht beobachtet wurden und können zu unserem Verständnis von geophysikalischen Strömungen beitragen.

Das von uns verwendete System besteht aus zwei konzentrischen Zylindern, die sich unabhängig voneinander drehen können, wobei sich zwischen beiden vertikalen Zylindern ein Silikonöl befindet. Um eine stabile Dichteschichtung entlang der Zylinderachse zu erhalten, wird der Boden des Aufbaus gekühlt und der Deckel erwärmt, wobei der Temperaturunterschied zwischen $3K < \Delta T < 4,5K$ beträgt. Die differentielle Heizung ergibt Froude-Zahlen

$Fr = \Omega_{in}/N$ zwischen $1,5 < Fr < 4,5$, wobei Ω_{in} die Drehung des inneren Zylinders und N die Auftriebsfrequenz ist. Das Strömungsfeld ergibt sich aus den Rotationen der Zylinder und durch Wechselwirkung mit der Schichtung. Mit Hilfe der PIV-Technik (Particle Image Velocimetry) wird die Strömung experimentell gemessen. Diese Arbeit konzentriert sich auf die Fälle mit moderater Reynolds-Zahl (Re , basierend auf dem inneren Zylinderradius und der Zylinderdrehzahl), die zwischen $Re = 300$ und $Re = 1300$ variiert. Das Rotationsverhältnis von innerem und äußerem Zylinder, $\mu = \Omega_{out}/\Omega_{in} = 0,35$, ist kleiner als das einer Kepler-Rotation, liegt jedoch über der sogenannten Rayleigh-Grenze. Direkte numerische Simulationen werden mit derselben Konfiguration wie beim Experiment durchgeführt. Die numerische Methode basiert auf einem inkompressiblen Code mit einem parallelen Kompaktschema hoher Ordnung. Sie löst die Boussinesq-Gleichungen durch Kombination einer 2D-Pencil Zerlegung und einem für die Parallelisierung optimierten Verfahren. Sowohl Simulationen als auch Experimente zeigen in Übereinstimmung mit den linearen Stabilitätsanalysen das Auftreten von stabilen Strömungen, wenn die Reynolds-Zahl zu stark erhöht wird. Es wurden auch niederfrequente Geschwindigkeitsamplitudenmodulationen gefunden, die durch zwei konkurrierende Spiralwellenmoden zustande kommen und die bislang unbekannt waren. Diese Moden wurden im Experiment und den numerischen Simulationen beobachtet. Solche Modulationen sind mit zeitlichen Schwankungen der spiralförmigen Wellen in axialer Richtung verbunden. Kürzlich gemachte astronomische Beobachtungen haben solche Spiralen in einem frühen Stadium der Sternentstehung in der Mitte einer Akkretionsscheibe nachgewiesen. Diese Beobachtung macht die SRI zu einem aktuellen und relevanten Thema für astrophysikalische Anwendungen.

Introduction

“We are all in the gutter, but some of us are looking at the stars.”

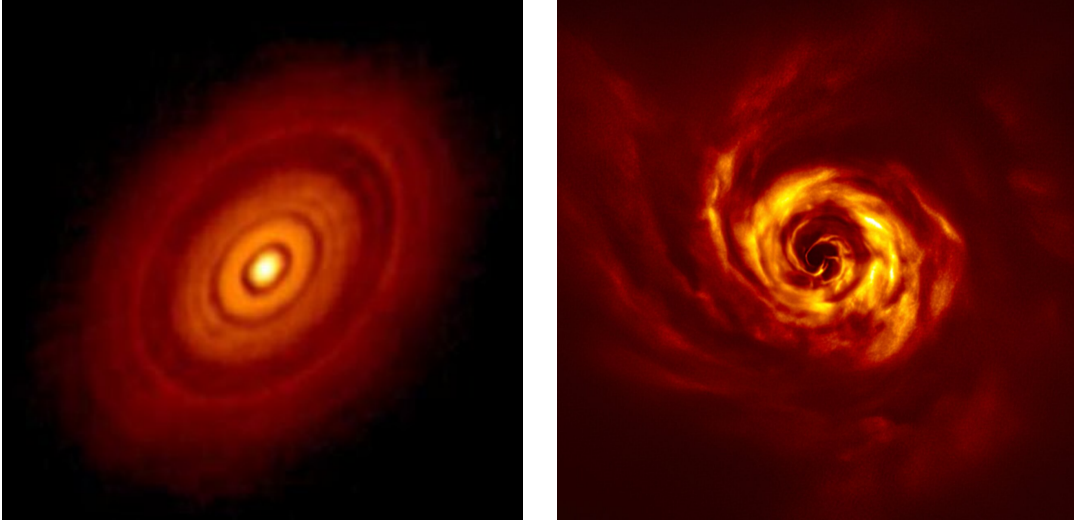
– Oscar Wilde –

1.1 Introduction to Strato-Rotational Instabilities in Accretion Discs

Understanding the hydrodynamical mechanisms that can result in an outward transport of angular momentum is a central problem regarding stars and planets formation, particularly in the theory of accretion discs (Fromang and Lesur 2017). Accretion discs are astrophysical disk-like shape objects composed of gas and dust that rotate around a central object, like a star or a planet. One example of such astrophysical objects is the one observed by the Atacama Large Millimeter/submillimeter Array (ALMA) collaboration (Brogan et al. 2015), shown in figure 1.1(a), which is an ideal system for the study of disk instabilities and early planet formation since it consists of a young star surrounded by a disk with high mass. The disk mass M_d is estimated between $0.03M_\odot < M_d < 0.14M_\odot$, and its outer radius is estimated to be $r_{out} \approx 130AU$, with Keplerian velocity profile. At a radius of $r \approx 25AU$, $|u| \approx 7.0km/s$. The mass of the HL Tauri star found in the center of the disk is estimated to be 30% higher than the solar mass ($M_* \approx 1.3M_\odot$), enclosed in a radius $r \leq 25AU$.

Central objects in accretion discs, as the HL Tauri star and the AB Aurigae shown in figure 1.1(a),(b) are formed by the gravitational collapse of the disk matter. The large mass and size values in these systems show that even the slight rotations lead to too much angular momentum (Fromang and Lesur 2017), large enough to overcome gravitational forces that would allow the formation of massive central objects. Since astrophysical observations show these massive bodies in the center of accretion discs, the gas flow surrounding the objects should be turbulent. Turbulence, unlike viscous diffusion, can efficiently transport these high angular momenta away from the center of the disk. By removing energy from the disk during this process, turbulence allows gravity to become stronger than the outer-radial angular momentum component, collapsing matter to form the observed astrophysical bodies.

The gas-dust region of the accretion discs can be approximated as a simple differentially rotating shear flow – known as Taylor-Couette (TC) flows – with near-Keplerian velocity profiles (Dubrulle et al. 2004). A classic TC system consists of two concentric cylinders rotating with



(a) Protoplanetary disk around the young HL Tauri star

(b) Inner region of the protoplanetary disk around AB Aurigae star

Figure 1.1: (a) Image of a circumstellar disk surrounding a young star called HL Tauri, located at the Tauri constellation, observed by the Atacama Large Millimeter/submillimeter Array (ALMA) collaboration. Image obtained from (Brogan et al. 2015). (b) Image of an accretion disc around the young *AB Aurigae* star, obtained by the ESO's Very Large Telescope (VLT) spotting signs of planet birth (Boccaletti et al. 2020), highlighting the spiral structure observed in accretion disks.

angular velocities Ω_{in} and Ω_{out} , and has a mean azimuthal velocity profile $\overline{u_\phi}$ given by:

$$\overline{u_\phi(r)} = \Omega_{in}r(\mu - \eta^2) + \frac{r_{in}^2\Omega_{in}(1 - \mu)}{r(1 - \eta^2)}, \quad (1.1)$$

where $\mu = \Omega_{out}/\Omega_{in}$ is the rotation ratio between inner and outer cylinders, and $\eta = r_{in}/r_{out}$ is the aspect ratio between inner and outer cylinder radius (r). Equation (1.1) is the analytical solution of the Navier-Stokes equations in cylindrical coordinates (ϕ, r, z) for incompressible Newtonian fluids in infinite long cylinders. When the first term of the right-hand side of (1.1) is zero, the velocity is a potential field, therefore curl-free. This defines the Rayleigh limit, $\mu = \eta^2$, which separates stable from unstable flows.

When $\mu < \eta^2$, $u_\phi(r)$ is unstable, and Taylor vortices can be observed. If $\mu > \eta^2$, $u_\phi(r)$ remains stable. In accretion disks, the Keplerian azimuthal angular velocity profile $\Omega(r) \propto r^{-3/2}$ (Dubrulle et al. 2004) leads to $\mu = \eta^{3/2}$, and hence to stable velocity profiles ($\mu > \eta^2$). This raises the question of which mechanisms could destabilize these rotating gas flows, generating the turbulent outward angular momentum transport.

Among other candidates, the strato-rotational instability (SRI) has attracted attention in recent years as a possible instability leading to turbulent motion in accretion disks (Dubrulle et al. 2004, Lyra and Umurhan 2019). In contrast to the Magnetorotational Instability (MRI), the SRI is a purely hydrodynamic instability consisting of a classical Taylor-Couette (TC) system with stable density stratification due to, for example, salinity (Withjack and Chen 1974, Boubnov et al. 1995, Park and Billant 2013, Le Bars and Le Gal 2007), or to a vertical temperature

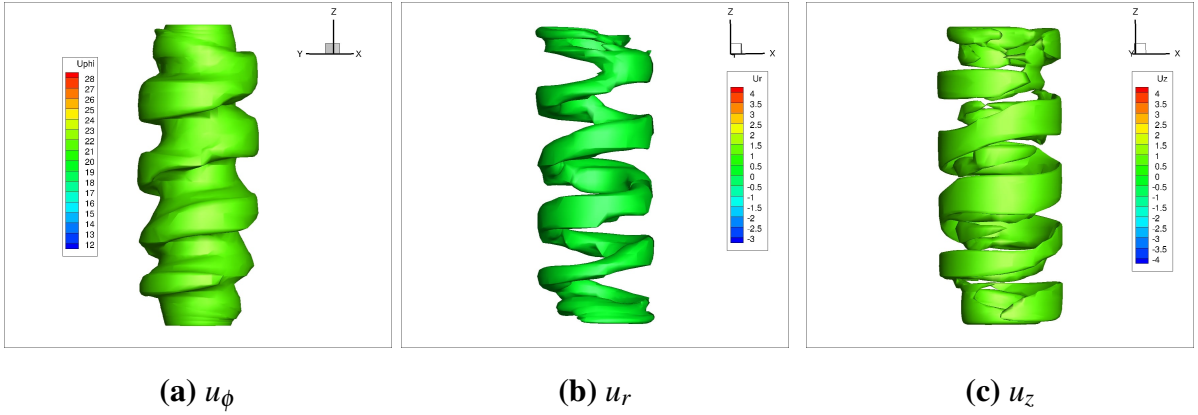


Figure 1.2: Velocity isosurfaces snapshots of the SRI showing its non-axisymmetric spirals obtained by numerical simulation with $\mu = 0.35$, $\eta = 0.517$, a linear stable axial temperature gradient with $\partial T / \partial z \approx 5.7 K/m$, $Fr \approx 1.5$ and $Re = 400$. The aspect ratio between cavity height and gap is $\Gamma = H / (r_{out} - r_{in}) = 10$. No-slip and impermeable Dirichlet boundary conditions are imposed ($u_\phi(r_{in}) = \Omega_{in} r_{in}$, $u_\phi(r_{out}) = \Omega_{out} r_{out}$, $u_z(z = 0) = 0$, $u_z(z = H) = 0$, $u_r(r_{in}) = 0$, $u_r(r_{out}) = 0$), and the bottom and top lids of the cavity rotate with the outer cylinder rotation Ω_{out} .

gradient (Rüdiger et al. 2017, Seelig et al. 2018). Dubrulle et al. (2004) concludes that, in astrophysical disks, stable stratification due to temperature differences is the rule rather than the exception. When a stable stratification is imposed on the TC system, the flow can be destabilized for $\mu > \eta^2$ leading to the SRI.

Experiments performed by Withjack and Chen (1974) found that, unlike the axisymmetric rolls in classic TC flows, the SRI presents non-axisymmetric spirals, confirmed by later experiments performed by Boubnov et al. (1995), as an example. Figure 1.2 shows isocontours of azimuthal (u_ϕ), radial (u_r), and axial (u_z) velocity components where these non-axisymmetric SRI spiral structures can be observed. Note that the spirals in figure 1.2 were obtained in a region where the flow is stable with respect to the non-stratified TC regime.

Due to new astronomical observations, as the one shown in figure 1.1.(b), the role of spirals in the planet formation mechanisms have been attracting attention recently (Brogan et al. 2015, Muro-Arena et al. 2020).

Caton et al. (2000) showed by linear stability analysis and experimental observations that the first SRI transition happens via a supercritical Hopf bifurcation that destabilizes purely azimuthal flows. Rüdiger et al. (2017) obtained marginal stability curves using linear stability analysis for different values of Rn , the Reynolds number based on the buoyancy frequency, defined as:

$$Rn = Nr_{in}(r_{out} - r_{in})/\nu. \quad (1.2)$$

where ν is the kinematic viscosity of the fluid, and N is the buoyancy frequency, also known as Brunt-Väisälä frequency

$$N = \sqrt{\alpha g \frac{\partial T}{\partial z}}. \quad (1.3)$$

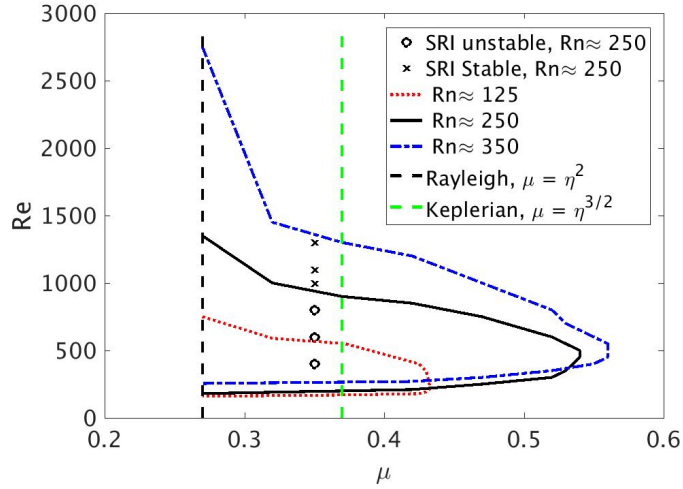


Figure 1.3: SRI marginal linear stability curves redrawn from Rüdiger et al. (2017) for 3 different values of Rn . Bigger values of Rn (and N) lead to larger instability regions. The black dashed vertical line in the left represents the Rayleigh limit $\mu = \eta^2$, which separates stable and unstable non-stratified TC cases (any to the left of this line in the diagram would be TC unstable). The green dashed vertical line in the right represents the Keplerian line $\mu = \eta^{3/2}$. SRI unstable (red circles) and stable (blue crosses) cases with $\eta = 0.517$, $Rn \approx 250$, $\mu = 0.35$ with different Reynolds numbers were investigated numerically and experimentally in this article.

Here, α is the coefficient of thermal expansion, g is the gravity constant, and $\partial T / \partial z$ is the axial temperature gradient. Note that, higher temperature gradients lead to higher values of N , and consequently, of Rn .

The Reynolds number of the stratified Taylor-Couette flows, based on the inner cylinder rotation (Ω_{in}), is defined as:

$$Re = \Omega_{in} r_{in} (r_{out} - r_{in}) / \nu. \quad (1.4)$$

The Froude number measures the relative importance of rotation and stratification, being defined as:

$$Fr = \frac{Re}{Rn} = \frac{\Omega_{in}}{N}. \quad (1.5)$$

Figure 1.3 shows marginal stability curves redrawn from Rüdiger et al. (2017) for different Rn values, and for the configurations we studied numerically and experimentally. Flows inside (outside) these curves are predicted to be SRI unstable (stable). Note that the SRI unstable regions increase with Rn . Obviously, stratified flows with $\mu > \eta^2$ can be unstable (to the right of the Rayleigh limit, shown by the black vertical dashed line). Most important, the Keplerian profile relevant for accretion disks can be unstable for all chosen Rn . The unstable regions in figure 1.3 were confirmed by experiments (Rüdiger et al. 2017, Seelig et al. 2018), but the upper transition back to stable regimes was not captured clearly in the previous experiments in the region $0.3 < \mu < 0.4$. On the other hand, Edlund and Ji (2014, 2015) and Lopez and Avila (2017) studied the turbulent boundary layer instabilities in quasi-Keplerian flows, and observed numerically and experimentally which increased Reynolds numbers relaminarize the flow, in agreement with the predictions of linear stability theory (Rüdiger et al. 2017). Following Lyra and Umurhan (2019), these uncertainties show the importance of understanding the

characteristics of stratified TC flows at increasingly higher Re values, highlighting the dangers of deriving conclusions regarding the behavior of protoplanetary disks based on relatively low Re quasi-Keplerian experiments and numerical simulations.

The SRI spirals are different from the ones observed in non-stratified TC flows. Yim and Billant (2015) investigated the reasons why the columnar vortex shape of strato-rotating fluids is different from the shear, centrifugal, or radiative instabilities. Leclercq et al. (2016) investigated connections between TC flows, radiative instabilities, and the SRI. Hoffmann et al. (2009) showed changes in the Taylor vortices of non-stratified TC systems when a low Reynolds number flow is forced in the axial direction. In these cases, the rolls assume inclination and shape similar to the ones observed in the SRI, traveling along the axial axis in the same direction as the flow imposed. These TC spiral propagation and inclination are affected by non-linear defects that are also observed in the SRI. When the external axial flow is stopped, there is a break of symmetry associated with a Hopf bifurcation, and a pattern change occurs, with changes in the spiral inclination, but keeping the same spiral shape observed in the SRI flow.

1.2 Outline

In this thesis, the strato-rotational instability is investigated both numerically and experimentally. Throughout this thesis, the SRI phenomena are studied in a temperature stratified Taylor Couette system. We focus on the astrophysical application of the SRI, mainly related to the theory of proto-planetary star development in accretion disks, composed of a gas and dust disk, where both differential rotation and stable thermal stratification can influence the fluid motion. The theoretical description of phenomena related to the investigation, the experimental setup, the numerical methods, the comparison of numerical and experimental investigations, and observations of physical pattern formation phenomena associated with the SRI are treated in different chapters, which will be described hereafter.

In chapter 2, the fundamental theory to describe the strato-rotational instabilities (SRI) will be presented. This chapter intends to provide the reader with a basic understanding of concepts that will be addressed in the following chapters, with further supplementary references indicated at the beginning and along with the chapter. The concepts addressed start with a presentation of the governing equations for the fluid motion on a stratified rotating media.; Then, internal wave phenomena are presented, followed by the description of the Taylor Couette instability. In the following, an overview of strato-rotational instability focusing on accretion disk applications will be presented. Then, the Ekman boundary layer effects are discussed and followed by the phenomena related to the turbulent kinetic energy distribution within the flow, and the turbulent energy spectra; Finally, a resume of non-dimensional numbers mentioned throughout the text is presented, so that the reader can easily consult their definitions while reading the text.

In chapter 3, the experimental setup designed at the Department of Aerodynamics and Fluid Mechanics (LAS) of the Brandenburg University of Technology Cottbus–Senftenberg (BTU) to study the SRI will be described. We will also present the methods implemented for measuring the velocity profiles that develop from the inner and outer cylinder rotation using a co-rotating mini-PIV system. Since the PIV camera has a tilted angle with respect to the laser sheets, an undistortion technique developed by Seelig et al. (2018) was applied to the images obtained, based on a polynomial distortion method, and will also be described. The experimental errors in the experimental velocity profiles are also evaluated in chapter 3, including a study of how many experimental measurements are necessary for the data to converge to average values. The procedure to establish an approximately linear temperature gradient in the axial direction, which

leads to a stable density stratification in the experimental setup, is also presented.

In chapter 4, the description of the CS2D-Annular numerical code is addressed. Since the SRI is an instability that develops different time-scale phenomena, the use of numerical methods, therefore, is not easy. It needs to comprehend fine meshes to solve all the scales involved in the problem, and long integration times are also required to fully develop all features of the instability evaluated. To overcome these difficulties, a direct numerical simulation (DNS) solver combining fourth-order accuracy space discretization and high-performance parallel computing (HPC) was developed by Abide et al. (2018) and was used in this thesis to investigate the SRI dynamics. The mathematical model, the time and space discretizations, as well as the strategies for the code parallelization will be presented in chapter 4.

In chapter 5, we will discuss physical phenomena observed in the SRI both numerically and experimentally with Reynolds number between $200 \leq Re \leq 1300$, $\mu = 0.35$ (slightly smaller than the Keplerian line, at $\mu \approx 0.375$ in the experiments here presented), and temperature difference between top and bottom lids of $\Delta T \approx 4K$. These values were chosen due to their possible practical implication on accretion disk theory. The results comparing experimental and numerical simulation data will be presented in the radial-azimuthal ($r - \phi$) cross-section, with values of $Re = 400$, $Re = 600$ and $Re = 800$, $Re = 1000$, respectively corresponding to inner cylinder angular velocities of $\Omega_{in}(Re = 400) \approx 0.381\text{rad/s}$, $\Omega_{in}(Re = 600) \approx 0.571\text{rad/s}$, and $\Omega_{in}(Re = 1000) \approx 0.952\text{rad/s}$. The objective of this comparison is not only the numerical code validation, since it has already been validated in previous works (Abide et al. 2017, 2018), but also to explore new physical phenomena associated with the SRI that can lead to a better understanding of this still not fully comprehended hydrodynamic instability.

The new high-performance computing numerical code allowed for the first time to observe long period phenomena of the SRI flow. This was not possible with comparatively much slower scalar codes, or with experiments performed during short periods. In chapter 6, we will evaluate the pattern formation in the SRI spiral structures, and slow varying phenomena associated with the changes in these patterns. We will also investigate how the secondary SRI instabilities associated with the pattern formation establishes in the flow. The effects of the pattern changes in the circulation and how it affects the SRI base flow will also be addressed in chapter 6. The relation of critical layer positions with the circulation cells and the flow structure will also be investigated. Different factors that could influence the SRI features, such as the Reynolds number, the geometrical parameter of the cavity (such as its height or gap size), and stronger or weaker stratification, will be explored numerically in separated sections of chapter 6. The energy spectra for different SRI regimes will also be investigated. This chapter also brings an evaluation of the SRI turbulent momentum transport in space and time, which will be related to important issues regarding how the SRI outwards transport of momentum in accretion disks. This will be related to the secondary instabilities found, and we will discuss how this could influence the aggregation of matter by gravity in the center of the disks, leading to proto-planetary star formation.

Finally, in chapter 7, the conclusions of the thesis are presented, including a summary of the work developed, and some suggestions of future works based on the results and questions raised throughout the thesis.

Chapter 2

Fundamentals

“Von den vielen Welten, die der Mensch nicht von der Natur geschenkt bekam, sondern sich aus eigenem Geist erschaffen hat, ist die Welt der Bücher die größte.”¹

– Hermann Hesse –

In this chapter, the fundamental theory used to describe the strato-rotational instabilities (SRI) studied with a temperature stratified Taylor Couette system will be presented, providing the reader with a basic understanding of concepts that will be addressed in the following chapters. In this thesis, we focus on the astrophysical application of the SRI, mainly related to the theory of proto-planetary star development in accretion disks, composed of a gas and dust disk, where both differential rotation and stable thermal stratification can influence the fluid motion. The full description of the topics addressed in this chapter is beyond the scope of this thesis. Therefore, the reader is referred to the works indicated in the literature for a more complete explanation of the phenomena presented in each section.

In section 2.1 the governing equations for the fluid motion on a stratified rotating media will be briefly presented. A complete derivation of the equations presented can be found in the textbooks Landau and Lifshitz (1959), Batchelor (2000), Kundu and Cohen (2001). In section 2.2, internal waves phenomena are presented, and the reader is encouraged to look at Sutherland (2010), Pedlosky (2013) for a complete description. The Taylor Couette instability is presented in section 2.3, and the supplementary text indicated are Taylor (1923), Drazin (2002), Kundu and Cohen (2001). Section 2.5 presents the Ekman boundary effects, and the supplementary textbooks indicated are Flor (2010), Childs (2011). Section 2.6 present phenomena related to the turbulent kinetic energy distribution within the flow and turbulent energy spectra, and the reader is encouraged to look at Pope (2001) and Dubrulle (2019) for more detailed discussions. Finally, the strato-rotational instability focusing on accretion disk applications will be presented in section 2.4. A review of instabilities in proto-planetary accretion disks can be found in Armitage (2019). Further supplementary references will be indicated along with this chapter, as more specific phenomena are addressed.

2.1 Equations of motion

Stable stratified rotating fluids are commonly found in nature, such as in the oceans and seas, which can be stratified due to an uneven distribution of salinity or due to temperature strat-

¹*Among the many worlds which man did not receive as a gift of nature, but which he created with his own mind, the world of books is the greatest.*

ification, when the bottom part gets colder than the surface due to smaller sun irradiation. The stable density stratification also occurs in the stratosphere region of the earth's atmosphere, in the earth's boundary layer at night, or in accretion disks, composed by a stable temperature stratified disk of gas and dust rotating in space (Dubrulle et al. 2004, Lyra and Umurhan 2019). Since these fluids are rotating, it is natural to write the momentum equations that describe their movements in a rotating coordinate. Due to the geometry of the problems that are investigated in this thesis, the equations are also presented in cylindrical coordinates. When the vertical length scales investigated are smaller than the density variation, density can be treated as constant in both continuity and momentum equations, except in the gravity term, to take into account buoyancy effects. This consideration is known as the **Boussinesq approximation** (Kundu and Cohen 2001). The Boussinesq approximation also takes into account the incompressibility of the flow, which can be considered in the cases addressed in this thesis, since the velocities involved in the problems evaluated are much smaller than the sound speed, leading to small Mach numbers ($\text{Mach} \ll 0.3$). The **Navier-Stokes equations** under the Boussinesq approximation in cylindrical coordinates on a reference frame rotating around the z axis with angular velocity $\Omega = |\vec{\Omega}|$ read

$$\begin{aligned} \frac{D\mathbf{u}}{Dt} + 2\vec{\Omega} \times \mathbf{u} &= -\frac{1}{\rho_0} \nabla p + \frac{\rho}{\rho_0} \mathbf{g} + \nu (\nabla^2 \mathbf{u}) + \mathbf{F}, \\ \nabla \cdot \mathbf{u} &= \frac{1}{r} \frac{\partial u_\phi}{\partial \phi} + \frac{1}{r} \frac{\partial (ru_r)}{\partial r} + \frac{\partial u_z}{\partial z} = 0, \end{aligned} \quad (2.1)$$

where $\mathbf{u} = (u_r, u_\phi, u_z)$ is the velocity vector field respectively in the radial, azimuthal and axial directions, p is the pressure, ν is the kinematic viscosity, ρ is the fluid density, ρ_0 is a constant reference density, \mathbf{g} is the gravity acceleration, and \mathbf{F} account for other body forces, such as the influence of magnetic fields, surface tensions, etc, that will not be considered here, therefore, we assume $\mathbf{F} = 0$. Note that, in other astrophysical and geophysical applications, such as magnetic excited regions on accretion disks, \mathbf{F} would play an important role. D/Dt is the material derivative, defined in cylindrical coordinates (figure 2.1) as

$$\frac{D}{Dt} \equiv \frac{\partial}{\partial t} + \frac{u_\phi}{r} \frac{\partial}{\partial \phi} + u_r \frac{\partial}{\partial r} + u_z \frac{\partial}{\partial z}. \quad (2.2)$$

The Laplacian operator is defined in cylindrical coordinates as

$$\nabla^2 \equiv \frac{1}{r^2} \frac{\partial^2}{\partial \phi^2} + \frac{1}{r} \frac{\partial}{\partial r} \left(r \frac{\partial}{\partial r} \right) + \frac{\partial^2}{\partial z^2}. \quad (2.3)$$

The term $f = 2\vec{\Omega} \times \mathbf{u}$ in (2.1) is the **Coriolis acceleration**.

Defining a characteristic length L , and a characteristic velocity U , we can introduce the following scaling

$$\begin{aligned} \mathbf{u} &= U \tilde{\mathbf{u}}, \quad \mathbf{r} = L \tilde{\mathbf{r}}, \quad t = \tilde{t}/\Omega, \\ p &= \rho_0 \Omega U L \tilde{p}, \quad \rho = \tilde{\rho} \rho_0, \\ T &= \tilde{T} T_0, \quad \tilde{\rho} = \alpha (\Delta T) \tilde{T} \end{aligned} \quad (2.4)$$

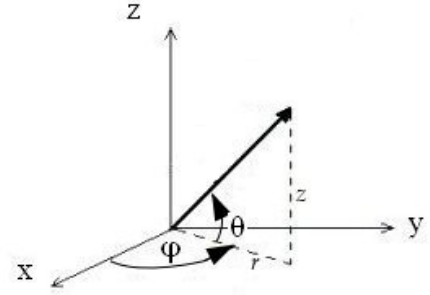


Figure 2.1: Cartesian and cylindrical coordinates.

where the tilde (\sim) indicates non-dimensional variables. Substituting (2.4) in (2.1), we obtain the non-dimensional momentum equations that read

$$\frac{\partial \tilde{\mathbf{u}}}{\partial \tilde{t}} + Ro (\tilde{\mathbf{u}} \cdot \tilde{\nabla}) \tilde{\mathbf{u}} + 2\mathbf{k} \times \tilde{\mathbf{u}} = -\tilde{\nabla} \tilde{p} + \frac{1}{Fr^2 Ro} \tilde{T} \mathbf{k} + E \tilde{\nabla}^2 \tilde{\mathbf{u}}, \quad (2.5)$$

where $\mathbf{k} \equiv \vec{\Omega}/|\vec{\Omega}|$, $\tilde{\nabla}$ is the non-dimensional gradient operator. Ro in (2.5) is the **Rossby number**, which measures the ratio between the non-linear advective and the Coriolis terms, defined as

$$Ro \equiv \frac{|(\mathbf{u} \cdot \nabla) \mathbf{u}|}{|\vec{\Omega} \times \mathbf{u}|} = \frac{U}{\Omega L}. \quad (2.6)$$

E in (2.5) is the **Ekman number**, that gives the relation between advection and viscous forces, and reads

$$E \equiv \frac{\nu}{\Omega L^2}. \quad (2.7)$$

The quantity Fr is the **Froude number**, that gives a ratio of inertial and gravitational forces, measures the relative importance of rotation compared to stratification, and reads

$$Fr \equiv \frac{\Omega}{N}, \quad (2.8)$$

where N is the buoyancy frequency, defined in equation (2.15).

2.1.1 Stable density stratification

We will now discuss the influence of stable density stratification due to a temperature gradient in the axial direction. In a stably stratified fluid, the density gradient $\partial \rho / \partial z$ decreases with the height, i.e., the density increases in the direction of the gravity acceleration. The flow is considered to be stably stratified because no natural convection occurs, since the less dense particles are placed on top of the “heavier” ones, and the system is stable with respect to Rayleigh-Bernard instabilities. The **energy equation** that governs the temperature evolution in stratified flow reads

$$\frac{DT}{Dt} = \kappa \nabla^2 T, \quad (2.9)$$

where κ is the fluid thermal diffusivity. The **density variation with temperature** follows the equation of state

$$\rho = \rho_0 (1 - \alpha \Delta T) \quad (2.10)$$

where α is the thermal expansion coefficient.

If we consider a stationary flow and neglect effects of viscosity on (2.1), we obtain an equation where the equilibrium is given by the hydrostatic balance between gravity and pressure forces that read

$$\frac{\partial p}{\partial z} = -\rho(z)g \quad (2.11)$$

where $\frac{\partial \rho}{\partial z}$ and $-\rho(z)g$ are the density and vertical pressure distributions respectively. The z -axis is taken vertically upward, leading to a stably stratified fluid with the density linearly increasing with depth.

If we now consider the vertical displacement δz of a particle initially at a vertical position z_0 in this stratified medium, a restoring force pushes this particle back to its original position. Newton's third law gives that this restoring force follows

$$\rho_0 \frac{d^2 z}{dt^2} = (\rho(z) - \rho_0) g. \quad (2.12)$$

The Taylor expansion of ρ around z_0 on the right-hand side of (2.12) leads to

$$(\rho(z) - \rho_0) g = g \left. \frac{d\rho}{dz} \right|_{z=z_0} \delta z + \mathcal{O}(\delta z^2) \quad (2.13)$$

If we consider the vertical displacement δz to be small, we can linearize (2.13) by neglecting terms of $\mathcal{O}(\delta z^2)$. Substituting then the linearized Taylor expansion on the right hand side of (2.12), we obtain the equation

$$\frac{d^2 \delta z}{dt^2} + N^2 \delta z = 0, \quad (2.14)$$

where N is known as the Brunt-Väisälä or buoyancy frequency, defined as

$$N^2 \equiv - \left. \frac{g}{\rho_0} \frac{d\rho}{dz} \right|_{z=z_0}. \quad (2.15)$$

The buoyancy frequency is associated with how a particle would oscillate around z_0 when it is displaced from its rest position in the vertical. When the particle is displaced, the density gradient accelerates it back to the z_0 position, which is indicated by the minus sign on the right-hand side of 2.15. Due to inertia, this particle would pass z_0 , and the buoyancy restoring force in the opposite vertical direction would force it back to z_0 again, leading to an oscillation around z_0 with frequency N . The oscillations of the particles displaced can also be observed by the fact that 2.14 is a harmonic oscillator equation, with solution $\delta z = Z \sin(Nt + \theta)$ where Z is the amplitude of the oscillation, and θ is the phase.

2.2 Wave propagation in a fluid

In a stably stratified fluid with the density linearly increasing with depth, internal waves can propagate in any direction and at any angle with respect to the vertical (Kundu and Cohen 2001), with the direction indicated by their wave number vector components $\mathbf{K} = (m, l, k)$. In geophysical stratified rotating fluids, internal waves can be generated by the flow over topography, by convection, and by spontaneous imbalance due to perturbations in the geostrophic equilibrium, when the pressure terms are balanced by Coriolis effects (Rodda 2019). Baroclinic processes, where surfaces of constant pressure do not coincide with the surfaces of constant density, can also create vortices that excite Internal waves in a rotating and continuously stratified fluid.

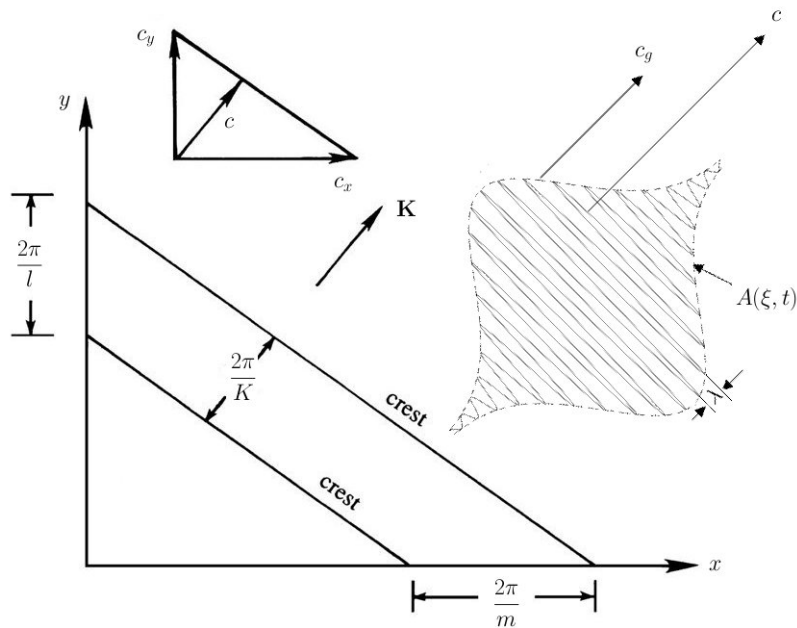


Figure 2.2: Schematic representation of wave crests and of the wave package propagating in the $x - y$ plane, adapted from Kundu and Cohen (2001), Pedlosky (2013). The crest spacing along the coordinate axes is larger than the wavelength $\lambda = \frac{2\pi}{K}$ inside the package. The vector diagram on the top left side of the image shows how the trace velocities c_x and c_y are combined to give the phase velocity vector c . In the wave package, it is represented how every individual crests moves with phase speed c , and how the whole package moves with a different group velocity c_g , of amplitude $A(\xi, t)$ in the direction of the wavenumber \mathbf{K} .

The crest (or trough) of a propagating wave moves a distance $\Delta x_{\text{crest}} = (\omega/k)\Delta t$ on a time increment Δt with the phase velocity c , that specifies the travel speed of a constant-phase wave. The **phase speed** is then defined as

$$c = \omega/k = \lambda v. \quad (2.16)$$

Figure 2.2 shows a schematic representation of how wave crests propagate with the phase velocity c on a $x - y$ plane, reproduced from Kundu and Cohen (2001). Note that, although the representation is made in 2 dimensions, in general, waves may propagate in any direction.

When waves propagate, the dynamics of the phenomena impose a relation between the wave vector and frequency (Pedlosky 2013) that shows if waves are dispersive. When the speed of propagation depends on wave number \mathbf{K} , the wave is dispersive, which means that a concentrated wave packet, composed of many different wavelengths (or frequencies), does not maintain a constant waveform (or shape). This makes waves spread out (disperse) as it travels, with longer wavelength components traveling faster than the shorter ones, so that an initial impulse evolves into a wide wave train. This spreading out can be observed, for example, when we throw a rock in a river, and a train of waves propagating separately arise (Kundu and Cohen 2001, Collard et al. 2009). This relation between frequency and wavenumber is therefore called

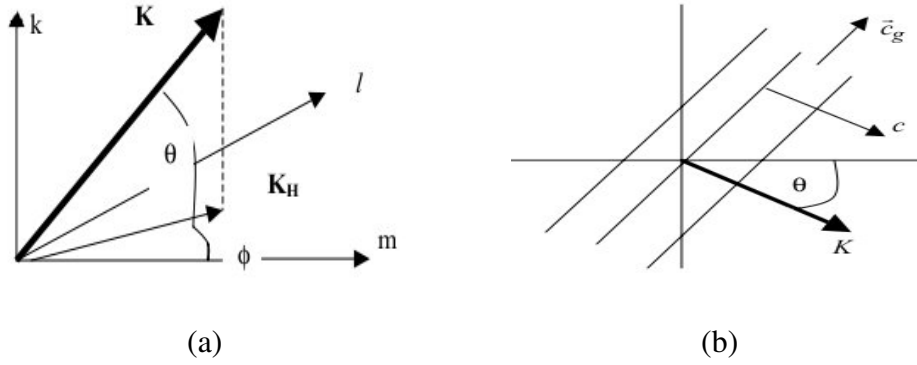


Figure 2.3: Schematic representation of (a) Wavenumber vector (\mathbf{K}) direction; (b) Phase velocity travelling in the direction of the wave number vector and orthogonal to the group velocity, as observed in internal waves generated by buoyancy and rotation. Reproduced from Pedlosky (2013).

the **dispersion relation** and can be written as

$$\omega = \omega(m, l, k) \quad (2.17)$$

highlighting that the wave frequency may depend on all three components of the wavenumber vector $\mathbf{K} = (m, l, k)$, shown in figure 2.3(a). Note that each wave vector has its own frequency, that often depends only on the magnitude of the wave vector, rather than on its orientation, but this is not always the case (Pedlosky 2013). For a specific wave number k and frequency ω , the phase of the wave propagating on an ξ spacial direction can be written as $\theta = k\xi - \omega t$, leading to the differential equation

$$\frac{\partial k}{\partial t} + \frac{\partial \omega}{\partial \xi} = 0. \quad (2.18)$$

Applying the chain rule to the dispersion relation presented in (2.17), the space derivative can be written as $\partial \omega / \partial x = \left(\frac{\partial \omega}{\partial k} \right) \left(\frac{\partial k}{\partial x} \right)$, and (2.18) can be re-written as the wave equation

$$\frac{\partial k}{\partial t} + c_g \frac{\partial k}{\partial x} = 0 \quad (2.19)$$

where

$$c_g = \frac{d\omega}{dk} \quad (2.20)$$

is called **group velocity**. Equation (2.19) shows that the group velocity is the speed at which wave numbers are advected in the flow. The energy of the wave also propagates with the group velocity c_g . Figure 2.2 schematically shows that, while the wave crests travel with a phase velocity c , a wave package travels with the group velocity c_g . Note that, although the phase speed and the group velocities are represented travelling in the same direction, this does not necessarily occur. In fact, for internal gravity waves (IGW), c is orthogonal to c_g , as schematically represented in figure 2.3(b). Note also that, if the waves propagate in a fluid that is moving at velocity \mathbf{u} (with respect the observer frame of reference), the phase speed is measured as $c_0 = c + u$, and the wave frequency ω_0 is Doppler shifted by the mean flow as

$$\omega_0 = \omega + \mathbf{u} \cdot \mathbf{K} \quad (2.21)$$

where ω is the intrinsic frequency measured by an observer moving with the flow with velocity u .

2.2.1 Gravity waves

In stably stratified fluids, **gravity waves** can be generated, for example, by the restoring buoyancy effects acting on a fluid particle that has been displaced from its original stable position by a perturbation (Gostiaux et al. 2007), as well as by oscillations in the cavity where a stably stratified fluid exists (Maas et al. 1997). The linearized non-rotating Boussinesq equations (2.1) for a fluid stably stratified has a solution in the form of a plane wave that can be written as

$$u = u_0 e^{i(\mathbf{k}\xi - \omega t)}, \quad (2.22)$$

and dispersion relation (ω), without taking into account the effects of rotation, given by

$$\omega^2 = \frac{N^2 K_H^2}{K^2} = N^2 \cos^2 \theta, \quad (2.23)$$

where $\mathbf{K} = (m, l, k)$ and $\xi = \xi_i, \xi_j, \xi_k$ are respectively the wavenumber and the space vector with components in the coordinates e_x, e_y, e_k . $K_H^2 = m^2 + l^2$ and $K^2 = m^2 + l^2 + k^2$, and u_0 is its amplitude. The angle θ in (2.23) is inclination of the wavenumber vector with respect to the horizontal plane, as shown on figure 2.3(a). Writing the dispersion relation of these waves in terms of the angle θ on (2.23) makes it more clear that their direction of propagation will not depend on the spatial scale, but only on the wave frequency and the stratification (Sutherland 2010).

The phase velocity c of the gravity waves without rotation is given by

$$\mathbf{c} = \frac{\omega}{|\mathbf{K}|^2} \mathbf{K} = N \cos \theta \frac{\mathbf{K}}{|\mathbf{K}|^2} \quad (2.24)$$

and the group velocity c_g is

$$\begin{aligned} \mathbf{c}_g &= \nabla_{\mathbf{k}} \omega = \left(\frac{\partial \omega}{\partial m}, \frac{\partial \omega}{\partial l}, \frac{\partial \omega}{\partial k} \right) \\ &= \left(\frac{Nk^2 m}{K^3 K_H}, \frac{Nk^2 l}{K^3 K_H}, -\frac{Nk K_H}{K^3} \right). \end{aligned} \quad (2.25)$$

Note that, for these gravity waves, the group velocity is orthogonal to the phase velocity, since

$$\begin{aligned} \mathbf{k} \cdot \mathbf{c}_g &= 0, \\ \mathbf{k} \times \mathbf{c} &= 0, \end{aligned} \quad (2.26)$$

which means that the group velocity propagates with a 90° angle with respect to the phase speed of the waves, as schematically represented in figure 2.3(b).

2.2.2 Inertial waves

When internal waves are generated in purely rotating flows, the Coriolis component $f\mathbf{k} \times \mathbf{u}$ in (2.1) acts as the restoring force, where $f = 2\Omega$ is the Coriolis parameter. In these cases, the waves are called **inertial waves**, and the linearized Boussinesq equations also lead to plane wave solutions, that was experimentally observed to propagate obliquely through the fluid, with

a fixed angle with respect to the rotation axis (Maas 2001). The dispersion relation of these gravity waves is given by

$$\omega^2 = f^2 \frac{k^2}{K^2} = f^2 \sin^2 \theta, \quad (2.27)$$

Note from (2.27) that, since $\omega/f = \sin\theta$, these waves only exist when the dispersion relation is smaller than the Coriolis parameter ($\omega < f$) (Batchelor 2000). The phase speed of the inertial waves is given by

$$\mathbf{c} = \frac{\omega \mathbf{K}}{K K} = \pm \frac{fk \mathbf{K}}{K K^2} \quad (2.28)$$

while the group velocity reads

$$\begin{aligned} \mathbf{c}_g = \nabla_{\mathbf{k}} \omega &= \left(\frac{\partial \omega}{\partial m}, \frac{\partial \omega}{\partial l}, \frac{\partial \omega}{\partial k} \right) \\ &= \left(-\frac{fmk}{K^{3/2}}, -\frac{flk}{K^{3/2}}, \frac{fK_H^2}{K^{3/2}} \right) \end{aligned} \quad (2.29)$$

Note that, again, the group and phase velocities propagate perpendicular to each other for gravity waves that arise from rotation, since $\mathbf{c}_g \cdot \mathbf{c} = 0$, as schematically represented in figure 2.3.

2.2.3 Inertial-gravity waves

Internal waves that are generated by the combined effect of rotation and stratification are known as **Inertial-gravity waves (IGW)**. These waves propagate shear within the flow, with both the Coriolis and buoyancy forces affecting their propagation (Maas 2001, Sutherland 2010). For IGW, the dispersion relation is given by

$$\omega^2 = N^2 \frac{m^2 + l^2}{K^2} + f^2 \frac{k^2}{K^2} = N^2 \cos^2 \theta + f^2 \sin^2 \theta \quad (2.30)$$

Note that (2.30) implies that IGW can only exist in the interval $N < |\omega| < f$ if $N < f$, or $f < |\omega| < N$ if $f < N$.

For IGW, considering \mathbf{c} in equation (2.28), the magnitude of phase velocity $c = |\mathbf{c}|$ reads

$$c = \frac{\omega}{(m^2 + l^2 + k^2)^{1/2}} = \frac{\sqrt{N^2(m^2 + l^2) + k^2 f^2}}{m^2 + l^2 + k^2}, \quad (2.31)$$

and the group velocity is given by

$$\begin{aligned} \mathbf{c}_g = \nabla_{\mathbf{k}} \omega &= \left(\frac{\partial \omega}{\partial m}, \frac{\partial \omega}{\partial l}, \frac{\partial \omega}{\partial k} \right) \\ &= \frac{N^2 - f^2}{(m^2 + l^2 + k^2)} \left(\frac{mk^2}{\omega}, \frac{lk^2}{\omega}, -\frac{k(m^2 + l^2)}{\omega} \right). \end{aligned} \quad (2.32)$$

Note that the group velocity is normal to the wavevector, but travels on an opposite vertical direction since the e_z (vertical) component of the group velocity in (2.32) assumes a negative sign. Again, we can see that $\mathbf{c}_g \cdot \mathbf{c} = 0$, i.e., that the group and phase velocities propagate perpendicular to each other.

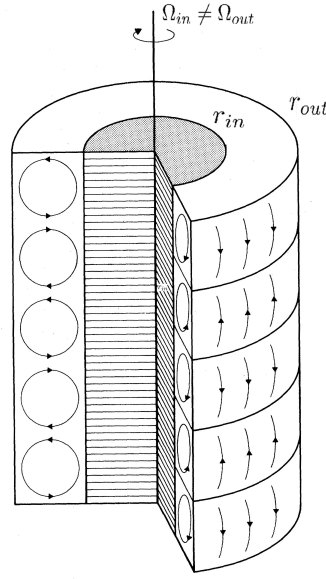


Figure 2.4: Schematic representation of Taylor vortices with counter-rotating pair of rolls reproduced from Cross and Hohenberg (1993).

The Coriolis parameter (f) was here considered to be constant, as we will not deal specifically with cases of varying Ω in this thesis, but it worth mentioning that, when f varies, the equations of motion allow another type of wave motion called *Rossby waves*, that are also important in several geophysical and astrophysical applications (Kundu and Cohen 2001, Pedlosky 2013).

2.3 Taylor-Couette Instability

To investigate the general hydrodynamic stability of a protoplanetary disk, we can approximate the gas flux as a circular shear flow known as Taylor-Couette (Klahr et al. 2018, Dubrulle et al. 2004). **Taylor–Couette (TC)** systems consist of two concentric cylinders that rotate with different angular velocities. Between the two cylinders, there is a fluid of density ρ that, depending on the amount of shear provided by the cylinder’s rotation, can develop an instability in the form of counter-rotating pairs of rolls known as Taylor vortices, as schematically represented in figure 2.4.

To understand the instability of TC systems, we will present the linear stability analysis following Kundu and Cohen (2001), Drazin and Reid (1981), Drazin (2002) and Klahr et al. (2018). Using the cylindrical coordinates ϕ , r and z (see figure 2.1), that are convenient to deal with the cylindrical geometry of the problem, and assuming axial symmetry, the 3 components of the incompressible inviscid momentum equations $D\mathbf{u}/Dt = -\nabla p/\rho$ read

$$\begin{aligned}
 \frac{\partial u_\phi}{\partial t} + u_r \frac{\partial u_\phi}{\partial r} + \frac{u_\phi}{r} \frac{\partial u_\phi}{\partial \phi} + \frac{u_\phi u_r}{r} + u_z \frac{\partial u_\phi}{\partial z} &= -\frac{1}{\rho r} \frac{\partial p}{\partial \phi}, \\
 \frac{u_r}{\partial t} + u_r \frac{\partial u_r}{\partial r} + \frac{u_\phi}{r} \frac{\partial u_r}{\partial \phi} - \frac{u_\phi^2}{r} + u_z \frac{\partial u_r}{\partial z} &= -\frac{1}{\rho} \frac{\partial p}{\partial r}, \\
 \frac{\partial r u_z}{\partial t} + u_r \frac{\partial u_z}{\partial r} + \frac{u_\phi}{r} \frac{\partial u_z}{\partial \phi} + u_z \frac{\partial u_z}{\partial z} &= -\frac{1}{\rho} \frac{\partial p}{\partial z},
 \end{aligned} \tag{2.33}$$

with the continuity equation $D\mathbf{u}/Dt = 0$ in cylindrical coordinates written as

$$\frac{1}{r} \frac{\partial u_\phi}{\partial \phi} + \frac{1}{r} \frac{\partial (ru_r)}{\partial r} + \frac{\partial u_z}{\partial z} = 0. \quad (2.34)$$

Note that the equations of motion (2.33) are not written here under the Boussinesq approximation as previously presented in (2.1), and no density stratification is considered. Using the Reynolds decomposition to separate variables corresponding to the base flow (capital letters) and the perturbation (primed variables), we can re-write the velocity and pressure terms as

$$\begin{aligned} \mathbf{u} &= \mathbf{U} + \mathbf{u}', \\ \mathbf{p} &= \mathbf{P} + \mathbf{p}'. \end{aligned} \quad (2.35)$$

In the TC system, the base state is given by

$$\begin{aligned} U_\phi &= V(r), \quad U_r = U_z = 0, \\ \frac{1}{\rho} \frac{dP}{dr} &= \frac{V^2}{r}, \end{aligned} \quad (2.36)$$

where

$$\begin{aligned} V(r) &= Ar + \frac{B}{r}, \quad \text{with} \\ A &= \frac{\Omega_{out} r_{out}^2 - \Omega_{in} r_{in}^2}{r_{out}^2 - r_{in}^2}, \quad \text{and} \\ B &= \frac{(\Omega_{out} - \Omega_{in}) r_{out}^2 r_{in}^2}{r_{out}^2 - r_{in}^2}. \end{aligned} \quad (2.37)$$

We can then substitute (2.35) into (2.33) and (2.34), and subtracting then the base flow from the results, we obtain the equations for the fluctuations, that read

$$\begin{aligned} \frac{\partial u'_\phi}{\partial t} + \left(\frac{dV(r)}{dr} + \frac{V(r)}{r} \right) u'_r + \frac{V(r)}{r} \frac{\partial u'_\phi}{\partial \phi} &= -\frac{1}{r\rho} \frac{\partial p'}{\partial \phi}, \\ \frac{\partial u'_r}{\partial t} + \frac{V(r)}{r} \left(\frac{\partial u'_r}{\partial \phi} - 2u'_\phi \right) &= -\frac{1}{\rho} \frac{\partial p'}{\partial r}, \\ \frac{\partial u'_z}{\partial t} + \frac{V(r)}{r} \frac{\partial u'_z}{\partial \phi} &= -\frac{1}{\rho} \frac{\partial p'}{\partial z}, \\ \frac{1}{r} \frac{\partial u'_\phi}{\partial \phi} + \frac{u'_r}{r} + \frac{\partial u'_r}{\partial r} + \frac{\partial u'_z}{\partial z} &= 0. \end{aligned} \quad (2.38)$$

Note that non-linear terms in (2.38) (containing products of fluctuations) were neglected because these perturbations are assumed to be infinitesimally small. Therefore, second-order terms are too small compared to the other terms in the equation and are dropped. Note that equations (2.38) admit plane wave solutions of the form

$$\left(u'_\phi, u'_r, u'_z, p' \right) = \left(u_\phi(r), u_r(r), u_z(r), p(r) \right) e^{i(\omega t + m\phi + kz)}. \quad (2.39)$$

Substituting (2.39) in the perturbation equations (2.38), we obtain

$$\begin{aligned}
i \left(\omega + \frac{V(r)}{r} \right) u'_\phi - \left(\frac{V(r)}{r} + \frac{dV(r)}{dr} \right) u'_r &= -\frac{imp'}{r\rho} \\
i \left(\omega + m \frac{V(r)}{r} \right) u'_r - \frac{2V(r)}{r} u'_\phi &= -\frac{1}{\rho} \frac{dp'}{dr}, \\
i \left(\omega + m \frac{V(r)}{r} \right) u'_z &= -ik \frac{p'}{\rho}, \\
\frac{du'_r}{dr} + \frac{u'_r}{r} + \frac{imu'_\phi}{r} + ik u'_z &= 0.
\end{aligned} \tag{2.40}$$

Drazin and Reid (1981) derived the equation for the perturbed flows in a Lagrangian frame of reference that allowed them to define the stability criteria for the Taylor-Couette-flow under an axisymmetric perturbation neglecting viscous effects called the **Rayleigh discriminant**, which is defined as

$$\Phi = 2 \frac{\Omega(r)}{r} \frac{d(r^2 \Omega(r))}{dr} < 0 \text{ Unstable}, \tag{2.41}$$

where $\Omega(r) = V(r)/r$ is the flow angular velocity as a function of the radial position. Equation (2.41) shows that when $\Phi < 0$, the motion becomes unstable, with epicyclic oscillations around the equilibrium state that make the perturbations grow exponentially, and the Taylor columns appear. When $\Phi > 0$, on the contrary, the instabilities decrease and the flow becomes stable. This criterion was demonstrated by Rayleigh to be a necessary and sufficient condition for the instability to occur (Kundu and Cohen 2001). Note that the circulation for inviscid flows is constant according to Kelvin's circulation theorem, and will be given by

$$\Gamma = 2\pi r V(r) = \text{constant}, \tag{2.42}$$

which means that perturbations will be conserved if an axisymmetric ring of radius r is perturbed, therefore, also $V(r)$ in equation (2.42) will be conserved. The horizontal swirls will then manifest themselves in the fluid due to a centrifugal force density $\frac{\rho V^2}{r} = \frac{\rho V^2(r)}{r}$ acting in the radial direction with a potential energy density $\frac{1}{2} \frac{\rho (rV(r))^2}{r^2} = \frac{1}{2} \rho u_\phi^2(r)$ (Drazin 2002). If we then consider the exchange of position of two rings with equal masses and arbitrary radial positions $r_2 > r_1$, the increase in kinetic energy after the exchange will be given by $\frac{r_2^2 V^2(r_2) - r_1^2 V^2(r_1)}{2} \left(\frac{1}{r_1} - \frac{1}{r_2} \right)$.

This exchange can only occur if $((r_1^2 V(r_1))^2 > (r_2^2 V(r_2))^2)$, otherwise, there will be no sufficient centrifugal force to drive the changes. Therefore, the Rayleigh criterion for the TC instability can also be written as

$$Ra \equiv \frac{d(r^2 V^2(r))}{dr} < 0, \text{ Unstable}. \tag{2.43}$$

For a TC experiment with concentric cylinders rotating with different inner (Ω_{in}) and outer (Ω_{out}) cylinders angular velocities (see chapter 3), the Rayleigh limit is found at η^2 , where $\eta = \frac{r_{in}}{r_{out}}$ is the ratio between inner and outer cylinder radii. Applying the Rayleigh criterion presented in equation (2.43), the instability of the fluid occurs when $\mu = \frac{\Omega_{out}}{\Omega_{in}}$ assume values of

$$\begin{aligned}
\mu &< \eta^2, \text{ unstable}, \\
\mu &> \eta^2, \text{ stable}.
\end{aligned} \tag{2.44}$$

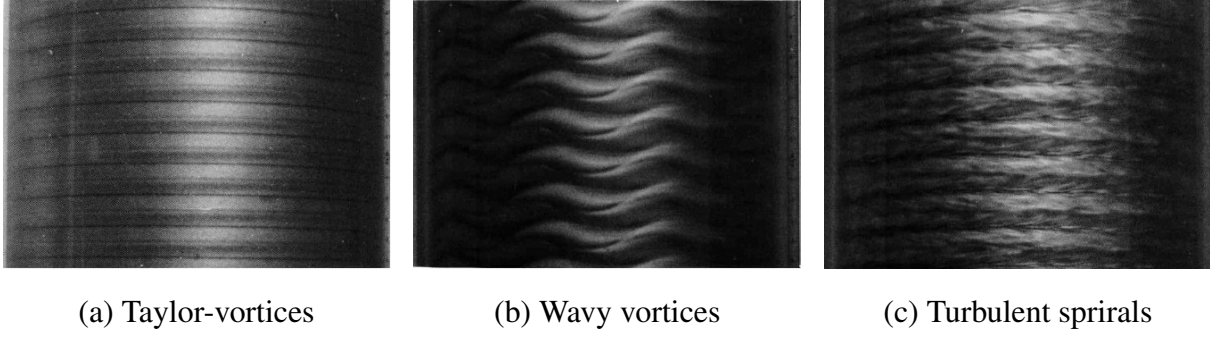


Figure 2.5: Different Taylor vortex spiral regimes visualized using machine oil with aluminum powder, reproduced by Van Dyke (1982). The different regimes are obtained by increasing the inner cylinder angular velocity (from left to right) while keeping the outer cylinder at rest. Considering the critical Reynolds numbers Re_{cr} where the spirals appear, and the Reynolds numbers based on the inner cylinder Re (a) $Re = 1.16Re_{cr}$ (b) $Re = 8.5Re_{cr}$ (c) $Re = 1625Re_{cr}$.

In accretion disks the gas of a protoplanetary disk orbits the star with an angular frequency close to $\Omega \approx \sqrt{\frac{GM_*}{r^3}}$, with M_* being the stellar mass, and $G \approx 6.6710^{-11} m^3 kg^{-1} s^{-2}$ is the gravitation constant, leading to a Keplerian azimuthal angular velocity of $\Omega \propto r^{-3/2}$ (Dubrulle et al. 2004). Note that, since $\mu \sim \eta^{3/2} > \eta^2$, the flow is stable with respect to the Rayleigh criterion.

For viscous flows, a similar linear stability analysis of the momentum equations and the control parameter obtained is the **Taylor number**, which reads

$$Ta \equiv \frac{4\Omega_{in}d^4}{\nu^2} \left(\frac{\Omega_{in}r_{in}^2 - \Omega_{out}r_{out}^2}{r_{out}^2 - r_{in}^2} \right), \quad (2.45)$$

where the **critical Taylor number** defines that the flow will be stable until reaching the Ta_{cr} value. Note that viscosity tends to stabilize the flow with respect to the inviscid Rayleigh solution, i.e., viscosity makes the flow remain stable with higher shear rates. That is why, in this thesis, we say that a system is stable concerning the TC instability when it is beyond the Rayleigh limit since this implies that the system is also stable considering viscous effects, therefore, making Ra a more conservative parameter than Ta to evaluate if the system is stable with respect to centrifugal instabilities.

Figure 2.5 shows Taylor spirals with different Reynolds numbers visualized by Van Dyke (1982) on a TC experimental setup with rotating inner cylinder and keeping the outer cylinder at rest. Note that the Taylor vortices become unstable themselves at higher values of Ta (higher Re). In figure 2.5(a), the Reynolds number value is close to the critical Reynolds numbers where the TC instability first appears (Re_{cr}), and asymmetric standing rolls in the form of counter-rotating toroidal vortices are observed. When the Reynolds number increases from $Re = 1.16Re_{cr}$ in 2.5(a) to $Re = 8.5Re_{cr}$ in figure 2.5(b), the axisymmetric structure changes into a wavy vortices regime, where $\partial/\partial\phi \neq 0$, associated to the next higher mode of the instability. When the Reynolds number is increased to $Re = 1625Re_{cr}$, turbulent features can be then observed superimposed to the Taylor vortices. Increasing the Reynolds numbers even more leads to fully turbulent flows, without a clear presence of the Taylor vortices. The transition of the Taylor rolls themselves is analogous to the primary TC flow transition from the stable regime to the appearance of Taylor vortices, therefore, they are called secondary instabilities. A marginal instability map for different TC regimes, obtained by Andereck et al. (1986), is presented in

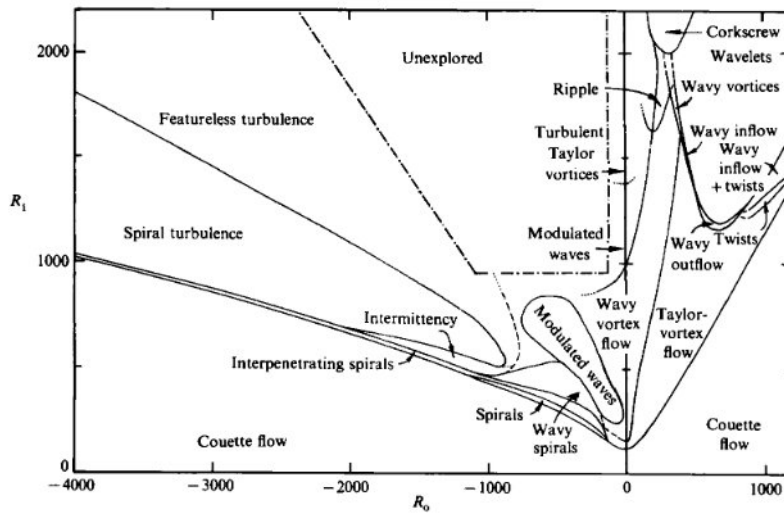


Figure 2.6: Different Taylor-Couette Regimes in cavities with long cylinders co-axially rotating with a different inner and outer Reynolds numbers (respectively represented by R_i , in the y-axis and R_o , in the x-axis). The diagram shows regimes for counter-rotating ($R_o < 0$) and co-rotating cylinders ($R_o > 0$), and is reproduced from Andereck et al. (1986).

figure 2.6. As we will see further, the strato-rotational instabilities (SRI) also present secondary instabilities, which will be investigated in chapter 6.

2.4 The Strato-Rotational Instability (SRI)

When the Taylor-Couette system presented in section 2.3 has a stable density stratification in the axial direction, the strato-rotational instability (SRI) can occur. This stratification is said to be stable when density increases in the direction of the gravity acceleration, and the flow is stable with respect to Rayleigh-Bernard instabilities, i.e., the flow is stable with respect to convection.

In nature, stable density stratification can be observed in many systems, such as in the stratosphere region of the atmosphere, or in the atmospheric boundary layer during the night, when the air is cooled near land bottom surfaces. In oceans and seas, salinity can lead to the stratification, or solar irradiation, that warms up the surface of the waters, decreasing the fluid density (see equation state (2.10)). As temperature decreases with depth in these cases, the water density increases towards the bottom, in the direction of gravity acceleration, creating then a stable density stratification. When stable density stratification establishes, a parcel of fluid that would be displaced upwards from its original position would be heavier than its surrounding environment and would tend to come back to its original position. Because this displaced parcel of fluid has inertia, it will pass again its original position and reach a surrounding environment that will now push it upwards due to buoyancy, since the surrounding fluid is now colder, therefore, denser than the displaced fluid parcel. The fluid pushed upwards would again pass its original position due to inertia. This mechanism makes a disturbed parcel of fluid oscillate in the direction of the stratification with a natural frequency N , that is the buoyancy frequency, presented in eq. (1.3).

In accretion disks, stable density stratification occurs along the axial direction, between the

outer and mid region of the disks. In the more external region of the disk, since matter becomes more sparse, opacity becomes smaller, and light can penetrate this region. Interactions of the gas that forms the disks with cosmic microwave background (CMB) radiation can then lead to the ionization of a thin layer in the outer regions of the disk (Gammie 1996). Since gravity tends to accumulate more matter in the mid regions of the disks, when we move towards the mid-plane region of the disks, the matter becomes more compact due to gravitational effects, and so that the CMB radiation can no longer ionize matter in a large inner region of the disks (Turner and Drake 2009), known as the 'dead zone' (Marcus et al. 2015). Although photons can not ionize the dead zone of the disks, the ionization in the bother of the disks increases the temperature in these outward regions, leading to stable density stratification in the axial direction. Stable density stratification in the axial direction, then, is expected to be the rule in accretion disks Dubrulle et al. (2004).

When stratification and rotation are present in a system, such as in the atmosphere, oceans, or in accretion disks, the interaction of inertia and buoyancy effects can lead to the hydrodynamical instability called the Strato rotational Instability (SRI). This instability manifests itself in the form of non-axisymmetric spirals (see figure 1.2), different from the axisymmetric Taylor-Couette vortices presented in section 2.3. This instability was first experimentally observed by Le Bars and Le Gal (2007). Although the SRI can arise from the interaction and resonances of internal waves within the fluid, that is generated in the presence of density stratification, the mechanisms that lead to the SRI, and how these resonances and interactions of waves can lead to the instabilities, remain to be better comprehended.

Marcus et al. (2013) propose that instabilities on flows that have shear and stratification can arise when critical layers are excited and transfer energy from the background shear to growing vortices. These vortices would then excite new critical layers themselves, that would replicate new self-similar vortices in a feedback process that can destabilize stratified Couette flows, as the dead zones of protoplanetary disks with Keplerian flows. Critical layers correspond to a particular region where singularities in the linear stability equations appear. A classical critical layer occurs when the phase speed (c) of a normal mode (of waves traveling in the azimuthal direction) would equal the mean flow ($\overline{u}_\phi - c = 0$) (Acheson 1976), while for stratified flows, critical layers that depend on the stratification can also exist, as when the phase speed equals a characteristic gravity-wave speed ($c = |N/m|$) (Wang and Balmforth 2018), with N being the buoyancy frequency, and m is the azimuthal wave number. Lesur (2007) considers that a rigid boundary could be necessary for the SRI to develop, if we consider it arising from the superposition of two Kelvin waves that result from the interaction between the Coriolis and the pressure terms, traveling in opposite directions in the near-wall region of stratified fluids. Park (2012), on the contrary, considers that the SRI could arise from the spontaneous radiation of internal waves that reflect and resonate interacting with critical layers that develop within the cavity, giving rise to the instability independently of the presence of a rigid outer boundary (Dizès and Riedinger 2010, Wang and Balmforth 2018).

Dubrulle et al. (2004) proposed that shear and stratification can onset the instability in a typical accretion disk by the spontaneous generation of linear modes when critical values of Reynolds numbers and stratification are combined, especially in weakly ionized regions of accretion disks, that would transit from stable to unstable SRI regimes via Hopf bifurcations. Furthermore, Dizès and Riedinger (2010), Park (2012), Armitage (2019) have shown that the instability depends upon the radiative properties of the disk.

In 2017, Rüdiger et al. (2017) presented marginal instability curves for the SRI obtained using linear stability results, reproduced in figure 2.7. The linear results show that stably stratified flows can become unstable beyond the Rayleigh critical values. These results showed how the

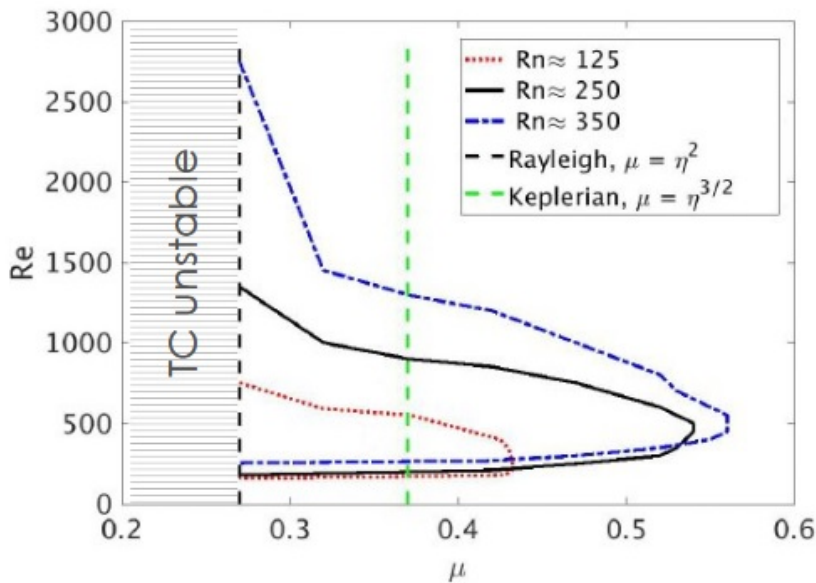


Figure 2.7: Marginal instability curves obtained by Rüdiger et al. (2017) with linear stability analysis for different values of Rn . The horizontal axis shows the ratio between outer and inner cylinder angular velocity (μ), and the vertical axis shows the Reynolds numbers. The vertical black dashed line on the left shows the Rayleigh limit, which separates non-stratified TC unstable and stable regimes, as indicated in the diagram (rotation ratios to the left of the Rayleigh line are TC unstable). The green vertical dashed line on the right represents the Keplerian line. The regions inside the marginal instability curves (for different Rn) represent SRI unstable solutions according to the linear theory.

SRI can destabilize the fluid outside the regime of the centrifugal instability, i.e., to the right of the black dashed vertical line in figure 2.7, including for the Keplerian azimuthal angular velocity of $\Omega \propto r^{-3/2}$ observed in accretion disks (Molemaker et al. 2001, Yavneh et al. 2001, Dubrulle et al. 2004).

Note that the SRI can also present secondary instabilities in the form of upwards and downwards traveling spirals in the axial direction that will be further investigated in chapter 6. Bengana and Tuckerman (2019) investigated numerically counter-rotating Taylor-Couette flows in which a Hopf-bifurcation also gives rise to branches of upwards and downwards traveling spirals, qualitatively similar to what was observed for the SRI in the present dissertation. Other upward and downward axial traveling spiral regimes were observed by Hoffmann et al. (2009) on co-rotating Taylor-Couette flows with a low Reynolds number flow imposed in the axial direction. When the axial flow is interrupted, changes in spiral directions of propagation occur spontaneously, also via Hopf-bifurcation, with similar features that will be presented here for the SRI.

2.5 Ekman boundary layers

Near the top and bottom boundaries of a rotating closed cavity, an **Ekman boundary layer** is established, where viscous forces are stronger and balanced by the pressure gradients and Coriolis force. Considering flows with small Rossby number in non-stratified media (as the TC

system), the non-dimensional momentum equation (2.5) can be written as

$$2\mathbf{k} \times \mathbf{u} = -\nabla p + E\nabla^2\mathbf{u} \quad (2.46)$$

where the term $E\nabla^2\mathbf{u}$ represents viscous effects. Note that this term becomes important when large velocity gradients are present somewhere in the flow domain (Flor 2010), which is the case for the near lid regions of closed rotating cavities. The thickness δ_{Ek} of Ekman boundary layers is given by

$$\delta_E \sim \sqrt{\frac{\nu}{\Omega}} \quad (2.47)$$

leading to $\delta_E \sim 3$ mm in the experimental setup and numerical simulations presented in chapters 3 and 4.

Equation (2.46) shows that within the Ekman layer near a solid surface, a three-way balance among the Coriolis, pressure, and viscous forces will result in a component of flow directed toward the lower pressure, and frictional forces can then cause the flow around a low-pressure center to spiral inwards (Kundu and Cohen 2001). Considering these mechanisms, the Ekman layer produces not only azimuthal velocity gradients near the end gaps of a cavity, but it can also lead to the development of radial and axial velocity components depending on the net horizontal convergence/divergence values. Although the radial and axial velocity components are small (Coles and Van Atta 1966), they can lead to momentum transport within the fluid, creating a non-azimuthal circulation. Such circulation may become significant under some conditions, generating large (and relatively weak) horizontal vortices that may extend from each end until the mid-plane of the system (Shionoya 1987, Coles and Van Atta 1966). When the fluid in the Ekman region can exchange momentum with the surrounding fluid outside the boundary layer, this is called **Ekman pumping**, and it can lead to Ekman instabilities in the flow (Lilly 1967, Aelbrecht et al. 1999). Figure 2.8 shows visualization using Kalliroscope particles performed by Shionoya (1987) of the Ekman layer in a TC experiment, with different inner and outer cylinder velocities, and with the upper and lower rigid boundaries attached to the outer cylinder (as in the experimental setup and numerical simulations presented in chapters 3 and 4). In figure 2.8(a), the outer cylinder rotation was spun from rest, with the Kalliroscope particles sedimented at the bottom of the cavity, showing how the Ekman cells can transport the particles in the flow until the mid-height position, and how it does not go beyond it. Figures 2.8(b),(c) show two different stable counter-rotating TC profiles with increasing Reynolds numbers, and the same rotation ratio $\mu = \Omega_{out}/\Omega_{in}$. Note that larger Re increase the Ekman influence in the axial direction, even if δ_{Ek} decreases, according to (2.47). Figure 2.8(d) shows how the Ekman effects can eventually impact the Taylor rolls outside the boundary layer, leading to an axial asymmetry of the spirals.

2.6 Turbulence Energy equations

Turbulence is a phenomenon that can efficiently transport and dissipate energy within a fluid (compared to diffusive processes). The analysis of how energy in a flow is affected by turbulence can be made by investigating the terms that govern the turbulent kinetic energy equations. Considering a turbulent flow in Cartesian coordinates under the Boussinesq approximation, with mean quantities in the flow indicated by an overbar, and fluctuations indicated by primed variables (considering the Reynolds decomposition in 2.35), the variation of **kinetic energy in the**

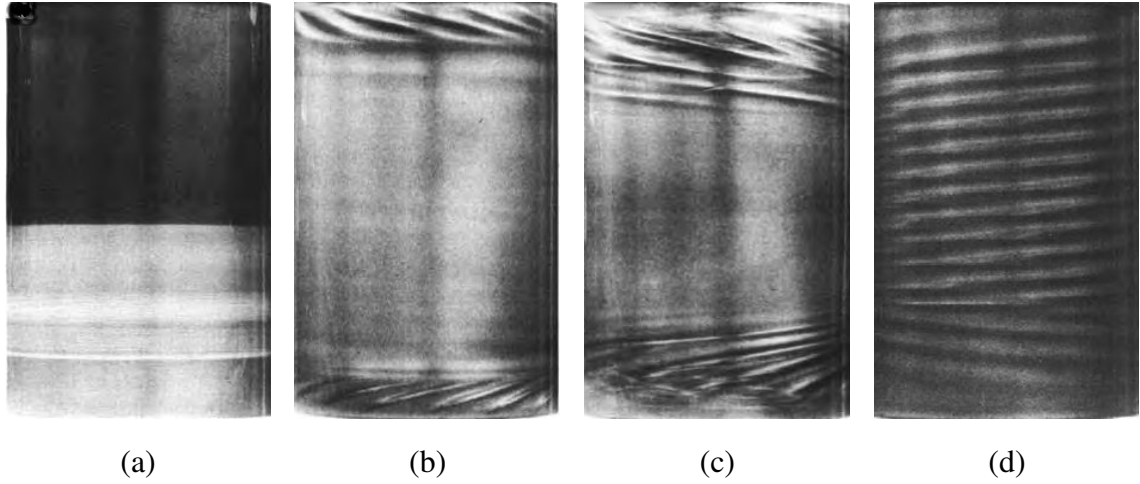


Figure 2.8: Experimental end gap effects visualized with Kalliroscope particles, reproduced from Shionoya (1987). (a) Inner cylinder at rest ($Re = 0$) and outer cylinder rotating with $Re_{out} = 1000$; Kalliroscope flakes fill only the lower half of the cylinder as the system is spun up from rest. (b) Laminar TC profile obtained for cylinders rotating in the same direction with $Re = 1124$, and $\mu = 0.89$; (c) Laminar TC profile obtained for cylinders rotating in the same with $Re = 4005$, $\mu = 0.89$; (d) Laminar Taylor vortices with $Re = 240$ and counter-rotating cylinders with $\mu = -1.25$.

mean flow per unit mass ($\bar{E} = \frac{1}{2}\bar{u}_i^2$) reads

$$\frac{D\bar{E}}{Dt} = \frac{\partial}{\partial x_j} \left(-\frac{\bar{u}_i p}{\rho_0} + 2\nu\bar{u}_i\bar{S}_{ij} - \overline{u'_i u'_j \bar{u}_i} \right) - 2\nu\bar{S}_{ij}\bar{S}_{ij} + \overline{u'_i u'_j} \frac{\partial \bar{u}_i}{\partial x_j} - \frac{g}{\rho_0} \bar{\rho} \bar{u}_k \quad (2.48)$$

where S_{ij} is the **strain rate tensor**, given by

$$S_{ij} = \frac{1}{2} \left(\frac{\partial \bar{u}_i}{\partial x_j} + \frac{\partial \bar{u}_j}{\partial x_i} \right). \quad (2.49)$$

The term on the left-hand side of (2.48) represents the variations of kinetic energy in the mean flow, and the right-hand side shows the mechanisms that lead to these variations. Other field forces, such as electromagnetic or surface tension forces, were not included in equation (2.48), since they will not be explored in this work, but they could be added when dealing with other applications, such as in studies of Magneto-Hydro Dynamics (MHD), also relevant for the theory of accretion disks.

The first three terms on the right-hand side of (2.48), inside the brackets, represent the **mean transport of kinetic energy** in the flow driven by **pressure** ($-\frac{\bar{u}_i p}{\rho_0}$), by **viscous forces**, ($2\nu\bar{u}_i\bar{S}_{ij}$), and due to **turbulent shear** ($-\overline{u'_i u'_j \bar{u}_i}$). These terms are not responsible for the turbulent production or dissipation, only for the transport and redistribution of kinetic energy from one region of the flow to another.

The fourth term on the right side of (2.48) is the product of viscous stresses and the mean shear stresses in the flow, and represents the kinetic **energy dissipation**, which is basically transformed to heat, given by

$$\varepsilon = (2\nu\bar{S}_{ij}\bar{S}_{ij}). \quad (2.50)$$

The fifth term on the right side of (2.48) is known as the **turbulence production**, and reads

$$P = \left(\overline{u'_i u'_j} \frac{\partial u_i}{\partial x_j} \right). \quad (2.51)$$

This term represents the interaction (transfer) of energy from the mean flow and the turbulent velocity fluctuations that are driven by shear, resulting in the increase of turbulent kinetic energy. Note that P is analogous to ε in the sense that they are both the product of the Reynolds stress by the shear rate. A region of the flow is then said to be in **local equilibrium** when the turbulence dissipation (2.50) and production (2.51) are equal in module, i.e., when all the energy that is being produced at the largest flow scales is being transferred to the smallest scales, where it is dissipated.

The influence of stable density stratification reflects in the last term on the right-hand side of (2.48), called the **buoyancy turbulent production**, and reads

$$\left(\frac{g}{\rho_0} \overline{\rho u_k} \right) = g \alpha \overline{u'_k T'}, \quad (2.52)$$

where the right-hand side was written considering the equation of state (2.10), so the buoyancy effect appears in terms of temperature fluctuations.

The equation for the **mean kinetic energy fluctuations** ($e = u_i'^2/2$) is given by

$$\frac{D\bar{e}}{Dt} = \frac{\partial}{\partial x_j} \left(-\frac{\overline{u'_i p}}{\rho_0} + 2\nu \overline{u'_i S'_{ij}} - \overline{u_i'^2 u'_j} \right) - 2\nu \overline{S'_{ij} \bar{S}'_{ij}} - \overline{u'_i u'_j} \frac{\partial \bar{u}_i}{\partial x_j} + g \alpha \overline{u'_k T'}, \quad (2.53)$$

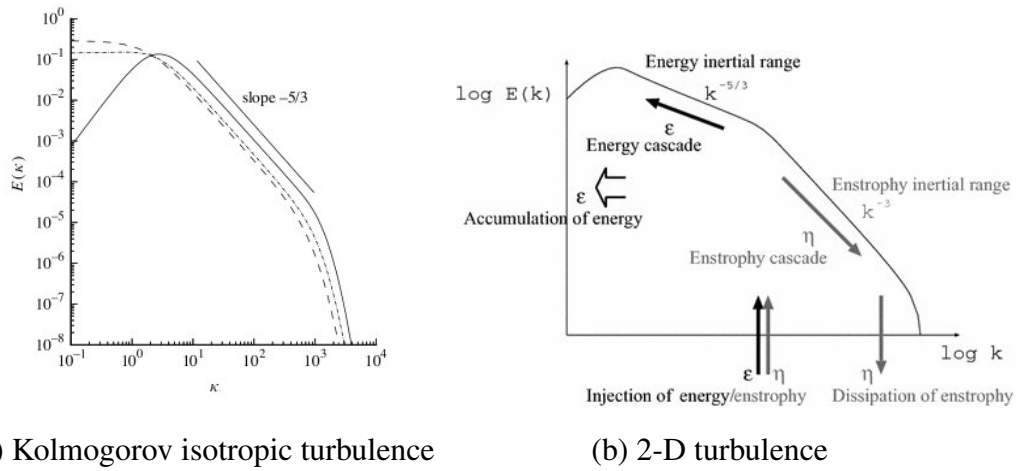
with the **strain rate tensor** S'_{ij} now given by

$$S'_{ij} = \frac{1}{2} \left(\frac{\partial u'_i}{\partial x_j} + \frac{\partial u'_j}{\partial x_i} \right). \quad (2.54)$$

Note that the density fluctuations term appears with a negative sign in (2.48), and with a positive sign in (2.53), showing how buoyancy removes energy from the mean flow and transfer it to the instability, increasing the buoyant generation of turbulent kinetic energy. The ratio of the buoyant term of turbulent kinetic energy (2.52) and the turbulence production by shear (2.51) is given by the **flux Richardson number**, defined as

$$Rf \equiv \frac{g \overline{\rho u_k} / \rho_0}{\left(\overline{u'_i u'_j} \frac{\partial u_i}{\partial x_j} \right)}. \quad (2.55)$$

The tensor correlation $\overline{u'_i u'_j}$ that appear in (2.48), (2.53), and in the flux Richardson number (2.55) is called the **Reynolds stress tensor**. This term is responsible for increasing momentum transfer in turbulent flows, which is often much larger than viscous stresses (except very near rigid and impermeable surfaces, where the fluctuations go to zero and mean flow gradients are large). The diagonal components of the Reynolds stress tensor $u_i'^2$ are normal stresses that augment the mean pressure, while its off-diagonal components $u'_i u'_j$ are shear stresses (Kundu and Cohen 2001). The average flux of turbulent momentum in the flow is then be given by $-\rho u'_i u'_j$, with $i \neq j$. Note that, when the Rf values become large, buoyancy can remove turbulence at a larger rate than its production by shear. Instead of using Rf to measure the ratio



(a) Kolmogorov isotropic turbulence

(b) 2-D turbulence

Figure 2.9: Energy spectra schematically representing (a) High Reynolds number Kolmogorov turbulence reproduced from Pope (2001); (b) Two-dimensional turbulent flow with an energy and enstrophy cascade reproduced from Kyushu University (2017).

between stratification and shear in a flow, it may be more convenient to measure the gradient **Richardson number** (Kundu and Cohen 2001), which is defined as

$$Ri \equiv \frac{N^2}{(d\bar{u}/dz)^2} = \frac{\alpha g (d\bar{T}/dz)}{(d\bar{u}/dz)^2}, \quad (2.56)$$

where N is the buoyancy frequency and the right-hand side of the equality follows for stratification by thermal variations (Kundu and Cohen 2001). The instabilities that lead to turbulence on a stratified flow can only occur for $0 < Ri < 0.25$ (Panofsky and Dutton 1984). When the critical Richards numbers $Ri_{cr} \approx 0.25$ is reached, the turbulent motion driven by shear is suppressed by the stratification.

2.6.1 Turbulent energy spectra

The turbulent energy cascade was initially based on the ideas of Richardson (1922), later quantified by Kolmogorov (1941), that turbulence can be considered as a composition of eddies with different sizes (Kundu and Cohen 2001). In turbulent flows, most of the energy is contained in large-scale vortices within the fluid, i.e., in the larger structures, corresponding to smaller wavenumbers (k), therefore, this is called the **energy region** of the spectrum. The energy is transferred from the larger scales to the smallest scales (where it is dissipated) along the so-called **inertial region**, which has a decay rate proportional to $k^{-5/3}$ in the classic Kolmogorov turbulent cascades (figure 2.9(a)). The energy transfer from the larger to the smallest scales is schematically represented in figure 2.10, reproduced from Pope (2001), with the length scales ℓ decreasing from the right to the left-hand side of the figure. The sub-index EI indicates the transition between the larger-scale energy region and the inertial region, while the DI indicates the separation between the inertial (I) and the dissipation (D) regions. ℓ_0 represents the typical length scale of the largest structures in the flow, where turbulence is produced, and η represents the Kolmogorov scale, which accounts for the smallest scales in the flow, where turbulent energy tends to be dissipated by viscous effects. At the Kolmogorov scales, turbulence tends to be isotropic.

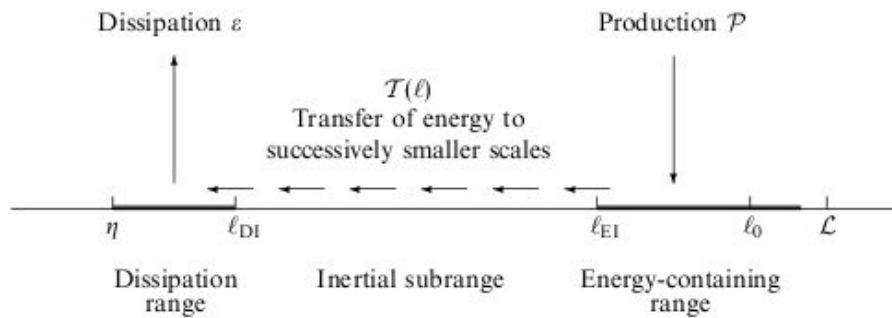


Figure 2.10: Schematic representation of energy input in the large scales, where turbulence production occurs, and its transference along the inertial region to the smallest scales, where energy is dissipated. The larger scales correspond to the small wavenumbers k . The sub-index EI stands for the interface between Energy (E) and Inertial (I) ranges, and DI for the separation of the dissipation D and I inertial scales of the flow, while ℓ_0 represent the larger scales, and η the Kolmogorov scales. Reproduced from Pope (2001)

Although astrophysical, climate and weather models are performed on an everyday basis for the most diverse applications, such as meteorological forecasts, climate modeling, or the study of turbulence in the astrophysical context, turbulence in these large scale flows is still not fully understood from a fundamental point of view. In particular, questions related to how the energy contained in the largest scales (where most of the turbulence production occurs due to energy input from sources such as solar or stars radiation, ocean dynamics, etc.) is transferred to the smallest scales of turbulence in geophysical and astrophysical flows, and where the energy is dissipated in these systems, remain largely without answer (Müller et al. 2005). Atmospheric and ocean dynamics, for example, are dominated by planetary rotation and the effects of stable density stratification, but the influence of these factors vary according to the scale of the structures present in the fluid. On larger scales, the effects of both rotation and density stratification are quite relevant in geophysical and astrophysical contexts, which can generate essentially two-dimensional flows, known as quasi-geostrophic. On small scales, the fluid motion is not strongly influenced by rotation and stratification and, in this way, turbulence becomes practically isotropic. Between the largest and the smaller scales, where there it is dissipated by viscosity, there are intermediate-scales on which the effects of rotation are weak while the stratification effects remain relevant. At these intermediate scales, the flows start to show relevant three-dimensional effects, and turbulence becomes highly anisotropic (Billant and Chomaz 2001).

Along the turbulence spectrum of stratified flows, between the production and dissipation regions, different flow regimes occur. These “paths” in the turbulent energy spectrum can involve processes of about eight different orders of magnitude that separate the scales of generation and dissipation. Until recently, these different regimes have generally been studied separately, using appropriate approaches valid for each of them. The quasi-geostrophic turbulence was first described by Charney (1971). In this regime, the force generated by the pressure gradient is balanced by the Coriolis and buoyancy forces, and two quadratic invariant quantities are conserved independently: the total energy and the potential enstrophy, which is defined as the square of the vorticity and is related to the dissipation effects of turbulent kinetic energy (Dubrulle 2019). Using these invariant quantities, and considering the geostrophic balance of buoyancy, rotational, and Coriolis forces mentioned, it is possible to predict that, in atmo-

spheric, oceans, and astrophysical flows, energy flows both in the direction of small scales, called **direct cascade**, and also in the direction of large scales, called the **inverse cascade**, as shown in figure 2.9(b). This is consistent with the idea that strong rotations lead to an inverse energy cascade, while strong stratification favors a cascade of energy towards small scales, but it is not clear how these two regimes are connected in strato-rotational flows. Note that the inertial range of quasi-geostrophic inverse energy cascades have decay rates proportional to $K^{-5/3}$, as in the Kolmogorov turbulence, and the enstrophic region follows a power law of K^{-3} , while other phenomena can lead to different slopes of the inertial region in the energy spectra. Other decay rates will be later explored in this work in section 6.3.

The inverse energy transfer seems to be inconsistent with the dissipation of energy in the region of the smallest scales, raising issues concerning the balance between the turbulent energy production and dissipation, with energy being accumulated at the larger scales. Vallgren et al. (2011) performed high-order numerical simulations that contemplate the quasi-geostrophic regime (and other regimes). They showed that for small and finite Rossby numbers (when the Coriolis terms in the momentum equations are larger than the advective terms) a direct energy cascade can coexist with an enstrophy cascade in the opposite direction. This could explain how part of the energy contained in the largest scales could indeed be transferred and dissipated in the small scales, solving the apparent contradiction associated with the absence of dissipation of the quasi-geostrophic turbulence. In addition to numerical simulations, ocean measurements performed by Ménesguen et al. (2009) have revealed the presence of layers and structures of small scales in large scale vortices.

2.7 Non-dimensional variables

Throughout this thesis, some non-dimensional quantities are frequently mentioned. These variables are used in the evaluation of the results obtained, or for analyzing concepts associated with the phenomena investigated. This section intends to provide the reader with a fast description of non-dimensional variables that can be consulted while reading the text, mentioning which quantities they relate.

- The **Reynolds number** (Re) is the most common dimensionless number in fluid mechanics. Low Re flows involve small sizes, low speeds, and high kinematic viscosity such as bacteria swimming through mucous. High Re flows involve large sizes, high speeds, and low kinematic viscosity such as an ocean liner steaming at full speed (Kundu and Cohen 2001). The Reynolds number of the stratified Taylor-Couette flows, based on the inner cylinder rotation (Ω_{in}), is defined as:

$$Re \equiv \frac{\text{inertia forces}}{\text{viscous forces}} = \frac{\Omega_{in} r_{in} (r_{out} - r_{in})}{\nu}, \quad (2.57)$$

where ν is the kinematic viscosity of the fluid, Ω_{in} is the angular velocity, and r_{in} r_{in} and r_{out} are respectively the inner and outer cylinder radii.

- The **Reynolds number based on the buoyancy frequency** (Rn) can be defined in a density-stratified fluid. Instead of considering the angular frequency Ω_{in} in the Reynolds

numbers, that takes into account inertia effects, we then consider the buoyancy frequency N to measure the relative importance of buoyancy with respect to viscous effect, as:

$$Rn \equiv \frac{\text{Buoyancy forces}}{\text{viscous forces}} = \frac{Nr_{in}(r_{out} - r_{in})}{\nu}, \quad (2.58)$$

where N is the buoyancy frequency, also known as Brunt-Väisälä frequency

$$N \equiv \sqrt{\alpha g \frac{\partial T}{\partial z}}, \quad (2.59)$$

where α is the coefficient of thermal expansion, g is the gravity constant, and $\partial T/\partial z$ is the axial temperature gradient.

- The **Froude number** (Fr) measures the relative importance of rotation and stratification, being defined as:

$$Fr = \frac{\text{Inertia forces}}{\text{buoyancy forces}} = \frac{Re}{Rn} = \frac{\Omega_{in}}{N}. \quad (2.60)$$

- The **Richardson number** (Ri) can alternatively replaced the Froude number, explicitly showing the relation between the buoyancy frequency (N) and shear stresses on a space direction z (Kundu and Cohen 2001). Ri is here defined as:

$$Ri \equiv \frac{\text{Buoyancy}}{\text{shear}} \equiv \frac{N^2(z)}{(\partial u/\partial z)^2} \quad (2.61)$$

- The **Prandtl number** (Pr) measure the ratio between momentum and thermal diffusivity, therefore, it is related to intrinsic properties of the fluid, and is computed as:

$$Pr \equiv \frac{\text{momentum diffusivity}}{\text{thermal diffusivity}} = \frac{\nu}{k/(c_p \rho)}. \quad (2.62)$$

- The **Mach number** (Ma) represents the ratio between flow velocity and the local speed of sound and is given by

$$Ma \equiv \frac{\text{flow velocity}}{\text{speed of sound}} = \frac{u}{c}. \quad (2.63)$$

A flow is considered to be incompressible if the flow speeds are low enough compared to the speed of sound, for Mach numbers < 0.3 .

- The **Rossby number** presents the ratio between inertial to Coriolis forces and is given by

$$Ro \equiv \frac{\text{Nonlinear acceleration}}{\text{Coriolis forces}} = \frac{U}{\Omega L} \quad (2.64)$$

A small Rossby number represents a system strongly affected by Coriolis forces, while a large Rossby number implies a system in which inertial and centrifugal forces are dominant.

- The **Ekman number** describes the ratio of viscous to Coriolis forces and is given by

$$E \equiv \frac{\text{viscous forces}}{\text{Coriolis forces}} = \sqrt{\frac{Ro}{Re}} = \frac{\nu}{\Omega L^2}. \quad (2.65)$$

Small Ekman numbers imply low frictional effects, and disturbances in the flow are able to propagate before decaying due to viscous dissipation. The Ekman number also describes the order of magnitude of the Ekman layer thickness, that is the boundary layer in which viscous diffusion is balanced by Coriolis effects, rather than the usual convective inertia (Kundu and Cohen 2001).

- The **Rayleigh criterion** indicates when an inviscid Taylor-Couette flow is unstable and is given by

$$Ra \equiv \frac{d(r^2 u^2(r))}{dr} < 0, \text{ unstable.} \quad (2.66)$$

For a TC experiment with concentric cylinders rotating with different inner (Ω_{in}) and outer (Ω_{out}) cylinders angular velocities (see chapter 3), the Rayleigh limit is found at η^2 , where $\eta = \frac{r_{in}}{r_{out}}$ is the ratio between inner and outer cylinder radii. Applying the Rayleigh criterion presented in equation (2.66), the instability of the fluid occurs when $\mu = \frac{\Omega_{out}}{\Omega_{in}}$ assume values of

$$\begin{aligned} \mu &< \eta^2, \text{ unstable,} \\ \mu &> \eta^2, \text{ stable.} \end{aligned} \quad (2.67)$$

Experimental methods

“Sanity is not statistical.”

– George Orwell, 1984 –

In this chapter, the experimental setup used to study the SRI is described. The experiment was designed at the Department of Aerodynamics and Fluid Mechanics (LAS) of the Brandenburg University of Technology Cottbus–Senftenberg (BTU). The methods implemented for measuring the velocity profiles that develop from the inner and outer cylinder rotation will also be presented.

Among different experimental techniques used to measure fluids velocity profiles, a few most common could be considered to investigate the SRI phenomena, such as Hot Wire Anemometry (HWA), Laser-Doppler Anemometry (LDA), particle tracking velocimetry (PTV), or Particle Image Velocimetry (PIV) (Ponchaut et al. 2005, Arroyo and Hinsch 2007).

Although hot wire measurements (HWA) have been successfully performed to obtain velocity profiles in fluids for a long time (Kovasznay 1949), being especially suitable to the study of turbulent with high Mach numbers for allowing high sampling rates, they bring the particular inconvenience of being an intrusive measurement technique, that can cause undesired perturbations in the flow. Also, among other problems, intrusive probes are more sensitive to multi-variable effects (temperature, humidity, etc.), and breakage (Jensen 2004). The Laser-Doppler Anemometry (LDA) is a non-intrusive optical point measurement technique that uses two laser beams superposed on a spatial point of the fluid, and the velocity is measured by the Doppler shift in the lasers caused by the flow. The LDA has several advantages, such as no calibration requirement, low noise in the data obtained, and high-frequency response, but it is more suitable to measure time varying phenomena at specific point locations in the fluid. With the fast developments of camera and laser technologies, techniques of particle tracking (PTV) started developing, where a particle in the fluid is followed on different images of the flow consecutively obtained in time. A particular way of dealing with the recognition of particles in the fluid, though, consists not of tracking one single particle, but of computing cross-correlations of groups of particles that can be observed in consecutive images. This method is called the Particle Image Velocimetry (PIV), and it has become one of the most popular techniques for flow measurements in numerous applications since it consists of a robust technique to evaluate space and time structures in fluids that are difficult be measured using other techniques.

A co-rotating mini-PIV system was used to measure the SRI instantaneous velocity profiles. Since the PIV camera has a tilted angle with respect to the laser sheets, an undistortion technique developed by Seelig et al. (2018) was applied to the images obtained, based on a polynomial

distortion method, and will also be described. The experimental errors in the velocity profiles obtained are also evaluated, including a study of how many experimental measurements are necessary for the data to converge to average values. The procedure to establish an approximately linear temperature gradient in the axial direction, which leads to a stable density stratification in the experimental setup, is also presented.

3.1 Experimental Setup

The experimental setup for studying the SRI was designed at the Department of Aerodynamics and Fluid Mechanics (LAS) of the Brandenburg University of Technology Cottbus-Senftenberg (BTU) and consists of a Taylor-Couette system (see section 2.3) where the top lid is heated, and the bottom lid is cooled for obtaining a stable density stratification in the axial (z) direction. A schematic drawing is shown in figure 3.1, and a photograph of the setup in figure 3.2. The outer

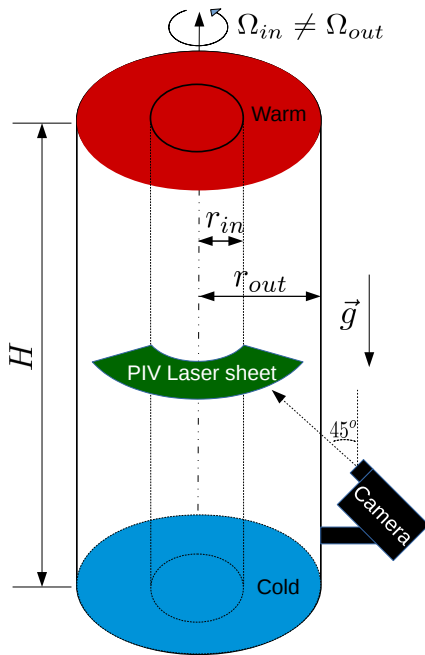


Figure 3.1: Schematic representation of the SRI experimental setup.

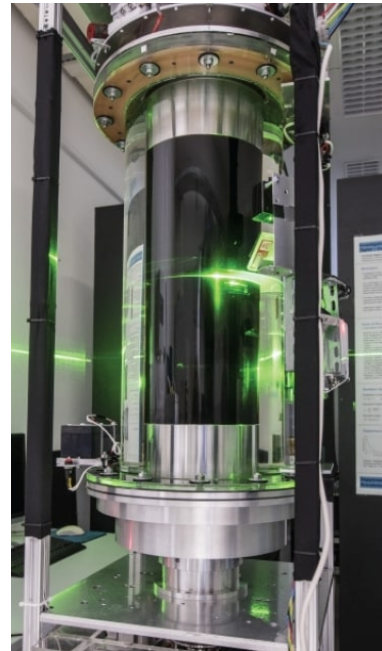


Figure 3.2: Experimental Setup.

cylinder, with radius r_{out} (inner wall of the outer cylinder), is made of transparent glass material to allow optical access to the flow that develops within the cavity.

The distance between inner and outer cylinders, also simply called gap, is given by $d = r_{out} - r_{in}$, where r_{in} is the (out wall) radius of the inner cylinder. Given the cylinders height H , the experimental geometric parameters are the aspect ratio $\Gamma = H/(r_{out} - r_{in})$, and the radii ratio $\eta = r_{in}/r_{out}$. The geometrical parameters of the experimental setup are listed in table 3.1.

The inner and outer cylinders of the setup are concentric and rotate independently, respectively with angular velocities Ω_{in} and Ω_{out} , driven by two different DC motor units that can be remotely controlled during operation by servo amplifiers. The energy of the system is provided by power banks also co-rotating with the camera and the laser. The energy provided to the

Table 3.1: Experimental setup parameters

inner cylinder radius	r_{in}	75 mm
outer cylinder radius	r_{out}	145 mm
gap size	d	70 mm
cylinders height	H	700 mm
aspect ratio	Γ	10
radii ratio	η	≈ 0.52

camera and laser are provided by two charged 5 V power banks, while one 12 V power bank provides energy for the motors, RC-controllers, and the servo amplifiers.

The top and bottom parts are closed and connected to the outer cylinder, so both lids rotate with angular velocity Ω_{out} .

The rotation ratio between the angular velocity of outer and inner cylinders $\mu = \Omega_{out}/\Omega_{in}$ can be set to different values in the experiments, from counter-rotation regimes ($\mu < 0$) to co-rotating cases ($\mu > 0$). Since the rotation ratio in accretion disks should be slightly sub-Keplerian (Visser and Dullemond 2010, Lyra and Umurhan 2019), the investigations were mainly focused at $\mu \approx 0.35$. This value is smaller than the pseudo-Keplerian line, found at $\mu = \eta^{3/2} \approx 0.372$ for the experimental setup, and greater than the Rayleigh line at $\mu = \eta^2 \approx 0.275$ (see section 2.3). Therefore, for the μ value chosen, the flow is stable with respect to non-stratified TC (see figure 1.3). Note that similar results have been obtained for $\mu \approx 0.372$, i.e. at the Keplerian-line.

The gap between inner and outer cylinders is filled with a Newtonian M5 silicon oil of viscosity (ν) 5 times higher than the viscosity of water and has a similar density $\rho \approx \rho_{H_2O}$. The higher viscosity of the oil allows us to achieve smaller Reynolds number values compared to water. The coefficient of thermal expansion (α) of the M5 oil at 25 °C is used to compute the buoyancy frequency N . Using the density ρ , the thermal conductivity (k) and the specific heat at constant pressure (c_p), the Prandtl number is computed as

$$Pr = \frac{\nu}{k/(c_p \rho)}. \quad (3.1)$$

The physical properties of the M5 oil can be seen on table 3.2.

Table 3.2: M5 silicone oil properties at 25°C

kinematic viscosity	ν	$5 \times 10^{-6} \text{ m}^2 \text{ s}^{-1}$
density	ρ	923 kg m^{-3}
coefficient of thermal expansion	α	$1.04 \times 10^{-3} \text{ K}^{-1}$
thermal conductivity	k	$0.133 \text{ W K}^{-1} \text{ m}^{-1}$
specific heat	c_p	$1630 \text{ J kg}^{-1} \text{ K}^{-1}$
Prandtl number	Pr	≈ 57

Stable density stratification can be obtained by adding salinity to the system (Withjack and Chen 1974, Boubnov et al. 1995, Shalybkov and Rüdiger 2005, Le Bars and Le Gal 2007), as occurs in the salty water of oceans and seas, for example, or also by imposing a temperature gradient to the fluid, that is more likely to happen in accretion disks (lyr, Dubrulle et al. 2004)

and also in the oceans when the surface of the waters are warmer than the bottom regions due to the highest solar irradiation. In the experiments, a stable density stratification is obtained by warming up the upper lid with twelve TEC263 Peltier elements installed equidistant from each other, six of them acting as heat sources, while the 6 other elements working as a cooling system were placed between them. The relation between temperature differences ΔT and density variation for incompressible fluids follow the approximate state equation (Pedlosky 2013)

$$\rho = \rho_0(1 - \alpha\Delta T). \quad (3.2)$$

The results were obtained with the temperature differences between top and bottom lids of $3K < \Delta T < 7K$.

The advantage of using temperature stratification for experimentally investigating the SRI, instead of salt stratification, is that the boundary condition can restore the stratification after turbulent mixing effects. The disadvantage is the time required for establishing a near-linear temperature profile to have a constant buoyancy frequency N . The process of heating and mixing the flow (by fast rotating the inner cylinder) takes between 2 and 5 hours, which makes measurements more time consuming compared to salt stratified experiments.

3.2 Particle image velocimetry (PIV) method

The PIV is an experimental technique that measures local velocity on a flow field using a camera, a laser source, and tracer particles that are carried by the fluid and have their displacement measured at consecutive images.

A mini-PIV system is used in the experimental setup to acquire instantaneous velocity fields in an azimuth-radial cross-section ($r - \phi$). Note that there are 2 mini-PIV mounted, one for evaluating the $\phi - r$, and the other for the radial-axial ($r - z$) cross-section, but unfortunately the radial velocities have higher orders of magnitude compared to the axial velocity components, and it was not possible to set a proper camera frequency acquisition suitable to correctly measure both simultaneously, so the PIV measurements in the $r - z$ cross-section could not be performed.

The mini-PIV system was developed at a lower cost than commercial PIV systems available, and all its structure has small dimensions when compared to a regular PIV system, which makes it also lighter and easier to be attached to rotating parts of the experiment avoiding unwanted vibrations in the system and reducing the technical difficulties involved on the fixation of the PIV system to rotating parts. The cheaper and lighter mini-PIV system was possible to be implemented because the instantaneous velocities involved in the SRI measurements are slow enough to be captured with the acquisition time of simpler commercial cameras, different from studies that measure faster varying phenomena, such as high Reynolds number shear turbulence. The experiment images are then obtained with a *GoPro Hero 4 black edition* camera with spatial resolution of $1080 \times 1920px$, with frequency of 24 frames per second. Figure 3.3(a) shows an example of a PIV image obtained with the *GoPro* camera.

Since the time between two images acquired is not too small, a continuous laser was employed for performing the measurements, instead of a pulsating laser synchronized with the image acquisition, necessary in fast varying phenomena. A continuous green laser ($\lambda = 532nm$) that produces a 2mm thick horizontal light sheet (in the $r - \phi$ plane) was used. All the experimental results that will be presented in this thesis were obtained with the laser sheet at the mid-height axial position $z = H/2 = 345mm$, but the camera and laser were attached to a train that can move in the axial direction to measure the flow at other heights. The camera field of view (set in the option 'medium' field of view (FOV)) allows the observation of $\Delta\phi \approx 65^\circ$ angle

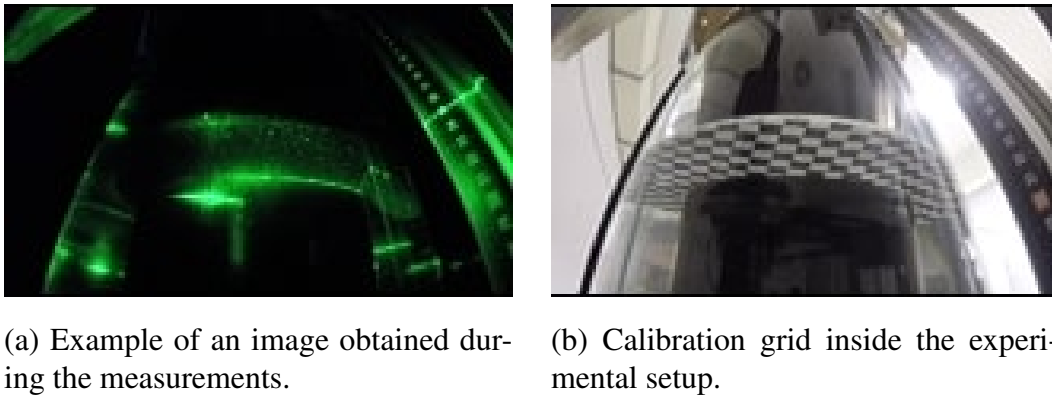


Figure 3.3: PIV images

in the azimuthal direction, i.e., approximately 18% of the full horizontal cross-section. The camera and the laser sets are mounted on a structure that co-rotates with the outer cylinder, so all experimental results are obtained in a reference frame moving with angular velocity Ω_{out} with respect to the laboratory. The energy for the PIV system is provided by 2 charged power banks.

The inner cylinder of the experimental setup is made of aluminum and anodized to minimize undesired laser reflections at the inner wall. Even with the dark color of the ionized aluminum, and because of laser reflection and refraction when the light passes from the acrylic material to the oil at the outer cylinder, the PIV measurements near the walls become spurious, so that, from the full gap ($75\text{ mm} < r < 145\text{ mm}$), PIV data are only considered in the interval $80\text{ mm} < r < 143\text{ mm}$.

For performing the PIV measurements, tracer particles that reflect the incident laser light were added to the fluid, and their displacement between images acquired and the consecutive ones was measured, with a time interval Δt between the images obtained. These particles are called passive tracers, since they have a similar density to the fluid evaluated, allowing them to be carried by the flow without perturbing it.

Different types of particles can be added to the flow for evaluating a flow field. among others, it is possible to cite the commonly used Kalliroscope particles, which are elongated filaments, being more suitable for the flow visualization than to PIV measurements, since they reflect more light due to their striped like shapes, leading to a relatively poor contrast between reflected light and the background that are important to obtain good PIV measurements in comparison to more spherical shaped particles. Another possible choice could be fluorescent particles such as Rhodamine, which re-emit the incident light on a specific frequency, but special filters that filter the specific frequency re-emitted become also necessary. Furthermore, Rhodamine particles demand a more frequent cleaning of the internal parts of the experimental setup because they deposit on the surfaces of the cylinders, which involve many time-consuming steps, such as the cleaning process itself, and the re-calibration of the system. Therefore, hollow glass spherical particles with mean diameters between $10\mu\text{m} < d < 20\mu\text{m}$ and density of 1.05 (with respect to the density of water) were employed as PIV passive tracing particles, since they provide good contrast between the light reflected by the particles and the background flow, and can also remain in the system for longer times without the necessity of frequently opening and cleaning the experimental setup.

To estimate the ideal amount of tracer particles added in the experiment, it was considered as a general rule that, in regions of $1\text{ mm} \times 1\text{ mm}$ on the acquired images, there should be counted

approximately 10 particles. This is because, a too big amount of particles in the fluid would lead to large laser reflected areas in clusters of particles, worsening the recognition of where a group of particles moved decreases, due to poor color contrast in the images. Very few particles to be traced in the flow, otherwise, leads to many 'holes' in the velocity vectors obtained. Note that these images are transformed to grayscale using *FFmpeg* package before computing the PIV velocity fields.

3.2.1 PIV Cross-correlation

Knowing how far the particles have moved between two consecutive images, i.e., the space covered by a set of particles in a given interrogation window, and the time interval between the acquisitions, it is possible to obtain the flow velocity profiles. Interrogation windows are the division of the full image obtained into smaller regions, containing a certain number of pixels (e.g. $32px \times 32px$, $64px \times 64px$, $32px \times 64px$, etc.). The particle displacement is measured by computing the cross correlation between two consecutive images obtained at given time intervals. The cross correlation can be computed as (Thomson and Emery 2014)

$$\frac{1}{M} \sum_{i=1}^M f(t)g(t + \Delta t), \quad (3.3)$$

where M is the number of interrogation windows measured at discrete times $t_i, \{i \in \mathbb{N}\}, i = 1, \dots, M$. An adaptive cross-correlation interrogation windows with $[128px \times 128px, 64px \times 64px, 32px \times 32px, 32px \times 32px]$ and 50% of overlap is used, that corresponded to a final spatial resolution of $0.11mm$.

By computing the cross-correlation between all interrogation areas (IA), the particles fields of displacement for several flow regions are obtained, with the maximum correlation (peak) corresponding to the most likely displacement of the tracers, as schematically presented in figure 3.4.

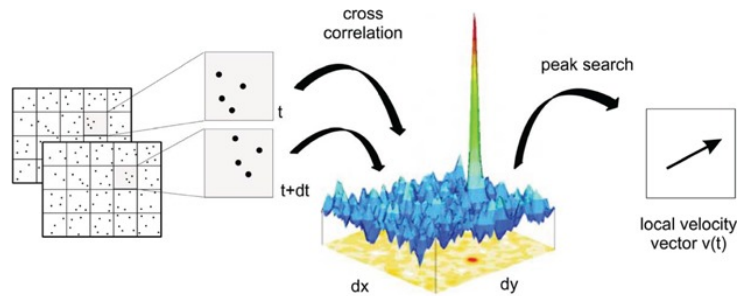


Figure 3.4: PIV cross correlation to obtain velocity profiles (Image obtained from Pawar et al. (2014)).

As the time interval Δt between two images is known, by dividing the displacements of the particles by this time interval between frames, the instantaneous velocity fields are obtained. Δt must be big enough so that particles move between the images acquired, but small enough for the same set of particles to be observed in the IA of both consecutive images considered. In these measurements, a good time resolution was obtained with $\Delta t = 1/24$ seconds. Figure 3.5 shows how convergence of measured u_ϕ and analytical TC-profile for $\Delta t = 1/24s$.

Note that the experiment 1st Exp in figure 3.5, computed with 12 fps and 24 fps, refers to the same measurement, and not different data sets. The difference between them is how many

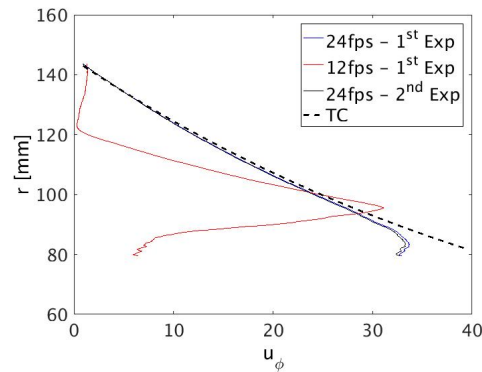


Figure 3.5: Comparison of analytical TC profile with $Re = 1000$ and $\mu = 0.35$ (black dashed curve) with two different experiments acquired with 24 frames per second (fps), 24fps - 1st Exp and 2nd Exp, that show good agreement between each other and with the TC profile, and the same experiment computed with 12 fps (12fps - 1st Exp), skipping one frame in the PIV computations, that shows no agreement with the TC profile, highlighting a poor time resolution.

images were considered for computing the PIV velocity profiles, using less (more) images, increasing (decreasing) the time interval between consecutive images, until a good time resolution (of 24 fps) was found. Note that, for other Reynolds numbers ($\leq Re = 600$), a time resolution of 12 fps was already sufficient for obtaining convergence of u_ϕ PIV measurements and the analytical TC-profile, but a time resolution of 24 fps was used in all computations since it was found to correctly measure the instantaneous velocity profiles for all measurements.

Since the PIV particle displacement has an error of approximately 0.1 pixel (Nobach and Bodenschatz 2009), a moving average with 25 vector fields window size is implemented after the final instantaneous velocity fields are obtained. As the displacements of the particles are then obtained in pixels, it needs to be transformed to meters (or mm). A $1 \times 1mm^2$ squares chessboard grid, shown in figure 3.3(b), is used for converting non-dimensional displacements, and consequently, non-dimensional velocities into dimensional. With this, the velocity components are initially obtained in Cartesian coordinates. The origin of the PIV segment is determined using the calibration grid of figure 3.3(b) to transform the results into polar coordinates.

3.2.2 Polynomial undistortion Method

The top and bottom end-plates that close the experimental apparatus are made of aluminum, therefore they cannot be optically accessed during the PIV measurements, so the images are obtained through the transparent glass outer cylinder wall, with the camera inclined about 45° with respect to the laser sheet, as represented in figure 3.1. This 45° tilted field of view, as well as other factors, distorts the PIV images. Some of the reasons for the PIV images distortion are:

- The curvature of the outer cylinder wall;
- The camera lens curvature;
- The differences in the index of refraction of the air, the glass wall, and the oil inside the cylinder;
- The parallax effect from the camera inclination with respect to the laser plane sheet.

To correct the image distortions related to all these factors, the calibration grid of square chessboard structure presented in figure 3.3(b) is used. The calibration grid is placed at the laser sheet position inside the tank filled with oil, with the angle $\phi = 0$ at the center of the images obtained. By correcting the distorted squares on the raw calibration image into their correct square shapes, an undistortion map is created and can be applied to all PIV images. To obtain the undistortion maps, a 5th-order polynomial method is applied in a parallel code developed by Seelig et al. (2018), that transforms control points and each pixel in the distorted images (x_d, y_d) into undistorted control points and pixels (x_u, y_u) . The control points (x_d, y_d) used are basically the nodes (corners) in the chessboard grid. The method uses pairs of control points to calculate the appropriate fitting coefficients (C_{nx}, C_{ny}) in equation 3.4, with $n = 0, 1, 2, \dots, 21$,

$$\begin{aligned} x_u &= C_{0x} + C_{1x}x_d + C_{2x}y_d + C_{3x}x_dy_d + \dots + C_{20x}x_d^5 + C_{21x}y_d^5, \\ y_u &= C_{0y} + C_{1y}x_d + C_{2y}y_d + C_{3y}x_dy_d + \dots + C_{20y}x_d^5 + C_{21y}y_d^5, \end{aligned} \quad (3.4)$$

where the sub-indexes d and u refer respectively to points in the distorted and undistorted images. The undistortion of the PIV images and of the calibration grid using this method can be seen in figure 3.6(a) The undistortion maps obtained from the transformation of the distorted

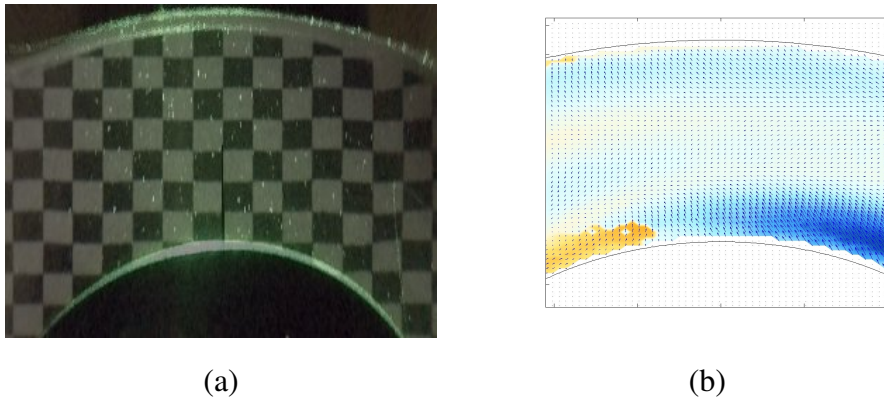


Figure 3.6: (a) Superposed calibration grid and PIV images, both undistorted using the 5th-order polynomial method; (b) PIV instantaneous velocity field. Reproduced from Seelig et al. (2018) with the friendly permission from *Torsen Seeling*, who developed the undistortion method here applied together with *Andreas Krebs* at the *BTU Cottbus-Senftenberg*.

chessboard grid to its undistorted shape is then applied to undistort all the PIV images using the *convert* library of *ImageMagick's* software package. From the undistorted PIV images, a parallelized version of *MatPIV* (Sveen 2004) was used to compute the instantaneous flow velocity fields. Note that the origin $(x, y) = (0, 0)$ is established at the center of the inner and outer concentric cylinder walls in the undistorted images (figure 3.6). This segment is used to transform the velocity fields obtained in Cartesian coordinates in (3.4) to polar coordinates as

$$\begin{aligned} r &= \sqrt{x_u^2 + y_u^2}, \\ \theta &= \tan^{-1} \left(\frac{y_u}{x_u} \right). \end{aligned} \quad (3.5)$$

Eliminating spurious vectors is also an important procedure to remove values obtained with the cross-correlations that do not make physical sense. To determine the vectors that will be discarded, those values that are too different compared to their neighborhood are verified by

applying a median filter that iteratively removes and replaces outlier values. If a vector has, for example, a magnitude greater than 1.5 times the median of surrounding vectors, it is discharged, and these discarded values are recalculated by interpolating the values of neighboring vectors. The tolerance of the standard deviation that excludes a spurious vector can be chosen arbitrarily, assuming values that properly eliminate spurious vectors, keeping the correct measurements.

3.3 PIV error measurements

Although it is difficult to determine accurately the uncertainty associated to each of the measurement steps, by comparing stable TC azimuthal velocity measurements (u) with analytical solutions (u_{TC}), it is possible to compute the final PIV percentage error as (Seelig et al. 2018)

$$\varepsilon = \frac{u - u_{TC}}{u_{TC}}. \quad (3.6)$$

An example of such comparison can be seen in figure 3.7. Note that, in figure 3.7, the deviations

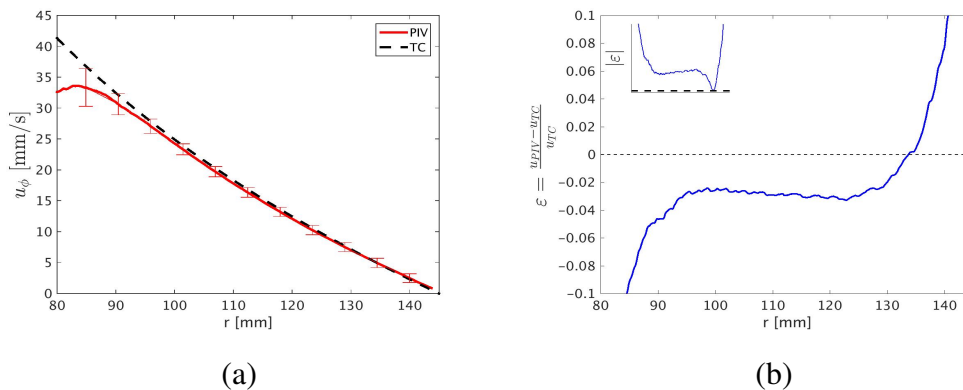


Figure 3.7: Stable u_ϕ Taylor-Couette profile with $Re = 1000$ and $\mu = 0.35$ (a) Comparison of TC analytical solution (black dashed line) and time mean PIV measurements (continuous red line) (b) Error ε between PIV measurements and analytical solutions in %. The left hand side of the images represent the region near the inner cylinder wall, and the right hand side is the region near the outer cylinder. The smaller figure inserted on the top left side of figure b shows the absolute error $|\varepsilon|$.

from Taylor-Couette profiles become larger near the inner and outer cylinders, due to higher laser parasite light reflections. For high Reynolds numbers, the Ekman circulation at the top and bottom lids (see section 2.5) can induce a redirecting flow along the vertical boundaries that can perturb the measurements (see figure 3.7, Avila et al. (2008) and sec. 2 of Seelig et al. (2018)). Far from the inner cylinder, the relative error observed was of $2\% < |\varepsilon| < 3\%$.

Seelig et al. (2018) made a similar and detailed study to estimate the experimental error (ε) on the experimental setup, several TC flows with different values of Reynolds numbers, varying between $200 < Re < 800$, and rotation ratios $0.3 < \mu < 0.6$, that agrees with the evaluation here presented. After obtaining these PIV measurements and comparing them to the respective analytical TC profiles (as in figure 3.7), probability distributions were adjusted to the differences measured, and with the computation of their standard deviations, the final error obtained was of $\varepsilon \approx 2\%$ of the velocities measured (far from the inner and outer cylinders).

3.3.1 Convergence and number of experimental images acquired

The number of instantaneous velocity fields that must be measured experimentally (number of pairs of images obtained) should be sufficient for the results to statistically converge to their average values, according to the central limit theorem. These values can vary with parameters such as the number of tracer particles used, the intensity of the laser brightness, the size of the interrogation window used, the Reynolds number, etc. To evaluate the data convergence, the quantity C was defined, given by

$$C(n) = \sum_{i=1}^n \frac{u(i)}{n} = \frac{u(1) + u(2) + \dots + u(n)}{n}, \quad (3.7)$$

where $u(i)$ is the velocity in the i^{th} point evaluated, i.e., on a data set of size n , the convergence of the first point evaluated will be $C(1) = U(1)/1$; of the second point is $C(2) = [u(1) + u(2)]/2$; until the n^{th} point, that will have its convergence given by $C(n) \approx \frac{u(n)}{n} =$ arithmetic mean. When the convergence values stop varying significantly with n , the measurements are considered to be converged.

Figure 3.8(a) shows the data convergence of the azimuthal velocity profiles (u_ϕ) with $Re = 400$, $\mu = 0.35$ and $\Delta T \approx 4K$ at mid-height location ($z \approx H/2$), on 3 different radial positions: $r = 83\text{mm}$ (closer to the inner cylinder), $r = 101\text{mm}$ (closer to the mid-gap region), and $r = 120\text{mm}$ (closer to the outer cylinder). In general, u_ϕ PIV data converges to its mean value between $4 \times 10^4 \lesssim n \lesssim 6 \times 10^4$ instantaneous velocity fields acquired, (between 30 and 50 minutes of measurements), as observed on figure 3.8(a).

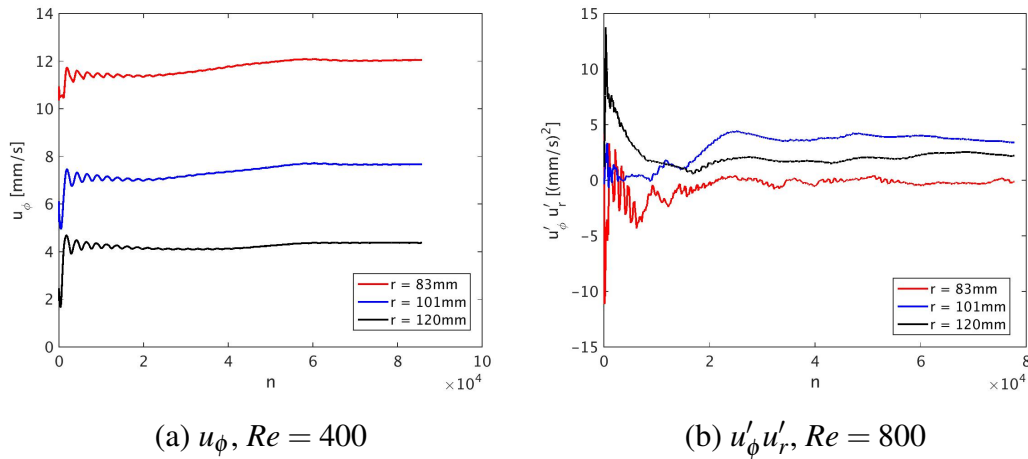


Figure 3.8: PIV data convergence of time series obtained at mid-height position ($z \approx H/2$) and at 3 different radial positions (a) u_ϕ convergence, $Re = 400$ (b) $u'_\phi u'_r$ convergence, $Re = 800$. The dashed lines indicate the final averaged velocities obtained.

For second-order parameters, such as $u'_\phi u'_r$ (as presented in figure 3.8(b)), the experiments converge after $3 \times 10^4 \lesssim n \lesssim 6 \times 10^4$ pairs of images computed (between 20 and 50 minutes of measurements). Although the convergence of $u'_\phi u'_r$ values show larger fluctuations around the mean values than the \bar{u}_ϕ data converged to the azimuthal mean flow, these variations are small

compared to the SRI amplitude oscillations (at least 50 times smaller than the variations in the velocity amplitudes).

To guarantee converged data for both first and second-order parameters measured, all the experiments were performed at least until $n \gtrsim 6 \times 10^3$ pairs of images were obtained.

3.4 Temperature stratification

After a quasi-linear temperature profile is established in the axial direction, the outer cylinder is rotated while the inner cylinder is kept at rest to eliminate perturbations generated during the temperature mixing process. After stopping the outer cylinder rotation, one should wait at least 20 minutes before starting each measurement to guarantee that the flow is at rest. No relevant heat losses or changes in the temperature linearity are observed at this moment. This is because there is almost no convective fluid motion, and the heat transfer happens mainly by conduction, which is a slow process due to the small thermal conductivity of the fluids used in the experiments.

For cooling the bottom end-plate of the experimental setup, a hose is connected to the lid and attached to an external cooler. Cold water leaving the cooler is pumped to the hose, removing heat from the bottom part of the experimental apparatus. Since the bottom plate is connected to the outer cylinder, and the hose is attached to the external cooler, which is fixed at the laboratory, the experimental setup cannot be cooled while the outer cylinder is moving. The Peltier elements for heating can still work while the experiment is running, but this makes the temperature control less precise. Therefore, the fluid heat up is stopped during the experiment, without affecting much the temperature gradient. Each experiment typically runs between 30 and 70 minutes. The temperature values along the vertical axis are measured with a PT-100 (Platinum Resistance Temperature Detector) probe, that has a precision $\delta T = 0.1K$. The temperature profile values and their linearity are also verified with an infrared camera IR-TCM 640hr, of $640px \times 480px$ resolution. The maximum temperature differences between top and bottom lids obtained at the beginning of the experiment are of $\Delta T = 7K$, but in the present measurements, it is kept between $3K < \Delta T < 4.5K$. An example of the temperature profiles before and after the measurements is shown in figure 3.9. After the stable linear temperature gradient

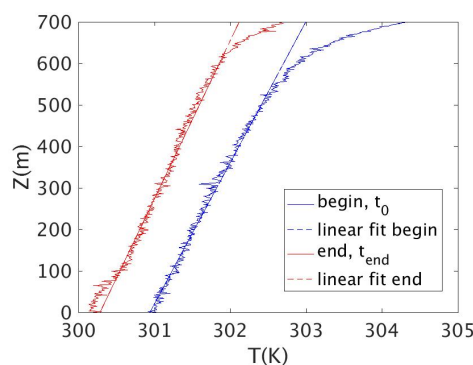


Figure 3.9: Experimental temperature profiles at the beginning (blue curve on the right), and at the end (red curve on the left) of a measurement. The dashed lines are the linear fits in the center height region where the PIV measurements are performed.

in the axial direction is established, the experiment is started by rotating the outer cylinder until

its final Ω_{out} value, avoiding initial perturbations that would occur by starting the experiment rotating the inner cylinder. When the outer cylinder reaches its final rotation, the inner cylinder rotation is gradually increased from rest until the desired Re and μ values are achieved.

After finishing the PIV measurements, the temperature profile is once again measured. In a one hour experiment, losses of $\approx 1K$ in the ΔT initially established are observed due to temperature mixing in the axial direction and to losses into the surrounding environment. Despite these temperature changes, the quasi-linearity of the profile is kept, and changes in N values are considered small (see figure 3.9).

Numerical Methods

The SRI is an instability that develops different time scale phenomena. The use of numerical methods therefore is not easy, as it needs to comprehend fine meshes to solve all the scales involved in the problem. Long time integration is also required to fully develop all features of the instability evaluated. To overcome these difficulties, a direct numerical simulation (DNS) solver combining fourth-order accuracy space discretization and high-performance computing (HPC) has been developed. In this chapter, the description of the C2D-Annular, the research code recently developed by Abide et al. (2018) to investigate the SRI dynamics, is addressed.

Hereafter, the mathematical model, the time and space discretizations, as well as the strategies for the code parallelization will be presented.

4.1 Problem formulation

The physical model solved by the CS2D-Annular code in this thesis consists of the Taylor-Couette configuration filled with an incompressible fluid. A temperature gradient is imposed in the axial direction with a higher temperature prescribed at the top boundary than the bottom one. The physical model is schematically presented in figure 4.1. Note that this is the same configuration used to study the SRI experimentally, schematically presented in figure 3.1, on chapter 3.

The SRI flow is modeled as an incompressible fluid, since all velocities involved in the problem are much smaller than the sound speed, leading to small Mach numbers ($\text{Mach} \ll 0.3$). Since the temperature gradients obtained in the experiments (and simulated numerically) are not too large, density can be considered constant in the continuity and momentum equations, except in the gravity term, to take into account buoyancy effects. This consideration is known as the Boussinesq approximation (Kundu and Cohen 2001). Comparisons with simulations using other approximations (as the low Mach number approximation (Raspo et al. 2018)) indicate that the temperature gradients here investigated are sufficiently small for using the Boussinesq approximation. The good agreement of numerical and experimental results also indicates that the approximation is valid for the problems investigated (see chapter 5).

The Navier-Stokes equations (NS) under the Boussinesq approximation on a fixed (non-rotating) frame of reference read

$$\nabla \cdot \mathbf{u} = 0, \tag{4.1}$$

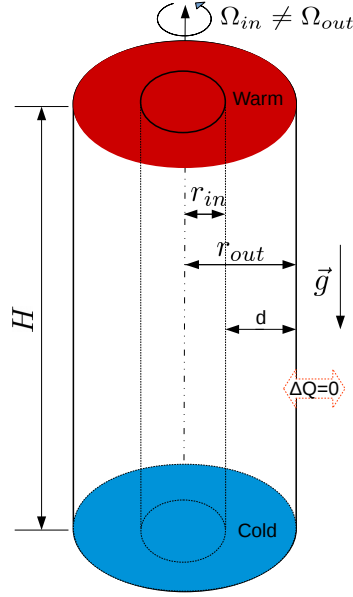


Figure 4.1: Schematic representation of the numerical configuration.

$$\partial_t \mathbf{u} + (\mathbf{u} \cdot \nabla) \mathbf{u} = -\nabla p + \nu \Delta \mathbf{u} + \mathbf{F}, \quad (4.2)$$

$$\partial_t T + (\mathbf{u} \cdot \nabla) T = \kappa \nabla^2 T, \quad (4.3)$$

where κ is the fluid thermal diffusivity, p is the pressure, T is the temperature field, and ν is the kinematic viscosity. $\mathbf{u} = (u_r, u_\phi, u_z)$ is the velocity vector field in radial, azimuthal and axial directions, respectively. The reference fluid density ρ_0 is included in the pressure term $\frac{p}{\rho_0}$ on the right-hand side of the equation 4.2. The reference fluid properties are considered constant, obtained at a temperature of $T = 25^\circ\text{C}$. In cylindrical coordinates, $\Delta \mathbf{u}$ is given by

$$\Delta \mathbf{u} = \begin{bmatrix} \nabla^2 u_r - u_r/r^2 - (2/r^2) \partial_\phi u_\phi \\ \nabla^2 u_\phi - u_\phi/r^2 + (2/r^2) \partial_\phi u_r \\ \nabla^2 u_z \end{bmatrix}, \quad (4.4)$$

where ∇^2 is the Laplacian scalar operator, defined in polar coordinates as

$$\nabla^2 = \partial_r^2 + (1/r) \partial_r + (1/r^2) \partial_\phi^2 + \partial_z^2. \quad (4.5)$$

To account for the buoyancy effect under the Boussinesq approximation, the body force \mathbf{F} is the buoyancy force driven by density variations:

$$\mathbf{F} = -\alpha \mathbf{g} \frac{\partial T}{\partial z} H, \quad (4.6)$$

where α is the coefficient of thermal expansion, \mathbf{g} is the gravity acceleration, $\frac{\partial T}{\partial z}$ is the approximate linear temperature gradient at the center region of the cavity, and H is the cavity height. Note that, using the Boussinesq approximation, the fluid properties such as ν , κ , and α are

treated as constant (Kundu and Cohen 2001). Note that Lopez and Marques (2020) attribute centrifugal buoyancy to the instability although the relevant term in the equations is small. For the experiments and simulations presented in this thesis, centrifugal buoyancy is even one order of magnitude smaller than in Lopez and Marques (2020). Hence, centrifugal buoyancy was assumed to not play a significant role in the experiments and it was not included in the numerical model.

4.2 Time discretization and projection method

The first step for numerically solving equations 4.1-4.3 consists in the time discretization. In the CS2D-Annular code, a semi-implicit scheme is considered to overcome the restrictive time step associated with time explicit treatment of the diffusive terms. Since the semi-discretized system of equations obtained leads to a coupling of the velocity and pressure, a strategy for splitting both terms, called *Improved projection scheme (IPS)*, is also implemented. These two steps for solving the unsteady Navier-stokes equations are presented hereafter.

4.2.1 Time discretization

The choice of a time discretization method needs to take into account an appropriate time resolution. The time step chosen must be small enough to resolve all the physical scales related to the problem, but should also take into account the computational costs involved.

The time discretization can be made fully explicitly, fully implicitly, or semi-implicitly. A fully time-implicit scheme is unconditionally stable, i.e., its numerical instability does not depend on the time step. These specific solvers are then well suitable for the simulation of permanent regimes, where Δt can become large without the problem of not resolving all time scales involved in transient regimes, with relatively fast variations in time. When the method is fully explicit, the discretization of the linear viscous terms leads to a quadratic stability constraint. This restriction means that the time step chosen is restricted to be, at maximum, of the same order as the square of the space discretization ($\Delta t \sim \mathcal{O}(\Delta x^2)$) for the simulation to be numerically stable. With the fully explicit scheme, because of the grid refinement required in the vicinity of walls, this limit becomes too restrictive.

The SRI physics demands simulations with small time steps to accurately describe its dynamic, but also need to cope with the time step constraint regarding the solutions of the non-linear convective terms. In this case, both full-implicit or full-explicit alternatives are not suited, and a semi-implicit method is indicated (Keyes et al. 2013). Using a semi-implicit scheme, the time step restriction applies exclusively to the non-linear terms of the equations, and a good compromise between complexity and the computational cost of the DNS can be achieved. Common temporal schemes that use an implicit discretization for the diffusive terms are Crank-Nicolson, backward Euler, or and backward difference (BDF2) methods (Press et al. 2007, Moukalled et al. 2016). Explicit schemes that could be cited as examples are the 3rd order Runge Kutta methods (RK3) (Williamson 1980), and the Adams-Bashforth method (Press et al. 2007, Karniadakis et al. 1991).

In this work, the time discretization is the combination of a second-order Backward Euler scheme to solve the linear diffusive terms implicitly, and the Adams-Bashforth scheme for explicitly solving the non-linear convective terms, as used in Raspo et al. (2002) and Abide

et al. (2018). The time discretization of equations (4.1), (4.2), and (4.3) then read

$$\begin{aligned} \nabla \cdot \mathbf{u}^{n+1} &= 0 \\ \frac{1}{2\Delta t} (3\mathbf{u}^{n+1} - 4\mathbf{u}^n + \mathbf{u}^{n-1}) + 2\mathcal{H}(\mathbf{u}^n) - \mathcal{H}(\mathbf{u}^{n-1}) &= -\Delta p^{n+1} + \nu \nabla^2 \mathbf{u}^{n+1} + \mathbf{F}^{n+1} \\ \frac{1}{2\Delta t} (3T^{n+1} - 4T^n + T^{n-1}) + 2\mathcal{H}(T^n) - \mathcal{H}(T^{n-1}) &= \kappa \nabla^2 T^{n+1}, \end{aligned} \quad (4.7)$$

where the terms $\mathcal{H}(\mathbf{u})$ and $\mathcal{H}(T)$ are the convective terms on equations (4.2) and (4.3).

This set of semi-discretized equations lead to time-evolution equations for the momentum and the temperature while imposing a constraint on the divergence of the velocity field at each time step $\nabla \cdot \mathbf{u}^{n+1} = 0$. Note that the Laplacian operator ∇^2 , in cylindrical coordinates (equation 4.5), leads to derivatives of the diffusive terms with coupled variables in the radial and azimuthal directions. These terms are also treated explicitly on time, as the non-linear terms (Kuo and Ball 1997, Abide et al. 2018).

Note also that the discretized NS equations presented in 4.7 has a coupled velocity/pressure system, that requires specific methods to solve equation 4.7 efficiently. This method will be addressed in the following section 4.2.2.

4.2.2 Projection method

The pressure velocity decoupling is an important step for reducing the computational costs involved in the numerical solution of incompressible Navier-Stokes equations. One can cite different algorithms that efficiently perform the velocity/pressure decoupling, such as the *UZAWA* algorithms (Arrow et al. 1958), or the *SIMPLE* method (Patankar and Spalding 1967), that is implemented in different commercial fluid mechanics solvers, or the projection methods, that are widely used in research codes for the simulation of the Navier-Stokes equations (Temam 1969, Chorin 1968).

Projection methods consist of techniques to separate the coupled velocity/pressure terms after the time discretization of the NS equations, and involves two stages (Goda 1979, Raspo et al. 2002):

1. In the first stage, a provisional velocity \mathbf{u}^* is computed from the time discretized momentum equations.
2. In the second stage, the provisional velocity is corrected to fulfill the incompressibility constraint. This step requires the solution of a Poisson equation which is a crucial point of this approach.

Projection methods are known to introduce a boundary layer error at the domain boundaries because the tangential velocity is not explicitly imposed. According to Brown et al. (2001), Guermond et al. (2006), one can define incremental or non-incremental projections method, where each variant of the projection methods tries to reduce the numerical errors in the vicinity of the boundaries. Kim and Moin (1985), Shen (1990) proposed projection schemes that solved the pressure boundary conditions mentioned, but that introduced a slip velocity on the boundaries. A splitting method that solved the velocity and pressure boundary conditions constraint was proposed by Karniadakis et al. (1991), but the method did not maintain the incompressibility of the flow within the whole domain. Hugues and Randriamampianina (1998) proposed

an incremental projection method that reduces error obtained by introducing the calculation of a preliminary pressure p^* . Provisional quantities are here indicated by the index \star . The steps implemented in this work for obtaining the preliminary pressure are described hereafter:

1. Computing a preliminary pressure as

$$\Delta p^* = \nabla \cdot [-2\mathcal{H}(\mathbf{u}^n) + \mathcal{H}(\mathbf{u}^{n-1}) + \mathbf{F}^{n+1}] \text{ in } \zeta, \quad (4.8)$$

with the following Neumann boundary conditions obtained by Gresho and Sani (1987) for the pressure terms at the cylinders walls

$$\frac{\partial p}{\partial n} = \mathbf{n} \cdot \left[-\frac{\partial \mathbf{u}}{\partial t} - \mathcal{H}(\mathbf{u}) + \nu \Delta(\mathbf{u}) + \mathbf{F} \right] \text{ on } \partial \zeta, \quad (4.9)$$

where $\partial \zeta$ is the boundary of the computational domain. Note that pressure at the boundaries, presented in equation 4.9 is numerically computed as

$$\begin{aligned} \frac{\partial p^*}{\partial n} = \mathbf{n} \cdot \left(\frac{-3\mathbf{u}_{in}^{n+1} + 4\mathbf{u}^n - \mathbf{u}^{n-1}}{2\Delta t} - 2\mathcal{H}(\mathbf{u}^n) + \mathcal{H}(\mathbf{u}^{n-1}) \right. \\ \left. + \nu [2\nabla(\mathbf{u}^n) - \nabla(\mathbf{u}^{n-1})] + \mathbf{F}^{n+1} \right) \text{ on } \partial \zeta, \end{aligned} \quad (4.10)$$

where \mathbf{u}_{in} is the velocity at the inner cylinder, \mathcal{H} is the convective term, ζ is the computational domain, and $\partial \zeta$ its boundary.

2. Computing a predictor velocity \mathbf{u}^*

Using the discretized momentum equation (4.7) and the preliminary pressure obtained from (4.8), the predictor velocity \mathbf{u}^* is given by

$$\begin{aligned} \frac{1}{2\Delta t} (3\mathbf{u}^* - 4\mathbf{u}^n + \mathbf{u}^{n-1}) + 2\mathcal{H}(\mathbf{u}^n) - \mathcal{H}(\mathbf{u}^{n-1}) = \\ -\Delta p^* + \nu \nabla \mathbf{u}^* + \mathbf{F}^{n+1}. \end{aligned} \quad (4.11)$$

3. Computing the pressure correction variable δ . This intermediate variable δ defined by Hugues and Randriamampianina (1998) is used to correct the preliminary pressure p^* , and reads

$$\delta = \frac{2\Delta t}{3} (p^{n+1} - p^*). \quad (4.12)$$

That will be obtained from the mass conservation equation (4.1), evaluating the distance of the predictor terms from a divergence free solution, and computed as

$$\Delta \delta = \nabla \cdot \mathbf{u}^* \text{ in } \zeta, \quad (4.13)$$

with the Neumann boundary condition

$$\frac{\partial \delta}{\partial n} = 0 \text{ on } \partial \zeta. \quad (4.14)$$

4. Performing the velocity and pressure correction.

Finally, δ is used to correct the predictor term and to obtain explicitly the pressure at time step $n + 1$

$$p^{n+1} = p^* + \frac{3}{2\Delta t}\delta, \quad (4.15)$$

and the velocity at the time step $n + 1$

$$\mathbf{u}^{n+1} = \mathbf{u}^* - \nabla\delta, \quad (4.16)$$

with pressure and velocity in equations 4.15 and 4.16 now decoupled.

Note that, concerning the accuracy of the time discretization, the *IPS* leads to a second-order approximation both in velocity and pressure.

In most projection methods, a homogeneous Neumann boundary condition is prescribed for the pressure correction and, therefore, for the pressure itself. This leads to a normal derivative of the pressure $\left(\frac{\partial p}{\partial n}\right)$ that remains constant as the one initially imposed. Using the *IPS* allows a time-dependent normal derivative of the pressure, consistently with the Navier-stokes equations (Karniadakis et al. 1991).

As in most projection methods, the main steps of the *IPS* consist of solving three Helmholtz equations to compute the velocity components, and two Poisson equations to compute the preliminary pressure and the δ terms in equation 4.11. These solutions are closely related to the space discretization, which will be detailed in the following section.

4.3 Spatial discretization

In the CS2D-Annular code, the spatial discretization of equations (4.7) is based on fourth-order compact scheme developed by Lele (1992), defined on a full staggered arrangement (Harlow and Welch 1965).

4.3.1 Variable layout

The variable layout consists of defining how the variables are located in the discrete domain. For structured grids, collocated or staggered arrangements are commonly used. Using collocated methods, all three components of velocity and the pressure are located at the same grid position (Olafadehan et al. 2018). The collocated layout is popular with spectral methods. However, for finite differences or finite volume methods, this arrangement is known to introduce a pressure uncoupling, and in the presence of nonlinear terms, it requires special treatments to correctly solve the equations (Ferziger et al. 2002). With staggered grids, the velocity and pressure components are shifted half a space grid (Cioranescu and Lions 2002), as schematically represented in figure 4.2, which reassures the decoupling of the velocity and pressure terms obtained with the projection method described in section 4.2.2. More precisely, the pressure and the velocity components are shifted in space by half a space grid as reported in figure 4.2, with velocity components u_r , u_ϕ and u_z located respectively at nodes $(x_{i+1/2}, y_j, z_k)$, $(x_i, y_{j+1/2}, z_k)$, and $(x_i, y_j, z_{k+1/2})$, while pressure nodes are located at nodes (x_i, y_j, z_k) . h is the distance between two nodes, and the sub-indexes of i , j , and k indicate each respective node. In addition to enforcing the pressure/velocity decoupling, the staggered layout allows to ensure the conservation

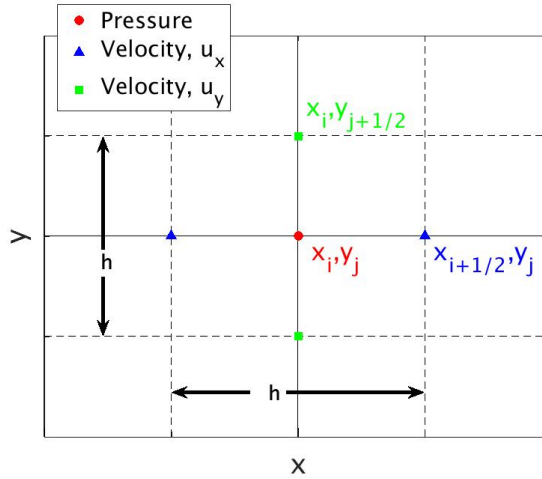


Figure 4.2: Schematic representation of the 2-D space full staggered grid arrangement with velocity and pressure shifted in space by half a grid ($h/2$).

of the kinetic energy in a discrete sense (Morinishi et al. 1998, Viazzo et al. 2001, Brazzoli et al. 2007). In this work, the staggered layout was then considered given the advantages mentioned above.

4.3.2 Compact schemes

Unlike the explicit standard finite difference methods, compact schemes are finite difference methods that are implicitly defined. These methods have better formal accuracy and resolution for high wavenumbers than standard finite differences (Lele 1992).

The staggered approximation of the first derivative at node i ($f'_i \approx \frac{\partial}{\partial x} f(x_i)$) using the 4th order compact scheme proposed by Lele (1992) on staggered grid reads

$$\alpha f'_{i-1} + f'_i + \alpha f'_{i+1} = \frac{a(f_{i+1/2} - f_{i-1/2})}{h} \quad (4.17)$$

The coefficients α and a in equation (4.17) are obtained by matching the Taylor series coefficients as such manner that fourth-order approximation accuracy is retrieved (Lele 1992, Abide et al. 2018). The numerical scheme and coefficients for the staggered derivative at the inner nodes of the domain and the interpolation between the staggered nodes using the 4th order compact scheme proposed by Lele (1992) are presented in table 4.1. The operators D_ξ and I_ξ stand respectively for the first derivative with respect to ξ , while I_ξ stands for the interpolation. The index cf stands for the evaluation of center-to-face positions and represents the nodes where the function is known. The indexes fc stand for face-to-center, and indicate the location where the numerical evaluation holds (the node where we want to obtain p or \mathbf{u}). For example, this means that D_r^{fc} is the first derivative operator in the r direction, evaluated at the center-node from face-nodes. In the CS2D-Annular code, second derivatives are currently obtained by applying successively two times the first derivative.

In order to close the system of equations formed by the previous approximations of deriva-

operator	scheme	α	a
D_{ξ}^{fc}	$\alpha f'_{i-1} + f'_i + \alpha f'_{i+1} = a \frac{f'_{i+1/2} - f'_{i-1/2}}{h}$	1/22	12/11
D_{ξ}^{cf}	$\alpha f'_{i-1/2} + f'_{i+1/2} + \alpha f'_{i+3/2} = a \frac{f_{i+1} - f_i}{h}$	1/22	12/11
I_{ξ}^{cf}	$\alpha f_{i-1} + f_i + \alpha f_{i+1} = \frac{a(f_{i+1/2} + f_{i-1/2})}{2}$	1/6	2/3
I_{ξ}^{fc}	$\alpha f_{i-1} + f_i + \alpha f_{i+1} = \frac{a(f_{i+1/2} + f_{i-1/2})}{2}$	1/6	2/3

Table 4.1: Fourth-order compact scheme coefficients for the inner nodes.

tives and interpolations, boundary relations are given by

$$\begin{aligned} f_1^{(q)} + \alpha f_2^{(q)} &= a f_{-1/2} + b f_{1/2} + c f_{3/2} \\ \alpha f_{n-1}^{(q)} + f_n^{(q)} &= a f_{n+1/2} + b f_{n-1/2} + c f_{n-3/2}, \end{aligned} \quad (4.18)$$

where $q = 0$ means interpolation and $q = 1$ means derivation. The coefficients α , a , b , and c and the discretization schemes at the boundary nodes in (4.18) are summarized in table 4.2.

Using these notations, the boundary conditions can be inserted together in the inner nodes relations, leading to a linear system $Mf^{(q)} = Bf$ where M is a tridiagonal matrix. Multiplying from the left both sides by the inverse matrix M^{-1} , we obtain $M^{-1}Mf^{(q)} = M^{-1}Bf \rightarrow f^{(q)} = M^{-1}Bf$, leading to

$$f^{(q)} = Df \quad (4.19)$$

Note that D is no longer be a sparse matrix as M .

operator	scheme	α	a	b	c
D_{ξ}^{cf}	$f'_0 + \alpha f'_1 = a f_{-1/2} + b f_{1/2} + c f_{3/2}$	-1	-1	2	-1
D_{ξ}^{fc}	$\alpha f'_{-1/2} + f'_{1/2} = a f_0 + b f_1 + c f_2$	23	-25	26	-1
I_{ξ}^{cf}	$f_0 + \alpha f_1 = a f_{-1/2} + b f_{1/2} + c f_{3/2}$	5	15/4	5/2	-1/4
I_{ξ}^{fc}	$\alpha f_{-1/2} + f_{1/2} = a f_0 + b f_1 + c f_2$	1	1/4	3/2	1/4

Table 4.2: Fourth-order compact scheme coefficients of the boundary relations .

Close to the annular walls and the lids, it is necessary to refine the mesh to account for strong velocity gradients. For this purpose, an analytic mesh transformation is used here to control the grid size where no-slip boundary conditions are prescribed. Consequently, evaluations of derivatives on non-uniform grids with better resolution near the boundaries (where smaller scales need to be accurately resolved) are achieved by multiplying the derivatives on the equally spaced nodes by a function proportional to an hyperbolic tangent (Knikker 2009), given by

$$x(X) = \beta \left[1 - \frac{\tanh \gamma(\beta - X)}{\tanh \gamma\beta} \right] \quad (4.20)$$

where γ in the stretching factor, and β is a control parameter. An example of grid refinement obtained with equation 4.20 is presented in figure 4.3(a), and an example of the grid refinement in the azimuth-radial ($\phi - r$) cross section near the boundary layers is shown in 4.3(b).

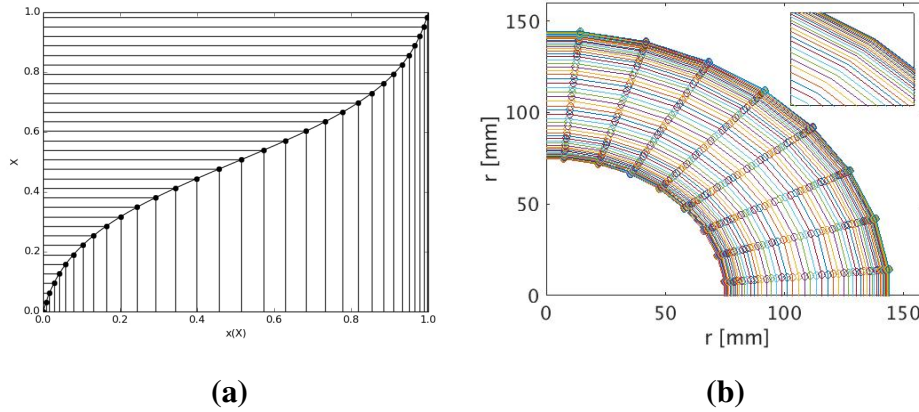


Figure 4.3: (a) Function applied to obtain a non-uniform grid, with $\beta = 5$, and different values of the control parameter γ . Examples of curves obtained with different values of γ ; (b) $\phi-r$ grid with a zoom near the cylinder wall to highlight grid refinement.

The use of compact schemes to evaluate the explicit terms arising from the time discretization is done without further difficulties, applying the method described in each non-periodic space direction. The solutions of the Helmholtz/Poisson equations that arise from the projection methods are less straight-forward, due to the implicit nature of compact schemes. It requires to write the discrete second-order operators as $D = M^{-1}B$. In the next section, the method implemented to solve the Poisson equation (4.11) will be described.

4.3.3 Solution of Poisson/Helmholtz equations

In section 4.2.2, the solution of the incompressible Navier-Stokes equations was reduced to solving Helmholtz and Poisson equations, and evaluating the leading explicit terms. The method of solution to solve the Poisson equation is described hereafter.

Let us consider the Poisson equation written in cylindrical coordinates :

$$\frac{1}{r} \frac{\partial}{\partial r} r \frac{\partial}{\partial r} \Phi + \frac{1}{r^2} \frac{\partial^2 \Phi}{\partial \phi^2} + \frac{\partial^2 \Phi}{\partial z^2} = s \quad (4.21)$$

This is the required equation to compute the pressure correction (eq. 4.15), or the preliminary pressure (eq. 4.8). Using periodic boundary conditions in the azimuthal direction allows to use pseudo-spectral discretization. Consequently, the 3D problem is reduced in the Fourier space to a sequence of 2D problems for each wavenumber as

$$\frac{1}{r} \frac{\partial}{\partial r} r \frac{\partial}{\partial r} \hat{\Phi}_m - \frac{m^2}{r^2} \hat{\Phi}_m + \frac{\partial^2}{\partial z^2} \hat{\Phi}_m = \hat{s}_m \quad (4.22)$$

where m stands for the azimuthal wavenumbers that arises from the decomposition $\Phi = \sum_m \hat{\Phi}_m e^{im}$. Noted that each mode in (4.22) is independent of each other. Using the tensorial notation the discrete form for (4.22) can be re-written in a more concise way as

$$(D_{mr}^2 \otimes \mathbf{I}_z + \mathbf{I}_r \otimes D_z^2) \hat{\Phi}_m = \hat{s}_m, \quad 0 \leq m \leq n_\phi/2 + 1, \quad (4.23)$$

with the operators D_{mr}^2 and D_z^2 in equation 4.23 given by

$$D_{mr}^2 = \frac{1}{r} \delta_r^{fc} r \delta_r^{cf} - \frac{m^2}{r^2}, \quad (4.24)$$

$$D_z^2 = \delta_z^{fc} \delta_z^{cf}$$

where δ^{cf} and δ^{fc} are the staggered derivatives, defined in the previous section (4.3.2).

The solution of the linear system presented in (4.24) is computed using the diagonalization method, which consists of solving D_{mr}^2 and D_z^2 on each respective eigenspace, which can be formulated as $D_{mr}^2 = M_{mr}\Lambda_{mr}M_{mr}^{-1}$ and $D_z^2 = M_z\Lambda_zM_z^{-1}$. In this way, the solution is given by

$$(\Lambda_{mr} \otimes \mathbf{I}_z + \mathbf{I}_r \otimes \Lambda_z)\tilde{\Phi}_m = \tilde{S}_m, \quad 0 \leq m \leq n_\phi/2 + 1, \quad (4.25)$$

$$\tilde{\Phi}_m = M_{mr}^{-1}\hat{\Phi}_mM_z^{-1} \quad \tilde{S}_m = M_{mr}^{-1}\hat{S}_mM_z^{-1} \quad (4.26)$$

After a preprocessing step, that is performed to compute the eigenvectors and eigenvalues of the D_{mr}^2 and D_z^2 operators, the main steps of the diagonalization method are

1. compute FFT of the right-hand-side \hat{S}_m
2. perform the tensor product $\tilde{S}_m = (M_{mr}^{-1} \otimes M_z^{-1})\hat{S}_m$
3. compute the elementwise solutions $\tilde{\Phi}_{m,ij} = \tilde{S}_{m,ij} / (\lambda_{mr,i} + \lambda_{z,j})$
4. perform the tensor product $\hat{\Phi}_m = (M_{mr} \otimes M_z)\tilde{\Phi}_m$
5. compute $\Phi = FFT^{-1}(\hat{\Phi}_m)$

Note that Neumann boundary conditions (as presented in equation 4.9) introduce a zero eigenvalue for the mode $m = 0$. Thus, the compatibility condition plays an important role to ensure that the problem will admit a solution that leads to an additive constant. In the present case of closed cavities, no renormalization of the velocity is required.

The main computational costs involved in the diagonalization methods are related to the computation of the tensorial products, in transforming them to the eigenspace and back. One strategy to reduce the simulation time is implementing adequate methods to perform the computations in parallel. This strategy will be addressed in the following section.

4.4 High-performance computing

In the framework of the SRI simulations, the purpose of HPC is to reduce the wall clock time of the simulations. The numerical methods described in the previous sections show that the main components to solve efficiently the Navier-Stokes equations are the evaluations of compact scheme derivatives or interpolations (mainly due to non-linear terms) and the solutions of Helmholtz/Poisson equations (algebraic linear systems). This corresponds to the time explicit and time implicit terms of the NS equations. In Abide et al. (2018) two different strategies have been proposed to benefit from parallel computing. The first one is specific for the parallel solution of the diagonalization method, while the second one focuses on the parallel calculations of compact schemes. These two strategies are presented hereafter.

4.4.1 The pencil decomposition

The core of the diagonalization method is the tensorial products and the FFT successively applied in each space direction. Thus, a strategy to distribute the computational load over different processors can be inspired in strategies from parallel computing of fast Fourier transforms (2decomp&FFT or P3DFFT). The key point is to dynamically distribute a 3D-array over a two-dimensional grid of processors. Note that there will always be one rank for which the full range

indices are not divided to be computed in parallel in the MPI-processors. The three-dimensional array configurations available, called r -pencil, ϕ -pencil and z -pencil decompositions are presented in figure 4.4. In each of these configurations, the original serial algorithm can be applied to the spatial direction that is not divided into the MPI-processors.

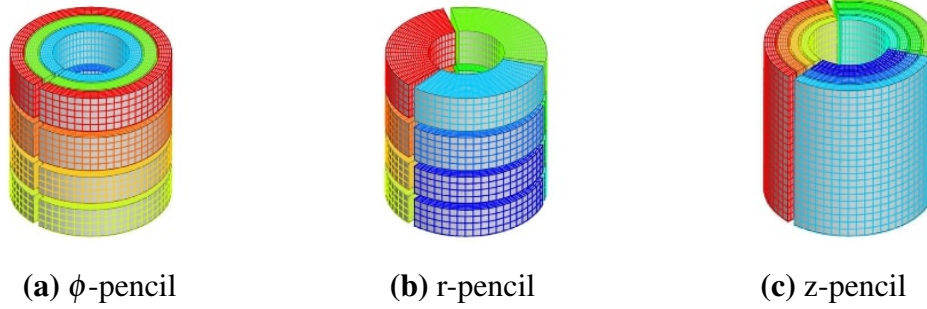


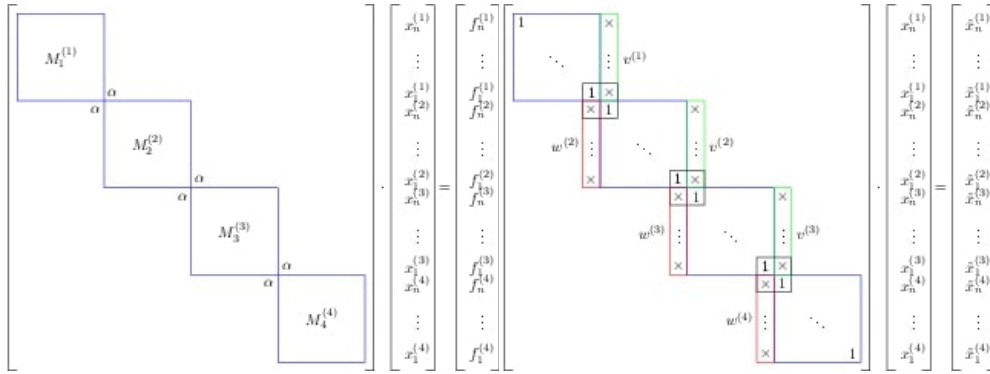
Figure 4.4: Three states of the 2d-pencil decomposition divided in 3×4 processor grids (respectively in r and z directions). Reproduced from Abide et al. (2018) with the friendly permission of Stéphane Abide

In the simulations performed here, the FFT is applied along the ϕ -pencil state, the tensorial product $M_z \otimes \mathbf{I}_r$ is computed when the data are distributed over the r -pencil, and $\mathbf{I}_z \otimes M_{mr}$ is computed on the z -pencil. One switch from one state to another applying global transposed functions, which performs MPI all-to-all global communications to redistribute the arrays. The 2d-pencil decomposition library implemented was the 2decomp&fft library (Li and Laizet 2010).

The algorithm to solve the linear terms using the parallelized diagonalization method consists of the following steps (Abide et al. 2018):

1. computing FFT of the source term $\widehat{S}_m = FFT_\phi(S)$ on the ϕ -pencil state (figure 4.4.(a));
2. distributing \widehat{S}_m from ϕ to r -pencil and computing $\widehat{F}_m = (M_{rm}^{-1} \otimes \mathbf{I}_z)\widehat{S}_m$;
3. distributing \widehat{F}_m computed in the previous step (step 2) from r to z -pencil then computing $G_m = (\mathbf{I}_r \otimes M_z^{-1})F_m$;
4. computing $\widehat{G}_{mij} = \frac{\widehat{G}_{mij}}{\lambda_{rmi} + \lambda_{zj}}$;
5. computing $\widehat{F}_m = (\mathbf{I}_r \otimes M_z)\widehat{G}_m$;
6. transposing \widehat{F}_m form z -pencil to r -pencil, and computing $\widehat{S}_m = (M_{rm} \otimes \mathbf{I}_z)\widehat{G}_m$;
7. transposing \widehat{S}_m form r -pencil to ϕ -pencil, and computing the inverse FFT to obtain the solutions back in the physical space.

It is worth mentioning that the serial algorithm of the diagonalization method detailed in the section 4.3.3 is easily implemented using the pencil decomposition. This method relies on a large volume of communications due to the dynamical redistribution. It still remains efficient, since this leads to a significant reduction of the total simulation time (Abide et al. 2017, Li and Laizet 2010).



$$(a) \quad Mx = (\tilde{M} + \Delta M)x$$

$$(b) \quad \tilde{M}^{-1}\tilde{M}x = \tilde{M}^{-1}b$$

Figure 4.5: Matrix partition of the over 4 processors. (a) Tridiagonal matrix $Mx = (\tilde{M} + \Delta M)x$; (b) Inverse of the tridiagonal matrix $\tilde{M}^{-1}\tilde{M}x = (\mathbf{I} + \tilde{M}^{-1}\Delta M)x = \tilde{M}^{-1}b$. Reproduced from Abide et al. (2017) with the friendly permission of *Stéphane Abide*.

4.4.2 Parallel Diagonal Dominant

A parallel strategy can be implemented to evaluate the compact scheme derivatives and interpolations described in section 4.3.2 using the pencil decomposition presented in the previous section. To reduce the computationally expensive global communications when compact scheme operators are evaluated, it is possible to take advantage of the diagonal dominance of the matrices. The Parallel Diagonal Dominant algorithm (PDD) allows us to efficiently solve tridiagonal linear systems on distributed architectures (Sun 1995, Polizzi and Sameh 2007). The PDD algorithm is based on the diagonal dominance assumption, where some matrix entry elements are dropped during the factorization procedure to increase the number of independent computational tasks, and so, to improve the parallelism efficiency. The accuracy of this approximate solver depends on the degree of the diagonal dominance (Sun 1995). Thus, for achieving an efficient approximation, one should take into account the accuracy of the compact finite difference schemes, but also the other DNS-code features such as the conservation properties. A detailed description of this approach for cartesian and cylindrical coordinate systems can be found in Abide et al. (2017, 2018). Hereafter, the main ingredients of the PDD method are presented.

The compact scheme evaluation of the derivatives and interpolations presented in section 4.3.2 involves the solution of multiple tridiagonal linear systems. For simplicity, we can focus only on the evaluation of the generic tridiagonal linear system. In the resulting algebraic linear system $Mx = b$, M is a tridiagonal matrix of size n , where $x = (x_1, \dots, x_n)$ and $b = (b_1, \dots, b_n)$. The original matrix M is then split into two parts $M = \tilde{M} + \Delta M$ and thus distributed over q processors. \tilde{M} is a block diagonal matrix composed of tridiagonal matrices $M(k)$, and ΔM is composed of the off block-diagonal entries. Considering the q number of processors, this partition leads then to $\mathbf{x} = (\mathbf{x}^1, \dots, \mathbf{x}^q)$ with $\mathbf{x}^{(k)} = (x_1^{(k)}, \dots, x_{n/q}^{(k)})$, where $1 \leq k \leq q$. The matrix M distributed over q processors is schematically represented in figure 4.5.

The product between the original tridiagonal linear system and the inverse matrix \tilde{M}^{-1} leads to a block identity matrix surrounded by two-column vectors $v^{(k)}$ and $w^{(k)}$, denoted as spike by Polizzi and Sameh (2007). Figure 4.5(b) schematically shows the structure of the matrix $\tilde{M}^{-1}M$. Adding the first and the last nodes of each partition (respectively $x_1^{(k)}$ and $x_{n/q}^{(k)}$) leads to a pentadiagonal linear system called the reduced system (Sun 1995). Note that, independently of

the diagonal dominance assumption, the parallel algorithm to solve $Mx = b$ can be implemented using the following steps:

1. Compute a guessed solution for the system $\tilde{x} = \tilde{M}^{-1}b$ on each processor independently.
2. To solve the pentadiagonal reduced system to compute the first and last nodes of each partition, $x_1^{(k)}$ and $x_m^{(k)}$.
3. use the spikes to correct the guessed solution $x^{(k)} = \tilde{x}^k - x_1^{(k)}v^{(k)} - x_{n/q}^{(k)}w^{(k)}$

Depending on the degree of the diagonal dominance, a truncated version of this algorithm can be implemented, which allows achieving a higher level of parallelism. In fact, in this case, the entries of the spikes $v^{(k)}$ and $w^{(k)}$ decrease as we move away from the diagonal. By dropping the spike entries that are far from the diagonal, the reduced system degenerates into independent linear systems of dimension 2, involving only the unknowns $x_1^{(k)}$ and $x_{n/q}^{(k)}$ at each interface. Abide et al. (2018) showed that this truncation does not deteriorate the accuracy nor any conservation properties, since it is an inherited feature of the diagonal dominance of the compact schemes. Note that the diagonalization of each modified operator is carried out only once during pre-processing stages (Abide and Viazzo 2005).

This reduced Partial Diagonal Dominant (rPDD) strategy (Sun 1995) thus constitutes a powerful tool in terms of reducing CPU-time cost, since the computations require only simple matrix–matrix products, that involves only neighbor-to-neighbor communications, instead of all-to-all parallel communications (Sun 1995, Abide et al. 2017).

4.5 Numerical code utilization

To carry out the SRI numerical investigations, Direct Numerical Simulations (DNS) were performed using the CS2D-Annular code, dedicated to high-performance computing based on Message Passing Interface (MPI) parallelization, developed by Abide et al. (2018).

Parallel strategies are implemented to reduce the large execution times demanded by scalar codes, which can often bring limitations to the numerical investigations of the SRI. Especially when slow occurring phenomena are investigated, that requires long integration times to be evaluated. Furthermore, the SRI configurations investigated have very long transient regimes, that demand time-consuming simulations. The algorithm presented introduces strategies to strongly reduce wall-clock times to study not-yet observed phenomena related to the SRI. The code description is presented hereafter.

4.5.1 Code description

To carry out the SRI numerical investigations, Direct Numerical Simulations (DNS) were performed using the CS2D-Annular code, written in Fortran90, dedicated to high-performance computing based on Message Passing Interface (MPI) parallelization, reported in Abide et al. (2018). The MPI strategies implemented can reduce the large execution times demanded by scalar codes from months to hours. The numerical data outputs are written out in HDF5 format that makes them easy to be stored, and post-processed mainly based using Matlab scripts.

The CS2D-Annular code ran on several parallel computer centers (eos CALMIP, muse HPC@LR, occigen CINES), different incompressible flow applications, and a good scaling was observed by Abide et al. (2017) up to 10^4 processors.

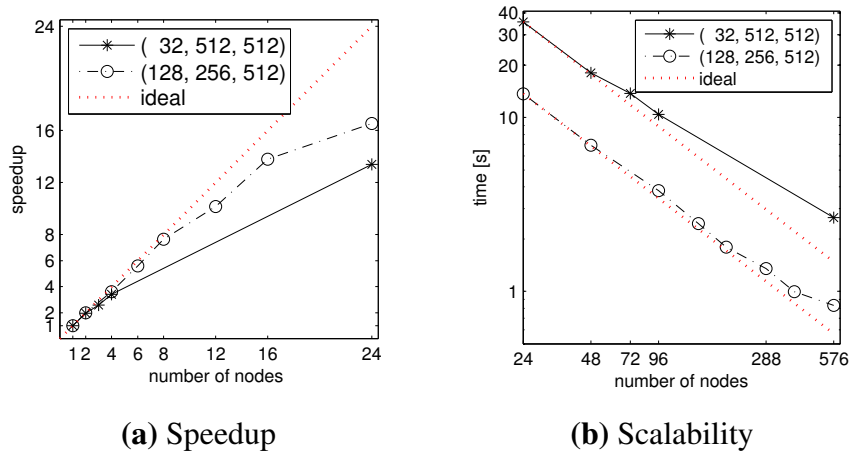


Figure 4.6: Scaling tests on *HLRN* computers for $\phi \times r \times z$ meshes of sizes $32 \times 512 \times 512$ and $128 \times 256 \times 512$. The x-axis is the number of nodes (n) used on the computations and the y-axis presents (a) the speedup (b) the time (in seconds) necessary to complete 100 iterations.

The SRI simulations here presented were all performed in the *High-performance Computing in Northern Germany (HLRN)* computers, where strong scaling tests were also performed. Figure 4.6 shows the speedup and the scalability with respect to the number of processors on two different $\phi \times r \times z$ meshes, with sizes $32 \times 512 \times 512$ and $128 \times 256 \times 512$, considering the time to complete 100 iterations. The speedup evaluates how the number of nodes used during the computations will make the processing speed increase. The scalability is the ability to maintain the average unit speed (Sun and Rover 1994), i.e., it shows the relation between the final computation time decrease and the number of processors (or nodes) n used in the computations.

The speedup depends on the number of processors involved in the computations, which must be chosen considering a good distribution of tasks among the processors. If the tasks are not distributed in a balanced way, it is possible that a load balancing occurs, i.e., a long time to complete the processing of a single task before proceeding with the program. An important aspect that should be observed for the good speedup of the code is the granularity, which is the ratio between computing time and the time spent on the communication between processors. A too large number of processors involved in the computations would lead to a performance decrease due to the time spent in the communication between the processors. An ideal parallelization would have a linear decrease in the simulation time with n (e.g., using 2 processors should decrease the total computation time using one processor in half; using 3 processors should make time decrease by a factor of 3, etc., leading to a linear relation), but the time demanded for the communication between the processors make the actual computational time bigger than this ideal situation. Form figure 4.6, we can see that the code speedup increases significantly with the number of nodes and that it scales practically linearly until at least 288 nodes, with a mesh of $128 \times 256 \times 512$. The meshes used for testing the scalability have more grid points than the usual meshes chosen for the simulations.

As an example, the $\phi \times r \times z$ number of grid points used for the SRI considering the same geometry of the experimental setup here presented was of $32 \times 64 \times 200$. In such simulations, computations are performed for approximately 12 hours to obtain 4 hours of results in physical time.

4.5.2 Example of a numerical simulation

An example of the numerical results obtained are presented in figures 4.7 and 4.8. These figures show snap shots of u_ϕ , u_r , u_z , and T respectively at the $\phi - r$ and $r - z$ cross sections, where the SRI structures can be observed.

The $\phi \times r \times z$ number of grid points used for the SRI in figures 4.7 and 4.8 was of $32 \times 64 \times 200$. For choosing sufficiently well-resolved meshes, the convergence of the time-mean velocity profiles is observed changing the number of grid points in one direction while keeping the other two directions constant. To exemplify, figure 4.9 shows the convergence of time-mean velocity profiles when the number of grid points on the radial direction changes from 64 to 128, keeping constant the number of grid points in $\phi = 32$ and $z = 200$.

In the same way as in the experimental procedure, the numerical simulations convergence can be investigated to evaluate how many instantaneous velocity fields must be computed and stored to obtain statistically converged results. To evaluate the data convergence, the quantity C defined on equation 3.7 is also computed for the numerical data as $C(n) = \sum_{i=1}^n \frac{u(i)}{n}$, where $u(i)$ is the velocity in the i^{th} point evaluated, and n is the number of instantaneous velocity fields computed.

Figure 4.10 shows the data convergence for numerical simulations with $\mu = 0.35$ and $\Delta T \approx 4K$ at mid-height location ($z \approx H/2$), at 3 different radial positions: at $r = 84mm$ (closer to the inner cylinder), at $r = 106mm$ (close to the mid-gap region), and at $r = 125mm$ (closer to the outer cylinder). Figure 4.10(a) shows the convergence of the azimuthal velocity (u_ϕ) with $Re = 400$, and figure 4.10(b) shows the convergence of $u'_\phi u'_r$ for a simulations with $Re = 800$.

In the numerical simulations, the data completely converges to their mean values after $n \gtrsim 5 \times 10^3$ terms computed, equivalent to approximately 3 hours of simulation (in physical time), therefore, all results presented were obtained in simulations performed for a minimum physical time of 4 hours. Note that, for such long computations, the parallelization strategies described in this section become crucial to analyze the SRI phenomena numerically.

Note that, the final convergence values of simulations presented in figure 4.10 are of the same order as the convergence obtained experimentally (figure 3.8), showing a consistency in the results obtained with both methods are consistent. The numerical results obtained will be compared with experimental data in chapter 5.

4.5.3 Flow control parameters

In the numerical simulations, the control parameters of the flow are given by the boundary conditions imposed. In the simulations presented here, velocity is prescribed at the lateral cylinder walls by applying Dirichlet no-slip boundary conditions, so the velocities imposed at the inner and outer cylinders are, respectively, $u_\phi(r_{in}) = \Omega_{in} r_{in}$ and $u_\phi(r_{out}) = \Omega_{out} r_{out}$.

Non-permeability boundary conditions at the cylinder walls lead to $u_r(r_{in}) = 0$ and $u_r(r_{out}) = 0$, while impermeability at the top and bottom end gaps lead to $u_z(r_{in}) = 0$ and $u_z(r_{out}) = 0$. Also, at the top and bottom lids, the azimuthal and radial velocity components are submitted to no-slip boundary conditions, therefore, u_ϕ rotates with the same angular velocity as the outer cylinder (as in the experiments), i.e., $u_\phi(z=0) = r\Omega_{out}$ and $u_\phi(z=H) = r\Omega_{out}$. The radial velocity component at the top and bottom lids become $u_r(z=0) = 0$ and $u_r(z=H) = 0$. The axial velocity at the top and bottom end caps, due to non-permeability boundary conditions, are $u_z(z=0) = 0$ and $u_z(z=H) = 0$. The vertical temperature gradient results from the temperature difference ΔT imposed between the top and bottom lids, generating the buoyancy force in equation 4.6. Since the experiment outer cylinder wall is made of glass material, that has

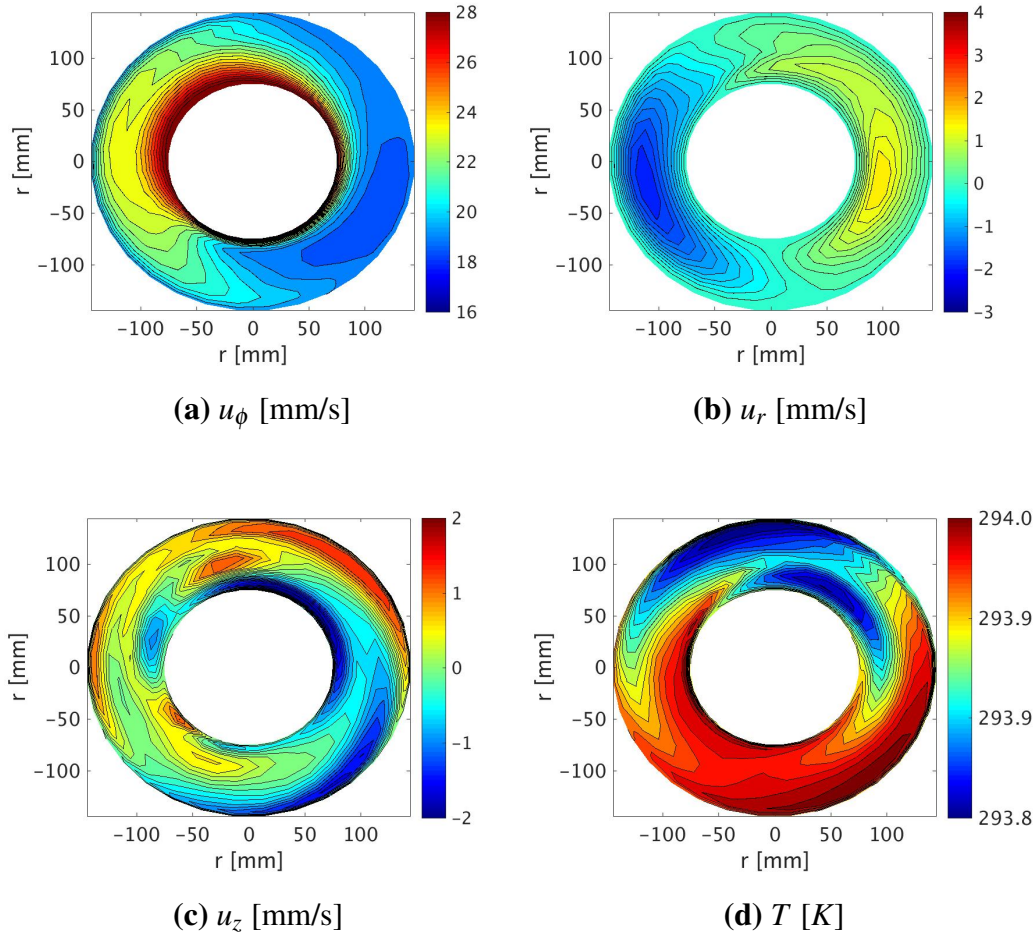


Figure 4.7: SRI snapshots showing the azimuthal-radial ($\phi - r$) cross section obtained with the CS2D-Annular code, with $\mu = 0.35$, $\eta = 0.517$, a linear stable axial temperature gradient with $\partial T / \partial z \approx 5.7 \text{K/m}$, $Fr \approx 1.5$ and $Re = 400$. The aspect ratio between cavity height and gap is $\Gamma = H / (r_{out} - r_{in}) = 10$. No-slip and impermeable Dirichlet boundary conditions are imposed ($u_\phi(r_{in}) = \Omega_{in} r_{in}$, $u_\phi(r_{out}) = \Omega_{out} r_{out}$, $u_z(z = 0) = 0$, $u_z(z = H) = 0$, $u_r(r_{in}) = 0$, $u_r(r_{out}) = 0$). The bottom and top lids of the cavity rotate with the outer cylinder Ω_{out} . The images are shown in the laboratory frame of reference

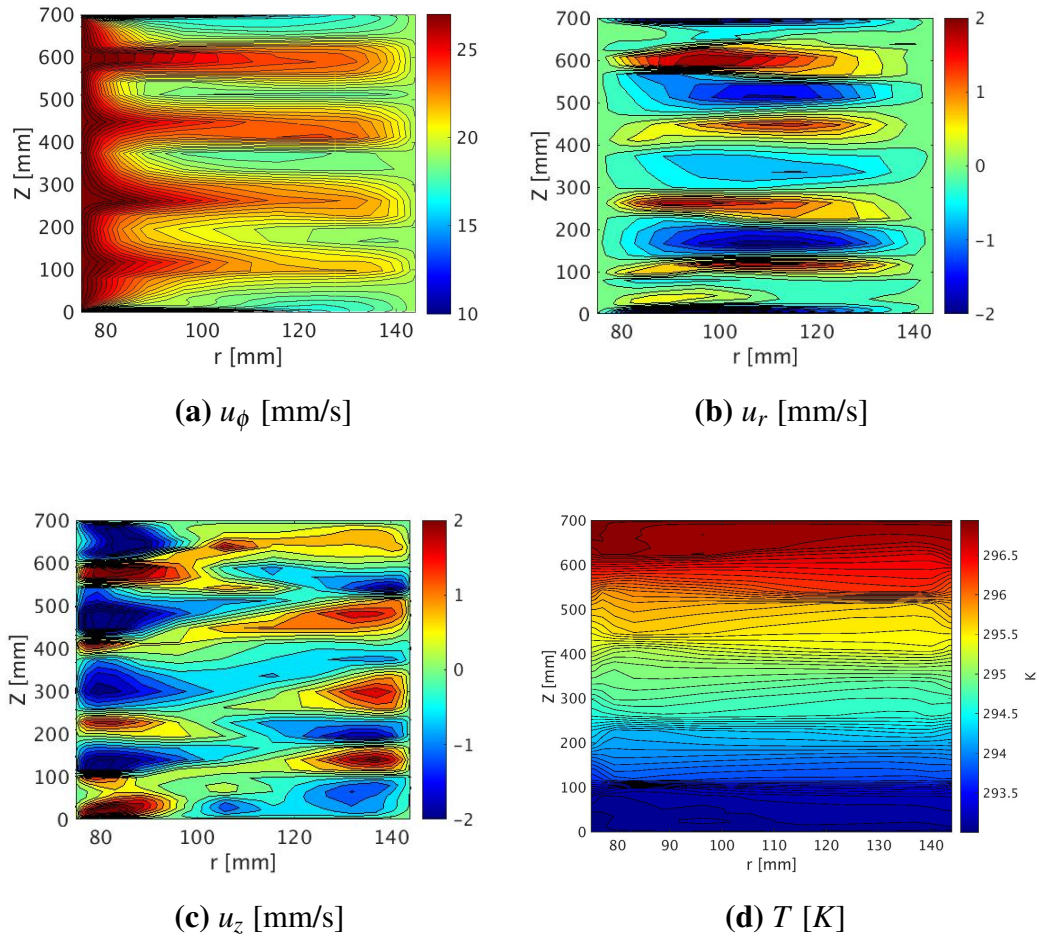


Figure 4.8: Velocity isocontour snapshots of the SRI showing non-axisymmetric spirals obtained by numerical simulation with $\mu = 0.35$, $\eta = 0.517$, a linear stable axial temperature gradient with $\partial T/\partial z \approx 5.7K/m$, $Fr \approx 1.5$ and $Re = 400$. The aspect ratio between cavity height and gap is $\Gamma = H/(r_{out} - r_{in}) = 10$. No-slip and impermeable Dirichlet boundary conditions are imposed ($u_\phi(r_{in}) = \Omega_{in}r_{in}$, $u_\phi(r_{out}) = \Omega_{out}r_{out}$, $u_z(z = 0) = 0$, $u_z(z = H) = 0$, $u_r(r_{in}) = 0$, $u_r(r_{out}) = 0$). The bottom and top lids of the cavity rotate with the outer cylinder Ω_{out} . The images are shown in a laboratory frame of reference

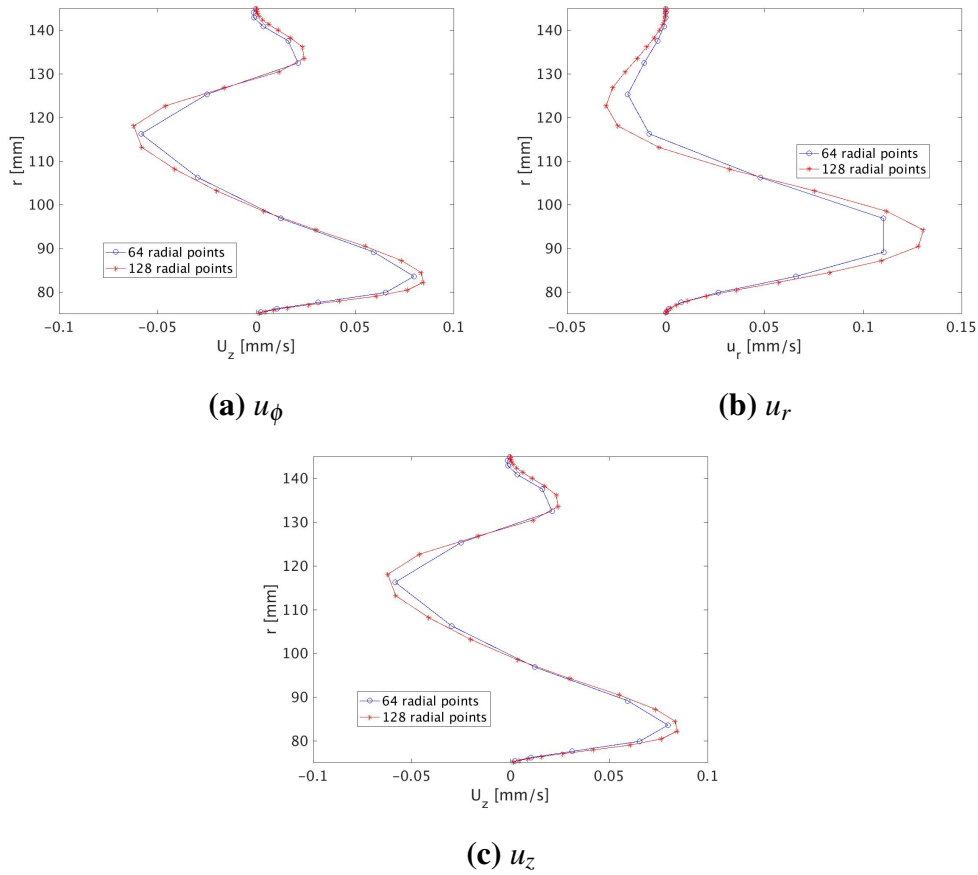


Figure 4.9: Comparison of mean time velocity profiles when the number of grid points in the radial direction increases from 64 to 128, keeping constant the number of grid points in $\phi = 32$ and $z = 200$.

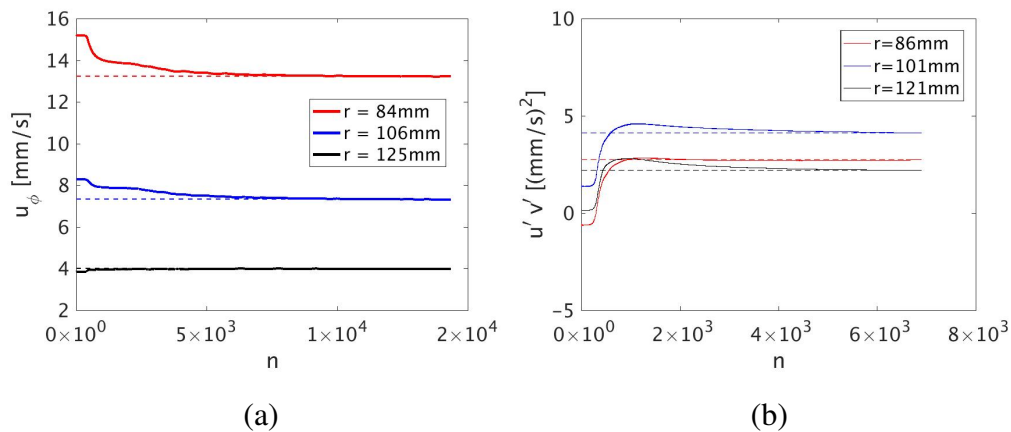


Figure 4.10: (a) Convergence obtained from numerical simulations at mid-height position ($Z = H/2$) for 3 different radial locations (a) u_ϕ time series convergence, $Re = 400$ (b) $u'_\phi u'_r$ convergence, $Re = 800$. The dashed lines indicate the final averaged velocities.

	Condition	Location
No-slip	$u_\phi(r_{in}, \theta, z) = \omega_{in} r_{in}$	Inner cylinder
	$u_\phi(r_{out}, \theta, z) = \omega_{out} r_{out}$	Outer cylinder
	$u_r(r_{in}, \theta, z) = 0$	Inner cylinder
	$u_r(r_{out}, \theta, z) = 0$	Outer cylinder
	$u_z(r_{in}, \theta, z) = 0$	Inner cylinder
	$u_z(r_{out}, \theta, z) = 0$	Outer cylinder
	$u_\phi(r, \theta, z = 0 \text{ or } H) = \omega_{out} r$	Top and bottom lids
	$u_r(r, \theta, z = 0 \text{ or } H) = 0$	Top and bottom lids
	$u_z(r, \theta, z = 0 \text{ or } H) = 0$	Top and bottom lids
Prescribed temperature	$T(z = 0) = T_0$	Bottom lid
	$T(z = H) = T_0 + (\partial T / \partial z)H$	Top lid
Adiabatic lateral walls	$\partial T / \partial n = 0$	Inner cylinder
		Outer cylinder

Table 4.3: Boundary conditions

a thermal conductivity of $\kappa_{\text{glass}} \approx 0.8 \text{ W m}^{-1} \text{ K}^{-1}$, while the top and bottom walls are made of aluminum, with thermal conductivity $\kappa_{\text{aluminum}} \approx 210 \text{ W m}^{-1} \text{ K}^{-1}$ (more than 250 times higher than the acrylic), heat losses can be neglected compared to the thermal forcing at the top and bottom lids, therefore, adiabatic boundary conditions are imposed at the lateral walls.

A summary of the boundary conditions prescribed can be seen in table 4.3.

Due to the cylindrical configuration, the solutions of \mathbf{u} and p in the azimuthal direction are 2π -periodic. Note that periodic simulations in the axial direction were also performed to isolate the SRI phenomena from end-cap and Ekman boundary layer effects.

To conclude, the numerical stability of the simulations are also controlled using the Courant-Friedrichs-Lewy number (CFL) defined by

$$CFL = \frac{|\mathbf{u}|\Delta t}{\Delta x}, \quad (4.27)$$

where $|\mathbf{u}|$ is a typical velocity (currently the maximum absolute value of the three components of velocity), Δt is the time step, and Δx is the grid size. Although it is not easy to define an analytical CFL criterion that ensures the stability of the present scheme, previous empirical observations showed that a $CFL \leq 0.3$ leads to numerically stable simulations.

Numerical and experimental observations

“Tenho pensamentos que, se pudesse revelá-los e fazê-los viver, acrescentariam nova luminosidade às estrelas, nova beleza ao mundo e maior amor ao coração dos homens¹.”

– Fernando Pessoa –

In this chapter, we will discuss physical phenomena observed in the SRI both numerically and experimentally with Reynolds number between $200 \leq Re \leq 1300$, $\mu = 0.35$ (slightly smaller than the Keplerian line, at $\mu \approx 0.375$ in the experiment here presented), and temperature difference between the top and bottom lids of $\Delta T \approx 4K$. These values were chosen by their possible practical implication on accretion disk theory, as discussed in chapter 1. The results comparing experimental and numerical simulation data are here presented in the radial-azimuthal ($r - \phi$) cross-section, with values of $Re = 400$, $Re = 600$ and $Re = 800$, $Re = 1000$, respectively corresponding to inner cylinder angular velocities of $\Omega_{in}(Re = 400) \approx 0.381\text{rad/s}$, $\Omega_{in}(Re = 600) \approx 0.571\text{rad/s}$, and $\Omega_{in}(Re = 1000) \approx 0.952\text{rad/s}$. The objective of this comparison is not only the numerical code validation, since it has already been validated in previous works (Abide et al. 2017, 2018), but also to explore new physical phenomena associated with the SRI that can lead to a better understanding of this still not fully comprehended hydrodynamic instability.

5.1 Comparison of experimental and numerical SRI data

Figure 5.1 shows a comparison between numerical and experimental space-time diagrams using a 12 minutes time-slice, for Reynolds number $Re = 400$ and $\mu = 0.35$ at mid-height axial position ($z \approx H/2$)². The initial temperature difference imposed between top and bottom lids is $\Delta T \approx 4K$, leading to $\partial T / \partial z \approx \frac{4K}{0.7m} \approx 5.7K/m$, $Rn \approx 250$ and $Fr \approx 1.5$. The reference frame is co-rotating with the outer cylinder for a direct comparison with the experiment results since the *PIV* data have been obtained in this frame of reference. When the results presented in this chapter will be obtained in a reference frame fixed in the laboratory, it will be explicitly indicated in the text. Figures 5.1(a),(b) demonstrate the good agreement between numerical simulations and *PIV* data, presenting SRI oscillations with a period of approximately 90 seconds in the

¹ “I have thoughts which, if I could bring them forth and make them living, would add a new lightness to the stars, a new beauty to the world and a greater love to the heart of men.”

²The indication of radial and axial position is written as approximated in the text (\approx) since it was not interpolated to obtain the precise position indicated, but taken from its closest point in the discrete data sets.

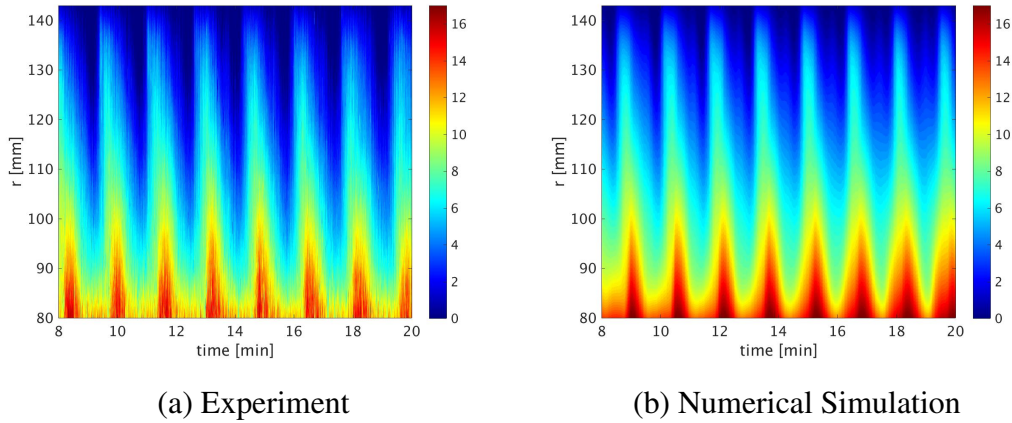


Figure 5.1: u_ϕ space-time diagram for $Re = 400$ in a reference frame co-rotating with the outer cylinder at mid-height axial position ($H/2$). The horizontal axis shows time in minutes and the vertical axis, the radius in mm (the bottom of the image is near the inner cylinder region, and the top, close to the outer cylinder). Both figures(a),(b) show 12 minutes of measurements.

co-rotating frame of reference. This time scale is relevant to be noticed since it is associated with the SRI most energetic frequency. When compared to the SRI lower frequency oscillations that will be later presented (in chapter 6), the SRI frequency is considered to be high. Note that in spite of the good agreement, there are small qualitative differences in the shape of the red spikes in figure 5.1(a),(b). In the simulation the spikes seem to become somewhat broader and more symmetric at later times, but no explanation was yet found for this slightly different shape at later times. In figure 5.2, the time mean azimuthal velocity profiles $\overline{u_\phi}$ from two different experiments are compared with the corresponding numerical simulations (the bar on top of a variable is used to indicate time average).

The TC profile (equation 1.1) is represented by a dashed black line. It should be noted that for all unstable SRI profiles observed, the flow is slower near the inner cylinder ($r \approx 80mm$) when compared to the non-stratified TC case, and slightly faster near the outer cylinder ($r \approx 143mm$), showing how the stratification affect the mean flow, transferring energy to the instability.

Figures 5.3(a),(b) show a comparison of u_ϕ spectra between the two experiments (performed at different days with the same parameters) and the numerical simulation, respectively for $Re = 400$ and $Re = 600$. The dominant SRI frequencies in the outer cylinder co-rotating frame of reference are $f_{SRI}(Re = 400) \approx 0.011Hz$ and $f_{SRI}(Re = 600) \approx 0.015Hz$. The amplitude of the spectra is computed as the square of the Fourier transformed azimuthal velocity ($P = |FFT(u_\phi)|^2$) at a fixed azimuthal and radial position $\phi = 0, r \approx r_{in} + d/2$, and height $z \approx H/2$. For both Re , the SRI peak corresponds to the mode $m = 1$ azimuthal wave number. To find out the mode m of each respective peak in the spectra, we can apply the transformation

$$f_{lab} = f_{rot} + m \frac{\Omega_{out}}{2\pi} \quad (5.1)$$

where f_{lab} is the frequency in the laboratory frame of reference, f_{rot} is the frequency in an outer cylinder co-rotating frame, Ω_{out} is the angular velocity of the outer cylinder, r is the radial position at which the time series have been measured. Then, to know which mode m corresponds to each peak, equation (5.1) can be applied with f_{rot} obtained from the experiments

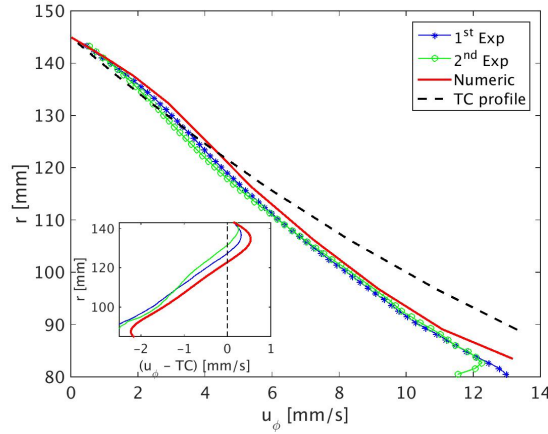


Figure 5.2: Time average azimuthal velocity profiles ($\overline{u_\phi}$). The lines with star and circle markers represent two different experimental data performed with $Re = 400$, $\mu = 0.35$ and temperature between top and bottom lids $\Delta T \approx 4K$, leading to $Rn \approx 250$ and $Fr \approx 1.5$. The solid red curve was obtained from numerical simulation, and the black dashed line is the non-stratified analytical TC profile. The bottom left figure is showing the deviations from the TC profile.

(which co-rotates with the outer cylinder) and f_{lab} from the numerical spectra (which is in obtained in the laboratory frame of reference). For a chosen m , only the peak associated with the mode of f_{lab} fulfils (5.1), while all the other peaks ($\neq m$) remain uncorrelated.

The spectra in figure 5.3 show good agreement between experimental and numerical data, although the experimental results have the tendency of showing slightly smaller frequencies than the ones obtained numerically. This might come more from small errors on controlling the experimental inner and outer cylinder velocities since slightly lower values in the experimental mean velocity profiles of figure 5.2 when compared to the numerical data were also observed. Besides showing the good agreement between numerical and experimental data, the log-scale FFTs presented here also reveal harmonics of the SRI's most energetic frequency, showing that non-linearities are starting to set in for the chosen parameters.

In figure 5.4, we can observe that the SRI oscillations are well captured in azimuth and radial velocity components. Similar frequencies and amplitudes are captured in u_ϕ and u_r of both experiments and numerical simulations. Note also that independent changes in the amplitude of u'_ϕ and u'_r occur in time, both in experiments and numerical simulations. The phenomena related to the amplitude changes in the SRI will be better investigated in the next chapter (6).

For comparing the $m = 1$ SRI oscillations directly (called here simply the SRI oscillations), the mean flow is removed from the signals so that the amplitudes vary around zero, allowing a better visualization and an easier comparison, therefore, figure 5.4 show perturbation velocity time series, being the perturbation velocities

$$\begin{aligned} u'_\phi &= u_\phi - \overline{u_\phi}, \\ u'_r &= u_r - \overline{u_r}. \end{aligned} \tag{5.2}$$

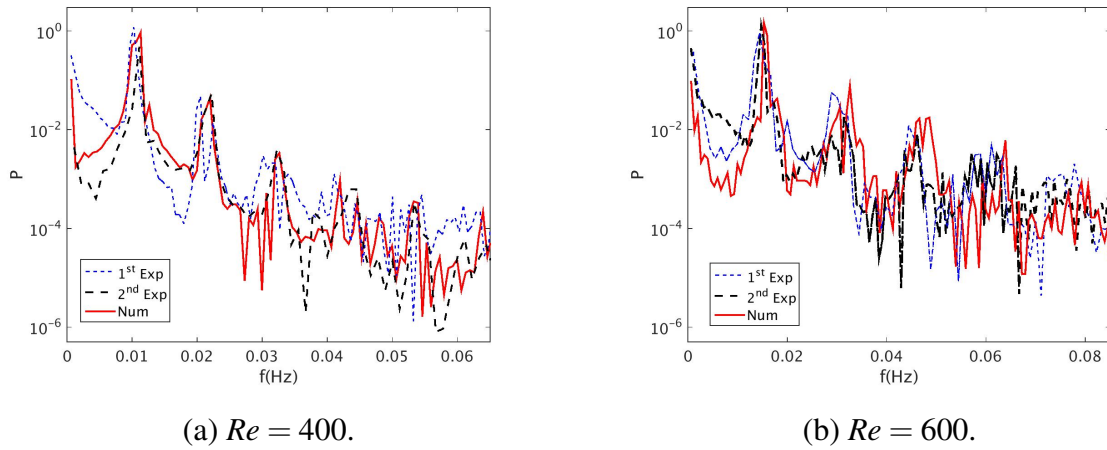
(a) $Re = 400$.(b) $Re = 600$.

Figure 5.3: Comparison of two different experiments and the numerical simulation spectra with the ordinate axis shown in logarithmic scale. The spectra are obtained from u_ϕ time series at axial position $z \approx H/2$ and radial position $r \approx r_{in} + d/2$, $\mu \approx 0.35$ and initial temperature between top and bottom lids of $\Delta T \approx 4K$, leading to $\partial T/\partial z \approx 5.7K/m$, $Rn \approx 250$ and $Fr = 1.5$.

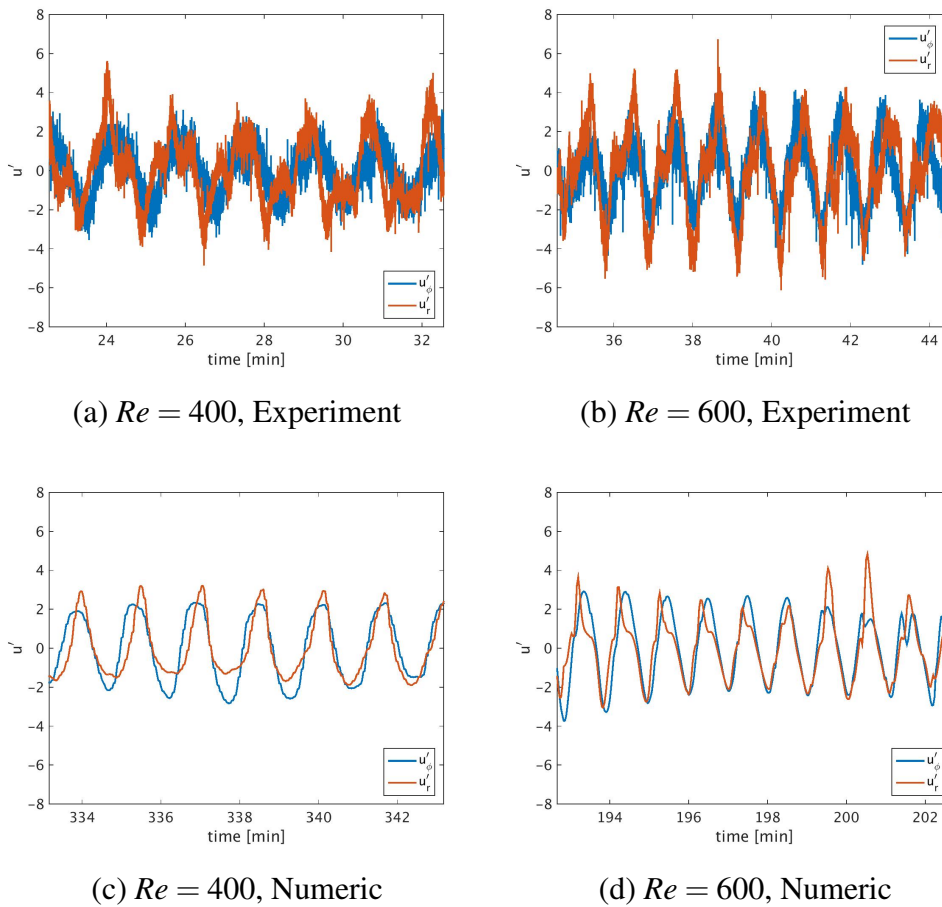
(a) $Re = 400$, Experiment(b) $Re = 600$, Experiment(c) $Re = 400$, Numeric(d) $Re = 600$, Numeric

Figure 5.4: Comparison of u'_ϕ and u'_r at $r \approx (r_{in} + r_{out})/2$ and $z \approx H/2$, with $\Delta T \approx 4K$. Figures (a),(b) show experimental data and figures (c),(d) show numerical simulation results with Reynolds numbers $Re = 400$ (left-hand side images) and $Re = 600$ (right-hand side images).

5.1.1 Numerical and experimental observations of the SRI linear stability marginal curves

For increasing Reynolds numbers with $\mu = 0.35$ and $Fr \approx 1.5$, the experiments and simulations give the same critical $Re \approx 1000$ as found by Rüdiger et al. (2017) (see figure 1.3). Stable SRI flows – when the stratification exists, but no SRI oscillations in the space-time diagram are observed – have the same $\overline{u_\phi^t}$ -profile as a classic TC flow with no stratification. This can be observed in figure 5.5 for $Re = 1000$ with $\mu = 0.35$ and a temperature difference from top to bottom $\Delta T \approx 4K$, leading to $Rn \approx 250$ and $Fr \approx 1.5$.

The symbols in figure 1.3 show where stable and unstable flows were found experimentally and numerically for constant values of $Rn = 250$ and $\mu = 0.35$. We found agreement with the linear stability analysis by Rüdiger et al. (2017). For $Re \leq 200$, with $\mu = 0.35$ and $\Delta T = 4K$, numerical simulations show that the flow is also stable, also in good agreement with the linear stability analysis performed by Rüdiger et al. (2017). Unfortunately, due to technical limitations, it was not possible to achieve such small angular velocities in the experimental setup, so this latest result could not be confirmed experimentally.

SRI stability for Reynolds numbers larger than 1000 may be counter-intuitive if we establish an analogy with other turbulent flows driven by shear, as such flows are turbulent above a critical Re . However, since the SRI flow investigated is above the Rayleigh limit, it can be expected that when rotation effect becomes more significant than stratification, i.e., for increasing Fr , the physics is approximately the same as non-stratified TC flows. From this point of view, it is quite clear that the flow should become stable when Fr becomes too large, i.e., when increase the Reynolds numbers is increased keeping the values of Rn constant (see figure 1.3 and figure 4 and 8 of Rüdiger et al. (2017)). Note that, in figure 5.5(a), there is high-frequency noise in the velocity time-series, while the numerical space-time diagram does not show these fluctuations (see figure 5.5(b)). The particular reasons for the noise are unknown, but they might be related to mechanical vibrations related to the cylinder's rotation, or either because the velocities become large enough so that some PIV particles start leaving the interrogation window, generating a noisier velocity in this range. However, the signal-to-noise ratio is small and it is obvious that neither in the experiment nor the simulation SRI oscillations are excited.

Figure 5.6(a) highlights how the SRI frequency increases with the Reynolds number until it disappears at $Re = 1000$. Note that the SRI frequencies are closer to the buoyancy frequency N than to the inertial frequency $f = 2\Omega_{in}$, and they become closer to f when the inner cylinder rotation increases. Furthermore, all peaks in the spectra are inside the interval $N - f$. This is an important remark because inertia-gravity waves (IGW) can not exist outside the interval $N - f$, where $f = 2\Omega_{in}$ (bigger than N in the cases presented). The dispersion relation of IGW with frequencies outside the $N - f$ interval assumes complex eigenvalues (Gill 1982), therefore, waves cannot exist.

Although it seems instructive to see that the SRI peak in the frequency domain increases with the Reynolds number in figure 5.6(a), where the amplitudes are presented in linear scale and the SRI peak amplitude is much higher than the amplitudes of its harmonics, this is not true at all different heights in the cavity. In other axial positions, the $Re = 600$ spectra can exhibit the most energetic peak, for example.

Figure 5.6(b) shows power spectra for different Reynolds numbers with the vertical axis in logarithmic scale, better showing the harmonics of each SRI spectrum. The spectra in figure 5.6(b) are in a reference frame fixed in the laboratory since the higher harmonics are better resolved than in the reference frame co-rotating with the outer cylinder as in figure 5.6(a).

Dashed vertical lines in figure 5.6(b) are used to highlight harmonics with the same fre-

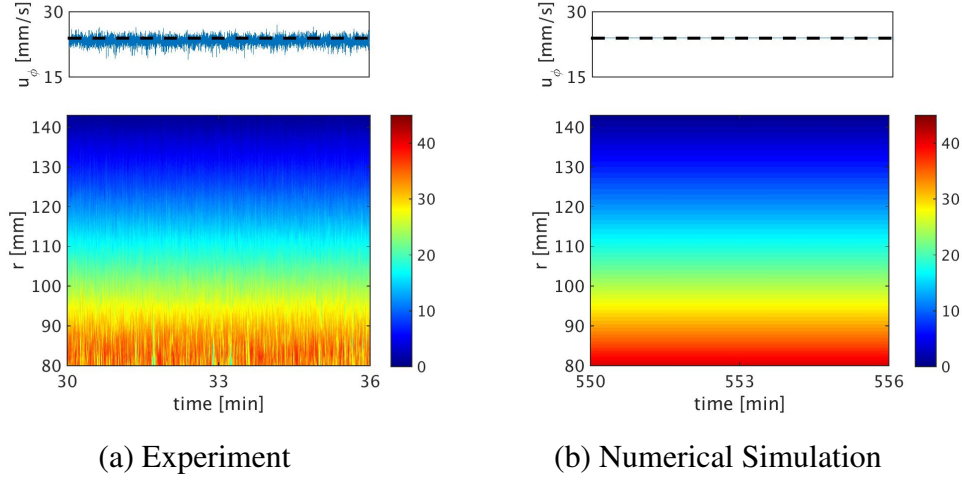


Figure 5.5: u_ϕ space-time diagrams (Hovmöller) showing the SRI stability with $Re = 1000$, $\mu = 0.35$ and a temperature difference from top to bottom of $\Delta T \approx 4K$ in the frame of reference co-rotating with the outer cylinder. On top of the space-time diagrams, the velocity profile at mid-gap position ($r \approx r_{in} + d/2$) in the space-time diagrams together the analytical TC-profile presented in black dashed line.

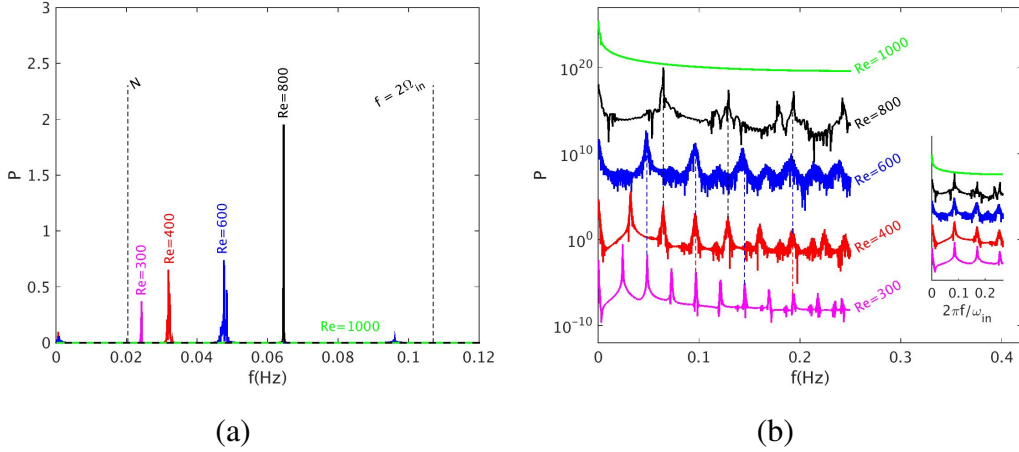


Figure 5.6: u_ϕ power spectra obtained from numerical simulations at mid-height ($z \approx H/2$) and mid-gap ($r \approx r_{in} + d/2$) position. The simulations were performed with $\mu = 0.35$ and initial temperature difference of $\Delta T = 4K$ ($Rn \approx 250$, $Fr \approx 1.5$). The horizontal axis shows frequencies in Hz , and the vertical axis shows spectra amplitudes $P = |FFT(u_\phi)|^2$ (a) shows the SRI amplitudes for increasing Re . Note that the SRI peak is no longer present in the spectrum for $Re \geq 1000$ (green dashed line at $P \approx 0$). The black dashed vertical line on the left corresponds to the buoyancy frequency for the $Re = 400$ case, while the dashed vertical line on the right corresponds to $f = 2\Omega_{in}$ for the same case, both corrected by the Doppler shift due to the azimuthal mean flow. The spectra have been taken from a reference frame co-rotating with the outer cylinder (b) Spectra for different Reynolds numbers with the amplitude (P) in logarithmic scale and obtained from u_ϕ time series in a laboratory frame of reference. For a better display, the spectra are staggered by multiplying constant exponential functions $c_{te} = e^n$ to displace them vertically in the log scale axis, where n is chosen arbitrarily. Dashed vertical lines are used for highlighting coincident peaks of different spectra. A small picture showing the spectra normalized by the inner cylinder rotation ($\Omega_{in}/2\pi$) is displayed on the bottom right corner.

quencies in spectra of different Reynolds numbers. For example, if f_{Re}^j is the j^{th} harmonic of an experiment for a certain Reynolds number Re (also equivalent to the $m = n^{\text{th}}$ azimuthal mode), then we have

$$f_{Re}^j / f_{(Re \times j/i)}^i = 1. \quad (5.3)$$

For instance, note that the second harmonic of the SRI with $Re = 300$ coincides with the first peak of the $Re = 600$ spectrum ($f_{300}^2 = f_{600}^1$), or that ($f_{300}^4 = f_{400}^3 = f_{600}^2$) and $m_8(Re = 300) = m_6(Re = 400) = m_4(Re = 600) = m_3(Re = 800)$. When the spectra are normalized by the inner cylinder rotation (therefore, also by the Reynolds numbers), all the frequencies collapse to the same values, i.e., all the spectra become coincident, as seen in the smaller figure inserted in the bottom right-hand side of 5.6(b).

Pattern formation

“Ora penso invece che il mondo sia un enigma benigno, che la nostra follia rende terribile perché pretende di interpretarlo secondo la propria verità.”¹

– Umberto Eco –

The efficiency of the implemented parallel high-performance code, described in chapter 4, reduced long computational times of DNS scalar codes previously employed to investigate the SRI (Raspo et al. 2002, Von Larcher et al. 2018, Abide and Viazzo 2005, Abide et al. 2018), which makes it convenient for evaluating low frequency (long time occurring) SRI phenomena. When velocity profiles are observed during long time simulations, strong amplitude modulations become evident (figure 6.1). These modulations are considered to have low frequency because they are more than 30 times smaller than the SRI frequency (for the experiments with $Re = 400$, $\mu = 0.35$, and $\Delta T \approx 4K$, the ratio between the low-frequency modulation period P_L and the higher frequency SRI oscillations period P_H was of $P_L/P_H \approx 31$). Note that, when the power spectra of the amplitude envelopes are obtained (figure 6.1(c)), harmonics of the most energetic peak appear, suggesting that the amplitude modulations arise from weak non-linear processes. Note also that the low-frequency peaks are found outside the interval $N - f$ mentioned previously in chapter 5 and, therefore, the amplitude modulations cannot be interpreted as low-frequency gravity wave modes. Note that similar amplitude modulation spectra are obtained from both u_ϕ and u_r time series (with peaks corresponding to the same frequencies), but with different amplitudes only in the most energetic peak of the spectra. The same harmonic peaks have the same amplitudes in both u_ϕ and u_r amplitude modulation spectra.

The modulations observed numerically in figure 6.1 are also observed experimentally. Space-time diagrams of u_ϕ for $Re = 600$ showing amplitude modulation numerically and experimentally are displayed in figures 6.2 and 6.3. In numerical simulations, these amplitude modulations are observed for all velocity components (u_ϕ , u_r , and u_z), and in the temperature T , and hence also in the Brunt-Väisälä frequency variations in time. It is also possible to see in figure 6.1 that the amplitude variations need approximately 100 minutes to achieve a permanent regime. During the transient regime ($t \lesssim 100$ minutes), amplitude variations also exist, but they are not regular in time. It is important to highlight that this mentioned transient regime is related to the amplitude modulations, and not to the SRI oscillations. The SRI oscillations show the mode $m = 1$ peak in the Fourier space presented in figures 5.3(a),(b) and 5.6, and they are

¹“I have come to believe that the whole world is an enigma, a harmless enigma that is made terrible by our own mad attempt to interpret it as though it had an underlying truth.”

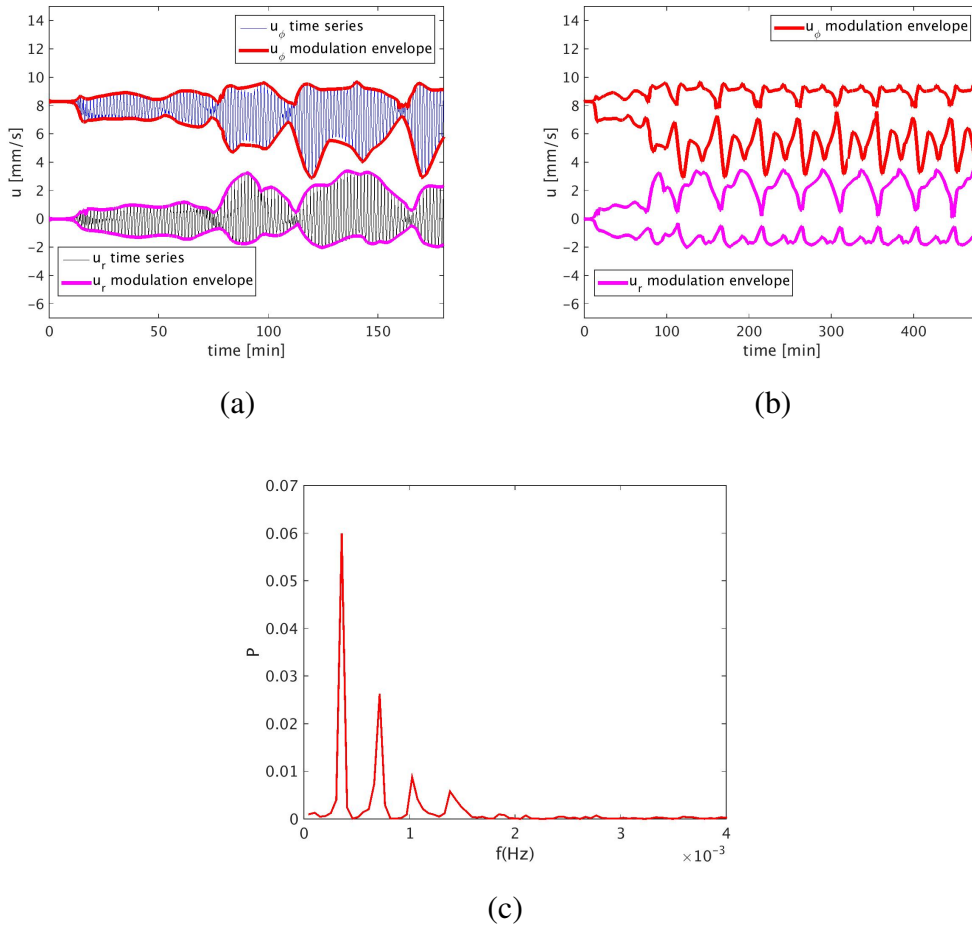


Figure 6.1: Numerical simulation time series for $Re = 400$, $\mu = 0.35$ and $dT \approx 4K$ at mid-gap position ($r \approx r_{in} + d/2$) and mid height position ($z \approx H/2$), and their respective amplitude envelopes highlighting low frequency amplitude variations in time (a) SRI time series in the time interval $0 < t < 3$ hours and their respective amplitude envelopes, highlighting low frequency amplitude modulations (b) Velocity amplitude envelopes, highlighting regular low frequency amplitude modulations within the time interval $0 < t < 8$ hours. Note that the time intervals are different in figures(a),(b) (respectively, $0 < t < 3$ hours and $0 < t < 8$ hours), so that the SRI oscillations have been included into figure (a) only. (c) Power spectrum of u_ϕ amplitude envelope (both u_ϕ and u_r envelopes present similar spectra).

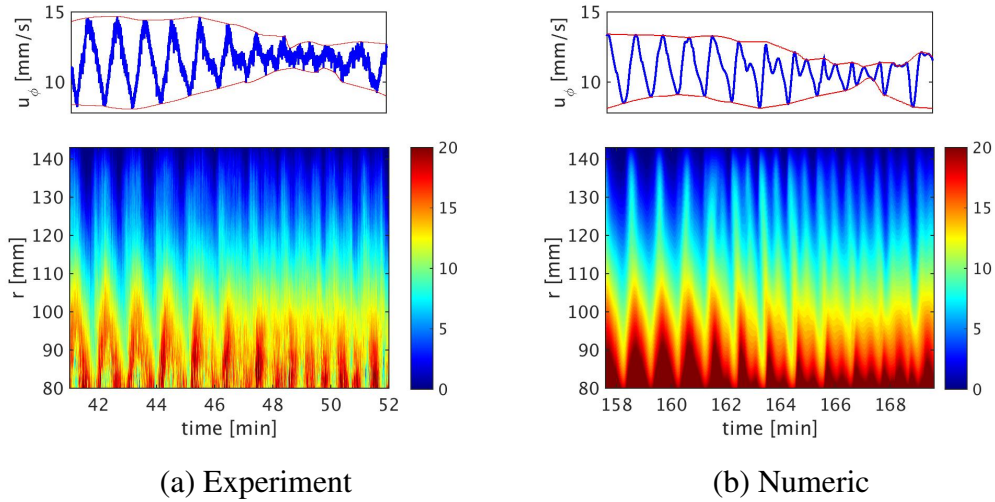


Figure 6.2: u_ϕ space-time diagrams at mid-height axial position ($z \approx H/2$) during amplitude modulation transition for $Re = 600$, $\mu = 0.35$ and $\Delta T/\Delta z = 5.71 \text{ K m}^{-1}$. The reference frame co-rotates with the outer cylinder, and the velocities represented by the colour scales are given in mm/s . The horizontal axis shows time in minutes, and the vertical axis, the radius in mm , where the bottom region is closer to the inner cylinder wall, and the top is closer to the outer one. On top of the space-time diagrams, the velocity time-series at mid-gap position ($r \approx r_{in} + d/2$) in the space-time diagrams is displayed that highlights its amplitude modulation.

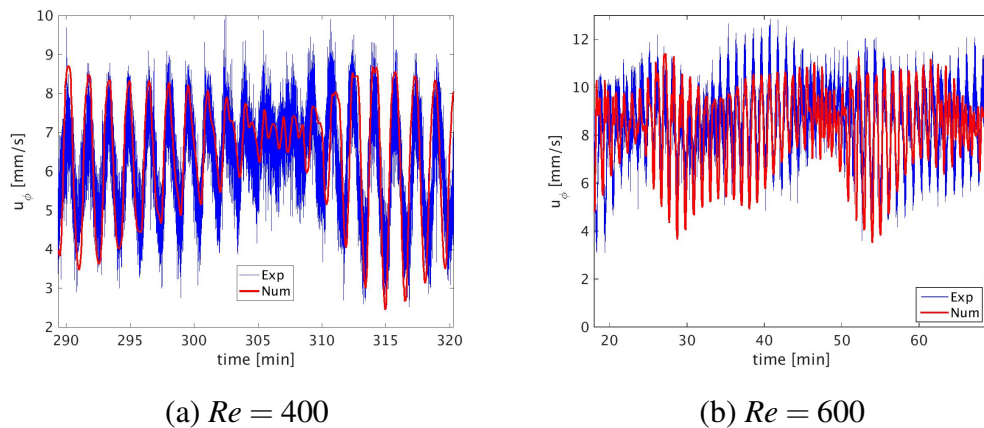


Figure 6.3: Comparison between experimental (blue curve) and numerical simulation (red curve) u_ϕ time series at mid-gap ($r_{in} + d/2$) and mid-height position ($H/2$). The results are for $\mu = 0.35$ and $\Delta T/\Delta z = 5.71 \text{ K m}^{-1}$. Please, note that the time intervals are different in figures (a) and (b).

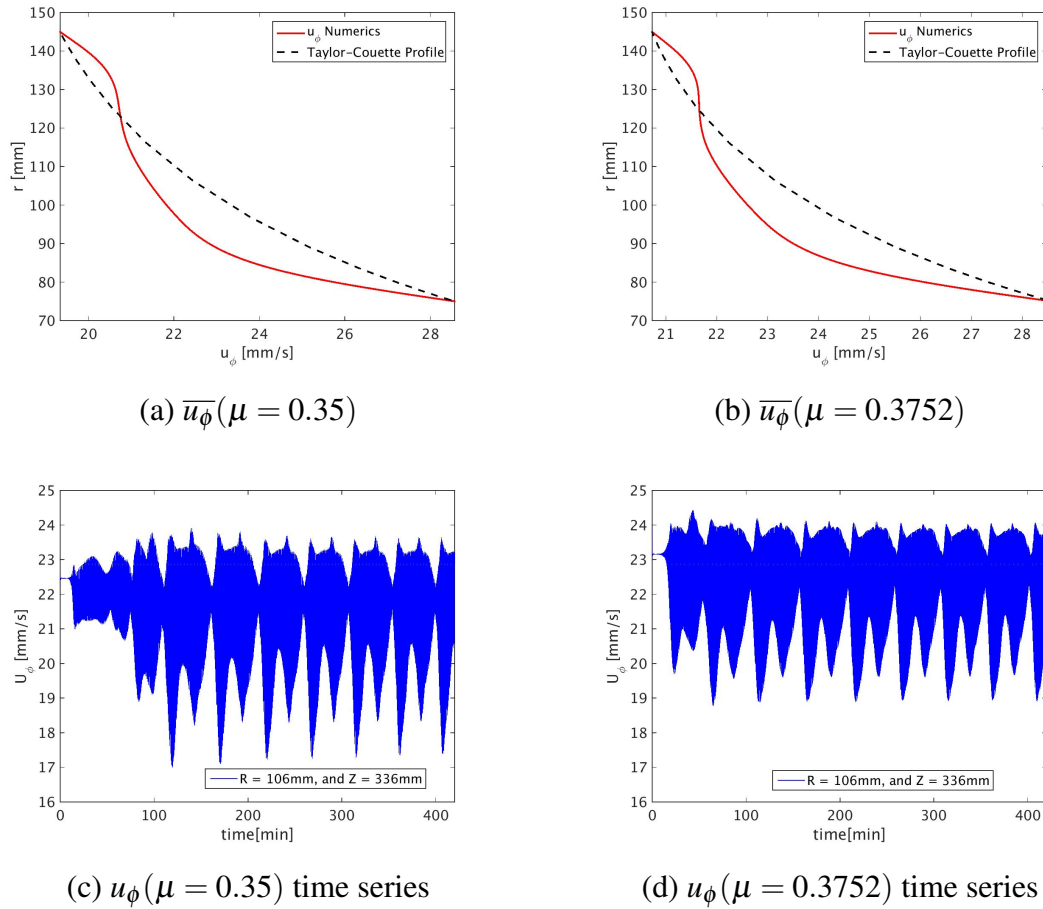


Figure 6.4: u_ϕ comparison obtained from numerical simulations with $\mu = 0.35$ (left hand side) and $\mu = 0.3752$ (Keplerian line, at the right hand side) in the laboratory frame of reference, highlighting similar mean flows on the top figures(a),(b), and similar the amplitude modulations in time in the bottom figures(c),(d). The results are for for mid-height position ($z \approx H/2$) with $\Delta T = 4K$, and the time series are for a mid-gap radial position ($r \approx r_{in} + d/2$).

already prominent approximately 10 minutes after starting the rotation for all SRI unstable Re investigated.

Note that the same pattern changes associated with the amplitude modulations described here for $Re = 400$ and $\mu = 0.35$ were also observed for other values of μ (e.g., $\mu = 0.3752$ – Keplerian line) and for different Reynolds numbers. A comparison of results obtained for $\mu = 0.35$ and $\mu = 0.3752$ are presented in figure 6.4. Note that similar mean flow behavior, are observed for the Keplerian profile (figure 6.4(b)) or for sub-Keplerian velocities (figure 6.4(a)), with similar amounts of energy being transferred from the base flow to the instabilities.

6.1 Pattern changes associated with the amplitude modulations

The analysis of the SRI flow during the amplitude modulations reveals particular flow patterns that are correlated with the modulations. In figure 6.5(a), 3 different time intervals have been

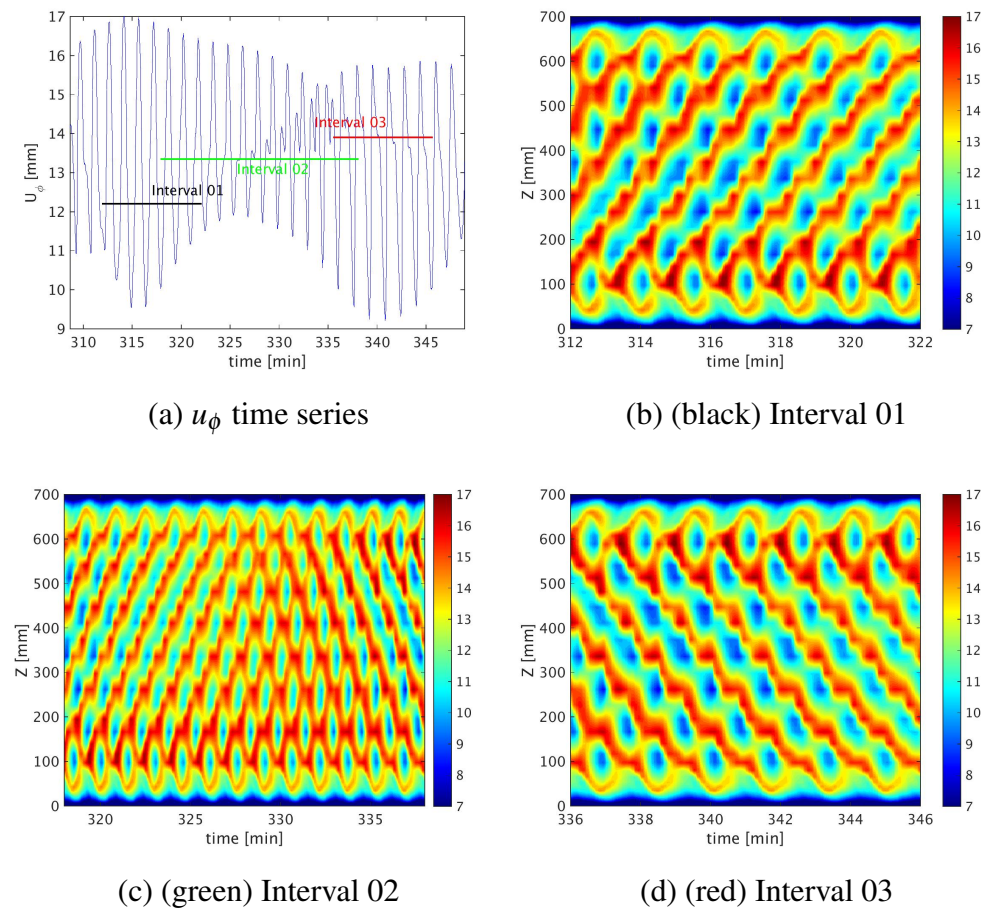


Figure 6.5: u_ϕ structures during amplitude modulation at radial position $r = r_{in} + d/2$; (a) Time series with horizontal coloured lines indicating intervals selected before (black), during (green), and after (red) a local minimum amplitude value; (b) Interval 01, from $t = 312$ to 322 minutes – SRI spiral with downward inclination; (c) Interval 02, from $t = 318$ to 338 minutes – transition from a SRI spiral with downward to upward inclination; (d) Interval 03, from $t = 336$ to 346 minutes – SRI spiral with upward inclination.

selected, indicated by colored horizontal lines. In each of these selected intervals, a different flow pattern is observed in the axial-time frame, shown in figures 6.5(b)-(d). The patterns represent different SRI spiral inclination and propagation in the axial direction, here named downward inclination (figure 6.5(b)) and upward inclination (figure 6.5(d)).

During the transition from the upward (downward) to the downward (upward) pattern, both spirals are activated and superposed. This leads to the chessboard type structure pattern in figure 6.5(c). The transition region is characterized by small SRI amplitudes.

Observations of the 3-dimensional structures obtained from numerical simulations show that not only the inclination changes during the amplitude modulation but also does the spiral propagation in the axial direction. The downward spiral inclination (figure 6.5(b)) travels from the top to the bottom lid in the axial direction, while the upward spiral (figure 6.5(d)) travels in the opposite axial direction. During the transition (figure 6.5(c)), the SRI spirals do not travel in the axial direction, and its angular velocity becomes smaller. When we evaluate longer time intervals than those presented in figure 6.5, or 3D-animations of the spirals, it is possible to observe the spiral rotation accelerating in the region where the amplitude grows, and decelerating when

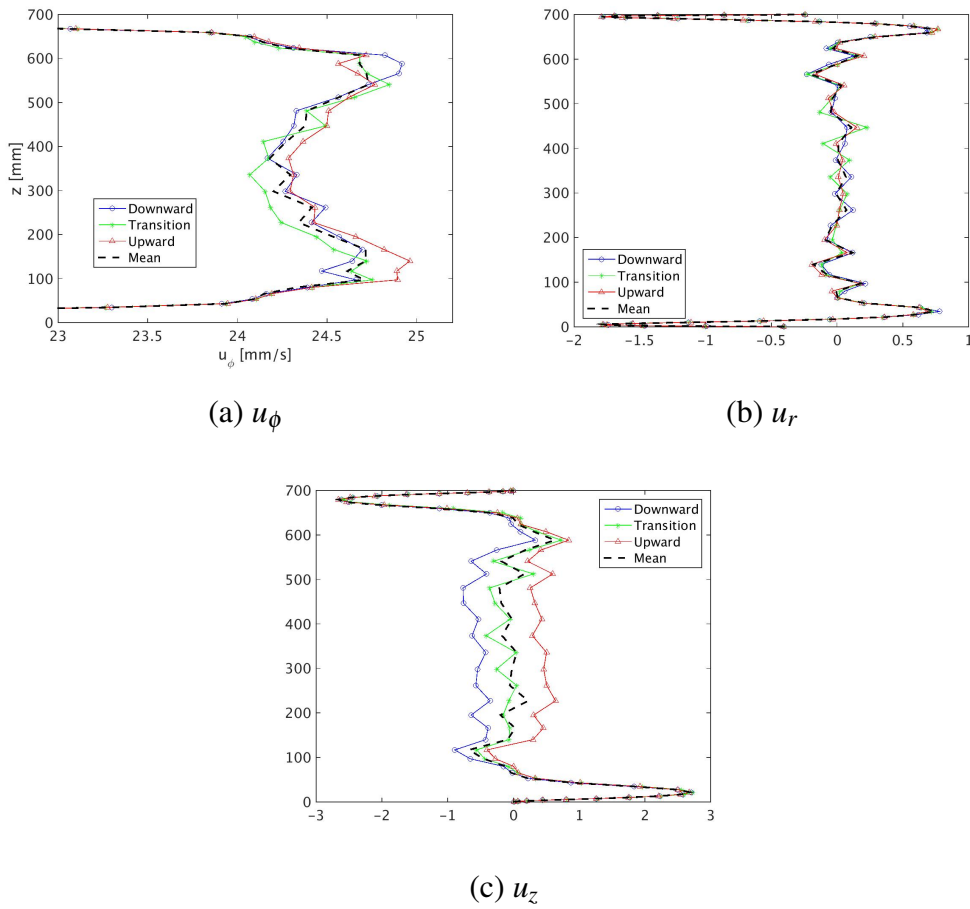


Figure 6.6: Comparison of the simulation time average axial velocity profiles with time averages taken during an upward traveling spiral period, during a downward traveling spiral period, and during the transition from an upward to a downward spiral period. The results are from numerical simulation performed with $Re = 400$, $\mu = 0.35$ and $\Delta T/\Delta z = 5.71 \text{ K m}^{-1}$ at a fixed radial position $r = r_{in} + d/2$.

the amplitude decreases. Note that the pattern changes also happen in the transition region of non-regular amplitude modulations (before 100 minutes in figure 6.1). Note also that, on average, u_ϕ and u_r velocity profiles time-averaged during the up of downward traveling spiral time windows do not vary considerably from the full averaged signal (see figure 6.6). Therefore, investigating the time evolution of the SRI, and not only its average values, is particularly relevant for a proper understanding of certain aspects of this instability. Note also that, near the top and bottom boundaries of figure 6.6(b), there is a strong radial inward flow due to the Ekman circulation. We can also observe a strong upward flow near the bottom wall, and downward near the top wall, also arising from Ekman effects (figure 6.6(c)).

The average spiral drift in the axial direction takes to travel from the bottom to the top of the cavity was compared with the period of the amplitude modulation (of approximately 50 minutes). the spiral drift was observed to be at least 10 times smaller than low-frequency modulation period. Furthermore, no clear correlation was noticed between the two periods. Therefore, since no relation was deduced, the possibility of wave reflecting on the lids to generate the amplitude

modulations was discarded. Furthermore, simulations with periodic boundary conditions at the bottom and top lids also developed amplitude modulations associated with pattern changes (see section 6.2.3.2), showing that the presence of lids is not a condition for the modulations and the pattern transitions to occur. Another possible explanation for the amplitude modulations observed in figure 6.1(b) could be a wave break process. In this case, the amplitudes of Inertia-gravity waves that lead to the SRI would grow to reach values that are large enough so that wave break would occur, dissipating the energy in a non-linear process, until reaching again a local minimum where the energy could again be extracted from the re-established base flow for the instabilities to start growing again. One argument against this possibility, when analyzing figure 6.1(b), is that more than one value of local maxima and minima amplitudes occur in the time series. As we can observe, two different values of consecutive local maxima (minima) amplitudes occur before the amplitude starts decreasing (increasing). Hence, something needs to trigger the wave break before reaching the maximum amplitude at the smaller local maximum values. Although this could still be considered as a possible mechanism for the modulations to occur, it was not yet possible to be confirmed. The influence of linear superposition of waves traveling out of phase in the cavity leading to a constructive/destructive interference pattern will be explored in sections 6.4 and 6.5.

6.1.1 Circulation cells and spiral inclination

When the SRI amplitude grows, it influences the flow circulation in the $r - z$ plane. This connects the modulations to the study of Hoffmann et al. (2009) for non-stratified TC flows with small Reynolds numbers forced additionally by an axial throughflow (with $Re_{axial} = 2$). The TC vortices with the forced axial flow exhibit shape and inclination similar to the ones observed for the SRI, and in general, travels along the axial axis in the same direction as the axial flow imposed, i.e., with the flow in the upward axial direction, the spirals exhibit an upward inclination. The TC vortices propagation described by Hoffmann et al. (2009) arises from non-linear defects. A structure qualitatively similar to the defects described by Hoffmann et al. (2009) were also observed in the numerical simulations presented in this thesis. These 'defects' in the SRI spirals can be easily observed, for instance, in the radial velocity profile, near the top lid in figure 1.2(b). In the study of Hoffmann et al. (2009), a change in the spiral inclination propagating upward occurs when the external axial flow is removed. At this moment, there is a spontaneous break of symmetry leading to a Hopf bifurcation, which implies a change to a downward inclined spiral propagating from the top to the bottom lid, similar to the changes in the SRI spiral observed. Note that the transition from stable SRI to an unstable SRI regime is also a Hopf-bifurcation (Dubrulle et al. 2004). One of the differences between the non-stratified TC flows observed by Hoffmann et al. (2009) and the SRI is that, for the SRI, no external flow in the axial direction is required for the pattern changes to occur, and the SRI spirals are naturally inclined due to the stratification.

When we evaluate time mean SRI streamlines ($\overline{\psi}$), we observe that a strong base flow establishes near the inner cylinder, and a weaker anti-clockwise circulation exists near the outer cylinder, presented in figure 6.7, where the circulation (ψ) has a positive value when moving in the clockwise direction, and a negative value when it circulates in the anti-clockwise direction. The stream function used to compute the streamlines were obtained as

$$u_r = \frac{1}{r} \frac{\partial \psi}{\partial z}, \quad u_z = -\frac{1}{r} \frac{\partial \psi}{\partial r}. \quad (6.1)$$

Note that the same qualitative results were observed when the steam functions was computed

in Cartesian coordinates using $u_r = \frac{\partial \psi}{\partial z}$ and $u_z = -\frac{\partial \psi}{\partial r}$.

Figure 6.8 shows how background circulation cells behave while the spirals travel upward, downward and during the transition, after subtracting the mean base flow (in figure 6.7) to obtain $\psi' = \psi - \bar{\psi}$. Figure 6.8(a) shows that, for a spiral traveling downward, a stronger background circulation in the clockwise direction is established near the inner cylinder, while a weaker anticlockwise circulation cell forms near the outer wall. This configuration of background circulation cells should force the spirals upwards in the region between the two circulation cells ($80\text{mm} \lesssim r \lesssim 140\text{mm}$). Since the forcing is asymmetric, the stronger circulation near the inner cylinder wall should lead to a stronger forcing near the inner wall cell, causing the spiral inclination. During the upward traveling spiral moment (figure 6.8(b)), the direction of the background circulation cells are inverted, but the circulation near the inner cylinder remains stronger than the one near the outer wall. The direction of the background circulations would now force the flow in the middle of the cavity upwards, with more intensity around the inner cylinder circulation, which also agrees with the changes in the spiral inclination observed. Snapshot of $\mathbf{v} = (u_r, u_z)$ at $\phi = 0$ during downward and upward traveling spirals moments is presented in figure 6.9(a),(b). These images show how the changes in the circulation cells are reflected in the velocity profiles. Note that the flow direction is practically inverted from figure 6.9(a) to figure 6.9(b). During spiral transition (figure 6.8(c)), no strong ψ' circulation pattern establishes in the cavity, and we see a few weak irregular elongated horizontal streamlines appearing between inner and outer cylinders. These investigations reveal that the SRI modifies the background circulation. The modified background circulation itself modifies the SRI inclination. The modified SRI inclination, again, interacts with the background circulation, in a feedback process.

The low-frequency pattern changes in the SRI spirals could therefore be interpreted as an oscillation of the system between two slightly unstable fixed points, one fixed point standing for the upward, the other for the downward spiral, associated with these asymmetric circulation cells. Furthermore, the stratification values were observed to be important for the secondary instability and the amplitude modulations to occur, as will be shown in the following section (6.2). Note that the spontaneous break of symmetries in the SRI spiral patterns happen irregularly during the transient phase (time < 100 minutes), and regularly after the modulation patterns are well established.

Note that, from figure 6.6(c), the circulation patterns observed here are associated with changes in the mean flow structure. When the spirals are traveling upward, the mean flow axial velocity travels upwards, and circulation cells have the configuration presented in figure 6.8(a). When the circulation changes directions to the configuration presented in figure 6.8(b), the mean axial velocity of the base flow is negative.

6.2 Influence of rotation, stratification, and geometry in the SRI spiral patterns

In the previous section, amplitude modulations associated with spiral pattern changes were observed numerically and experimentally for Reynolds numbers $Re = 400$ and $Re = 600$, with $\mu = 0.35$ and $\Delta T / \Delta z = 5.71 \text{ K m}^{-1}$, but several factors can change the behavior of these axial traveling spirals, as the Reynolds number, the geometrical parameter of the cavity (such as its height or gap size), and stronger or weaker stratification in the axial direction. In this section, we will investigate how changes in these parameters can influence the spiral behavior, leading to amplitude modulations or suppressing it. The evaluation of axially periodic results, with no

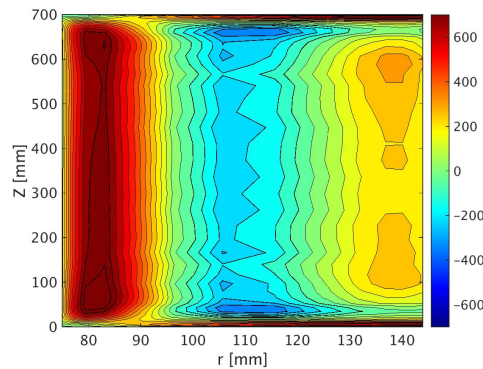


Figure 6.7: Time mean stream lines $\overline{\langle \psi \rangle}$ showing the base flow circulation for $Re = 400$, $\mu = 0.35$ and $\Delta T/\Delta z = 5.71 \text{ K m}^{-1}$. The time mean $\overline{\langle \psi \rangle}$ is obtained from u_r and u_z averaged over ϕ .

influence of Ekman effects, is also explored.

6.2.1 The role of stratification

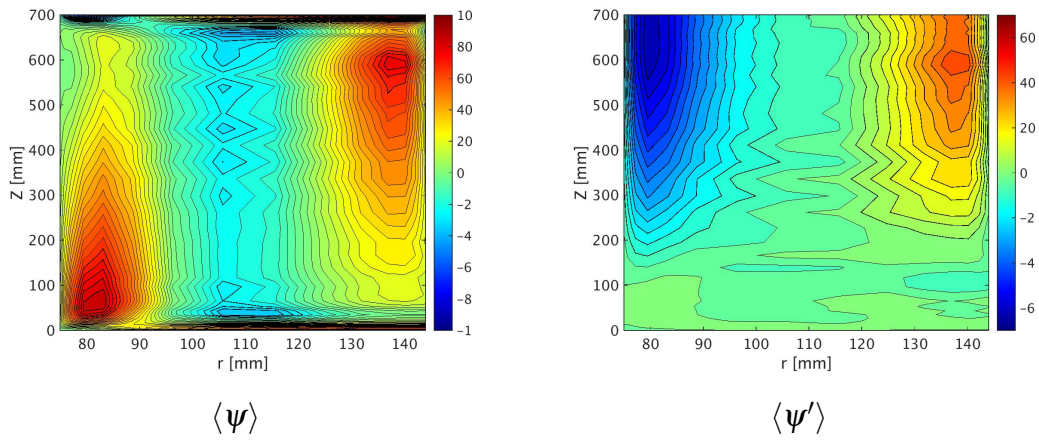
To investigate how the stratification can influence the SRI flow, different simulations were compared changing the temperature differences between top and bottom lids, keeping $Re = 400$ fixed, and the same geometrical parameters of the experimental setup ($H = 700\text{mm}$, $r_{in} = 75\text{mm}$, and $r_{out} = 145\text{mm}$). The changes in the parameters investigated are presented in table 6.1.

Case	Re	μ	H [mm]	r_{in} [mm]	r_{out} [mm]	Rn	Fr	ΔT [K]	$\frac{\Delta T}{\Delta z}$ [K m^{-1}]
01)	400	0.35	700	75	145	182.7	2.2	2	2.86
02)						258.4	1.5	4	5.71
03)						365.4	1.1	8	11.43

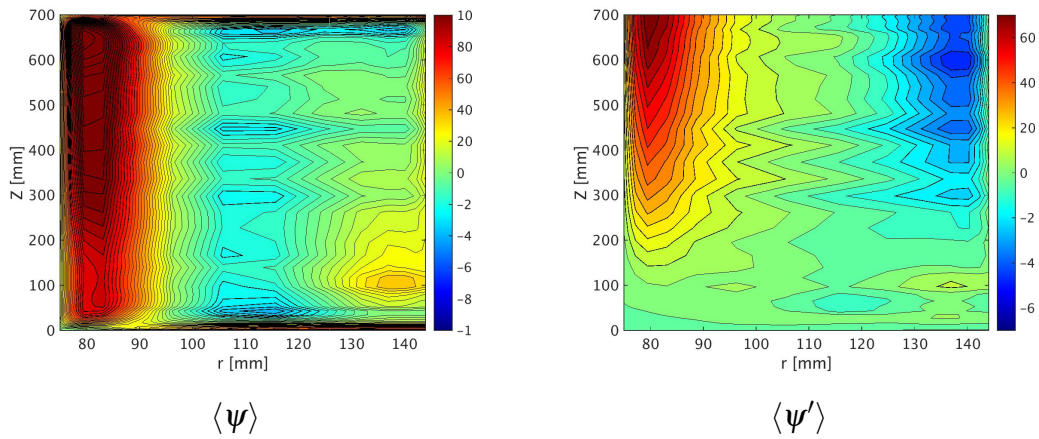
Table 6.1: Parameters of simulations changing stratification

When the axial temperature stratification is modified, we observe changes in the axial wavenumber k , as shown in figure 6.10. For the case 01 in table 6.1, with temperature differences between top and bottom walls of $\Delta T = 2\text{K}$, the flow has axial wavenumber $k = 3$. For case 02 ($\Delta T = 4\text{K}$) and case 03 ($\Delta T = 8\text{K}$), the axial wavenumbers increase respectively to $k = 4$ and $k = 7$. This shows that changes in the stratification leads to relevant changes in the spirals axial structure.

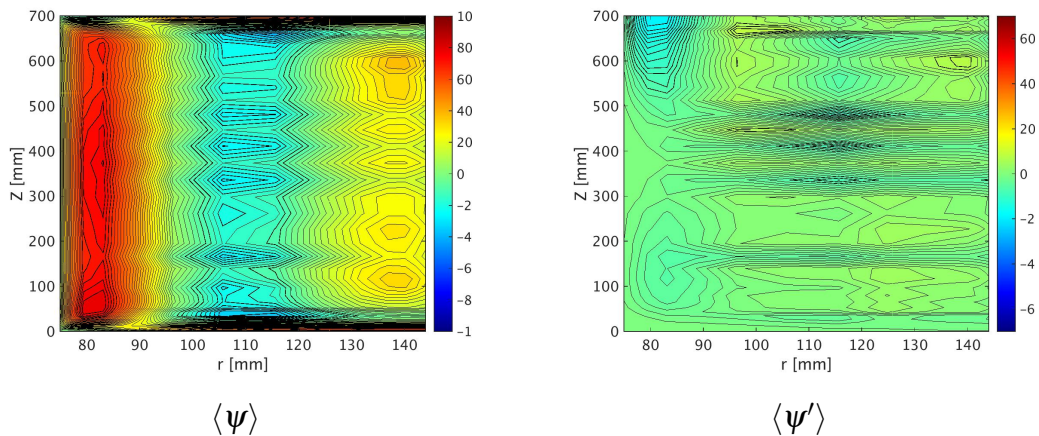
On figure 6.11(a), we see how the mean flow also changes with the stratification, reaching larger deviations from the TC profile for higher temperature differences (smaller Fr). The deviations from the TC profile (black dashed line) are similar for $\Delta T/\Delta z = 5.71 \text{ K m}^{-1}$ and $\Delta T/\Delta z = 11.43 \text{ K m}^{-1}$ (respectively cases 02 and 03 in table 6.1), but slightly higher for $\Delta T/\Delta z = 5.71 \text{ K m}^{-1}$ (case 02). The deviations from the base flow drop to approximately half its values when the stratification drops to $\Delta T/\Delta z = 2.86 \text{ K m}^{-1}$ (cases 01 in table 6.1)), indicating that more energy is transferred from the base flow to the instability when the stratification becomes stronger (smaller Fr , and larger Rn). Evaluating the impact of the stratification in the SRI time series (figure 6.11(b)-(d)), we observe that the higher energy transferred from the base flow to the instability is related to the activation of amplitude modulations. By reducing the stratification to half its value, i.e., when $\Delta T = 2\text{K}$ (case 01) instead of $\Delta T = 4\text{K}$ (case 02), keeping all the other parameters constant, the modulation vanished, although the primary SRI



(a) Downward traveling spiral



(b) Upward traveling spiral



(c) Transition

Figure 6.8: Circulation patterns obtained with stream lines $\langle \psi \rangle$ averaged over ϕ (left-hand side) and background circulation patterns $\langle \psi' \rangle = \langle \psi \rangle - \langle \psi \rangle$ (right-hand side) in $[\text{mm s}^{-2}]$. Note that the base flow $\langle \psi \rangle$ was removed from the right-hand side images for taking into account the only background circulation, excluding Ekman effects. The results are from numerical simulation performed with $Re = 400$, $\mu = 0.35$ and $\Delta T / \Delta z = 5.71 \text{ K m}^{-1}$ in the $r - Z$.

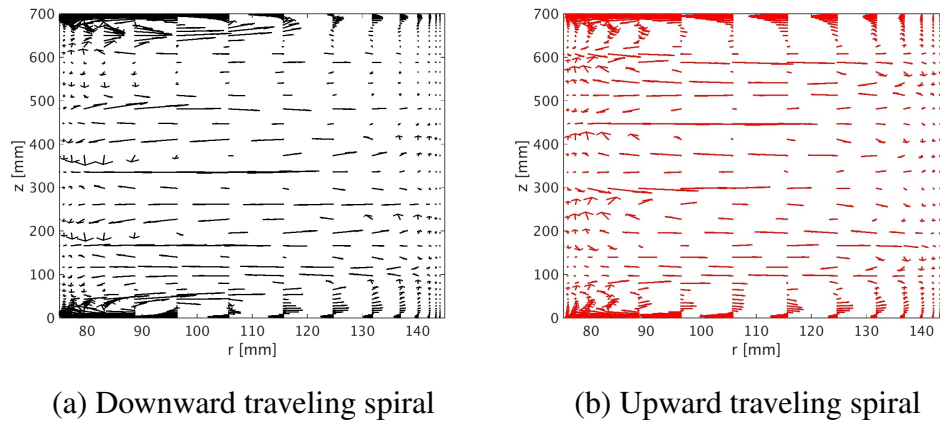


Figure 6.9: $\mathbf{v} = (u_r, u_z)$ snapshots during an upward and downward traveling spiral moment. The results are from numerical simulation performed with $Re = 400$, $\mu = 0.35$ and $\Delta T/\Delta z = 5.71 \text{ K m}^{-1}$.

instability still exists (see the SRI oscillations in the bottom right figure inside 6.11(b)). This shows that the SRI can occur without the low frequency the amplitude modulations. For an increased temperature difference of $\Delta T = 8 \text{ K}$ (case 03), the modulations are again observed (figure 6.11(d)). Note that stronger amplitude modulations are achieved for an imposed temperature difference of $\Delta T = 4 \text{ K}$ than for $\Delta T = 8 \text{ K}$. Note also that $\overline{u_\phi}$ deviations from the TC profile are also slightly larger for $\Delta T = 4 \text{ K}$ than for $\Delta T = 8 \text{ K}$ when the $\overline{u_\phi} - u_{TC} < 0$ (in the region between $85 \text{ mm} \lesssim r \lesssim 125 \text{ mm}$ on figure 6.11(a)). Values of $\Delta T \geq 10 \text{ K}$ can no longer be reached in the experimental setup. Moreover, simulations performed comparing the Boussinesq to low Mach number approximation using water as the fluid between the cavities (Raspo et al. 2018) showed that, in this case, the Boussinesq approximation would be no longer valid if $\Delta T/\Delta z$ gets too large. Therefore, values of $\Delta T/\Delta z > 11.43 \text{ K m}^{-1}$ were not investigated under the Boussinesq approximation.

6.2.2 Influence of the Reynolds numbers in the amplitude modulations

In the previous section, we saw that increasing $\Delta T/\Delta z$ values allowed more energy to be transferred from the base flow to the instability, which coincides with the appearance of the amplitude modulations. This gives the idea that the spiral propagation in the axial direction depends on Re , i.e., that a stronger stratification provides enough energy for this secondary instability to occur. That is not what we observe when keep the stratification is kept constant but the Reynolds number increase. The parameters of the simulations chosen to investigate the Reynolds number influence in the secondary instabilities are presented in table 6.2.

When the Reynolds number is increased from $Re = 400$ to $Re = 800$ (case 06 to case 08 in table 6.2), keeping $\Delta T/\Delta z$ and μ unaltered, the modulations disappear, even if the higher frequency SRI oscillations are still present. Note that the amplitude modulations are observed for the same stratification value (but smaller Re), and the amount of energy in the system for higher Re should increase since velocities are higher, leading to bigger energy input in the system. What leads to the secondary instability, then, should not the amount of rotation energy and stratification in the system, but the interaction and balance between them (rotation and stratification), allowing enough energy to be transferred from the base flow so that the spiral

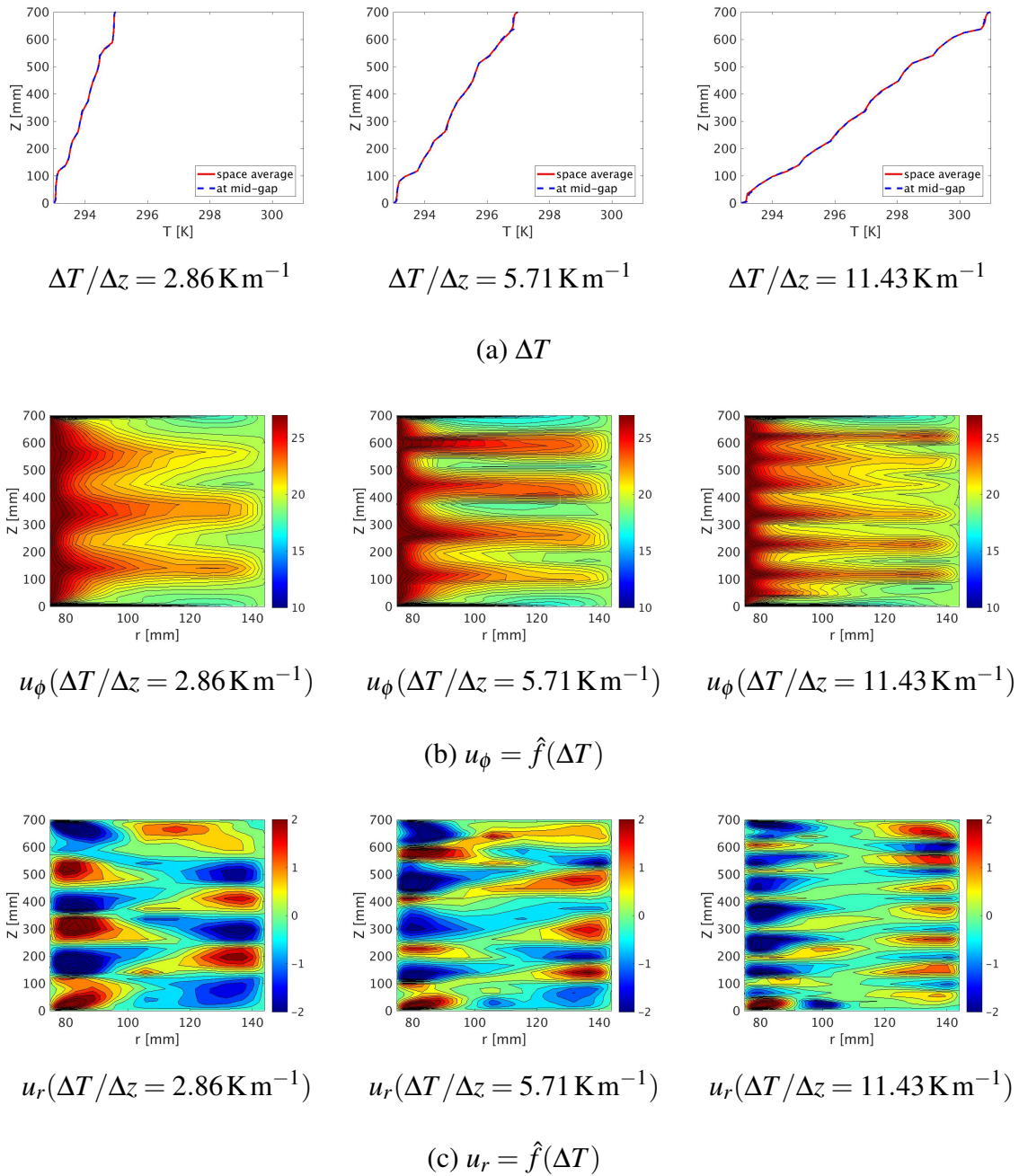


Figure 6.10: Numerical simulation snapshot showing changes in the axial wavenumber in simulations with temperatures $\Delta T/\Delta z = 2.85 \text{ K m}^{-1}$ (left-hand side), $\Delta T/\Delta z = 5.71 \text{ K m}^{-1}$ (middle images) and $\Delta T/\Delta z = 11.43 \text{ K m}^{-1}$ (right-hand side images), respectively corresponding to Froude numbers $Fr \approx 2.2$, $Fr \approx 1.5$, and $Fr \approx 1.0$. Figure (a), on top, show temperature averaged on the azimuth direction $\langle \Delta T \rangle$ for one snapshot (in full red line), and the temperature at the mid gap position $r = 110 \text{ mm}$ (in blue dashed line), highlighting the equivalence of these profiles. Figure (b), in the middle, show snapshots of u_ϕ in the radial-axial cross section. The bottom figure (c) show the snapshot of u_r in the radial-axial cross section. The parameters of the simulation are: $Re = 400$, and $\mu = 0.35$.

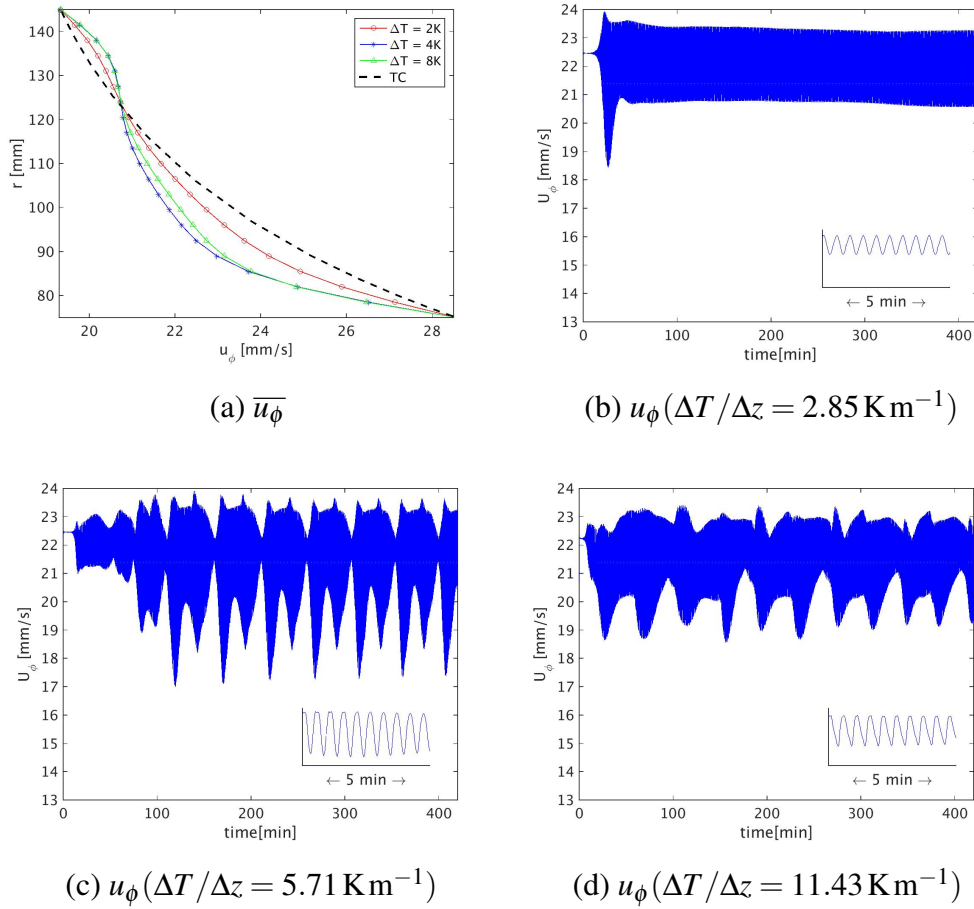


Figure 6.11: Changes in u_ϕ when different temperature gradients in the axial direction are imposed. (a) Mean velocity profiles ($\overline{u_\phi}$). (b)-(d) show the time series near the mid-gap and mid-height position ($r \approx r_{in} + d/2$ and $z \approx H/2$), highlighting changes in the low-frequency modulations with the temperature gradient. The smaller images inserted inside (b)-(d) show smaller time intervals of each respective time series (intervals where chosen arbitrarily, in regions where amplitudes do not vary much), highlighting the SRI oscillations. The velocities are presented in the laboratory frame of reference.

propagation occurs. u_ϕ SRI time series is similar for $Re = 400$ with $\Delta T/\Delta z = 2.86 \text{ K m}^{-1}$ (case 01 in table 6.1) and with $Re = 800$ and $\Delta T/\Delta z = 5.71 \text{ K m}^{-1}$ (case 08 in table 6.2). In both cases, we are near the transition between stable and unstable SRI regimes in presented in figure 1.3. These cases also present similar behavior during the transient phase, including similar periods of time before reaching the permanent regime of the secondary instability. After reaching the permanent regime, no amplitude modulations are observed in these cases, although the first SRI instability exists. Note that, in both cases, the flow is closer to the non-stratified TC flow with respect to SRI linear marginal instability curve presented in figure 1.3. This means that the unstable modes related to the secondary instabilities can be activated when we are more inside the instability diagram, and they can not be activated at regions closer to stable SRI regimes.

Case	Re	μ	H [mm]	r_{in} [mm]	r_{out} [mm]	Rn	Fr	ΔT [K]	$\frac{\Delta T}{\Delta z}$ [K m^{-1}]
05)	300	0.35	700	75	145	258.4	1.2	4	5.71
06)	400						1.5		
07)	600						2.3		
08)	800						3.1		
09)	900						3.5		

Table 6.2: Parameters of simulations changing Re

6.2.3 Cavity geometry changes

To understand how the cylinder geometry impacts the SRI and the spiral patterns observed, the cylinder height H is modified, from smaller values until an infinitely long cavity (axial periodic boundary condition). Then we will look at the influence of the cylinder walls in the SRI development, by increasing the cavity gap size d . The parameters of the simulations chosen to investigate the impact of changing the cylinder height are presented in table 6.3.

Case	Re	μ	H [mm]	r_{in} [mm]	r_{out} [mm]	Rn	Fr	$\frac{\Delta T}{\Delta z}$ [K m^{-1}]
10)	400	0.35	350	75	145	258.4	1.5	5.71
11)			700					5.71
12)			1400					5.71
13)			2800					5.71
14)			periodic					5.71
15)	periodic	11.43						

Table 6.3: Parameters of simulations changing the cylinder height

6.2.3.1 Smaller height

Figure 6.12 shows results of numerical simulations with $H = 350\text{mm}$ (case 10 in table 6.3), a cavity half as long as the experimental setup schematically presented on figure (3.1). Figure 6.12(a) presents the temperature time series at a mid-gap position ($r \approx H/2$) and at 3 different cavity heights ($z \approx H/3$, $z \approx H/2$, and $z \approx 2H/3$). Note that, as mentioned before, the SRI amplitude modulations can be equivalently observed in the temperature or in any of the 3 velocity components. It is possible to observe from the time series in 6.12(a) that, even if $\Delta T/\Delta z \approx 5.71 \text{K m}^{-1}$ and $Fr \approx 1.5$ in case 10, after a transient phase ($t \gtrsim 100\text{min}$), the first SRI instability is established, but the secondary instabilities do not develop. This results are similar to what was observed when the stratification values were reduced to $\Delta T/\Delta z \approx 2.86 \text{K m}^{-1}$ (case 01, in table 6.1, figure (6.11(b))). This behavior was also observed when Reynolds number was increased to $Re = 800$ keeping other parameters constant (case 08 in table 6.2). In this cases, once the instability was established, the spiral pattern (observed on figure 6.12(b)) did not change anymore (for the considered simulation time). This suppression of the modulations are related to the fact that larger scales of the flow can not fit in a cavity with length $H = 350\text{mm}$ (this will be better described in section 6.3). The circulation patterns established in the smaller cavities are presented in figure 6.13. Note that, the circulation at a given time, presented in figure 6.13(a), is almost the same as its time average $\bar{\psi}$, presented in figure 6.13(b). This occurs because strong background circulation can no longer establish and change the spiral inclination

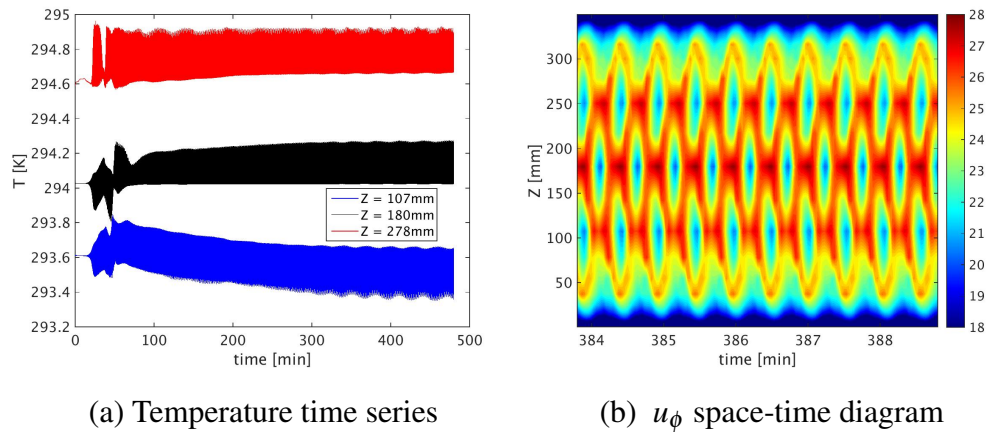


Figure 6.12: Simulation with $Re = 400$, $\mu = 0.35$, $\Delta T/\Delta z \approx 5.71 \text{ K m}^{-1}$ and cylinder's height half of the experimental height $H = 0.35m$ (case 10 in table 6.3). (a) Temperature time series obtained at mid-gap region $r \approx r_{in} + d/3$ and in 3 different axial positions; (b) u_ϕ space-time diagram at $r \approx r_{in} + d/3$ showing the standing chessboard pattern achieved when the secondary instability is not reached.

and axial propagation. The intensity of the fluctuation circulation (ψ') observed at cavities with $H = 350mm$ (case 10) is more than 50 times smaller than the base flow circulation presented in figure 6.13(b).

When the temperature time series of the simulation with $H = 350mm$ is observed (case 10) on figure 6.12(a), we notice that one strong amplitude oscillation occur during a transient regime, for $35 \lesssim t \lesssim 50$ minutes. On figure 6.14(a), u_ϕ time series at $r \approx r_{in} + d/3$ and $z \approx H/2$ is presented for a time interval between $0 \leq t \leq 85$ minutes, highlighting the transient region where a strong amplitude modulation occurs. Figure 6.14(b)-(d) shows in u_r space-time diagrams how the spiral patterns are different before (figure 6.14(c)) and after (figure 6.14(d)) the amplitude modulation, when it achieves the permanent regime. Note that on figures 6.12 and 6.14, the modulation patterns in temperature, in T , u_ϕ and in u_r , to indicate how the modulations impact any of those parameters. The presence of this one modulation during the amplitude transient phase shows that they are not necessarily forbidden in smaller cavities, but that the activation of the spiral propagation does not occur during the permanent regime.

6.2.3.2 Larger cavity heights

Differently from the cavity with reduced length, when the cylinder's height becomes larger than $H = 700mm$, amplitude modulations once again re-appear. Figure 6.15(a),(b) show u_ϕ time series at $r \approx r_{in} + d/3$ and $z \approx H/2$ respectively to cylinders lengths $2 \times$ ($H = 1400mm$) and $4 \times$ ($H = 2800mm$) larger than the experimental setup height (cases 12 and 13 in table 6.3 respectively). Note that the amplitude modulations become less regular in both time series (6.15(a),(b)), and the associated spiral patterns (figure 6.15(c)-(f)) also exhibit more complicated behavior than those observed for a $H = 700mm$ cavity, with different spiral inclinations existing along the cavities' axial direction. The comparison between different time intervals selected in the space-time diagrams in figures 6.15(c)-(f) clearly shows that changes in the spiral patterns occur. The pattern changes observed are also associated with the more irregular amplitude modulations observed on figures 6.15(a),(b).

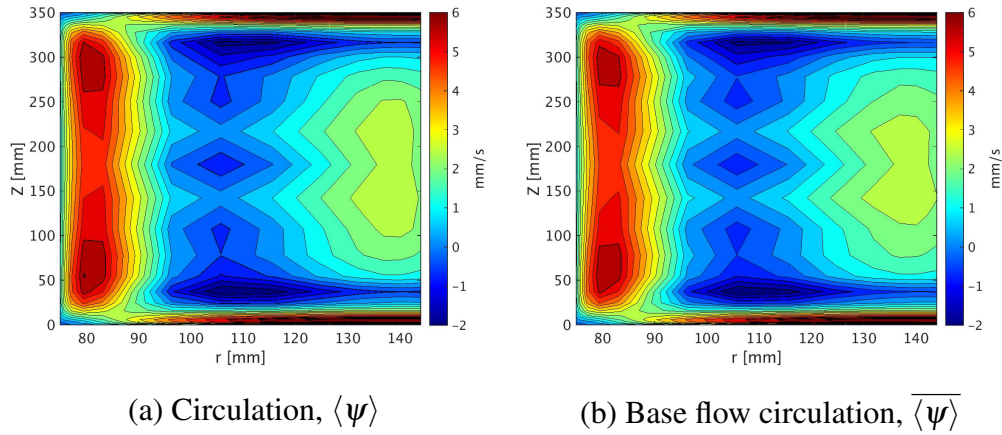


Figure 6.13: Stream lines comparing the base flow circulation to the circulation at a given time, averaged on the azimuthal direction. The simulations are performed with half experimental height ($H/2$) and $Re = 400$, $\mu = 0.35$ and $\Delta T/\Delta z = 5.71 \text{ K m}^{-1}$ (case 10 in table 6.3). Note that base flow circulation and instantaneous circulation are almost the same.

To study the flow in "infinitely long cavities", axially periodic simulations were performed. These are relevant for different reasons, including that many studies investigating the SRI analytically considering infinitely long cylinders (Dubrulle et al. 2004, Dizès and Riedinger 2010, Rüdiger et al. 2017). Note that axially periodic boundary conditions are not necessarily equivalent to infinitely long cavities, but it removes the boundary layer influence on the SRI and amplitude modulations development, showing if Ekman effects could be responsible for the modulations to occur. Furthermore, periodic boundary conditions can also eliminate the possibility of waves and spiral reflections at the top and bottom boundaries leading to the upward and downward traveling spirals, although it is not likely that this is the mechanism to change the spirals propagation direction, since the time scale of the spiral drift traveling from bottom to top lid (and vice-versa) is far smaller than the amplitude modulations observed, and they have no clear relation, as mentioned previously in section 6.1.

Figure 6.16 presents u_ϕ time series obtained from axially periodic numerical simulations with $Re = 400$, $\mu = 0.35$, and different stratification values in 6.16(a) $\Delta T/\Delta z \approx 5.71 \text{ K m}^{-1}$ (case 14 in table 6.3); and 6.16(b) with $\Delta T/\Delta z \approx 11.43 \text{ K m}^{-1}$ (case 15 in table 6.3). The simulations show that the flow is still unstable when the top and bottom boundaries are removed, and irregular amplitude modulations are still observed in the temporal velocity behavior. Although amplitude modulations are still observed for the axially periodic simulations with both $\Delta T/\Delta z$ imposed (in figure 6.16), we do not observe similar behavior in their spiral patterns. Figure 6.17 shows that the space-time pattern of the axial periodic simulations with $\Delta T/\Delta z \approx 5.71 \text{ K m}^{-1}$ (case 14 in table 6.3). When the axial periodic simulations were initialized without the top and bottom boundaries, and with $\Delta T/\Delta z \approx 5.71 \text{ K m}^{-1}$, an upward spiral pattern was activated, and no changes in the propagation direction was observed after 8 hours of simulations, i.e., the pattern observed in figure 6.17(a) was never altered once established. To evaluate if a preferential spiral direction was being selected by the stable stratification forcing, another simulation starting from a downward traveling spiral solution was performed. The simulation, in this case, used as initial conditions the results obtained from the top and bottom bounded solution (case 11 in table 6.3), at the moment when the spiral was traveling in the downward axial direction. With

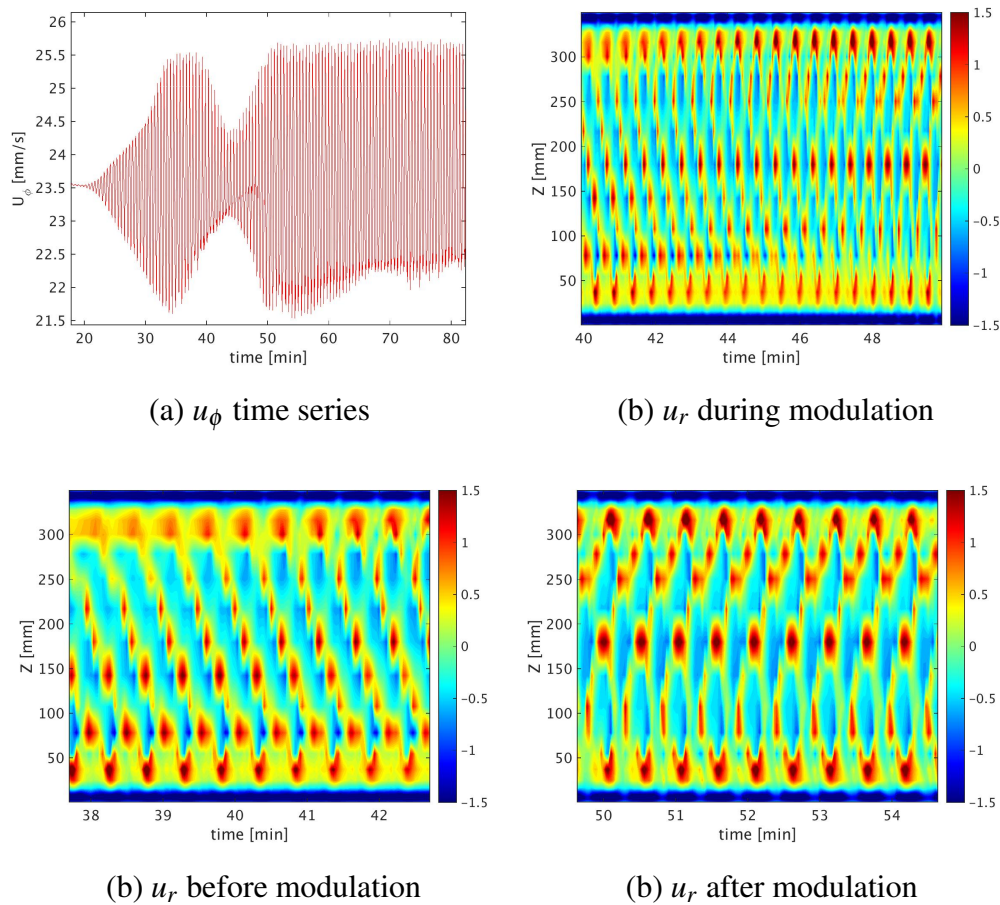


Figure 6.14: Space-time diagram with $Re = 400$, $\mu = 0.35$, $\Delta T/\Delta z \approx 5.71 \text{ K m}^{-1}$ and height $H = 0.35 \text{ m}$ (half of the experimental cavity). The x-axis show time in minutes, and the y-axis shows the axial direction (z). (a) u_ϕ time series obtained closer to the inner cylinder (at $r \approx r_{in} + d/3$) and at an axial position $z \approx H/3$. (b)-(d) u_r space-time diagrams on different time intervals.

this downward initial forcing, the downward traveling spiral presented in figure 6.17(b) does not change to an upward traveling regime. This shows that no preferential direction of propagation is selected in unbounded systems, i.e., the spiral continued to travel in the direction it started propagating. Note that this is a different regime than those observed in the chessboard pattern of the previous non-modulated cases. In figure 6.17, the spirals are propagating in the axial direction instead of standing.

When the temperature gradient increases from $\Delta T/\Delta z \approx 5.71 \text{ K m}^{-1}$ to $\Delta T/\Delta z \approx 11.43 \text{ K m}^{-1}$ (change from case 14 to case 15 in table 6.3), spiral pattern changes are again observed, shown in figure 6.18. The pattern changes are again related to the amplitude modulations in figure 6.16(b). These axially periodic results demonstrate that the base flow and secondary instabilities associated with amplitude modulations do not depend on the top and bottom boundaries to exist. They also show that modulations and pattern changes do not result from Ekman pumping effects, since it also occurs without the presence of the lids.

Although top and bottom boundaries do not lead to the modulations, they do have an impact on the spiral propagation phenomenon, since stronger stratification is necessary for the spiral

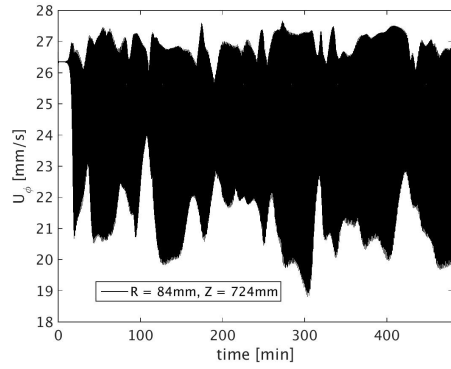
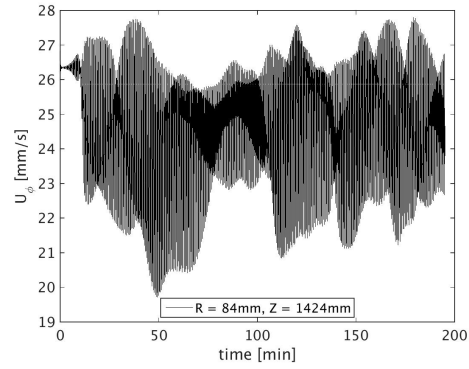
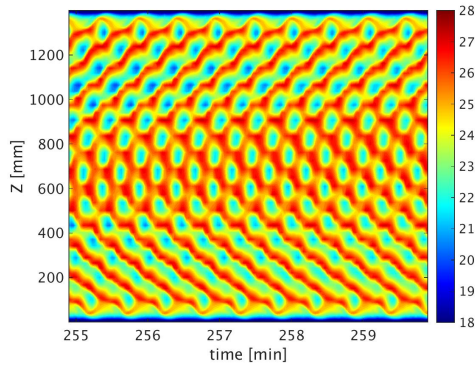
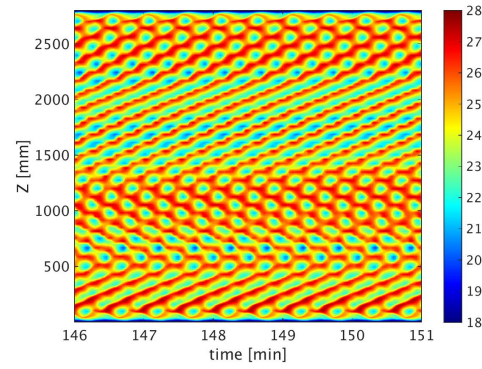
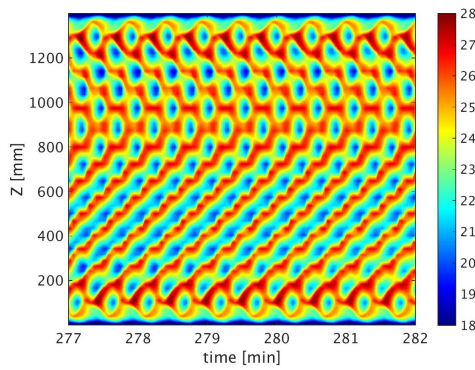
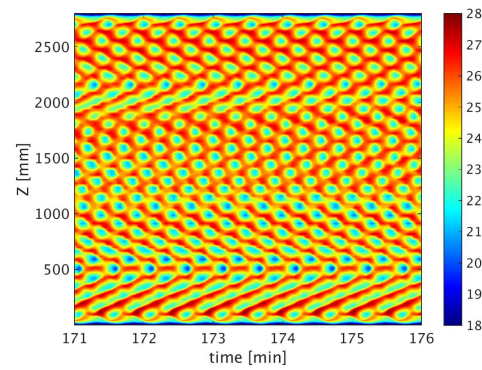
(a) $H = 1400\text{mm}$, time series(b) $H = 2800\text{mm}$, time series(c) $H = 1400\text{mm}$, interval 01(d) $H = 2800\text{mm}$, interval 01(e) $H = 1400\text{mm}$, interval 02(f) $H = 2800\text{mm}$, interval 02

Figure 6.15: u_ϕ numerical simulations for cavities with large heights (H) compared to the experimental setup at $r \approx r_{in} + d/3$, with $\mu = 0.35$ and $\Delta T/\Delta z \approx 5.71 \text{ K m}^{-1}$ (a) time series at $z \approx H/2$ for $H = 1400\text{mm}$ (b) time series at $z \approx H/2$ for $H = 2800\text{mm}$ (c)-(f) Space-time diagrams at different time intervals showing the occurrence of different spiral patters in time.

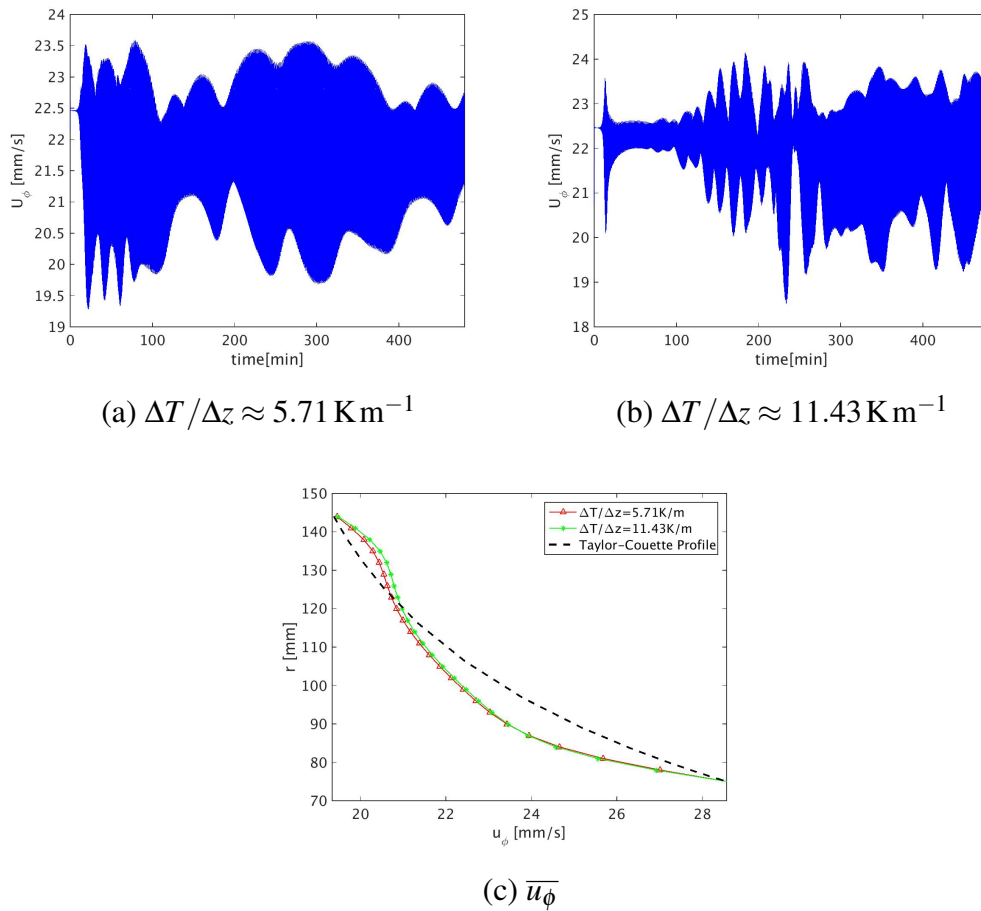


Figure 6.16: u_ϕ numerical simulations with $Re = 400$, $\mu = 0.35$ and periodic solutions in the axial direction z ($\Delta z \rightarrow \infty$) (a) Time series obtained at $r \approx r_{in} + d/2$ and $z \approx H/2$ with temperature gradient $\Delta T/\Delta z \approx 5.71 \text{ K m}^{-1}$ (case 14 in table 6.3); (b) Time series obtained at $r \approx r_{in} + d/2$ and $z \approx H/2$ with temperature gradient $\Delta T/\Delta z \approx 11.43 \text{ K m}^{-1}$ (case 15 in table 6.3); (c) Mean flow ($\overline{u_\phi}$) comparison of the axial periodic simulations with $\Delta T/\Delta z \approx 5.71 \text{ K m}^{-1}$ and $\Delta T/\Delta z \approx 11.43 \text{ K m}^{-1}$ with the non-stratified TC profile (black dashed line).

to change its pattern. The reason for this is still unclear, since the energy transferred from the mean flow is practically the same for axial periodic simulations (cases 14 and 15 in table 6.3) with both $\Delta T/\Delta z$ values imposed (see figure 6.16(c)). Note that the deviations from the mean flow in axially periodic simulations are smaller than the differences observed in top and bottom bounded systems with $H = 700 \text{ mm}$ (case 11 in table 6.3), but larger than the differences obtained in simulations with $H = 350 \text{ mm}$ (case 10 in table 6.3).

6.2.3.3 Wide gap and critical layer position

Simulations performed with increased gap size are intended to contribute to the discussion about the importance of a rigid boundary for the SRI to exist, or if critical layers could be activated and generate the instabilities without the need of a rigid outer cylinder wall. The idea to verify if a rigid outer boundary is relevant for the SRI development was simply to increase $d = r_{out} - r_{in}$, and to observe if this would lead to the suppression of the instability. The parameters of the

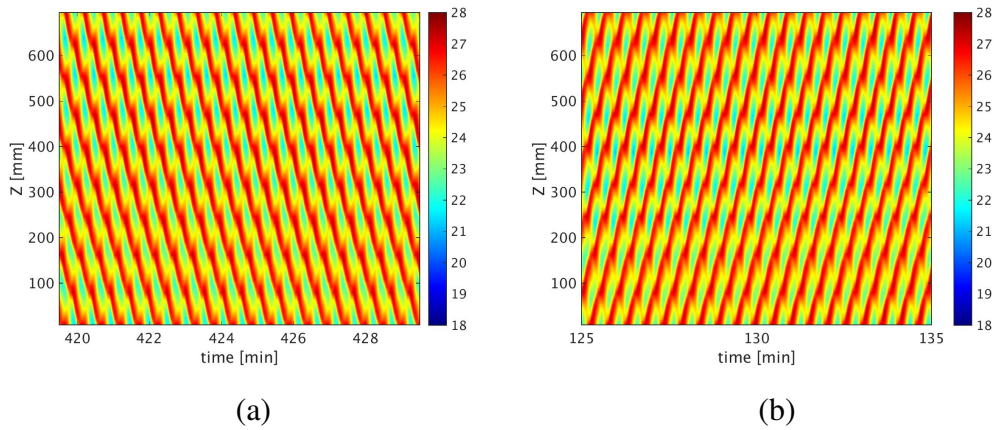


Figure 6.17: u_ϕ space-time diagram with $Re = 400$, $\mu = 0.35$, $\Delta T/\Delta z \approx 5.71 \text{ K m}^{-1}$ and periodic boundary conditions in the axial direction. The x-axis show time in minutes, and the y-axis shows the axial direction. (a) Simulation starting from the initial condition described on chapter 4. (b) Simulation using as initial conditions a downward travelling spiral obtained from a bounded top and bottom lids simulation.

simulations performed to investigate the impact of a larger gap width in the SRI are presented in table 6.4.

Case	Re	μ	H [mm]	r_{in} [mm]	r_{out} [mm]	d [mm]	Rn	Fr	$\frac{\Delta T}{\Delta z}$ [K m^{-1}]
16)	400	0.35	700	75	145	70	258.4	1.5	5.71
17)					170	95			5.71
18)					180	105			5.71
19)					180	105			11.43
20)					290	215			11.43

Table 6.4: Parameters of simulations changing the gap width

The critical layers to be considered are the traditional critical layer and the baroclinic critical layers. The traditional critical layer occurs when $u_\phi = \omega/m$, where $c = \omega/m$ is the drift velocity, which consists on the wave frequency ω divided by the azimuthal wavenumber m . The baroclinic critical layers occur when $u_\phi = \omega/m \pm N/m$, where m in the buoyancy frequency. Figure 6.19 shows the the critical layer position for a numerical simulation with $Re = 400$, $\mu = 0.35$, and considering our experimental configuration (case 16 in table 6.4) at a given time. Considering the first mode $m = 1$, the traditional critical layer position in figure 6.19 is found slightly below the mid gap position (at $r \approx 106\text{mm}$). The velocity profile (blue curve in figure 6.19(a)) is averaged in the azimuthal direction. The drift velocity is shown as a dashed line in figure 6.19(a), and the full straight red lines represent the curves $c/m \pm N/m$. In figure 6.19(b), the critical layer's position is displayed together with streamlines ψ at a given time, showing the circulation patterns. Figure 6.19(c) shows the background circulation pattern when the mean circulation is subtracted by the instantaneous circulation. Note that, qualitatively, the classical critical layer position seems to play an important role in the process of generating vortices and internal waves in the fluid, since its position coincides with the propagation of disturbances in the circulations in 6.19(a). Note also that this influence seems to be impacting the

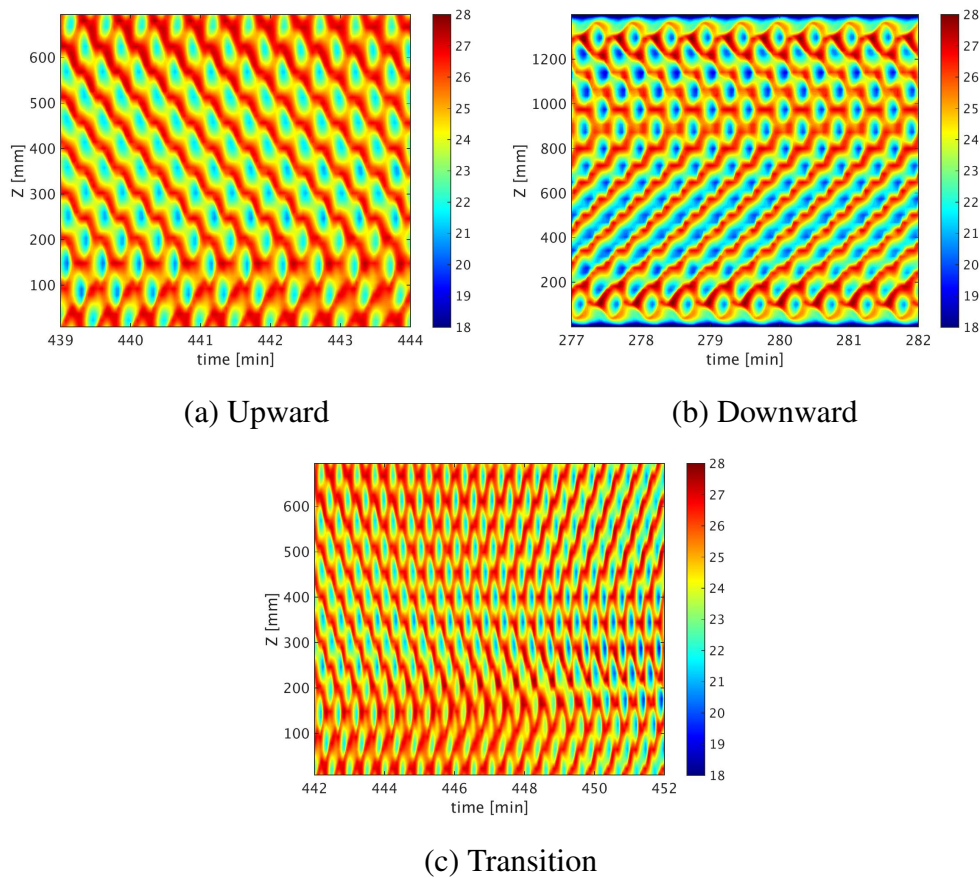


Figure 6.18: u_ϕ space-time diagram with $Re = 400$, $\mu = 0.35$, $\Delta T/\Delta z \approx 11.43 \text{ K m}^{-1}$ and periodic boundary conditions in the axial direction at different time intervals, revealing changes in the spiral pattern in time. (a) Upward spiral propagation; (b) Downward spiral propagation; (c) Transition from an upward to a downward spiral propagation.

base flow, as these waves emissions are not seen in the perturbation circulation in figure 6.19(c). This is an indication that the base flow may be interacting with the traditional and baroclinic boundary layers to generate the instabilities observed. The baroclinic critical layers also seem to be interacting with the circulation cells, since they seem to be confined between these critical layers and cylinder walls. Therefore, the effect of the baroclinic critical layers seems to affect both the base flow and the perturbation. Naturally, since this is a qualitative observation, further investigations are necessary for a more conclusive understanding of the impact of the critical layer in the SRI development.

The impact of the outer cylinder wall in the SRI development is investigated as the circulations seem to be confined between the walls and the baroclinic critical layer. To do so, the inner cylinder radius $r_{in} = 75 \text{ mm}$ was kept unchanged, and the outer radius was increased ($r_{out} > 145 \text{ mm}$) (see table 6.4), keeping other parameters constant. A suppression of the SRI was observed when an outer cylinder radius of $r_{out} = 180 \text{ mm}$ was reached (case 18 in table 6.4), as shown in figure 6.20(b). Note that, in this case, small oscillations occur at the very beginning of the simulations, but they soon vanish into a stable flow and do not develop the SRI oscillations after more than 3 hours of simulations evaluated.

Although increasing the external radius to $r_{out} \geq 180 \text{ mm}$ led to stable SRI flows, when the

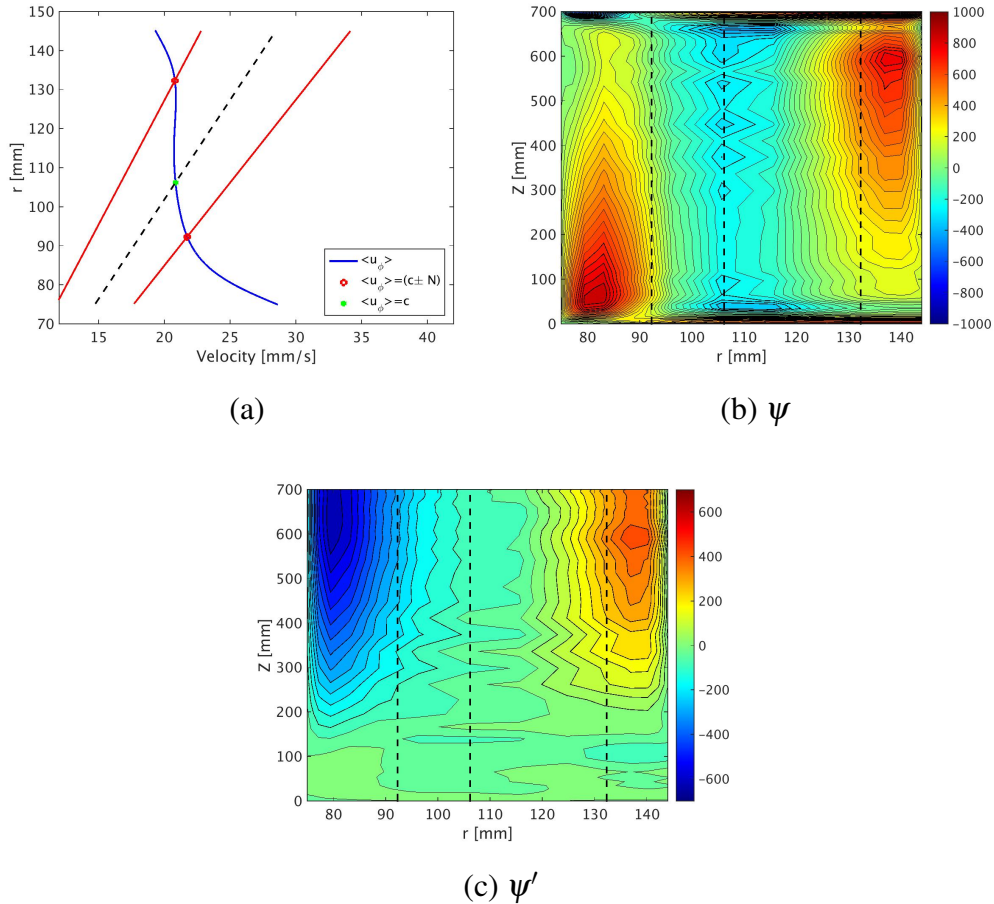


Figure 6.19: Critical layers position for the mode $m = 1$, when the mean flow velocity equals the drift speed ($\langle u_\phi \rangle = \omega/m$) and $\langle u_\phi \rangle = \omega/m \pm N/m$. The simulation was performed with $Re = 400$, $\mu = 0.35$, and the experimental geometry (case 16 in table 6.4). (a) Presents $\langle u_\phi \rangle$ space averaged in ϕ (blue curve). The dashed black line shows the drift speed $c = \omega/m$, and the red lines show $c \pm N/m$. The intersection of the curves with the mean flow are the critical layer positions. (b),(c) Present the circulation of the flow at a given time, and the radial position of the critical layers as vertical dashed lines. The dashed vertical line in the middle represents the classical critical layer, where $\langle u_\phi \rangle = \omega/m$, and the other two dashed vertical lines represents the radial position where $\langle u_\phi \rangle = c \pm N/m$. (b) shows the instantaneous circulation at a given time; and (c) Shows the fluctuation circulation ψ' .

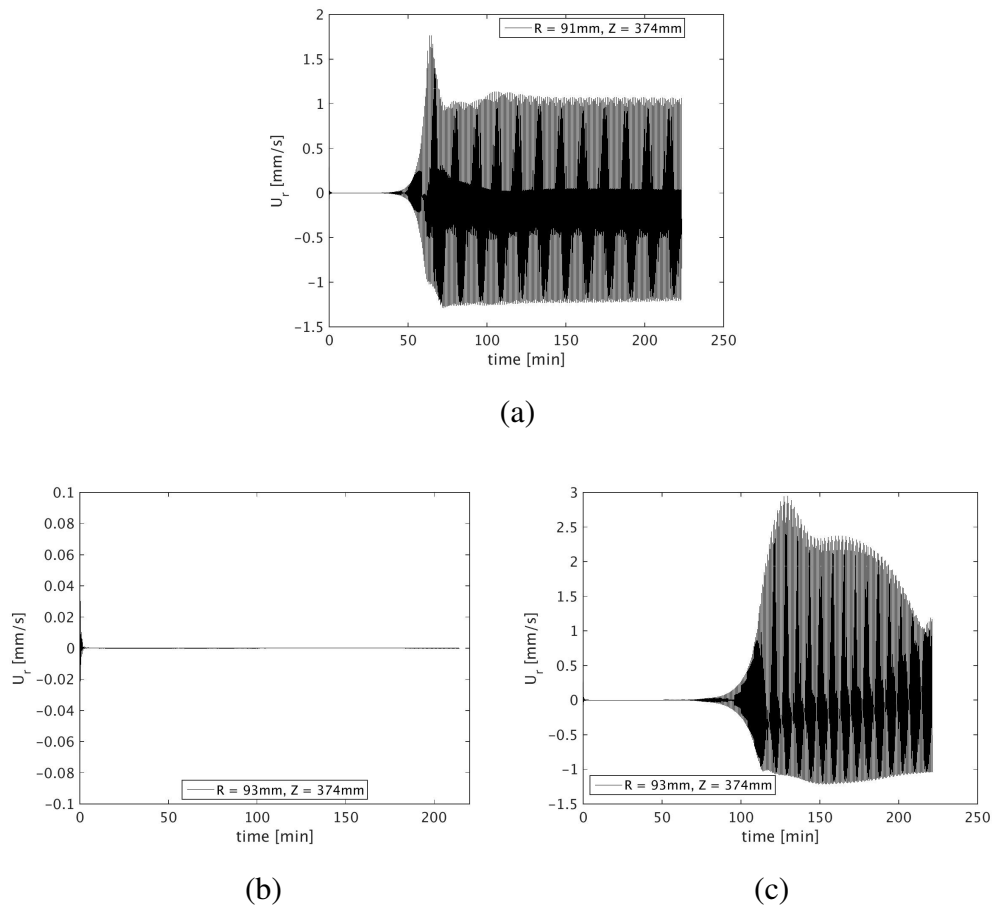


Figure 6.20: u_r time series at $r \approx 90\text{mm}$ and $z \approx H/2$, with $Re = 400$, $\mu = 0.35$, and height $H = 700\text{mm}$, for different values of $d = r_{out} - r_{in}$, obtained by changing the outer radii and maintaining $r_{in} = 75\text{mm}$. (a) $r_{out} = 170\text{mm}$, $\Delta T/\Delta z = 5.71\text{K m}^{-1}$; (b) $r_{out} = 180\text{mm}$, $\Delta T/\Delta z = 5.71\text{K m}^{-1}$; (c) $r_{out} = 180\text{mm}$, $\Delta T/\Delta z = 11.43\text{K m}^{-1}$.

stratification was increased from $\Delta T/\Delta z = 5.71\text{K m}^{-1}$ to $\Delta T/\Delta z = 11.43\text{K m}^{-1}$ (from case 18 to case 19 in table 6.4), the SRI oscillations were again observed (figure 6.20(c)). Note that early amplitude modulations in the velocity profile also start to develop in figure 6.20(c). These results are different for those observed by Rüdiger and Shalybkov (2009) related to linear analysis of the SRI, where a wider gap demanded a rather weak stratification to support the SRI, but it agrees with their results when variations in the Froude number lead to a stable SRI solution. Note that, the changes in r_{out} led to a delay in the instability development. Note also that the evaluation presented here takes into account the influence of non-linearities in the simulations, differently from Rüdiger and Shalybkov (2009). Simulations with the experimental gap-size $d = 70\text{mm}$ (case 16 in table 6.4) fully developed SRI oscillations in $t \approx 10$ minutes. Simulations with $d = 95\text{mm}$ (case 17 in table 6.4) develops the SRI only after $t > 50$ minutes (figure 6.20(a)). And when $d = 105$ and $\Delta T/\Delta z = 11.43\text{K m}^{-1}$ (case 19), the time necessary for the first SRI oscillations to occur increases to $t > 100$ minutes (figure 6.20(c)). Therefore, it is not possible to say from this investigation if for case 19 (figure 6.20) the instability is suppressed, or if it will develop at a later time. Note that, when the outer cylinder wall was increased to $r_{out} = 290\text{mm}$ keeping the higher $\Delta T/\Delta z = 11.43\text{K m}^{-1}$ (case 20), the SRI oscillations were

once again suppressed. Therefore, it was not possible to conclude from this simple qualitative investigation if the SRI will no longer occur in larger gap widths, or simply if its development will be delayed, but it is possible to conclude that the presence of the outer wall can affect the SRI development. A more complete study of the SRI parameters would be important to obtain a better understanding of the outer cylinder wall and on critical layer influences in the development of these instabilities.

6.3 Energy spectra

In section 6.2, we evaluated how stratification, the Reynolds number, and the cylinder geometry changes the SRI structure and leads to amplitude modulations (or to its suppression). It was possible to observe that the pattern changes are related to a higher deviation of mean azimuthal velocity ($\overline{u_\phi}$) from non-stratified TC profiles, considering the comparison of the TC velocity profile (u_{TC}) and the SRI velocity profile when the first and second instabilities occur. Larger deviations from the TC profile occur when the secondary instability establishes, compared to cases where only the first instability occurs, showing that more energy is transferred from the base flow. In this section, we will study how the kinetic energy spectra are modified by the different parameters addressed in section 6.2.

The energy spectra are here considered in different spatial directions. To obtain each spectrum, the Fourier transform of the velocity components is computed in each space direction (equivalent to the spectra of the velocity fluctuations u'_ϕ , u'_r , and u'_z). The energy spectra are then computed as

$$\begin{aligned} E_\phi &= \frac{1}{2}\rho \left(C_\phi(u_\phi)C_\phi^*(u_\phi) + C_\phi(u_r)C_\phi^*(u_r) + C_\phi(u_z)C_\phi^*(u_z) \right) d\phi d\phi, \\ E_r &= \frac{1}{2}\rho \left(C_r(u_\phi)C_r^*(u_\phi) + C_r(u_r)C_r^*(u_r) + C_r(u_z)C_r^*(u_z) \right) dr dr, \\ E_z &= \frac{1}{2}\rho \left(C_z(u_\phi)C_z^*(u_\phi) + C_z(u_r)C_z^*(u_r) + C_z(u_z)C_z^*(u_z) \right) dz dz, \end{aligned} \quad (6.2)$$

where $C_\phi(u_\xi)$, $C_r(u_\xi)$ and $C_z(u_\xi)$ are the fast Fourier transform of $u_\xi = u_\phi$, u_r , and u_z , with the sub-index indicating respectively the space directions $\xi = \phi$, r , and z , and C_ξ^* is the complex conjugate. In equation (6.2), $d\phi$, dr , and dz are the space resolution respectively in the azimuth, radial and axial directions. Three different energy spectra are then obtained as function of the wavenumber $K = m, l, k$: one for the azimuthal, another for the radial, and a third one for the axial direction, respectively called E_ϕ , E_r , and E_z , keeping fixed the other 2 space coordinates. The spectra in the azimuth direction (E_ϕ) were computed at fixed radial and axial position $r \approx r_{in} + d/2$ and $z \approx H/2$. In the radial direction, E_r was computed for fixed $\phi = 0$ and $z \approx H/2$, and in the axial direction, $\phi = 0$ and $r \approx r_{in} + d/2$ are fix. The power density spectra presented in this section are computed at each time step, and then temporally averaged. Additionally, the transition region of the amplitude modulation was not taken into account. Figure 6.21 shows E_ϕ , E_r and E_z for simulations with $\mu = 0.35$, $\Delta T/\Delta z \approx 5.71 \text{ K m}^{-1}$. Figure 6.21(a) corresponds to $Re = 400$ (case 06 in table 6.2) and figure 6.21(b) to $Re = 800$ (case 08 in table 6.2), with power laws fitting the inertial region of the energy spectra in dashed lines. Note that in the case presented in figure 6.21(a) the flow develops amplitude modulations, while the case presented in figure 6.21(b) is simply SRI unstable.

On figure 6.21 we observe different slopes in E_z with $Re = 400$, that has a decay rate proportional to a power law k^{-3} , and on figure 6.21(b) with $Re = 800$, a power law with decay rate

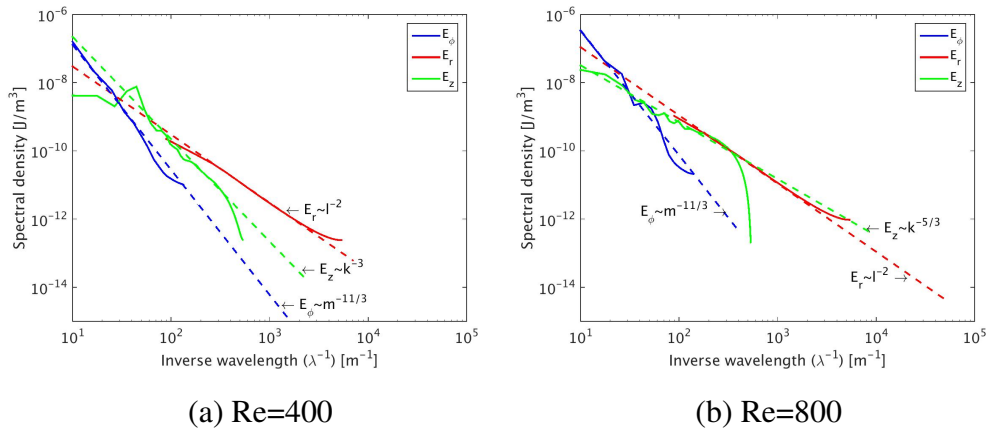


Figure 6.21: Energy spectra in the azimuthal (E_ϕ), radial (E_r) and axial (E_z) directions with different power laws fitting the energy transfer region of the spectra presented in dashed lines. The spectra were obtained from simulations with $\mu = 0.35$ and $\Delta T = 4K$, and bounded cavity height $H = 700mm$ (same geometry as the experimental setup). Figure (a) presents a $Re = 400$ simulation where amplitude modulations and pattern changes are observed (case 02 in table 6.1); (b) shows a simulation with $Re = 800$, where no pattern changes or amplitude modulations occur (case 08 in table 6.2).

$-5/3$. An energy spectrum (E_z) with power-law -3 was observed on vertical measurements of the atmosphere performed by Dewan and Good (1986), Cot (2001) and was confirmed by numerical simulations of strongly stratified fluids by Lindborg (2006). A k^{-3} spectrum decay is interpreted as occurring on enstrophic cascades (Charney 1971, Nastrom and Gage 1985), which transfers energy from larger to smaller scales in quasi-geostrophic turbulence. In these cases, the spectrum may also allow an inverse cascade, i.e., the energy transfer from smaller to the larger scales. For the case with higher Reynolds number and no amplitude modulation ($Re = 800$) in figure 6.21(b), a $k^{-5/3}$ power-law fits the E_z decay rate, similar to three-dimensional isotropic Kolmogorov turbulence spectra (Pope 2001, Dubrulle 2019). This means that, compared to the -3 power law, the energy transfer within the fluid is driven by shear, and the stronger anisotropies imposed by stratification become less important.

The power spectra in the radial direction on figures 6.21 (E_r), have slope with a decay rate proportional to l^{-2} . This is the same slope observed by ocean measurements performed by Garrett and Munk (1972, 1975), related to a random superposition of linear internal waves (i.e., that exist between the inertial frequency f and the buoyancy frequency N) known as the Garrett and Munk (GM) model, or related to a weakly nonlinear wave turbulence (Lvov et al. 2004, Allen and Joseph 1989). Note that, although the GM spectra decay rate of l^{-2} and the Kolmogorov slope of $l^{-5/3}$ are similar, the $l^{-5/3}$ slope fits very poorly the E_r slope.

A power law $m^{-11/3}$ fits well the slope measured in E_ϕ on figures 6.21(a),(b). This decay has already been associated with different phenomena, such as the influence of potential energy available in turbulent diffusion of quasi-geostrophic cascades (Smith et al. 2002), or with Kelvin waves propagating along a vortex line (Lvov and Nazarenko 2010). Curiously, in an astrophysics context, $m^{-11/3}$ power law was measured over a broad length-scale domain in energy spectra of diffuse molecular clouds surrounding young stars, where turbulent pressure largely exceeds the system's thermal pressure (Falgarone et al. 2011). These astrophysical observations

were performed in the North Celestial Pole loop, which has a cylindrical gap morphology, with a cylindrical radial velocity profile fitting its radial expansion (Meyerdierks et al. 1991).

The power laws that fit the energy decay in E_ϕ and E_r do not change when we compare figures 6.21(a) and (b), i.e., no changes in their decay rates are observed. On figures 6.22, we can see that no relevant changes in E_ϕ and E_r were observed for changes in any of the different parameters investigated in section 6.2, i.e., from numerical simulations with different Reynolds number (top images), with different stratifications (different ΔT and Rn) in the middle images, and for different cavity heights H (bottom images). For E_r , the SRI spectra were also confronted with the stable TC spectrum with $Re = 400$, $\mu = 0.35$, $H = 700$ mm and $\Delta T = 0$ K (right hand side images on 6.22). This comparison shows that stratification slightly reduces the energy in large scales compared to the non-stratified flow in the radial spectra (E_r). The differences are small but systematically observed in all experiments. For mid and larger wavenumbers (respectively associated with the energy transfer within the flow, and with the energy dissipation in direct isotropic energy cascades), no relevant changes in E_r compared to the non-stratified spectrum were observed. The stable energy spectra in the azimuthal direction (E_ϕ) with no stratification was not confronted with the different unstable E_ϕ SRI spectra because, when $\Delta T = 0$, E_ϕ drops to zero, since no velocities variations occur, i.e., $\mathbf{u}' = \partial \mathbf{u} / \partial \phi = 0$. Besides the small deviation in the large scale region of E_r comparing SRI with the non-stratified TC flow, we can observe a small increase in the E_ϕ and E_r total energy with the Reynolds number (top images on 6.22), that dislocate the spectra in the y-axis without changing their shapes. No other relevant changes in the radial and azimuthal energy spectra were noticed with changes in the stratification, height or Re , and the spectra decay rates of E_ϕ and E_r remain similar to those observed in figures 6.21(a),(b).

Besides the changes in E_z decay rates, the presence of a peak in the spectra with $Re = 400$, that is not observed with $Re = 800$, is another difference that can be observed in the axial energy spectra of figures 6.21(a) and 6.21(b). On figures 6.23, axial energy spectra E_z changes with stratification, Reynolds number, and with the cavity height are shown. thus, we can evaluate which signatures of the SRI and of the spiral propagation in z (and modulations) can be observed, i.e., which modes are activated in E_z when the spiral propagation occurs, and how the different parameters investigated in section 6.2 can change the energy transfer from the base flow to the unstable modes. On figures 6.23, the x-axis presents the axial wavenumber k . Smaller figures were introduced on the top right corner of each image showing the inverse wavenumber (λ^{-1}) in the x-axis, and with the spectra arbitrarily dislocated the y-axis for better visualization of the results. The relation between λ and the wave numbers are given by

$$m = \frac{2\pi}{\lambda_\phi}, l = \frac{2\pi}{\lambda_r}, k = \frac{2\pi}{\lambda_z}. \quad (6.3)$$

On figure 6.23(a), the changes E_z with the Reynolds number are evaluated, maintaining a constant stratification $Rn \approx 258.4$. It is possible to observe that, for $Re = 300$, $Re = 400$, and $Re = 600$, where the amplitude modulations and pattern changes are observed, a peak in E_z is also observed. This peak is associated with an injection of energy from the base flow to the instability at a certain wavenumber. As the Froude number increases and rotation becomes stronger compared to the stratification, the peak dislocates to smaller wavenumbers (and to larger scales), until it disappears for $Re = 800$, where no modulation is observed. The peak is also not observed on stable TC spectra (black dashed lines on figure 6.23). Reducing the stratification leads to similar results, i.e., reducing ΔT and making Fr larger also leads to a dislocation of the peaks in the direction of the larger scales (smaller wavenumbers).

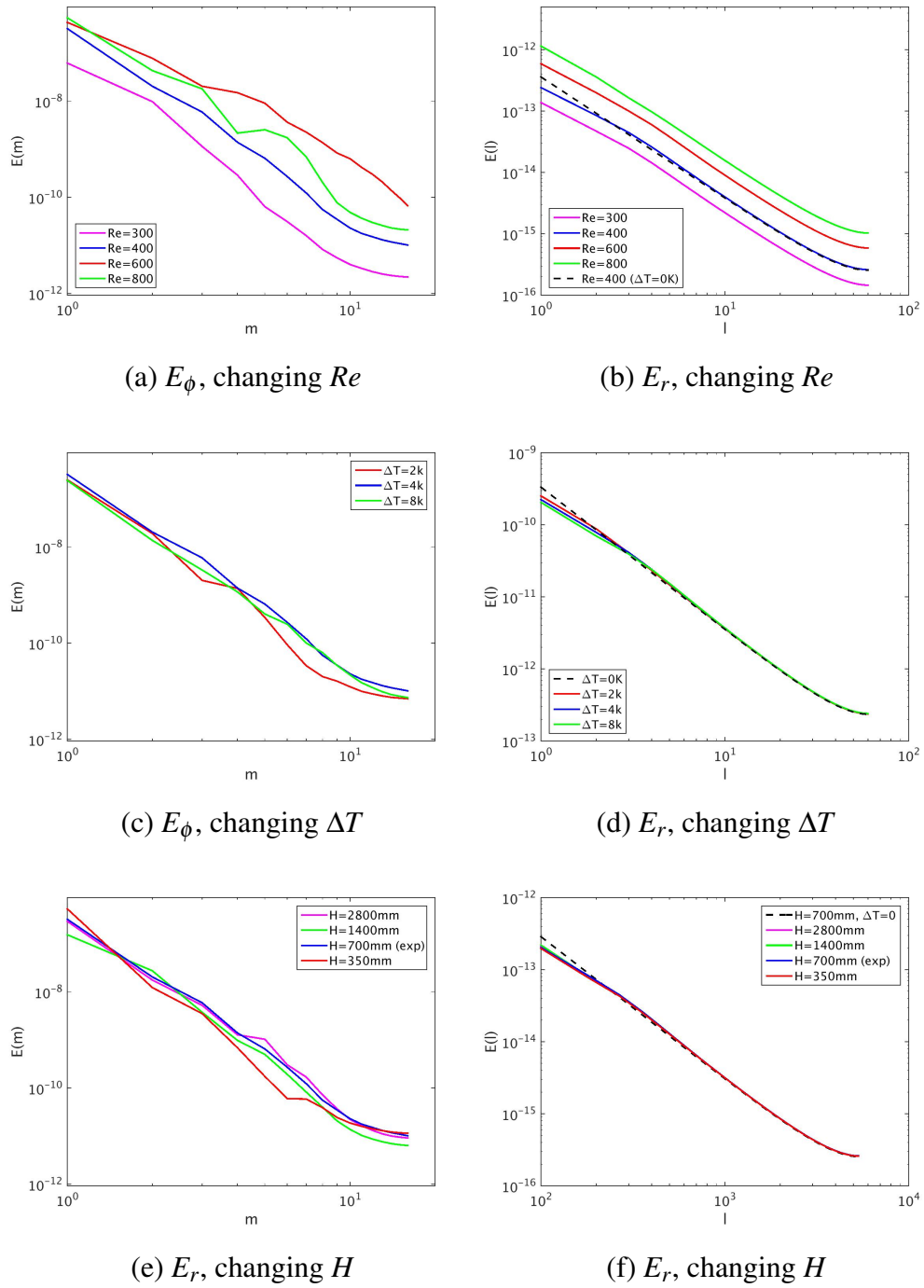


Figure 6.22: Comparison of E_ϕ (left hand side images) and E_r (right hand side images) with (a,b) different Reynolds number (top images); (c,d) different stratification values (middle images); (e,f) different cavity heights H (bottom images). The x-axis in figures 6.22 shows the azimuthal (m) and radial (l) wavenumbers. All parameters are changed with respect to a standard simulation with $Re = 400$, $\mu = 0.35$, $H = 700$ mm and $\Delta T / \Delta z = 5.71$ K m $^{-1}$. The non-stratified TC flow is presented as black dashed lines.

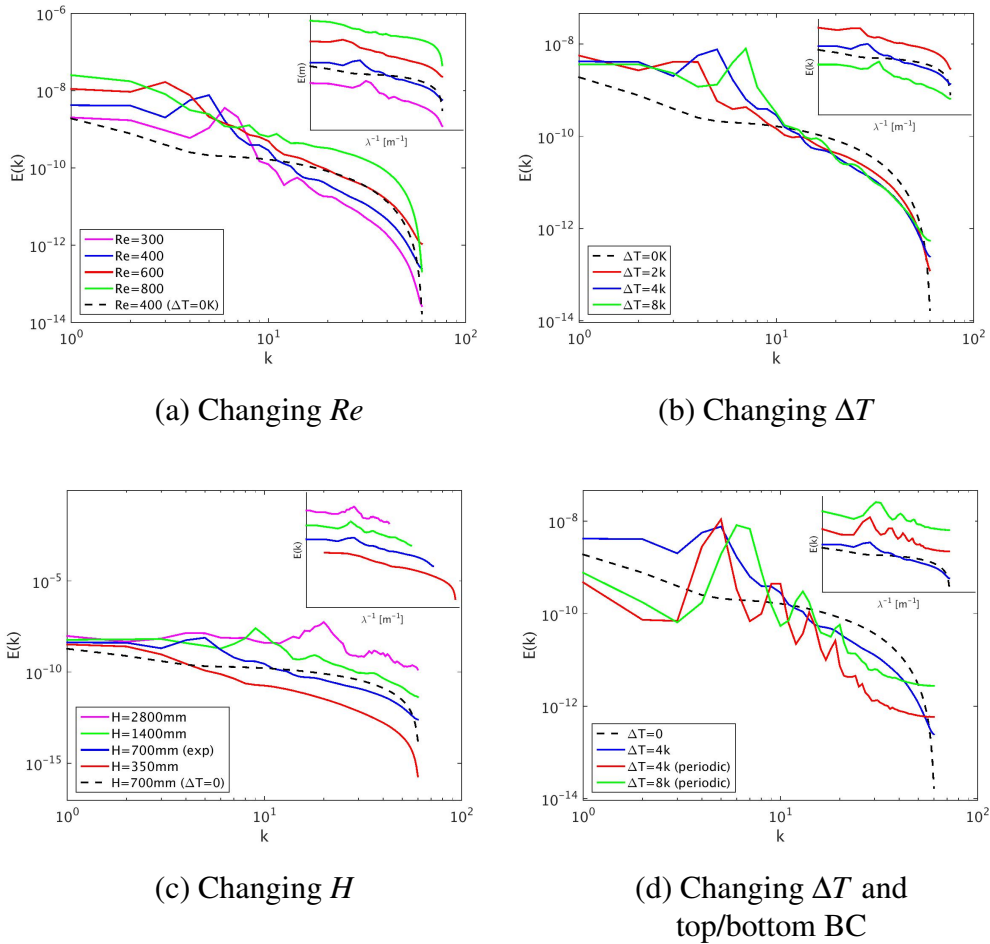


Figure 6.23: Energy spectra in the axial direction (E_z). (a) Different Re , for fixed $H = 700$ mm, $\Delta T = 4$ K. (b) Different stratification (ΔT), with fixed $Re = 400$, and $H = 700$ mm. (c) Different cylinder's heights, with fixed $Re = 400$ and $\Delta T/\Delta z \approx 5.71$ K m $^{-1}$; (d) Comparison of axial periodic and non-periodic top and bottom boundary conditions; The x-axis in all figures present the axial wavenumber k . The smaller figures inserted on the top right corner of each image show the spectra arbitrarily dislocated in the y-axis for better visualization of the results, and have the inverse wavelength (λ^{-1}) in the x-axis, instead of the wavenumber k . The non-stratified TC flow is presented in black dashed line in all figures (with $Re = 400$, $\mu = 0.35$, $H = 700$ mm and $\Delta T = 0$ K). All simulations were performed with $\mu = 0.35$.

In figure 6.23(c), we observe E_z changes with the cylinder's height, and the peaks in E_z are observed when the changes in spiral patterns occur. For $H = 350\text{mm}$, where the SRI is observed with no amplitude modulations (section 6.2.3.1), the peak in E_z is not present. Although the wavenumber increases with the cylinder's height, the image on the top right corner of figure 6.23(c) shows that changing H did not change the wavelength, and also that larger scales are not able to develop in the smaller height cavity (of $H = 350\text{mm}$), leading to the suppression of the spiral pattern changes in z . When "infinite heights" are simulated, i.e., axial periodic boundary conditions on figure 6.23(d)), weak non-linearities start to appear, with harmonics in the E_z spectra. Note that, although no pattern changes are observed in the periodic simulations with $\Delta T/\Delta z \approx 5.71\text{K m}^{-1}$ in section 6.2.3, relatively strong amplitude modulations were present, and peaks in the E_z spectrum are also observed in this case. Also note that the simulation with $Re = 400$, $\mu = 0.35$, $\Delta T = 4\text{K}$, and $H = 700\text{mm}$ (similar conditions to the experimental configuration), has a peak associated to the wavenumber $k = 4$, as well as the unbounded axially periodic simulations (also with $H = 700\text{mm}$).

The influence of rotation, stratification, and height in the SRI axial structure, observed as a peak in the energy spectra on figures 6.23 that dislocates towards smaller axial wavenumbers k when the Froude number increases, can be explained by the work of Rüdiger et al. (2017), where it is shown that the SRI axial length scale (λ_z), normalized by the gap size d , follows the relation

$$\frac{\lambda_z}{d} \simeq \frac{\pi}{4} Fr. \quad (6.4)$$

Equation 6.4 (eq. (19) in Rüdiger et al. (2017)) shows that the length-scale of the SRI axial structure grows linearly with the Reynolds number, and is inversely proportional to the buoyancy frequency. Larger Fr , therefore, will make λ_z increase, corresponding to a dislocation towards smaller axial wavenumbers, as observed in figure 6.25(a),(b), until no pattern changes occur in simulations with $Re = 400$ and half of the experimental cavity height ($H = 350\text{mm}$) (figure 6.25(c)), or with $Re = 800$ and the same experimental cavity height ($H = 700\text{mm}$) (figure 6.25(a)), when λ_z reaches the same order of H . Note that, differently from what is proposed by Rüdiger et al. (2017), a suppression of the SRI first instability was not observed here when $\lambda_z \sim \mathcal{O}(H)$, but a suppression of the amplitude modulations.

In the next session, we will investigate how the wavenumbers associated with the peaks in E_z are related to upward and downward spiral components traveling in the axial direction.

6.4 Wavenumbers of upward and downward traveling spirals

To investigate if a linear superposition of waves travelling with different frequencies and wavenumbers could explain the amplitude modulations observed. Figure 6.24 shows the 2D-Fast Fourier Transform (2D-FFT) obtained from u_ϕ space-time diagrams in the axial direction (figure 6.5) associated with the spiral traveling upwards (figure 6.24(a)), downwards (figure 6.24(b)), and during the transition from the upward to the downward propagation (figure 6.24(c)). The simulations are performed with $Re = 400$, $\mu = 0.35$, $\Delta T = 4\text{K}$ and the same geometry of our experimental setup (case 02 in table 6.1). The diagrams in figure 6.24 present the frequencies f on the x -axis, and the axial wavenumber k in the y -axis. Note that the peaks have the same frequencies $f = 0.032\text{ Hz}$ (in laboratory frame of reference) independently of the

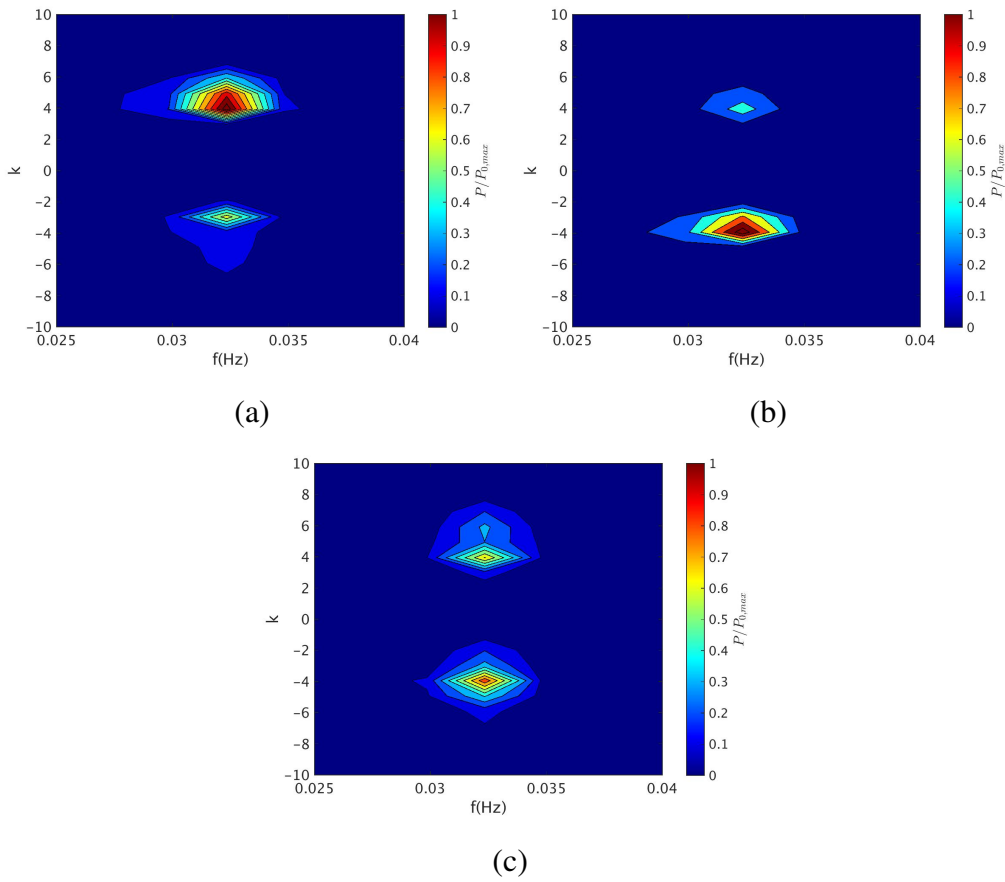


Figure 6.24: 2-dimensional power spectra obtained from numerical simulations space-time diagrams of u_ϕ in the axial direction during (a) upward spiral propagation; (b) downward spiral propagation (c) transition from a downward an upward propagating spiral. The y-axis represents axial wavenumber k (axial modes), while the x -axis is the frequency in Hz . The amplitudes of the spectra are normalized by the maximum amplitude value of the upward (and downward) propagating spirals $P_{0,max}$. The spectra are obtained in a frame of reference fixed in the laboratory. During the transition, the maximum amplitude of the spectra were half of the maximum amplitude found while the spiral is travelling upward or downward ($P/P_{0,max} = 0.5$).

spiral propagation in the axial direction, but they show changes in their wavenumbers from positive to negative values, with different modes activated and suppressed. During the transition (figure 6.24(c)), both modes are selected by the instability with half of the maximum amplitude observed during the upward or downward spiral propagation ($P_{max}(\text{transition}) = \frac{P_{0,max}}{2}$). During the upward travelling spiral, the wavenumber activated in figure 6.24(a) is $k_{up} = 4$, with maximum amplitude $P_{0,max}$, and the downward mode has wavenumber $k_{down} = -4$ is non activated. The wavenumber activated with $P_{0,max}$ in figure 6.24(b), related to the downward propagating spiral, is $k_{down} = -4$, while $k_{up} = 4$ has smaller amplitude. On figure 6.24(c), both modes $k_{up} = 4$ and $k_{down} = -4$ are activated, with half of the maximum amplitude of the spiral traveling upward or downward ($P_{0,max}/2$). Note that results (frequencies and wavenumbers) presented obtained in the 2D-FFT are the same for u_ϕ and for u'_ϕ .

Figures 6.25 show the 2D-FFT of simulations where the spiral propagation no longer occurs.

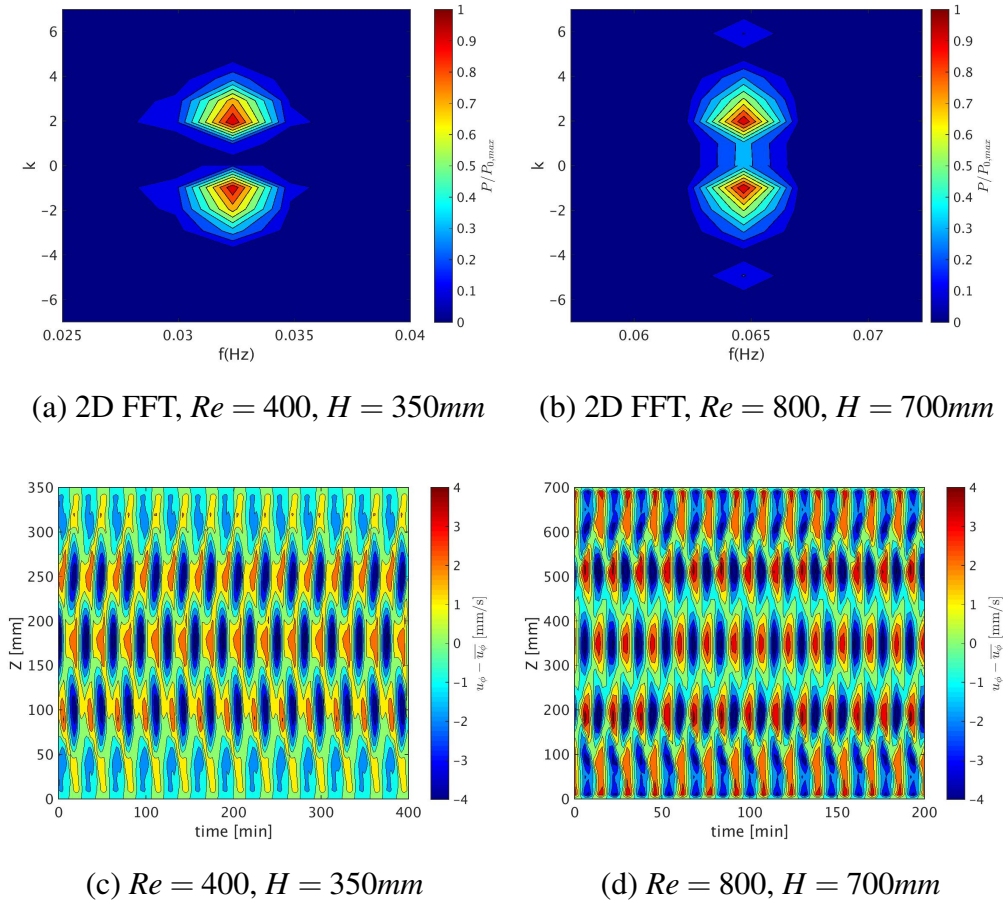


Figure 6.25: u'_ϕ 2D-fft (top images (a),(b)) and space-time diagrams (bottom images (c),(d)) of two simulations that do not change their spiral patterns in time. The left hand side images (a),(c) show simulations with $Re = 400$ and half of the experimental cavity height ($H = 350mm$). The right hand side images correspond to simulations with the same experimental height ($H = 700mm$) and $Re = 800$. Note that the time interval in the x-axis of figures c ($\Delta t = 400$ min) and (d) ($\Delta t = 200$ min) are different. In both simulations, $\mu = 0.35$ and $\Delta T / \Delta z \approx 5.71 \text{ K m}^{-1}$.

In these cases, both the spiral axial propagation or the amplitude modulations are not observed, but the SRI can still develop, and a standing chessboard pattern with no changes in time is established in the axial direction (figures 6.25(c),(d)) associated to a simultaneous positive and negative mode activation, respectively with $k_{up} = 2$ and $k_{down} = -1$. Note that, doubling the Reynolds number led to a similar SRI pattern as obtained by decreasing the height in half its original length.

6.5 Modes and spiral components separation

In this section, we will investigate how the wavenumbers of the axially propagating spirals can be separated in two waves of positive and negative wavenumbers, and how each of these two waves is modulated themselves in time, i.e., how the wavenumbers of the different parts that compose the axial traveling spirals are periodically activated and suppressed, depending on the

final spiral direction of propagation.

To better understand the process of mode selection, the up- and downward propagating wave were separated by applying the Radon Transform (RT) to a full simulation capturing phases of dominating up, downward, and mixed spiral propagation. The Radon transform is a Fourier technique to select wave components having different directions of propagation. The RT is particularly suited for finding individual waves that compose noisy or irregular fields (Almar et al. 2014). These techniques are interesting to evaluate the results directly using the data obtained, without knowing the wave's dispersion relation, and without the necessity of an analytical model of the SRI. The description of the Radon transforms can be found in the appendix A.1

Figure 6.26 shows the separation of the upward and downward components of u_ϕ on a space-time diagram while the spiral is traveling downward (left-hand side) and upward (right-hand side) using the RT. The results are from a simulation with $Re = 400$, $\mu = 0.35$ and $\Delta T = 4K$. After the two wavefields have been separated, the 2D-FFT spectra from the corresponding space-time diagrams are again compute.

In figure 6.26(a), we can observe that the 2D-FFT of the downward spiral component is the same as the bottom wavenumber in the full 2D-FFT spectrum presented in figure 6.24 (see section 6.4), and the positive frequency is no longer observed, as expected. The upward wavenumber in figure 6.24 (section 6.4) was also captured in figure 6.26(b), where the downward traveling spiral component is removed. Therefore, the wavenumbers we observe on figures 6.24 can be associated with a superposition of one upward and one downward spiral of axial wavenumber $k = 4$ and $k = -4$ propagating in time with the SRI frequency. While the spiral is propagating downwards, we see in figure 6.26 that the spiral traveling upwards is suppressed, reaching smaller amplitudes and a more vertical inclination (figure 6.26(c)). The same occurs with the downward component when the spiral is propagating upwards (figure 6.26(f)). This approach fully confirms the results shown in figure 6.24, namely that each separated mode is indeed associated with the spiral components traveling upward and downwards without any changes in the frequency, but with changes in their wavenumbers. This implies that the two spiral components travel with slightly different phase speeds, and a linear superposition of the waves could explain some part of the amplitude modulation. However, this linear dynamics cannot explain the reversals of spiral propagation associated with the modulation.

The RT was used to separate the upward and downward traveling spirals in the more complicated patterns observed in a cavity four times larger than the experimental setup. On figures 6.27, the separation of the more complicated patterns in the $H = 2800$ mm cavity height also leads to two spirals with similar wavelengths traveling in opposite axial directions, with the final spiral pattern formed by a linear superposition of these 2 separated components. Note that the separation of the spiral components using u_ϕ and $u'_\phi = u_\phi - \overline{u_\phi}$ are equivalent, since the base flow propagates in the azimuth direction, therefore, it is filtered out by the RT in the axial direction. From figures 6.27, it gets clear that the changes in the final spiral direction are associated with the amplitude of each separated axial spiral component, that are enhanced in different regions of the axial axis. Note that, when the amplitudes in the upward traveling component are enhanced, the amplitude in the downward component becomes smaller, and the opposite is also true, maintaining constant the energy contained in both amplitudes, with $A_1 + A_2 = \text{constant}$. Adding the upward (figure 6.27(c)) and downward (figure 6.27(d)) spiral components, the initial spiral pattern in figure 6.27(a) is reconstructed, showing that the spiral patterns arise from the linear superposition of these two upward and downward spiral components with different wave numbers, traveling in time with the same frequencies ω .

Note that the modulations occur in the amplitude of each upward and downward spiral

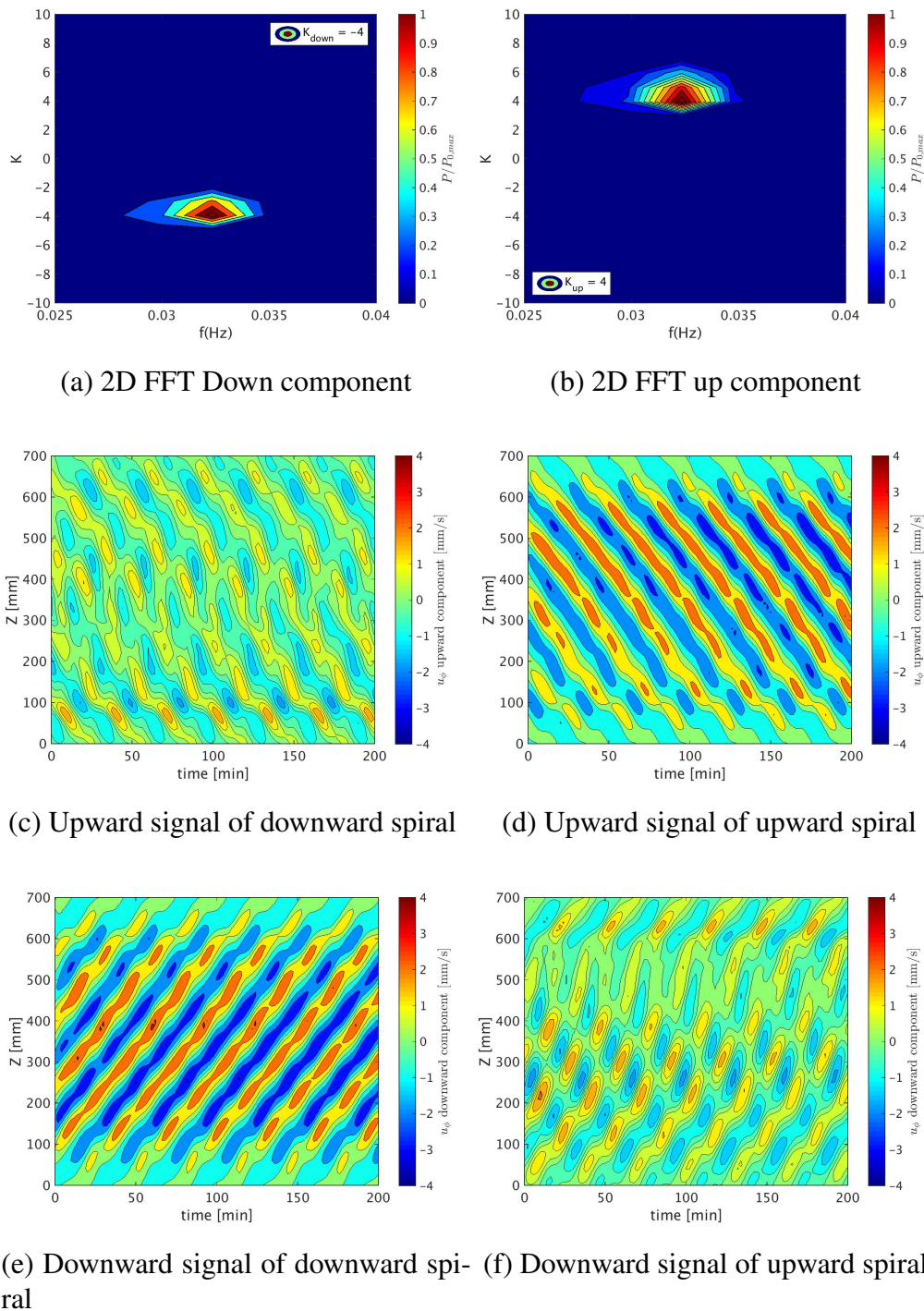


Figure 6.26: Separation of upward and downward axial traveling components in u_ϕ space-time diagram using the Radon Transform. Figures (a),(c),(e), on the left hand side, show time intervals when the spiral is traveling downwards. Figures (b),(d),(f), on the right hand side, show a time interval when the spiral is traveling upwards. Figures (a),(b) on top show the 2D-FFT of the upward and downward space-time diagrams. Simulation performed with $Re = 400$, $\mu = 0.35$, $\Delta T / \Delta z \approx 5.71 \text{ K m}^{-1}$, and $H = 700 \text{ mm}$.

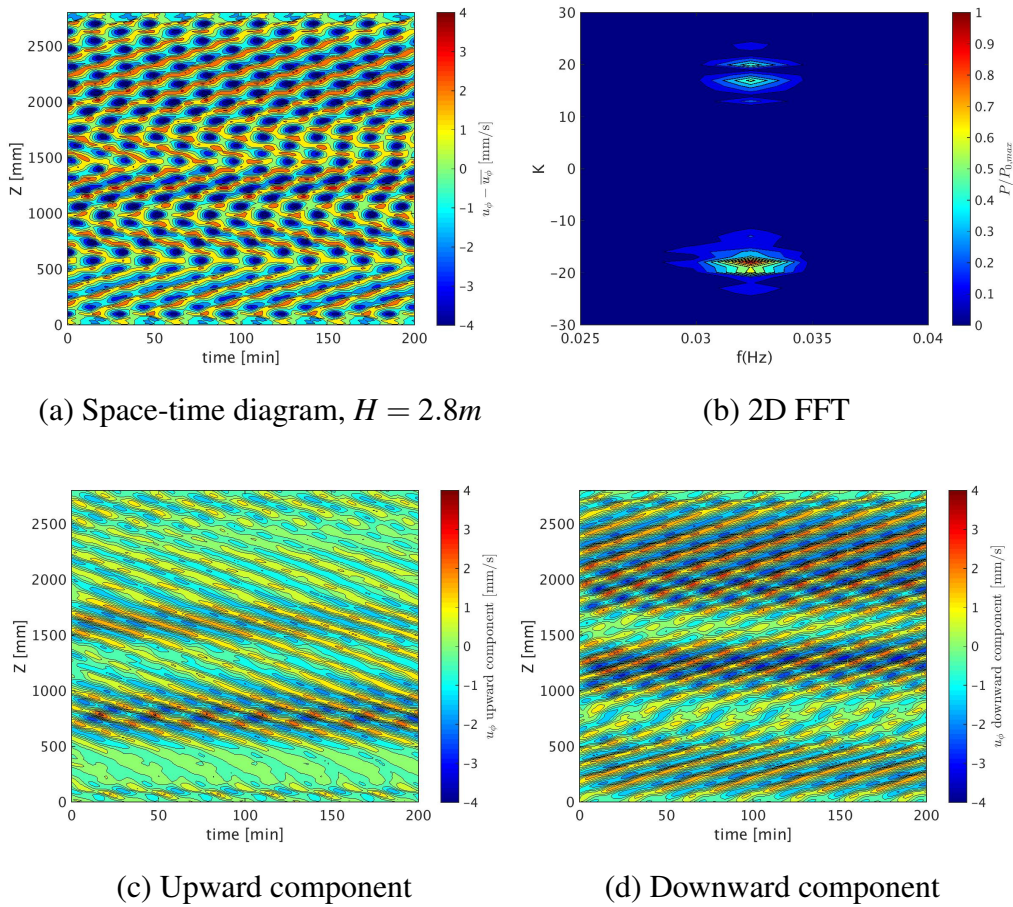


Figure 6.27: Separation of upward and downward axial traveling components space-time diagram using the Radon Transform. Results are of u_ϕ numerical simulations with $Re = 400$, $\mu = 0.35$, $\Delta T/\Delta z \approx 5.71 \text{ K m}^{-1}$ and cavity height four times larger than the experimental setup ($H = 2800\text{mm}$). (a) Space-time diagram showing the full spiral propagation; (b) 2D-FFT of the full spiral. (c) Space-time diagram of the spiral component traveling upward; (d) Space-time diagram of the spiral component traveling downward.

components, since each mode individually present different patterns at different time periods, with strengthened or weakened amplitudes in different spacial regions of the separated components. Since the amplitude modulations show harmonics in their spectra themselves (see figure 6.1(c)), and affects each separated spiral component, the modulations should come from a weak non-linear interaction between the base flow and the SRI, or from a wave-wave interaction process, and not simply from a linear interaction of two waves traveling with different frequencies. On both experimental and numerical results, each individual frequency associated with an azimuthal wavenumber in the power spectra, at a fixed point in space, is also individually modulated. Figures 6.28 shows the separation of the signal related to each azimuthal wavenumber in the power spectra of numerical simulations and experiments with $Re = 400$, $\mu = 0.35$, $\Delta T \approx 4\text{K}$ and $H = 700\text{mm}$. The separation of each mode was performed by applying a top-hat filter in the Fourier space, where the values inside a band containing (separately) one individual peak are kept intact (as well as its complex conjugated values), and all values outside this band are set to zero. After separating the frequencies corresponding to each azimuthal

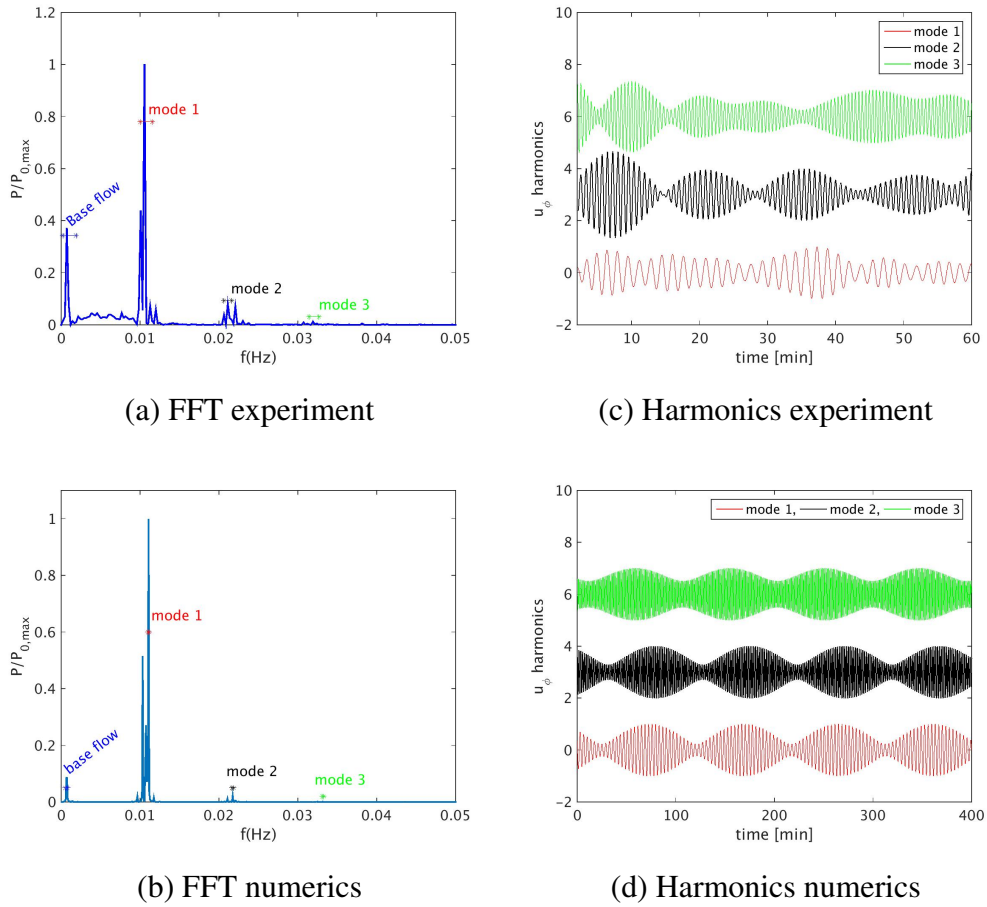


Figure 6.28: (a) Experimental and (b) numerical power spectra with $Re = 400$, $\mu = 0.35$ and $\Delta T/\Delta z \approx 5.71 \text{ Km}^{-1}$; (c) Experimental and (d) numerical harmonic signals corresponding to one peak in the different frequency bands selected. The harmonics were normalized by their maximum amplitude value, and arbitrarily dislocated in the y-axis, for better visualization and comparison. Note that the time interval in figures (a) and (b) are different.

wavenumber, the inverse FFT can be applied to evaluate the signal in time, corresponding to each mode selected. Figure 6.28(a),(b) show the bands that selected each azimuthal wave number in the numerical and experimental power spectra (left-hand side figures), and the signals associated to each mode in the physical space on the left-hand side (figures 6.28(c),(d)). When this filtering is performed, we note that each peak in the spectrum is modulated itself. Note that the band is chosen to be small enough so that only one peak with a certain width remains. Note also that there is a small phase shift among the modulation of each individual harmonic. These individually modulated harmonics show that waves should be non-linearly interacting with the mean flow so that the modulations can occur in each peak with different phases. Since a linear interaction alone possibly does not explain the amplitude modulations observed, it seems that waves/mean-flow interaction leads to an alternating strengthening and weakening of each of the SRI wave components, leading to alternating upward and downward propagating modes that have different amplitudes. Although this process is still not yet fully understood, an investigation of how these two individually modulated components could lead to the pattern formations observed will be addressed in the following section 6.6.

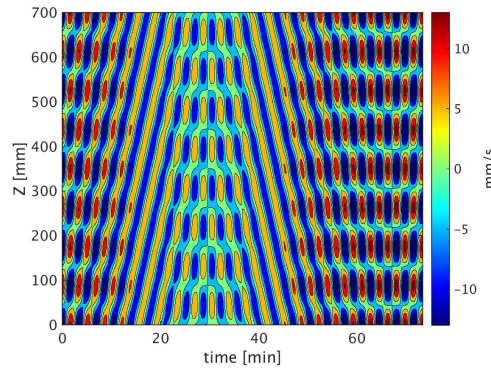


Figure 6.29: u_ϕ space-time diagram of the toy model composed of 2 plane waves with sinusoidal amplitude modulations with $\omega_A = 7 \times 10^{-4}$, out of phase an angle $\theta = \pi/3$, and traveling in opposite axial directions with wavenumbers of wave₁ and wave₂ respectively $(m_1, l_1, k_1) = (1, 1, 4)$ and $(m_2, l_2, k_2) = (1, 1, -4)$. The frequency $\omega = 0.03$, and the maximum amplitude of each wave is $A = 10$.

6.6 Toy model

Although the reason for the amplitude modulations to occur in each separated spiral is still not comprehended, a toy model of two waves traveling in opposite axial directions was implemented to understand how this could lead to the pattern changes observed in the previous section, based on the numerical and experimental results previously presented. The plane wave equations read

$$\begin{aligned} \text{wave}_1 &= A_1 \cos((m_1 x + l_1 y + k_1 z) - \omega t), \\ \text{wave}_2 &= A_2 \cos((m_2 x + l_2 y + k_2 z) - \omega t), \\ u_{toy} &= \text{wave}_1 + \text{wave}_2, \end{aligned} \quad (6.5)$$

with $0 \leq x, y, z \leq 2\pi$, and amplitudes A_1 and A_2 . The values of $0 < x, y, z < 2\pi$ are after normalized for the size of the experimental cavity (e.g., $0 \text{ mm} < z < 700 \text{ mm}$). The amplitude of each plane wave is modulated, and they must be out of phase to achieve the inclined spirals with constructive and destructive interference while they propagate. In the toy model, sinusoidal amplitude modulations A_1 and A_2 are considered out of phase with an angle θ , written as

$$\begin{aligned} A_1 &= A \sin(\omega_A t), \\ A_2 &= A \sin(\omega_A t + \theta), \end{aligned} \quad (6.6)$$

where A is a given real value, and $\omega_A \ll \omega$ is the amplitude modulation of each wave, here considered to be the same for A_1 and A_2 .

Figure 6.29 shows the space-time diagram obtained with the toy model, with wavenumbers in the azimuthal, radial and axial directions $(m = 1, l = 1, k = 4)$ and $(m = 1, l = 1, k = -4)$, similar to the ones observed in the numerical simulations with $Re = 400$, $\mu = 0.35$, and the same geometric parameters the experimental setup. It is possible to see that the linear superposition of both upward and downwards waves traveling out of phase could lead to the final spiral pattern transitions observed in the previous sections. The amplitude modulations of the waves are out of phase with an angle $\theta = \pi/3$, but other different phase shifts and wavenumbers produce similar pattern changes.

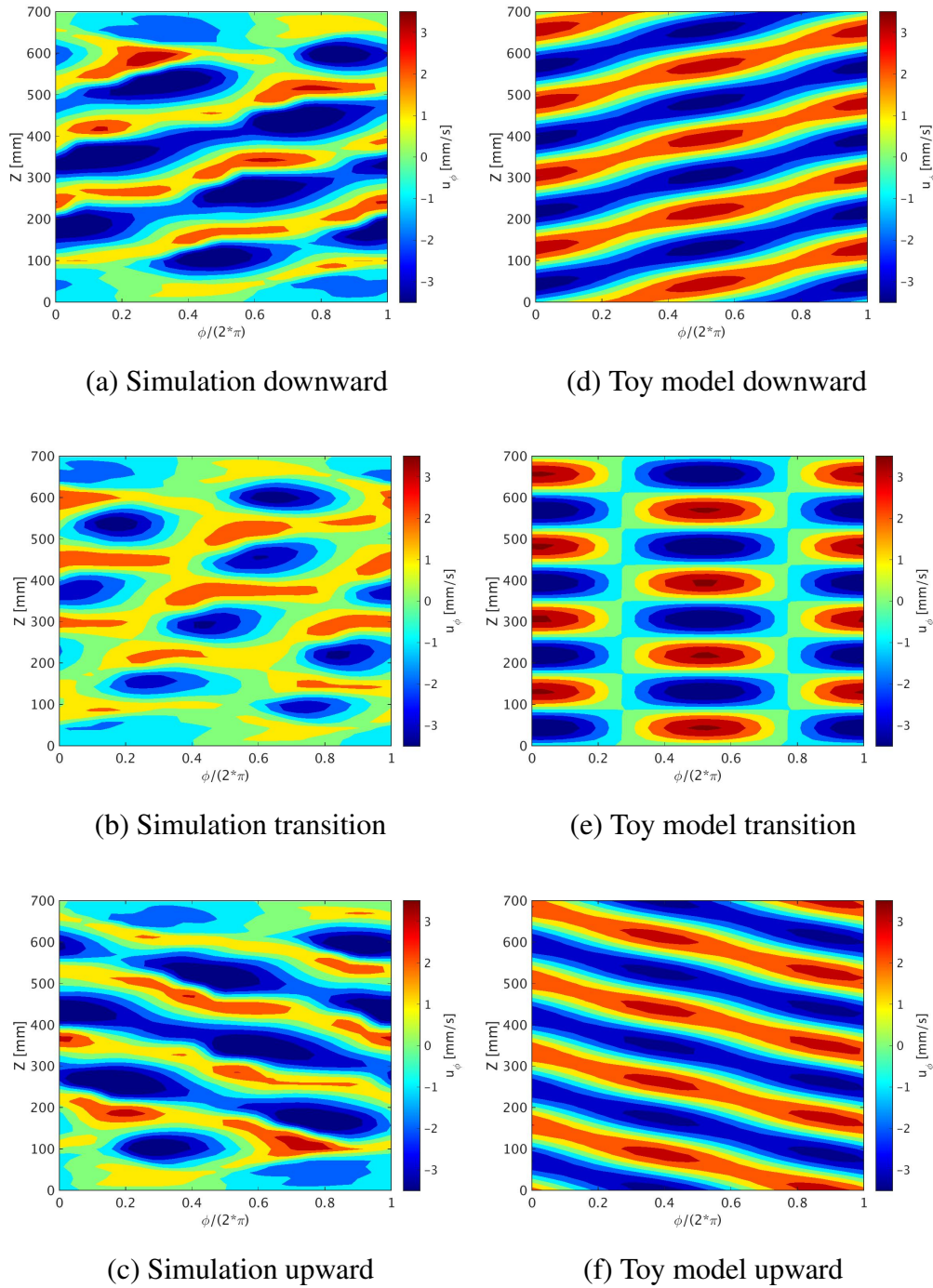


Figure 6.30: Snapshots with different spiral patterns in the ϕ - z cross-section comparing $u'_\phi = u_\phi - \bar{u}_\phi$ obtained from numerical simulations (a,b,c) and the toy model (d,e,f). The radial position is fixed at $r \approx r_{in} + d/3$. Figures (a),(d) on top, show moments when the spirals are traveling downwards; Figures (b),(e), in the middle, show the transition from upward to downward spiral propagation; Figures (c),(f) in the bottom, show spirals traveling upwards. The simulations were performed with $Re = 400$, $\mu = 0.35$ and $\Delta T = 4K$. The toy model is composed by two plane waves with frequencies $\omega = 0.01$, and wavenumbers $(m_1, l_1, k_1) = (1, 1, 4)$ and $(m_2, l_2, k_2) = (1, 1, -4)$, maximum amplitude of the waves is of $A = 3mm/s$, and the frequency of the sinusoidal amplitude modulations of $\omega_A = 0.001$, 90° out of phase ($\theta = \pi/2$).

The toy model and the numerical simulation snapshots while the spirals are traveling upward, downward and during the transition also show good qualitative agreements in figure 6.30, except for the fact that the spirals in the simulations are confined in a smaller region, due to Ekman effects. The good qualitative agreement of the toy model and numerical simulations, as well as the possibility of reproducing the spiral pattern changes previously investigated using similar wavenumbers and frequencies obtained from numerical simulations and experimental measurements, indicate that this can be the mechanism that drives the spiral pattern changes. In this case, each up and downward component should be interacting with the mean flow, that in times provide more energy to the upward traveling spiral, and in other times, provides more energy to the downward component, but the reason for the amplitude modulations of each individual wave to occur still is not clear. It is clear though, that the spiral propagation direction affects the mean flow structure (see figure 6.6), and its total circulation (see 6.1.1). Therefore, each spiral component must be interacting with the mean flow for achieving its individual modulation, and the linear superposition of these two modulated components will lead to the reversal spiral direction as presented in the toy model. Since the modulations presented harmonics (see figure 6.1(c))

6.7 Impacts of the SRI modulation on momentum transport

In this section, we will investigate the SRI turbulent momentum transport behavior in space and time, that is an important issue regarding how the SRI could transport momentum outwards from the center of accretion disks, allowing matter to aggregate by gravity in the center, leading to proto-planetary star formation.

Figures 6.31 shows the spatial structure of $u'_\phi u'_r$ for different stratification values (ΔT , or Rn), where we can observe that momentum transport in the SRI should be carried by the SRI spirals. This can be observed by characteristics of $u'_\phi u'_r$ behavior such as increasing axial wavenumbers with the stratification, in similar patterns as those observed for the velocity and temperature axial spiral profiles (see section 6.2.1). Note that the axial $u'_\phi u'_r$ structure observed on the right hand side of figure 6.31 are similar to those observed by Gellert and Rüdiger (2009) (see figure 4 in Gellert and Rüdiger (2009)).

Since momentum transfer within the flow is related to the spiral structure, it is relevant to show how the previously observed amplitude modulations, associated with the spiral axial propagation, will also affect $u'_\phi u'_r$ temporal behavior. The results are presented for the numerical simulations, since longer time series with more than one hour can be evaluated, i.e., after the transient low frequency amplitude modulated regimes. Figures 6.32 shows $u'_\phi u'_r$ time series for numerical simulations obtained with constant stratification ($\Delta T/\Delta z = 5.71 \text{ K m}^{-1}$) and different Reynolds number, while figures 6.33 shows different stratification values ($\Delta T = 2K$ and $\Delta T = 8K$) with fixed $Re = 400$. The values of $\mu = 0.35$ and $H = 700 \text{ mm}$ are kept constant in all results presented in this section, and the time series are obtained on a fixed space position at mid-height cavity ($z = H/2$), and near the inner cylinder, because we are interested on understanding how momentum could be affected near the center regions of accretion disks (associated to the inner cylinder region). Note that the top figures 6.32(a),(b) present the time interval $0 \leq t \leq 400$ minutes, while the time interval on figures 6.32(c)-(e) are smaller, varying from $0 \leq t \leq 220$ min. For Reynolds numbers $Re = 300$, $Re = 400$, and $Re = 800$ and fixed $\Delta T/\Delta z = 5.71 \text{ K m}^{-1}$ (figures 6.32(a)-(c)), and for higher stratification values with $Re = 400$ and $\Delta T = 8K$ (figure 6.33(b)), low frequency amplitude modulations in $u'_\phi u'_r$ are observed, indicating that, for smaller values of the Froude number, momentum can indeed be transferred in

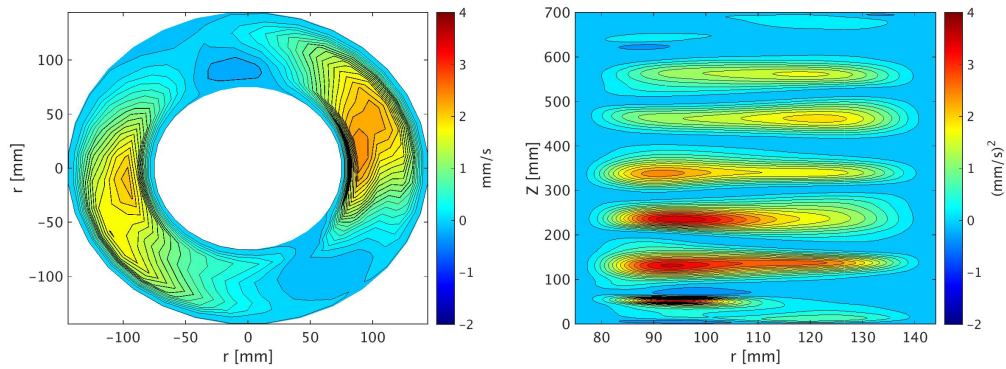
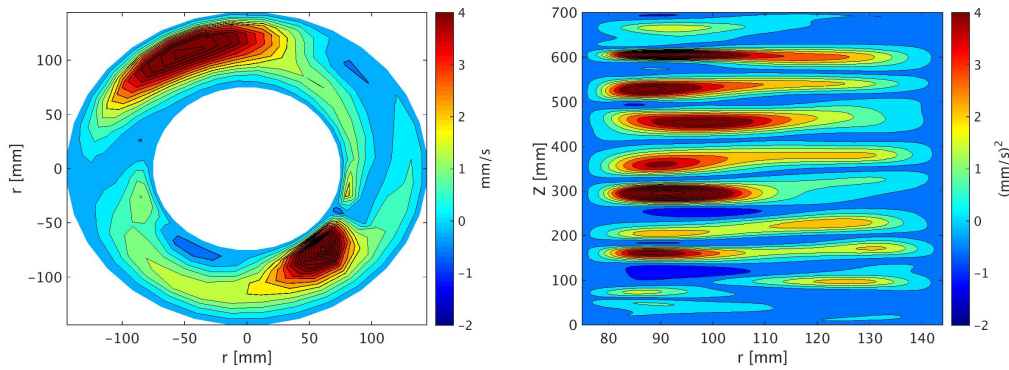
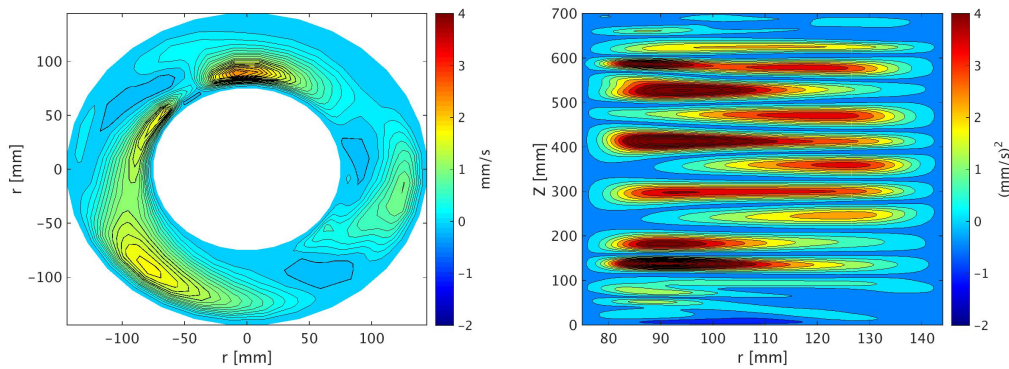
(a) $\Delta T = 2 \text{ K}$, $\Delta T/\Delta z \approx 2.86 \text{ K m}^{-1}$ (b) $\Delta T = 4 \text{ K}$, $\Delta T/\Delta z \approx 5.71 \text{ K m}^{-1}$ (c) $\Delta T = 8 \text{ K}$, $\Delta T/\Delta z \approx 11.43 \text{ K m}^{-1}$

Figure 6.31: $u'_\phi u'_r$ snapshots of numerical simulations with $Re = 400$ and $\mu = 0, 35$ and different stratification values ($\Delta T/\Delta z$). The left hand side show the azimuth-radial cross section ($\phi - r$) at mid-height position ($z \approx H/2$), and the right hand side shows the radial-axial cross section at $\phi = 0$.

bursts. The frequency of the amplitude modulations increase with the Froude number, until it reaches a regime where no amplitude modulation occurs, leading to a continuous momentum transfer, as seen in figures 6.33(a) and 6.32(d). Intervals of 5 minutes in $u'_\phi u'_r$ time series are presented inside each image on figures 6.32 and 6.33, to highlight the SRI higher frequency oscillations in time.

The modulations observed in the momentum transport may have an impact on accretion disk theory since a constant or an intermittent regime might play different roles if they lead to different conditions to aggregate matter in the center of the disks. Note that intermittent momentum transport was already measured in astrophysical contexts, such as in the measurements of molecular clouds in the north Celestial pole loop performed by Falgarone et al. (2011), where the turbulent energy dissipation was reported to occur in bursts (Meyerdierks et al. 1991). These systems guard some similarities with the SRI geometry, such a cylindrical gap morphology, and energy spectra of dust clouds surrounding young stars with decay rates of $k^{-11/3}$ (the same decay rate of E_ϕ obtained in the numerical simulations here presented (see section 6.3)).

Other time-dependent momentum transfer regimes are observed in the amplitude modulation transient regions on figures 6.32 and 6.33, for $t \lesssim 100$ minutes, before a more regular amplitude modulation is established. In figure 6.33(e), when Froude number reaches approximately 3.5, the transition region has a relevant impact in the momentum transfer, since for time $\gtrsim 90$ minutes, the flow is stable but in the interval $50 \lesssim t \lesssim 90$ minutes, a burst of momentum transfer occurs. This phenomenon can be important on accretion disks applications, as that might allow a proto-planetary star to form at the early stages of the SRI development, even in cases where the regime achieve the stability for $t \rightarrow \infty$. According to Shtemler et al. (2010), shear flow mechanisms may give rise to transiently growing perturbations in accretion disks, while the work of Rebusco et al. (2009) shows that there would be enough time for these small perturbations to grow significantly by few orders of magnitude and for secondary SRI instabilities to develop (such as the amplitude modulations) before viscous or non-linear effects take over and suppress the instability. Yecko (2004) examined viscous three-dimensional linear disturbances associated with Keplerian accretion disks-like flows, and predicted that non-modal disturbances can lead to large transient amplification factors, that can make asymptotically stable flows transiently unstable. In figure 6.34, the temporal behavior of $\langle u'_\phi u'_r \rangle$ spacial mean in the azimuthal direction is presented. The average is performed at a fixed radial position very near the radial cylinder, and at an axial position far from the end-gap boundaries. these results show how the outward flux of momentum at a given radial position near the inner cylinder will also occur in bursts when the amplitude modulations are activated, and continuously when no pattern changes occur.

As can be seen, there are many interesting, although preliminary, findings concerning the momentum transport in the SRI systems and its relation to observed accretion disks. These aspects deserve a deeper investigation, that will be performed in upcoming projects.

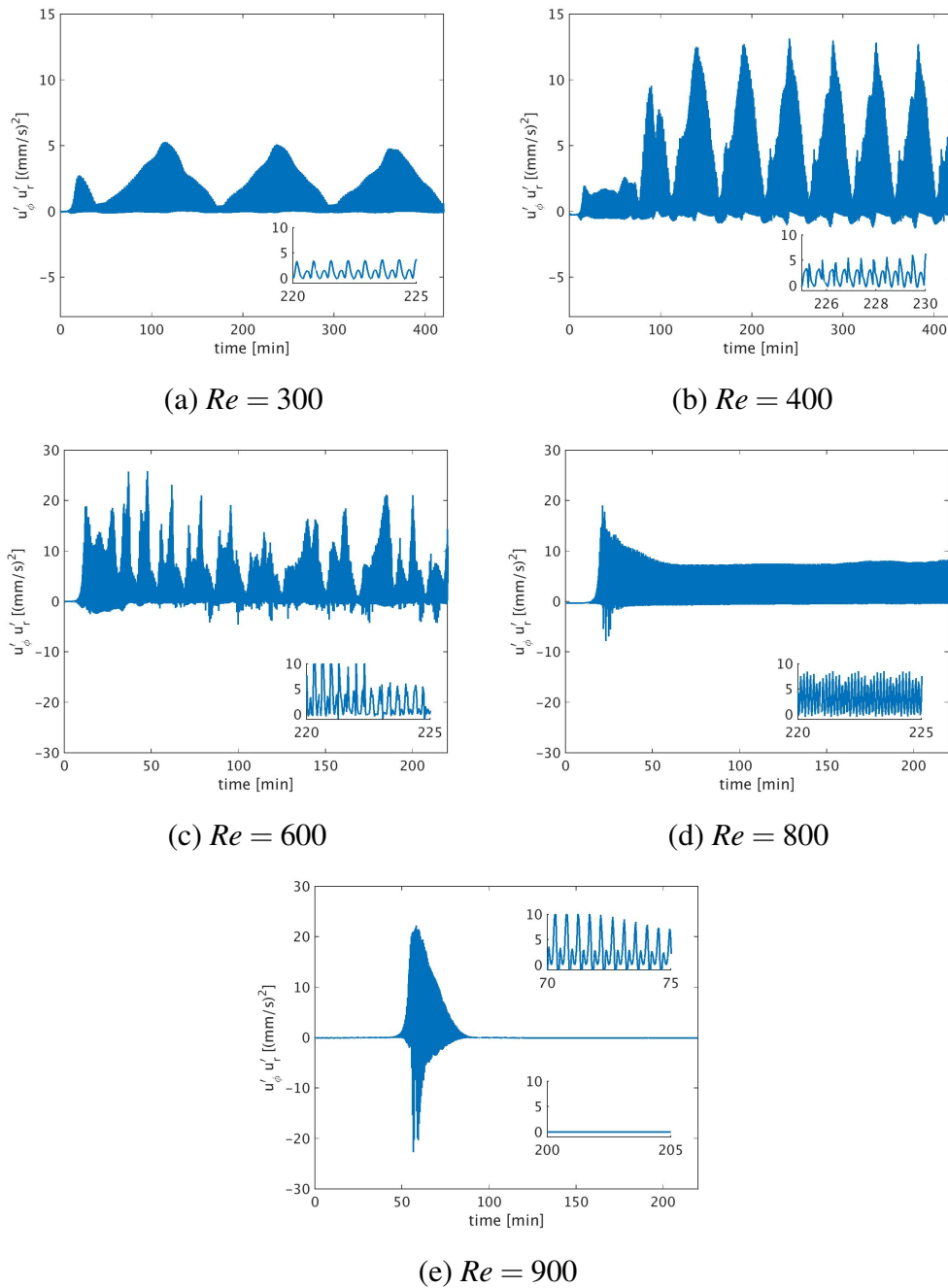


Figure 6.32: $u'_\phi u'_r$ time series for increasing Reynolds number with a fixed temperature gradient $\Delta T/\Delta z = 5.71 \text{ K m}^{-1}$. The velocities are obtained at position $r = 90 \text{ mm}$ (near the inner cylinder) and $z \approx H/2$ (mid-height). Note time of the upper figures (a),(b) is of $0 \leq t \leq 420$ minutes, and of the bottom images (c),(d),(e) are of $0 \leq t \leq 220$ minutes. The small figures inserted show the SRI oscillations in a 5 minutes time window. Figure (e) has two inserted figures, when the SRI occur at the transient phase ($t < 90$ minutes) and another inserted image after the flow becomes stable (for $t > 90$ minutes).

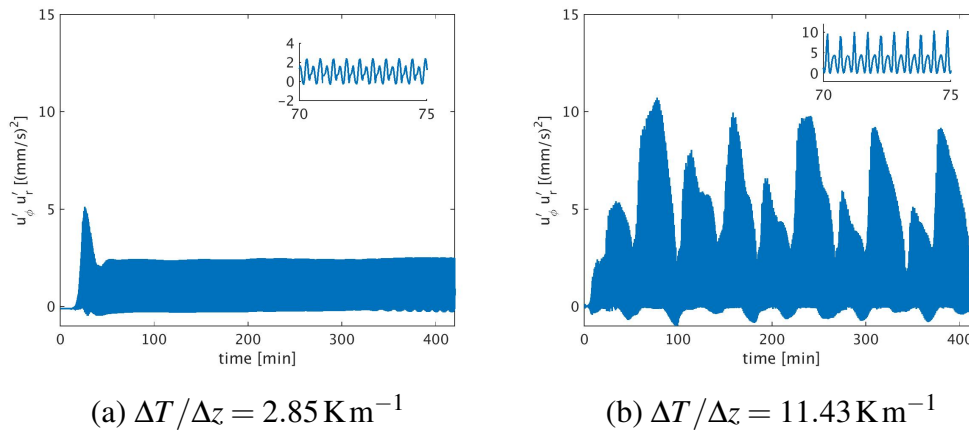


Figure 6.33: $u'_\phi u'_r$ numerical simulations time series at $r = 90 \text{ mm}$ and $z \approx H/2$ for different stratification values, and with $Re = 400$, $\mu = 0.35$, and $H = 700 \text{ mm}$. The images inserted inside each figure show a smaller time interval of 5 minutes, highlighting the higher frequency SRI oscillations.

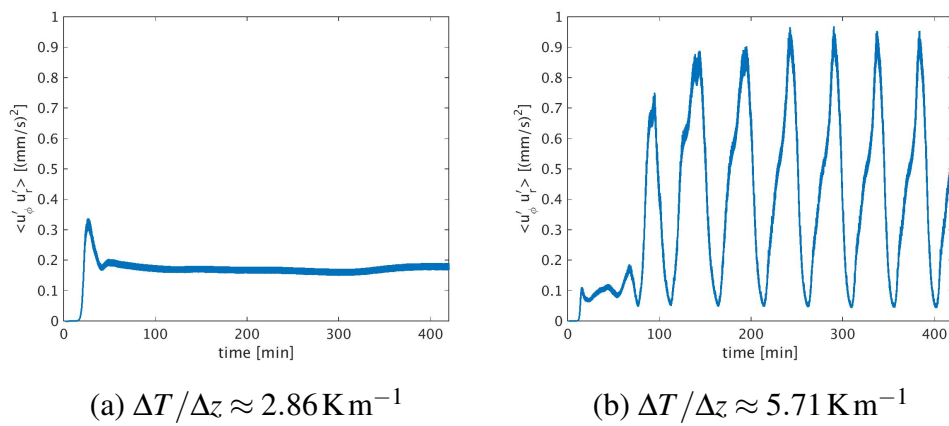


Figure 6.34: Mean azimuthal space mean $\langle u'_\phi u'_r \rangle$ at a fixed radial position very close to the inner cylinder wall ($r \approx 76.14 \text{ mm}$) and mid-height axial position $z \approx H/2$. The results are from numerical simulation with different stratification values ($\Delta T / \Delta z$) and with the same $Re = 400$, $\mu = 0.35$ and the same geometry of our experimental setup (cases 01 and 02 in table 6.1, of section 6.2.1).

Conclusions

*“No llores porque ya se terminó, sonrío porque sucedió.”
 (“Don’t cry because it’s over. Smile because it happened.”)*

– Gabriel García Márquez –

In this thesis, the phenomena related to the strato-Rotational Instability (SRI) were investigated using PIV experimental data and high-performance computing Direct Numerical Simulations (DNS). The SRI occurs in a fluid between two concentric boundaries rotating at different angular velocities, and with a stable density stratification due to a temperature gradient in the axial direction. The SRI manifests itself in the radial-axial direction as non-axisymmetric spirals that were first experimentally observed by Le Bars and Le Gal (2007), which provided quantitative experimental evidence of the strato-rotational instability and its expected helicoidal modes. In the radial-azimuthal direction, the SRI is associated with a peak in the spectrum with an azimuthal wavenumber $m = 1$.

The experimental setup to study the SRI was designed at the Department of Aerodynamics and Fluid Mechanics (LAS) of the Brandenburg University of Technology Cottbus–Senftenberg (BTU). It consists of a Taylor-Couette system where the top lid is heated, and the bottom lid is cooled for obtaining a stable density stratification in the axial (z) direction. The experimental setup has concentric inner and outer cylinders that rotate independently, with different angular velocities. The gap between the cylinders is filled with a Newtonian M5 silicon oil of viscosity (ν) 5 times higher than the viscosity of water. The outer cylinder wall, with radius r_{out} , is made of transparent glass material to allow optical access to the flow that develops within the cavity. A co-rotating mini-PIV system was then used to measure the SRI instantaneous velocity profiles. Peltier elements are installed for heating the experiment’s upper lid and creating a temperature gradient along the axial axis, and consequently, imposing a stable density stratification. The bottom part of the cavity can be cooled using a chiller.

To carry out numerical investigations of the SRI, Direct Numerical Simulations were performed using the finite differences method reported in Abide et al. (2018), dedicated to high-performance computing. The physical model solved by the code is the Taylor-Couette flow configuration filled with an incompressible fluid endowed with a vertical temperature gradient. The numerical code then solves the Navier-Stokes equations under the Boussinesq approximation to account for the buoyancy forces that arise from the stable density stratification. The efficiency of the implemented parallel high-performance code reduced long computational times of DNS

scalar codes previously employed to investigate the SRI (Raspo et al. 2002, Abide and Viazzo 2005, Abide et al. 2018, Von Larcher et al. 2018), which made it convenient for evaluating these low frequency (long time occurring) SRI phenomena.

The comparison between numerical simulations and experimental results show good agreements, with similar phenomena captured using both approaches. The investigations were concentrated on Reynolds number between $200 \leq Re \leq 1300$, and $\mu = 0.35$ (slightly smaller than the Keplerian line, at $\mu \approx 0.375$ in the experimental setup). These values were chosen due to their possible practical implication on accretion disk theory. The temperature differences between top and bottom lids were maintained at $2K \lesssim \Delta T \lesssim 8K$.

The comparison of mean velocity profiles and power spectra of numerical simulations and *PIV* experimental data present SRI oscillations with the same period in both cases. When the mean SRI velocity profile is compared to the non-stratified TC profile, the flow is slower near the inner cylinder and slightly faster near the outer cylinder. This shows how the stratification affects the mean flow, transferring energy to the instability, and implying a mean outward momentum flux. Besides showing the good agreement between numerical and experimental data, the power spectra of the data also reveal harmonics of the SRI's most energetic frequency, showing that non-linearities are starting to set in for the chosen parameters. The transition to stable regimes can be observed in the velocity profiles by the absence of SRI oscillations, and by achieving the same $\overline{u_\phi}$ time mean profile as a classic TC flow with no stratification. The velocity power spectra also attest to the stability since the SRI peak disappears. The SRI instability was well described by linear stability analysis both in numerical and experimental results, as they confirmed linear-stability marginal curves, with increasing moderate Reynolds numbers making the flow return to a stable regime as described by Ibanez et al. (2016), Rüdiger et al. (2017) and Seelig et al. (2018).

The SRI frequencies observed are closer to the buoyancy frequency (N) than to the inertial frequency ($f = 2\Omega_{in}$), and they become closer to f when the inner cylinder rotation increases. Furthermore, the most energetic SRI frequencies are found inside the interval $N - f$. This is an important remark because inertia-gravity waves (IGW) can not exist outside this range. The power spectra of experiments and numerical simulations highlight harmonics with the same frequencies in spectra of different Reynolds numbers. When the spectra are normalized by the inner cylinder rotation (therefore, also by the Reynolds numbers), all the frequencies collapse to the same values, i.e., all the spectra become coincident.

The new high-performance computing numerical code allowed for the first time to observe long period phenomena in the SRI flow. This was not possible with comparatively much slower scalar codes, or with experiments performed during short periods. This is, in particular, due to the large time demanded to establish SRI solutions, clearly showing the suitability of the present numerical tool to treat such problems. These longer simulations revealed that the SRI velocity profiles present strong low-frequency amplitude modulations, also observed in the experimental measurements. The amplitude modulations are related to pattern changes of the $m = 1$ SRI mode. This means that the SRI spiral inclination in the radial-axial ($r - z$) cross-section changes coupled with a change in the direction of the axial drift speed of the spiral. In contrast to the most unstable non-stratified Taylor-Couette modes that have the structure of rolls, SRI modes have a nonzero azimuthal wavenumber where the phase of the wave depends on the axial direction, and hence show a spiral structure. For SRI spirals in the non-turbulent flow regime, the connection to amplitude modulations has not yet been described in the literature. The SRI spirals observed have some similarities with those found in experiments performed by

Flór et al. (2018) and discussed in numerical simulations by Lopez and Marques (2020). In these studies, two spirals are moving upward and downward resulting in a standing pattern with low-frequency modulations. The latter seems to come from differences in the axial drift speed of the two waves. In this study, the drift speed shows some variations but the mean upward and downward speeds are the same. It should be noted that Flór et al. (2018) and Lopez and Marques (2020) use a very different geometry, with a radius ratio of just $\eta = 1/15$ and $\Gamma = 1$, much smaller than, for instance, the values of $\eta = 0.52$ and $\Gamma = 10$ for the experimental and numerical setup. Moreover, in contrast to the investigations presented in this thesis, they use a smaller Froude number $Fr < 1$ and a larger Reynolds number $Re > 6000$. The SRI modulations observed are considered to have low frequency because they are more than 30 times smaller than the SRI frequency.

When the power spectra of the amplitude envelopes are obtained, harmonics of the most energetic peak appear, suggesting that the amplitude modulations arise from weak non-linear processes. The low-frequency peaks are found outside the interval $N - f$, therefore, the amplitude modulations cannot be interpreted as low-frequency gravity wave modes. Similar amplitude modulation spectra are obtained from both u_ϕ and u_r time series (with peaks corresponding to the same frequencies), but with different amplitudes only in the most energetic peak of the spectra. The harmonic peaks, though, have the same amplitudes in both u_ϕ and u_r amplitude modulation spectra. Note that the SRI first instability shows a mode $m = 1$ peak in the Fourier space, and they are already prominent approximately 10 minutes after starting the rotation for all SRI unstable Re investigated. The secondary instabilities associated with the amplitude variations, on the other hand, needs approximately 100 minutes in the cases investigated to achieve a permanent regime. During the transient regime ($t \lesssim 100$ minutes), amplitude variations also exist, but they are not regular in time.

The analysis of the SRI flow during the amplitude modulations reveals three particular flow patterns that are correlated with the modulations. In different time intervals selected, a different flow pattern is observed in the axial-time frame. The patterns represent different SRI spiral inclination and propagation in the axial direction. During the transition from the upward (downward) to the downward (upward) pattern, both spirals are activated and superposed. This leads to the chessboard type structure pattern. The transition region is characterized by small SRI amplitudes. Observations of the 3-dimensional structures obtained from numerical simulations show that not only the inclination changes during the amplitude modulation but also does the spiral propagation in the axial direction. The downward spiral inclination travels from the top to the bottom lid in the axial direction, while the upward spiral travels in the opposite axial direction. When the SRI amplitude grows, it influences the flow circulation in the $r - z$ plane, which causes the SRI spiral inclination. The low-frequency pattern changes in the SRI spirals can be interpreted as an oscillation of the system between two slightly unstable fixed points, one fixed point standing for the upward, the other for the downward spiral.

Critical layers position were qualitatively associated with the circulation patterns established in the SRI. This is the case since circulation cells seem to be confined between the baroclinic critical layers and the cylinder's walls. The traditional critical layer also seems to play an important role in the process of generating internal waves in the fluid that leads to the instabilities observed. But this is a qualitative observation, and further investigations are necessary for a more conclusive understanding of the critical layers' impacts in the SRI development and on its circulation patterns. Note that increasing the cylinder gap showed to have an impact on the time demanded for the SRI to develop, but this phenomenon is not yet well comprehended and

needs further investigation.

For the cases investigated in this thesis, there are approximately 5 minutes of delay between u_ϕ amplitude minima and those of u_r or u_z (u_r and u_z pattern transitions occur at the same moment). The reason why the minimum amplitude does not happen at the same moment for the different velocity components was not yet understood, but it indicates that theoretical models to describe these modulations should take into account such amplitude phase-shifts. The SRI oscillations, otherwise, do not show any phase shift between u_ϕ , u_r , and u_z . The average time that one point in the spiral takes to travel from the bottom to the top of the cavity was also investigated (or vice-versa, in case of the downward pattern). The axial period of the spiral was observed to be at least 10 times smaller than the period of the amplitude modulation (of ≈ 50 minutes), and no clear correlation was noticed between these two periods. Therefore, since no relation was deduced, the possibility of waves reflecting on the lids to generate the amplitude modulations was discarded. Furthermore, simulations with periodic boundary conditions at the bottom and top lids also showed amplitude modulations associated with pattern changes, showing that the presence of lids is not a condition for the modulations and the pattern transitions to occur.

Several factors were able to change the behavior of the axial traveling spirals, such as the Reynolds number, the geometrical parameter of the cavity (such as its height or gap size), and stronger or weaker stratification in the axial direction. The secondary instability associated with the low-frequency amplitude modulations and spiral pattern changes were observed to be suppressed depending on the parameters evaluated, independently of the occurrence of first SRI instability. Larger deviations from the TC profile occur when the secondary instability establishes, compared to the case where only the first instability occurs, showing more energy being transferred from the base flow.

The energy spectra in the azimuthal, radial, and axial directions were investigated for different SRI regimes. The power laws that fit the energy decay in E_ϕ and E_r do not change with the SRI regime, i.e., no relevant changes in their decay rates are observed. For the axial energy spectra, changes in the axial kinetic energy spectra (E_z) slope were observed when the secondary instability occurs. When the modulations are established, the decay rate of the inertial range of E_z is proportional to a power law k^{-3} . When only the first SRI instability is achieved, and no amplitude modulations occur, a power law with a decay rate $-5/3$ is observed. An energy spectrum (E_z) with power-law -3 was observed on vertical measurements of the atmosphere performed by Dewan and Good (1986), Cot (2001) and was confirmed by numerical simulations of strongly stratified fluids by Lindborg (2006). A k^{-3} spectrum decay is interpreted as occurring on enstrophic cascades (Charney 1971, Nastrom and Gage 1985), which transfers energy from larger to smaller scales in quasi-geostrophic turbulence. For the axial kinetic energy spectra E_z , besides the changes in their decay rates, the presence of a peak is observed when the secondary instability occurs. As the Froude number increases and rotation becomes stronger compared to the stratification, the peak dislocates to smaller wavenumbers (and to larger scales), until it disappears when no modulation is observed. When "infinite heights" are simulated by applying axial periodic boundary conditions, weak non-linearities start to appear in the kinetic energy spectra, with harmonics in E_z .

The power spectra in the radial direction (E_r) have slope with a decay rate proportional to l^{-2} . This is the same slope observed by ocean measurements performed by Garrett and Munk (1972, 1975), related to a random superposition of linear internal waves known as the Garrett and Munk (GM) model, or related to weakly nonlinear wave turbulence (Lvov et al. 2004, Allen

and Joseph 1989).

A power law $m^{-11/3}$ fit well the slope measured in the azimuthal kinetic energy spectra (E_ϕ). This decay has already been associated with different phenomena, such as the influence of potential energy available in turbulent diffusion of quasi-geostrophic cascades (Smith et al. 2002), or with Kelvin waves propagating along a vortex line (L'vov and Nazarenko 2010). In the astrophysics context, a $m^{-11/3}$ power law was measured over a broad length-scale domain in energy spectra of diffuse molecular clouds surrounding young stars, where turbulent pressure largely exceeds the system's thermal pressure (Falgarone et al. 2011).

To investigate if a linear superposition of waves traveling with different frequencies could explain the amplitude modulations observed, the power spectra during the upward and downward axial spiral propagation, and during the transition, were analyzed separately. They were investigated using 2D-FFT diagrams that present the frequencies on the x -axis, and the wavenumber on the y -axis. The SRI frequencies do not change with the spiral propagation regime, but the wavenumbers of the most energetic peaks change from positive to negative values, with different modes activated and suppressed. During the transition spiral regimes, both modes are selected by the instability with half of the maximum amplitude observed during the upward or downward spiral propagation ($P_{max}(\text{transition})=P_{0,max}/2$).

To better understand the process of mode selection, the up- and downward propagating waves were separated by applying the radon transform (RT) to simulations capturing phases of dominating up, downward, and mixed spiral propagation. This approach fully confirms that each separated mode is indeed associated with the spiral components traveling upward and downwards without any changes in the frequency, but with changes in their wavenumbers. The RT was also used to separate the upward and downward traveling spirals in more complicated patterns observed in longer cavities. In these cases, it became clear that when the amplitudes in the upward traveling component are enhanced, the amplitude in the downward component becomes smaller, and the opposite is also true. This leads to a constant energy contained in both amplitudes, with $A_1 + A_2 = \text{constant}$. Adding the upward and downward spiral components, the initial spiral pattern is reconstructed, showing that the spiral patterns arise from the linear superposition of these two upward and downward spiral components with different wave numbers, traveling in time with the similar frequencies ω . However, this linear dynamics cannot explain the reversals of spiral propagation associated with the modulation.

On both experimental and numerical results, each mode in the power spectra was also separated and it was observed to be individually modulated. Since the amplitude modulations show harmonics in the spectra themselves, the modulations of these separated components should come from a weak non-linear interaction between the base flow and the SRI. As a linear interaction alone possibly cannot explain the amplitude modulations observed, it seems that wave mean flow interactions lead to an alternating strengthening and weakening of each of the SRI wave components, creating alternated upward and downward propagating modes that have different amplitudes. A toy model of two waves traveling in opposite axial directions was implemented to understand how the pattern changes could occur from the interaction of the individually modulated components observed. The model considers two individual plane waves, linearly superposed and, traveling in different axial directions. The amplitude of each plane wave is individually modulated, and they are phase-shifted to achieve the inclined spiral patterns with constructive and destructive interference while they propagate. It was observed that a linear superposition of both upward and downward modulated waves traveling out of phase could lead to the final spiral pattern transitions observed. The good qualitative agreement of the

toy model and numerical simulations, as well as the possibility of reproducing the spiral pattern changes previously investigated using similar wavenumbers and frequencies obtained from numerical simulations and experimental measurements, indicate that this can be the mechanism that drives the spiral pattern changes, but the reason for the amplitude modulations of each individual wave to occur still is not clear. The possibility of describing the modulations using the complex Ginzburg-Landau equation is an interesting route that should be followed in the future (Deissler 1985, Bekki and Nozaki 1985, Landamn 1987, Bartuccelli et al. 1990, Lopez and Marques 2020).

The SRI turbulent momentum transport behavior in space and time is an important issue regarding how the SRI could transport momentum outwards, allowing matter to aggregate by gravity in the center of accretion disks, leading to proto-planetary stars formation. The spatial structure of $u'_\phi u'_r$ for different stratification values (ΔT , or Rn), shows that the momentum transport in the SRI should be carried by the spirals. Since momentum transfer within the flow is related to the spiral structure, the amplitude modulations are also associated with the spiral axial propagation. This affects $u'_\phi u'_r$ temporal behavior. Low-frequency amplitude modulations in $u'_\phi u'_r$ were observed, indicating that, for smaller values of Froude numbers, momentum can indeed be transferred in bursts. The frequency of the amplitude modulations increases with the Froude number until it reaches a regime where no amplitude modulation occurs, leading to a continuous momentum transfer. A continuous momentum transport regime or a momentum transport occurring in bursts might play different roles and have different impacts on accretion disk theory. Note that different time-dependent momentum transfer regimes were also observed in the amplitude modulation transient regions, for $t \lesssim 100$ minutes, before a more regular amplitude modulation is established. When Froude number reaches $Fr \approx 3.5$, this transition region showed to have a relevant impact in the total momentum transfer, since for time $\gtrsim 90$ minutes, the flow is stable but in the interval $50 \lesssim t \lesssim 90$ minutes, a burst of momentum transfer occurs. This phenomenon could also be important on accretion disk applications, as that might allow proto-planetary stars to form at the early stages of the SRI development, even in cases where the regime becomes stable for $t \rightarrow \infty$.

Finally, the experimental setup at the BTU laboratories also gives the opportunity of exploring counter-rotation SRI regimes. Although counter-rotating regimes may have no direct application in the accretion disk theory, it can also give relevant information about the physics of the SRI (Park et al. 2018), therefore, these regimes should be explored in future investigations.

Appendices

A.1 Radon transforms

The Radon transform $R(r, \phi)$ consists on a Fourier-like technique developed by Radon (1917). This technique that transforms a function defined on a given plane $\eta(z, t)$ into a line domain (Radon 2005). These lines are inside the original 2-d space, with the values of a particular line being equal to the line integral of the original function (over that projected line). Therefore, the Radon transform consists on an angular projection given by:

$$R(r, \phi) = \iint \eta(z, t) \delta(z \cos \phi + t \sin \phi - r) dz dt, \quad (\text{A.1})$$

where δ the Dirac delta function. $r = z \cos \phi + t \sin \phi$ and ϕ are respectively the radius and angle, in polar coordinates, that define the line where the 2-D space will be projected. ϕ can vary from 0 to π . The use of the Dirac delta function forces the integration of $\eta(x, t)$ along the line on which the plane will be projected. If we consider a two-dimensional spatiotemporal wave signal $\eta(z, t)$, traveling in the z direction, the angle ϕ can be converted into a wave drift velocity c through the transformation (Almar et al. 2014)

$$c = \tan(\phi) \frac{dz}{dt}, \quad (\text{A.2})$$

where dz and dt are respectively the spatial and temporal resolution. If the $\eta(z, t)$ signal contains multiple waves, multiple local peaks (r, ϕ) will appear in the Radon spectra. Each propagating crest in the spatiotemporal $\eta(z, t)$ field is detected from their signatures in the Radon space corresponding to a peak value, where the ϕ angle indicates the direction of propagation with respect to the z spatial direction considered. The phase speed of a wave propagating in the z direction will then be obtained using equation A.2. In the case of a spatiotemporal wave field containing incoming (η_{up}) and outgoing (η_{down}) waves, such that $\eta(z, t) = \eta_{up}(z, t) + \eta_{down}(z, t)$, each component can be separated using the inverse RT. The inverse RT is a back-projection of $R(r, \phi)$ at given angles ϕ . The total initial wave signal $\eta(z, t)$ can be reconstructed

from the Radon space to the physical space as (Almar et al. 2014)

$$\eta = \iint R(r, \phi) d\phi dr, \quad (\text{A.3})$$

therefore, the separated wave components can be obtained by applying the limits of integration to the inverse Radon transform as

$$\begin{aligned} \eta_{up}(z, t) &= \int_{-\infty}^{+\infty} \int_1^{89} R(r, \phi) d\phi dr, \\ \eta_{up}(z, t) &= \int_{-\infty}^{+\infty} \int_{91}^{179} R(r, \phi) d\phi dr. \end{aligned} \quad (\text{A.4})$$

Note that the Radon transforms have been successfully applied for separating wave components in different fields, such as surface or internal ocean wave dynamics, to pressure fluctuation concerning aeroacoustic applications (Copeland et al. 1995, Challenor et al. 2001, Yoo et al. 2011, Zhang et al. 2009, Martarelli et al. 2013, Almar et al. 2014).

References

- S. Abide and S. Viazzo. A 2d compact fourth-order projection decomposition method. *Journal of Computational Physics*, 206(1):252–276, 2005.
- S. Abide, M. S. Binous, and B. Zeghamati. An efficient parallel high-order compact scheme for the 3d incompressible navier–stokes equations. *International Journal of Computational Fluid Dynamics*, 31(4-5):214–229, 2017.
- S. Abide, S. Viazzo, I. Raspo, and A. Randriamampianina. Higher-order compact scheme for high-performance computing of stratified rotating flows. *Computers & Fluids*, 174:300–310, 2018.
- D. Acheson. On over-reflexion. *Journal of Fluid Mechanics*, 77(3):433–472, 1976.
- D. Aelbrecht, G. C. D’Hieres, and D. Renouard. Experimental study of the ekman layer instability in steady or oscillating flows. *Continental Shelf Research*, 19(15-16):1851–1867, 1999.
- K. Allen and R. Joseph. A statistical mechanical explanation of the garrett and munk model of oceanic internal waves. *John Hopkins APL Technical Digest*, 10(4):348–361, 1989.
- R. Almar, H. Michallet, R. Cienfuegos, P. Bonneton, M. Tissier, and G. Ruessink. On the use of the radon transform in studying nearshore wave dynamics. *Coastal Engineering*, 92:24–30, 2014.
- C. D. Andereck, S. Liu, and H. L. Swinney. Flow regimes in a circular couette system with independently rotating cylinders. *Journal of fluid mechanics*, 164(3):155–183, 1986.
- P. J. Armitage. Physical processes in protoplanetary disks. In *From Protoplanetary Disks to Planet Formation*, pages 1–150. Springer, 2019.
- K. J. Arrow, H. Azawa, L. Hurwicz, and H. Uzawa. *Studies in linear and non-linear programming*, volume 2. Stanford University Press, 1958.
- M. P. Arroyo and K. D. Hinsch. Recent developments of piv towards 3d measurements. In *Particle image velocimetry*, pages 127–154. Springer, 2007.
- M. Avila, M. Grimes, J. M. Lopez, and F. Marques. Global endwall effects on centrifugally stable flows. *Physics of fluids*, 20(10):104104, 2008.
- M. Bartuccelli, P. Constantin, C. R. Doering, J. D. Gibbon, and M. Gisselgård. On the possibility of soft and hard turbulence in the complex ginzburg-landau equation. *Physica D: Nonlinear Phenomena*, 44(3):421–444, 1990.
- G. Batchelor. *An introduction to fluid dynamics*. Cambridge university press, 2000.
- N. Bekki and K. Nozaki. Formations of spatial patterns and holes in the generalized ginzburg-landau equation. *Physics Letters A*, 110(3):133–135, 1985.
- Y. Bengana and L. S. Tuckerman. Spirals and ribbons in counter-rotating taylor-couette flow: Frequencies from mean flows and heteroclinic orbits. *Physical Review Fluids*, 4(4):044402, 2019.
- P. Billant and J.-M. Chomaz. Self-similarity of strongly stratified inviscid flows. *Physics of fluids*, 13(6):1645–1651, 2001.
- A. Boccaletti, E. Di Folco, E. Pantin, A. Dutrey, S. Guilloteau, Y. Tang, V. Piétu, E. Habart, J. Milli, T. Beck, et al. Possible evidence of ongoing planet formation in ab aurigae—a showcase of the sphere/alma synergy. *Astronomy & Astrophysics*, 637:L5, 2020.

- B. Boubnov, E. Gledzer, and E. Hopfinger. Stratified circular couette flow: instability and flow regimes. *Journal of Fluid Mechanics*, 292:333–358, 1995.
- I. Brazzoli, S. Corgnati, M. Filippi, and S. Viazzo. On a kinetic theory approach to modelling degradation phenomena in conservation sciences. *Mathematical and computer modelling*, 45(9-10):1201–1213, 2007.
- C. Brogan, L. Pérez, T. Hunter, W. Dent, A. Hales, R. Hills, S. Corder, E. Fomalont, C. Vlahakis, Y. Asaki, et al. The 2014 alma long baseline campaign: first results from high angular resolution observations toward the hl tau region. *The Astrophysical Journal Letters*, 808(1):L3, 2015.
- D. L. Brown, R. Cortez, and M. L. Minion. Accurate projection methods for the incompressible navier–stokes equations. *Journal of computational physics*, 168(2):464–499, 2001.
- F. Caton, B. Jانياud, and E. J. Hopfinger. Stability and bifurcations in stratified taylor–couette flow. *Journal of Fluid Mechanics*, 419:93–124, 2000.
- P. G. Challenor, P. Cipollini, and D. Cromwell. Use of the 3d radon transform to examine the properties of oceanic rossby waves. *Journal of Atmospheric and Oceanic Technology*, 18(9):1558–1566, 2001.
- J. G. Charney. Geostrophic turbulence. *Journal of the Atmospheric Sciences*, 28(6):1087–1095, 1971.
- P. R. Childs. *Rotating Flow*. 2011. ISBN 9780123820983.
- A. J. Chorin. Numerical solution of the navier–stokes equations. *Mathematics of computation*, 22(104):745–762, 1968.
- D. Cioranescu and J.-L. Lions. *Nonlinear Partial Differential Equations and Their Applications: College de France Seminar Volume XIV*. Elsevier, 2002.
- D. Coles and C. Van Atta. Measured distortion of a laminar circular couette flow by end effects. *Journal of Fluid Mechanics*, 25(3):513–521, 1966.
- F. Collard, F. Ardhuin, and B. Chapron. Monitoring and analysis of ocean swell fields from space: New methods for routine observations. *Journal of Geophysical Research: Oceans*, 114(C7), 2009.
- A. C. Copeland, G. Ravichandran, and M. M. Trivedi. Localized radon transform-based detection of ship wakes in sar images. *IEEE Transactions on Geoscience and Remote Sensing*, 33(1):35–45, 1995.
- C. Cot. Equatorial mesoscale wind and temperature fluctuations in the lower atmosphere. *Journal of Geophysical Research: Atmospheres*, 106(D2):1523–1532, 2001.
- M. C. Cross and P. C. Hohenberg. Pattern formation outside of equilibrium. *Reviews of modern physics*, 65(3):851, 1993.
- R. J. Deissler. Noise-sustained structure, intermittency, and the ginzburg-landau equation. *Journal of statistical physics*, 40(3-4):371–395, 1985.
- E. Dewan and R. Good. Saturation and the “universal” spectrum for vertical profiles of horizontal scalar winds in the atmosphere. *Journal of Geophysical Research: Atmospheres*, 91(D2):2742–2748, 1986.
- S. L. Dizès and X. Riedinger. The strato-rotational instability of Taylor–Couette and Keplerian flows. *J. Fluid Mech*, 660:147–161, 2010.
- P. Drazin and W. Reid. Hydrodynamic stability. *NASA STI/Recon Technical Report A*, 82:17950, 1981.
- P. G. Drazin. *Introduction to hydrodynamic stability*, volume 32. Cambridge university press, 2002.

- B. Dubrulle. Beyond kolmogorov cascades. *Journal of Fluid Mechanics*, 867, 2019.
- B. Dubrulle, L. Marié, C. Normand, D. Richard, F. Hersant, and J.-P. Zahn. An hydrodynamic shear instability in stratified disks. *Astronomy & Astrophysics*, 429:1–13, 2004.
- E. M. Edlund and H. Ji. Nonlinear stability of laboratory quasi-keplerian flows. *Physical Review E*, 89(2):021004, 2014.
- E. M. Edlund and H. Ji. Reynolds number scaling of the influence of boundary layers on the global behavior of laboratory quasi-keplerian flows. *Physical Review E*, 92(4):043005, 2015.
- E. Falgarone, B. Godard, and P. Hily-Blant. Turbulence in the diffuse interstellar medium. *Proceedings of the International Astronomical Union*, 7(S280):187–202, 2011.
- J. H. Ferziger, M. Perić, and R. L. Street. *Computational methods for fluid dynamics*, volume 3. Springer, 2002.
- J.-B. Flor. *Fronts, waves and vortices in geophysical flows*, volume 805. Springer, 2010.
- J.-B. Flór, L. Hirschberg, B. Oostenrijk, and G. J. F. van Heijst. Onset of centrifugal instability at a rotating cylinder in a stratified fluid. *Physics of Fluids*, 30(8):084103, 2018.
- S. Fromang and G. Lesur. Angular momentum transport in accretion disks: a hydrodynamical perspective. *arXiv preprint arXiv:1705.03319*, 2017.
- C. F. Gammie. Layered accretion in t tauri disks. *The Astrophysical Journal*, 457:355, 1996.
- C. Garrett and W. Munk. Space-time scales of internal waves. *Geophysical Fluid Dynamics*, 3(3):225–264, 1972.
- C. Garrett and W. Munk. Space-time scales of internal waves: A progress report. *Journal of Geophysical Research*, 80(3):291–297, 1975.
- M. Gellert and G. Rüdiger. Stratorotational instability in Taylor–Couette flow heated from above. *J. Fluid Mech*, 623:375–385, 2009.
- A. E. Gill. *Atmosphere-ocean dynamics*. Elsevier, 1982.
- K. Goda. Inverse modeling for large-eddy simulation, a multistep technique with implicit difference schemes for calculation two and three dimensional cavity flows. *J. Comput. Phys*, 30(12):76–95, 1979.
- L. Gostiaux, H. Didelle, S. Mercier, and T. Dauxois. A novel internal waves generator. *Experiments in Fluids*, 42(1):123–130, 2007.
- P. M. Gresho and R. L. Sani. On pressure boundary conditions for the incompressible navier-stokes equations. *International Journal for Numerical Methods in Fluids*, 7(10):1111–1145, 1987.
- J.-L. Guermond, P. Mineev, and J. Shen. An overview of projection methods for incompressible flows. *Computer methods in applied mechanics and engineering*, 195(44-47):6011–6045, 2006.
- F. H. Harlow and J. E. Welch. Numerical calculation of time-dependent viscous incompressible flow of fluid with free surface. *The physics of fluids*, 8(12):2182–2189, 1965.
- C. Hoffmann, M. Heise, S. Altmeyer, J. Abshagen, A. Pinter, G. Pfister, and M. Lücke. Nonlinear defects separating spiral waves in taylor-couette flow. *Physical Review E*, 80(6):066308, 2009.
- S. Hugues and A. Randriamampianina. An improved projection scheme applied to pseudospectral methods for the incompressible navier–stokes equations. *International Journal for Numerical Methods in Fluids*, 28(3):501–521, 1998.

- R. Ibanez, H. L. Swinney, and B. Rodenborn. Observations of the stratorotational instability in rotating concentric cylinders. *Physical Review Fluids*, 1(5):053601, 2016.
- K. D. Jensen. Flow measurements. *Journal of the Brazilian Society of Mechanical Sciences and Engineering*, 26(4):400–419, 2004.
- G. E. Karniadakis, M. Israeli, and S. A. Orszag. High-order splitting methods for the incompressible navier-stokes equations. *Journal of computational physics*, 97(2):414–443, 1991.
- D. E. Keyes, L. C. McInnes, C. Woodward, W. Gropp, E. Myra, M. Pernice, J. Bell, J. Brown, A. Clo, J. Connors, et al. Multiphysics simulations: Challenges and opportunities. *The International Journal of High Performance Computing Applications*, 27(1):4–83, 2013.
- J. Kim and P. Moin. Application of a fractional-step method to incompressible navier-stokes equations. *Journal of computational physics*, 59(2):308–323, 1985.
- H. Klahr, T. Pfeil, and A. Schreiber. Instabilities and flow structures in protoplanetary disks: Setting the stage for planetesimal formation. *arXiv preprint arXiv:1806.03896*, 2018.
- R. Knikker. Study of a staggered fourth-order compact scheme for unsteady incompressible viscous flows. *International journal for numerical methods in fluids*, 59(10):1063–1092, 2009.
- A. Kolmogorov. Local structure of turbulence in an incompressible fluid for very large reynolds numbers,” dokl. akad. nauk. sssr 30, 299–303 (1941);“energy dissipation in locally isotropic turbulence. *ibid.*, 32:19–21, 1941.
- L. Kovasznay. Hot-wire investigation of the wake behind cylinders at low reynolds numbers. *Proceedings of the Royal Society of London. Series A. Mathematical and Physical Sciences*, 198(1053):174–190, 1949.
- P. K. Kundu and I. M. Cohen. *Fluid mechanics*. Elsevier, 2001.
- D.-C. Kuo and K. S. Ball. Taylor–couette flow with buoyancy: Onset of spiral flow. *Physics of Fluids*, 9(10):2872–2884, 1997.
- Kyushu University. *Environmental Fluid Dynamics*. Springer, 2017.
- M. J. Landamn. Solutions of the ginzburg-landau equation of interest in shear flow transition. *Studies in Applied Mathematics*, 76(3):187–237, 1987.
- L. Landau and E. Lifshitz. Fluid mechanics. *Course of theoretical physics*, 6, 1959.
- M. Le Bars and P. Le Gal. Experimental analysis of the stratorotational instability in a cylindrical couette flow. *Physical Review Letters*, 99(6):064502, 2007. ISSN 00319007.
- C. Leclercq, F. Nguyen, and R. R. Kerswell. Connections between centrifugal, stratorotational, and radiative instabilities in viscous taylor-couette flow. *Physical Review E*, 94(4):043103, 2016.
- S. K. Lele. Compact finite difference schemes with spectral-like resolution. *Journal of computational physics*, 103(1):16–42, 1992.
- G. Lesur. *Instabilités et sources locales de turbulence dans les disques d’accrétion*. PhD thesis, 2007.
- N. Li and S. Laizet. 2decomp & fft-a highly scalable 2d decomposition library and fft interface. In *Cray user group 2010 conference*, pages 1–13, 2010.
- D. K. Lilly. Instability of ekman boundary flow. *Physics of Fluids*, 10(9):S307–S307, 1967.

- E. Lindborg. The energy cascade in a strongly stratified fluid. *Journal of Fluid Mechanics*, 550:207–242, 2006.
- J. M. Lopez and M. Avila. Boundary-layer turbulence in experiments on quasi-keplerian flows. *Journal of Fluid Mechanics*, 817:21–34, 2017.
- J. M. Lopez and F. Marques. Impact of centrifugal buoyancy on strato-rotational instability. *J. Fluid Mech*, 890(A9), 2020.
- Y. V. Lvov, K. L. Polzin, and E. G. Tabak. Energy spectra of the ocean’s internal wave field: Theory and observations. *Physical review letters*, 92(12):128501, 2004.
- W. Lyra and O. M. Umurhan. The initial conditions for planet formation: Turbulence driven by hydrodynamical instabilities in disks around young stars. *Publications of the Astronomical Society of the Pacific*, 131(1001):072001, 2019.
- V. S. L’vov and S. Nazarenko. Spectrum of kelvin-wave turbulence in superfluids. *JETP Letters*, 91(8):428–434, 2010.
- L. R. Maas. Wave focusing and ensuing mean flow due to symmetry breaking in rotating fluids. *Journal of Fluid Mechanics*, 437:13, 2001.
- L. R. Maas, D. Benielli, J. Sommeria, and F.-P. A. Lam. Observation of an internal wave attractor in a confined, stably stratified fluid. *Nature*, 388(6642):557–561, 1997.
- P. S. Marcus, S. Pei, C.-H. Jiang, and P. Hassanzadeh. Three-dimensional vortices generated by self-replication in stably stratified rotating shear flows. *Physical review letters*, 111(8):084501, 2013.
- P. S. Marcus, S. Pei, C.-H. Jiang, J. A. Barranco, P. Hassanzadeh, and D. Lecoanet. Zombie vortex instability. i. a purely hydrodynamic instability to resurrect the dead zones of protoplanetary disks. *The Astrophysical Journal*, 808(1):87, 2015.
- M. Martarelli, P. Castellini, and E. P. Tomasini. Subsonic jet pressure fluctuation characterization by tomographic laser interferometry. *Experiments in fluids*, 54(12):1626, 2013.
- C. Ménesguen, B.-L. Hua, C. Papenberg, D. Klaeschen, L. Geli, and R. Hobbs. Effect of bandwidth on seismic imaging of rotating stratified turbulence surrounding an anticyclonic eddy from field data and numerical simulations. *Geophysical Research Letters*, 36(24), 2009.
- H. Meyerdierks, A. Heithausen, and K. Reif. The north celestial pole loop. *Astronomy and Astrophysics*, 245:247–256, 1991.
- M. J. Molemaker, J. C. McWilliams, and I. Yavneh. Instability and equilibration of centrifugally stable stratified taylor-couette flow. *Physical review letters*, 86(23):5270, 2001.
- Y. Morinishi, T. S. Lund, O. V. Vasilyev, and P. Moin. Fully conservative higher order finite difference schemes for incompressible flow. *Journal of computational physics*, 143(1):90–124, 1998.
- F. Moukalled, L. Mangani, and M. Darwish. Temporal discretization: The transient term. In *The Finite Volume Method in Computational Fluid Dynamics*, pages 489–533. Springer, 2016.
- P. Müller, J. McWilliams, and M. Molemaker. Routes to dissipation in the ocean: The 2d/3d turbulence conundrum. *Marine turbulence: theories, observations and models*, pages 397–405, 2005.
- G. A. Muro-Arena, C. Ginski, C. Dominik, M. Benisty, P. Pinilla, A. Bohn, T. Moldenhauer, W. Kley, D. Harsono, T. Henning, et al. Spirals inside the millimeter cavity of transition disk sr 21. *Astronomy & Astrophysics*, 636:L4, 2020.

- G. Nastrom and K. S. Gage. A climatology of atmospheric wavenumber spectra of wind and temperature observed by commercial aircraft. *Journal of the atmospheric sciences*, 42(9):950–960, 1985.
- H. Nobach and E. Bodenschatz. Limitations of accuracy in piv due to individual variations of particle image intensities. *Experiments in fluids*, 47(1):27–38, 2009.
- O. A. Olafadehan, K. E. Abhulimen, and M. Anubi. Grid design and numerical modeling of multiphase flow in complex reservoirs using orthogonal collocation schemes. *Applied Petrochemical Research*, 8(4):281–298, 2018.
- H. A. Panofsky and J. A. Dutton. Atmospheric turbulence john wiley. *New York*, 1984.
- J. Park. *Waves and instabilities on vortices in stratified and rotating fluids*. PhD thesis, 2012.
- J. Park and P. Billant. The stably stratified Taylor–Couette flow is always unstable except for solid-body rotation. *Journal of Fluid Mechanics*, 725:262–280, 2013.
- J. Park, P. Billant, J.-J. Baik, and J. M. Seo. Competition between the centrifugal and strato-rotational instabilities in the stratified taylor–couette flow. *Journal of Fluid Mechanics*, 840:5–24, 2018.
- S. Patankar and D. Spalding. A finite-difference procedure for solving the equations of the two-dimensional boundary layer. *International Journal of Heat and Mass Transfer*, 10(10):1389–1411, 1967.
- S. K. Pawar, R. H. Abrahams, N. G. Deen, J. T. Padding, G.-J. van der Gulik, A. Jongsma, F. Innings, and J. Kuipers. An experimental study of dynamic jet behaviour in a scaled cold flow spray dryer model using piv. *The Canadian Journal of Chemical Engineering*, 92(12):2013–2020, 2014.
- J. Pedlosky. *Waves in the ocean and atmosphere: introduction to wave dynamics*. Springer Science & Business Media, 2013.
- E. Polizzi and A. Sameh. Spike: A parallel environment for solving banded linear systems. *Computers & Fluids*, 36(1):113–120, 2007.
- N. Ponchaut, C. Mouton, H. Hornung, and D. Dabiri. 3d particle tracking velocimetry method: Advances and error analysis. 2005.
- S. B. Pope. *Turbulent flows*, 2001.
- W. H. Press, S. A. Teukolsky, W. T. Vetterling, and B. P. Flannery. *Numerical recipes 3rd edition: The art of scientific computing*. Cambridge university press, 2007.
- J. Radon. Über die bestimmung von funktionen durch ihre intergralwerte längs gewisser. 1917.
- J. Radon. 1.1 über die bestimmung von funktionen durch ihre integralwerte längs gewisser mannigfaltigkeiten. *Classic papers in modern diagnostic radiology*, 5:21, 2005.
- I. Raspo, S. Hugues, E. Serre, A. Randriamampianina, and P. Bontoux. A spectral projection method for the simulation of complex three-dimensional rotating flows. *Computers & fluids*, 31(4-7):745–767, 2002.
- I. Raspo, S. Viazzo, A. Randriamampianina, G. Meletti, U. Harlander, T. Seelig, and A. Krebs. Low mach number modeling of stratorotational instability in a water-filled taylor-couette cavity. 2018.
- P. Rebusco, O. M. Umurhan, W. Kluźniak, and O. Regev. Global transient dynamics of three-dimensional hydrodynamical disturbances in a thin viscous accretion disk. *Physics of Fluids*, 21(7):076601, 2009.

- L. Richardson. *Weather prediction by numerical process* (Cambridge U. Press), 1922.
- C. Rodda. *Gravity wave emission from jet systems in the differentially heated rotating annulus experiment*. PhD thesis, 2019.
- G. Rüdiger and D. A. Shalybkov. Stratorotational instability in MHD Taylor-Couette flows. *Astronomy & Astrophysics*, 493:375–383, 2009.
- G. Rüdiger, T. Seelig, M. Schultz, M. Gellert, C. Egbers, and U. Harlander. The stratorotational instability of Taylor-Couette flows of moderate Reynolds numbers. *Geophysical & Astrophysical Fluid Dynamics*, 111(6):429–447, 2017.
- T. Seelig, U. Harlander, and M. Gellert. Experimental investigation of stratorotational instability using a thermally stratified system: instability, waves and associated momentum flux. *Geophysical & Astrophysical Fluid Dynamics*, 112(4):239–264, 2018.
- D. Shalybkov and G. Rüdiger. Stability of density-stratified viscous Taylor-Couette flows. *Astronomy & Astrophysics*, 438(2):411–417, 2005.
- J. Shen. Hopf bifurcation of the unsteady regularized driven cavity flow. *Journal of Computational Physics*, 91(1):254, 1990.
- S. Shionoya. Flow regimes between two independently rotating cylinders. In *Proc. 19th Turbulence Symposium, 1987*, pages 177–181, 1987.
- Y. M. Shtemler, M. Mond, G. Rüdiger, O. Regev, and O. M. Umurhan. Non-exponential hydrodynamical growth in density-stratified thin Keplerian discs. *Monthly Notices of the Royal Astronomical Society*, 406(1):517–528, 2010. ISSN 00358711.
- K. Smith, G. Boccaletti, C. Henning, I. Marinov, C. Tam, I. Held, and G. Vallis. Turbulent diffusion in the geostrophic inverse cascade. *Journal of Fluid Mechanics*, 469:13, 2002.
- X.-H. Sun. Application and accuracy of the parallel diagonal dominant algorithm. *Parallel Computing*, 21(8):1241–1267, 1995.
- X.-H. Sun and D. T. Rover. Scalability of parallel algorithm-machine combinations. *IEEE Transactions on Parallel and Distributed Systems*, 5(6):599–613, 1994.
- B. R. Sutherland. *Internal gravity waves*. Cambridge University Press, 2010.
- J. K. Svein. An introduction to MatPiv v. 1.6. 1. *Preprint series. Mechanics and Applied Mathematics*, NBN: no-23418, 2004.
- G. Taylor. Stability of a viscous liquid contained between two rotating cylinders. *Phil. Trans. R. Soc. Lond.* A January. 1923.
- R. Temam. Sur l’approximation de la solution des équations de Navier-Stokes par la méthode des pas fractionnaires (ii). *Archive for Rational Mechanics and Analysis*, 33(5):377–385, 1969.
- R. E. Thomson and W. J. Emery. *Data analysis methods in physical oceanography*. Newnes, 2014.
- N. Turner and J. Drake. Energetic protons, radionuclides, and magnetic activity in protostellar disks. *The Astrophysical Journal*, 703(2):2152, 2009.
- A. Vallgren, E. Deusebio, and E. Lindborg. Possible explanation of the atmospheric kinetic and potential energy spectra. *Physical Review Letters*, 107(26):268501, 2011.
- M. Van Dyke. *An album of fluid motion*. 1982.

- S. Viazzo, A. Dejoan, and R. Schiestel. Spectral features of the wall-pressure fluctuations in turbulent wall flows with and without perturbations using les. *International Journal of Heat and Fluid Flow*, 22(1):39–52, 2001.
- R. Visser and C. Dullemond. Sub-keplerian accretion onto circumstellar disks. *Astronomy & Astrophysics*, 519:A28, 2010.
- T. Von Larcher, S. Viazzo, U. Harlander, M. Vincze, and A. Randriamampianina. Instabilities and small-scale waves within the stewartson layers of a thermally driven rotating annulus. *Journal of Fluid Mechanics*, 841:380–407, 2018.
- C. Wang and N. J. Balmforth. Strato-rotational instability without resonance. *Journal of Fluid Mechanics*, 846:815–833, 2018.
- J. Williamson. Low-storage runge-kutta schemes. *Journal of Computational Physics*, 35(1):48–56, 1980.
- E. Withjack and C. Chen. An experimental study of Couette instability of stratified fluids. *Journal of Fluid Mechanics*, 66(4):725—737, 1974.
- I. Yavneh, J. C. McWilliams, and M. J. Molemaker. Non-axisymmetric instability of centrifugally stable stratified Taylor–Couette flow. *J. Fluid Mech*, 448:1–21, 2001.
- P. Yecko. Accretion disk instability revisited-transient dynamics of rotating shear flow. *Astronomy & Astrophysics*, 425(2):385–393, 2004.
- E. Yim and P. Billant. On the mechanism of the gent–mcwilliams instability of a columnar vortex in stratified rotating fluids. *Journal of Fluid Mechanics*, 780:5–44, 2015.
- J. Yoo, H. M. Fritz, K. A. Haas, P. A. Work, and C. F. Barnes. Depth inversion in the surf zone with inclusion of wave nonlinearity using video-derived celerity. *Journal of waterway, port, coastal, and ocean engineering*, 137(2):95–106, 2011.
- S. Zhang, C. Zhang, and Z. Qi. Wave swash velocity estimation using ridgelet transform. In *2009 9th International Conference on Electronic Measurement & Instruments*, pages 4–1078. IEEE, 2009.

Acknowledgement

During this time developing my PhD thesis, I had the wonderful opportunity to meet incredible people that contributed a lot to my development professionally, but most of all, personally. And I would like to thank these people enormously and try to show in these next few words how important for me they are.

Firstly, I would like to thank my advisor in Germany, Uwe Harlander, that besides having an impressive vast knowledge and helping me a lot with my learning process, my development, and with my work on such interesting topics, is an extremely helpful, kind, understanding, and interesting person.

I would also like to thank my advisor in France, Stéphane Viazzo, for all the help, caring, conversations, and the wonderful moments I always passed with him. For all the discussions on which I learned a lot of things either related to my thesis, to the french language and culture, and related to many other topics.

I really can not express how lucky I feel to have had such wonderful advisors during the development of my PhD thesis.

I would like to enormously thank my very good Friend Torsten Seelig, for all the scientific discussions, for very carefully explaining and helping me with many of the experimental procedures I used to develop my thesis, for helping me understanding many physical phenomena related to my topics of studies and other topics, for reviewing carefully many chapters of this thesis, and most of all, for being such a wonderful friend always. Torsten is sure a very essential person for me, not only in the development of this thesis but in my life. I truly can not explain how important to me my friendship with this wonderful human being is.

I would also like to thank (infinitely!) Stéphane Abide for being such an essential person in the development of this thesis, and for always being an incredibly nice, understanding, and patient person. I would like to thank Stéphane for helping me so much understanding the many aspects of the numerical techniques developed to investigate the interesting phenomena in this thesis, for helping me understand all the details of the code, for helping to write the numerical chapter of this thesis, and for the few beers around Perpignan, Marseille, and hopefully for the many future beers and works together to come. This thesis could not be developed as it was without the very close help of Stéphane Abide. But it would be even unfair not to thank Stéphane even more for being such a nice, caring, and wonderful person that as he is.

I would also like to thank a lot my very dear friend Costanza Rodda, that helped me reviewing part of this thesis, which always helped me with many relevant discussions and also for being such a nice and wonderful friend since the beginning of my PhD. And this wonderful friendship, I definitely will carry for all my life.

I also thank a lot Andreas Krebs, for all the help, for the close contact, for the friendly discussions, and for the very nice time spent around in Cottbus.

I would also like to thank Peter Szabo for helping me with the German abstract in this thesis, and for being the smelliest person I could ever imagine to share my office with.

I also thank very much the incredibly lovely Isabelle Raspo and Anthony Randriamampianina in Marseille, for all the helpful contribution and all the caring during my PhD time in Marseille.

I would also like to the many kind people that helped me with several bureaucratic issues, especially mentioning the very friendly Birte Seffert, Erick Serre, Pascal Campion, Robert Rode, and Michel Pognant.

I would like to thank a lot my family and the many colleagues and friends that were part of my life during the development of my thesis, all those that were near or far during this period, old friends and new ones. You are very important. I know I will carry many of you as close friends wherever I and all you wonderful people will be.

Finally, I thank the DFG, the Procope collaboration, the BTU CS, and the AMU for the financial support and the structure during the development of this thesis.